Department of Civil and Environmental Engineering

University of Strathclyde

Deriving field-based statistical relationships to characterize the geometry, heterogeneity and permeability of faults in mixed sand-shale sequences: a new tool for upscaling flow properties

A Thesis presented for the Degree of Doctor of Philosophy

by

Yannick Kremer

July 2014

This thesis is the result of the author's original research. It has been composed by the author and has not been previously submitted for examination which has led to the award of a degree.

Signed:

Date:

Abstract

Fault zones can strongly affect fluid flow in the subsurface. Faults can act as (partial) barriers to flow, as conduits and as combined conduit-barrier systems. Understanding the relationship between faulting and fluid flow has many practical applications, including hydrocarbon exploration and production, mineral exploration, groundwater management, radioactive waste disposal, geothermal energy and carbon sequestration. This study is primarily focussed at the applications in the hydrocarbon industry.

For hydrocarbon exploration, faults are important because they can act as long term barriers (fault sealing), in which case they can be part of structural traps. Faults acting as conduits also need to be considered, hydrocarbons moving vertically along a fault can either migrate into a reservoir, or the hydrocarbons can leak out of the reservoir along the fault. For hydrocarbon production also the short term effect of faults needs to be considered, as faults can block or baffle flow towards a well.

For all these scenarios it is currently difficult to reliably predict the behaviour of the fault deep underground. The research presented in this thesis aims to improve this prediction. Several studies have shown that fluid flow along and across fault zones is strongly affected by the heterogeneity of the fault zone and the presence of connected high permeability pathways. Both heterogeneity and high permeability pathways cannot be detected or predicted using currently available hydrocarbon industry tools. Therefore this study uses extensive field studies of faults exposed at the earth's surface, to characterize these features in detail. For this study 12 fault exposures have been studied in SE Utah and the western Sinai in Egypt. The faults are mapped with mm to cm-scale detail and samples are taken for petrophysical analysis. These data are further analyzed by numerical modelling of fluid flow through the fault zones. By combining fieldwork and flow modelling, the features that most strongly affect fluid flow (key flow controls) can be identified. Key flow controls provide a tool for efficient collection of data that allow the statistical characterization of fault zones. Statistical characterization of fault zone fluid flow properties can be used to improve hydrocarbon industry workflows.

This study has revealed a wide variety in fault architectures for faults in sand-shale sequences. None of the faults studied here is dominated by a single homogenous gouge of mixed sand and shale, as is assumed by many current workflows for predicting (upscaled) fault permeability. With such a wide variety of fault architectures, it is impossible to define a simple rule for the fluid-flow characteristics of faults. For successful prediction of fault sealing and fault permeability it will be necessary to successfully predict fault architecture. Predicting fault architecture will require the detailed evaluation of host rock stratigraphy, fault structure and the deformation, fluid flow and thermal history.

Acknowledgements

So here it finally is: my PhD thesis. This would not have been possible without the help, support and inspiration offered by people from all over the world. First of all I would like to thank my supervisors Zoe Shipton and Rebecca Lunn for their expert advice, enthusiasm, encouragement, support and friendship during this PhD. In addition I am thankful to all the members of the Fault and Fluid Flow research group here at the University of Strathclyde for stimulating debates, good advice and the many great times we have had both in the office and the field.

I am grateful to Total for funding this PhD. In addition I would like to thank all the Total staff who have provided so much advice and useful reflection during the years. I would especially like to thank Christopher Wibberley who made this project possible and whose input was particularly vital for this research. In addition I would like to thank Claude Gout, Alan Irving, Philippe Ruelland, Marc Giba, Gilles Drullion, Raymi Castilla and Livinus Nosike. In addition I would like to thank Bernard Geiss, José van Koppen and Koenraad Elewaut for their help during my internship at Total The Hague, which provided an invaluable introduction to the hydrocarbon industry and fault sealing and permeability in particular.

This PhD study included four months of fieldwork. During this time I have enjoyed the company and help of a great deal of people. I would like to thank Jonathan Caine and Andy Manning of the USGS for inviting me to join them for a study in Elk Basin. It was a great opportunity to learn about characterizing fluid flow near faults. I am grateful to Alvar Braathen, Jan Tveranger and Eivind Bastesen for inviting me to come to the Centre for Integrated Petroleum Research and join them during the fieldwork in the Sinai desert. I efficiently gathered many useful data in Egypt. I am very thankful to all those who assisted me in the field. Alistair McCay, thank you for coming along to Bornholm, it was a beautiful island, if only there had been an actual outcrop. Kathryn Schuller, thank you for your help and hospitality in Colorado. Rachael Ellen, thank you for assisting me in Sinai and more importantly Toyota good! Euan Macrae, Damien Hay, Kieran Connolly, Elodie Saillet and Nyree Mackay thank you so much for your time helping me with the fieldwork in Utah. I have had a great time with all of you, working and camping in the many amazing landscapes you can find in Utah. Stephanie and Toby, thank you for your help over the years, it was nice to see a friendly face each time I came to Salt Lake City. Jim Evans and others at USU Logan, thank you for all the good advice and help with equipment.

I would like to thank Professor Quentin Fisher, Dr. Carlos Grattoni and Dr. John Martin from the University of Leeds for their help with the permeability measurements. This work has benefitted greatly from their expertise. Thanks to Dr. Nic Odling for his help with the preparation of sampled for the XRD analysis. And thanks to John Gilleece and John Carlin

for their help with preparing samples.

I am grateful to my friends and family for their support during this research. Thank you for a great time. Thank you for coming to visit me here in Scotland, thank you for the trips we have made, thank you for the games of Frisbee and thank you for all the fun we have had. Thank you to my parents John and Annemarie, it would not have been possible without your support. And finally, thank you Cheryl for your love and support.

Contents

Chapter 1

Introduction

1.1 Rationale

Fault zones are common features in the earth's crust. They form when rocks deform brittly due to tectonic stresses. Deformation is localized to a narrow zone, with the rocks on both sides of the fault moving in opposite directions. After the movement ceases, the fault remains as a zone with different properties to the surrounding host rocks.

Faults have long been known to affect the flow of fluids in the subsurface; they can act as barriers to flow, as conduits or combined barrier-conduits. The complicated permeability structure of faults presents a problem to industries dealing with fluids flowing through the shallow crust. These problems are frequently encountered in the hydrocarbon industry but also relevant to geothermal energy production, geological disposal of radioactive waste, groundwater management, carbon capture and storage and the formation of ore deposits.

1.2 Fault structure

Faults are often referred to as planes. This makes sense when considering the whole fault on the scale of a geological map or seismic data set. However when looking at a fault in an outcrop, it is very clear that it also has a thickness. It is therefore important to consider faults as zones. These zones have a different structure, permeability and often composition than the surrounding protolith.

Fault zone architectures are commonly subdivided (figure 1.1) into a fault core, a damage zone and protolith (Caine et al., 1996). The definition is based on strain; the fault core has accommodated most deformation, the damage zone hosts subsidiary structures and the protolith is not mechanically affected by the fault. Precise strain threshold values for the different components are not provided by the original definition. In practice this does usually not present a problem, as in most outcrops the fault core and damage zone are very distinct. In the fault core the original depositional features such as bedding have been overprinted. In the damage zone, bedding is still clearly recognizable, but the rock is intensely fractured and can contain subsidiary faults. The fault core and damage zone commonly have different structural, compositional and hydrological characteristics. Commonly the fault core is considered to be a barrier to flow, whereas the fractured damage zone forms a pathway for flow along the fault

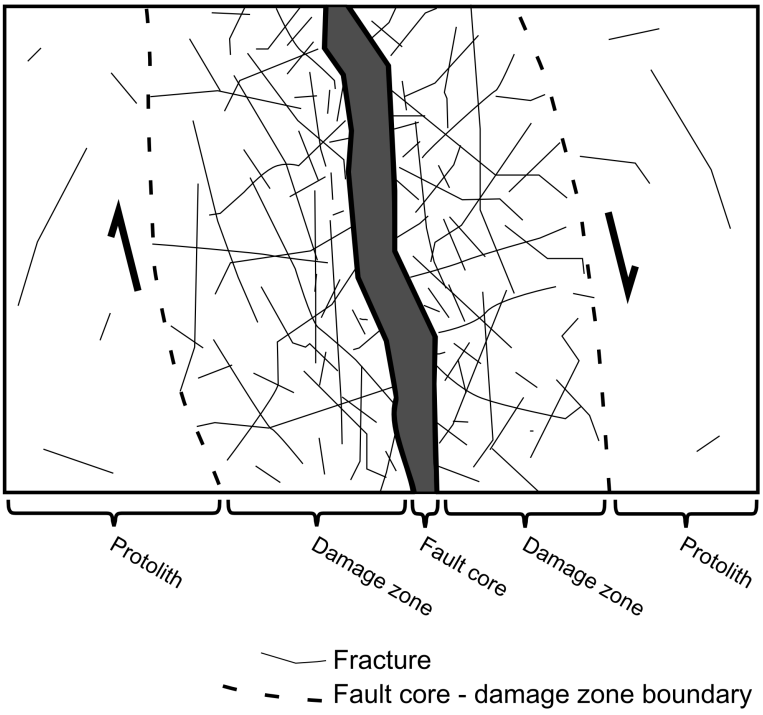

Figure 1.1: Sketch illustrating the fault core damage zone concept for fault structure.

(Evans et al., 1997). This model is often appropriate, but it is a clear simplification and several exceptions have been observed during this study.

The fault core and damage zone model describes architecture on an outcrop scale, but does not describe the large scale structure of the fault. Because of this, the model has been criticised as being an oversimplification (Childs et al., 2012). For fluid flow, larger scale fault structure can be much more important. E.g. fluids could bypass the fault zone through a relay ramp. In addition the model does not capture the complexity of many faults (e.g. Faulkner et al., 2003, van der Zee and Urai, 2005). Minor strands could be considered to be part of the damage zone or could be considered to have fault cores themselves. In this thesis I have chosen to use the terms as defined above, because despite the problems, the terms have proven useful for a basic first order classification of fault architecture in the outcrop.

1.2.1 Displacement

An important parameter for describing and quantifying faults is their displacement. Displacement or net slip describes the distance a point on the fault surface has moved along the fault. Displacement is not continuous along the fault. For an idealized fault, the fault plane is elliptical with the maximum displacements occurring near the centre of the fault plane, decreasing to zero at the edges. Real world faults typically have more complicated geometries and displacement profiles, because they develop in a heterogeneous medium and grow by the linkage of smaller faults (Tchalenko, 1970, Larsen, 1988, Walsh et al., 1999, Childs et al., 2009).

It is often difficult to determine the net slip of a fault. In both the field and on seismic data often the only available indicator of displacement is provided by the separation of a stratigraphic horizon by the fault. Without knowing the direction of the fault movement this only provides a

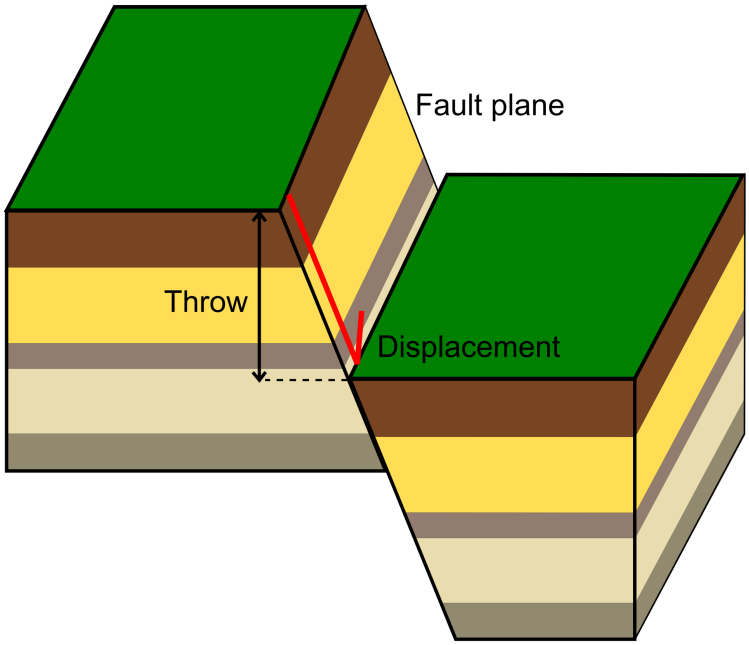

Figure 1.2: Sketch illustrating the difference between fault throw and displacement.

minimum estimate of fault displacement. In the field the direction of the slip vector can often be obtained from striations. In some cases the fault displaces linear elements such as fold axes or fluvial channels which can be used to determine the exact displacement.

A commonly used term is throw, which is the vertical component of fault displacement. It is easy to measure on seismic data or from geological maps. The downside is that it only provides the slip if the dip of the fault plane and the slip vector are known .

1.2.2 Sub-seismic and seismic scale faults

On the seismic reflection data used for hydrocarbon exploration and production, faults can be detected by the offset of (usually sub-horizontal sedimentary) reflectors. Imaging the fault plane directly is rarely possible. The seismic data has a limited resolution, which forms a limit to the minimum offsets that can be detected. The effective resolution can strongly vary, depending on several factors (survey technology, data processing, lithology, depth, etc.). In hydrocarbon industry-focussed literature, a distinction is commonly made between seismic and sub-seismic scale faults. Seismic scale faults can be detected on seismic data, whereas the offset of subseismic scale faults is too small to alllow detection. Commonly a cut off value of 10 to 30 m offset are used to distinguish between seismic and subseismic-scale faults (Gauthier and Lake 1993, Maerten et al., 2006). In this study a threshold of 10m is used.

1.3 Faults in the hydrocarbon industry

It has long been recognized that faults can have a pronounced effect on the flow of hydrocarbons in the subsurface. Emmons, 1921 discusses several examples of oil fields in which impermeable faults form part of structural traps and other examples where faults act as conduits for fluid

flow along the fault. It is now widely recognized that faults can act as barriers, conduits and combined conduit barrier systems (Caine et al., 1996).

1.3.1 Faults as barriers to flow

Faults acting as barriers are commonly encountered in the hydrocarbon industry and being able to predict this behaviour presents a critical advantage. Faults acting as a barrier to fluid flow can do so in several ways.

1.3.1.1 Juxtaposition

The most obvious way for a fault to form a barrier to across fault-flow, is when fault displacement juxtaposes a reservoir rock against a less permeable rock type. Where detailed information on the subsurface structure (e.g. 3D seismic data) is available, careful analysis of the fault plane and faulted horizons can establish the juxtaposition relationships (Allan 1989, Knipe, 1997, Yielding et al., 1997, Cerveny et al., 2004, Dee et al., 2005). As pointed out by van der Zee and Urai, 2005 and Faerseth et al., 2007 using the seismic data it is usually only possible to resolve a single fault plane whereas in many fault exposures we can see displacement being distributed over several slip surfaces. This strongly complicates juxtaposition relationships, as for example a sliver of reservoir rock entrained in the fault zone could connect two reservoir units which appear disconnected on a seismic scale.

1.3.1.2 Membrane seals and baffles

Where two reservoir rocks are juxtaposed on both sides of a fault, the fault zone itself can still act as a barrier. In the fault seal literature this is commonly referred to as membrane sealing after Watts, 1987. Several mechanisms have been identified in the literature which reduce the permeability of the fault zone. Most authors focus on processes which incorporate shale into the fault zone (e.g. Weber 1987, Yielding et al., 1997, Harris et al., 2002, Yielding 2002, Bretan et al., 2003, Faerseth, 2006). Shale has a very low permeability, and therefore its inclusion in the fault zone can strongly reduce the bulk permeability of the fault. Other commonly reported causes for the fault zone itself to form a barrier to flow are cementation and grain size reduction (e.g. Knott 1993, Leveille et al., 1997, Shipton et al., 2002, Shipton et al., 2005, Eichhubl et al., 2009).

The work presented in this study is first and foremost relevant to the analysis of membrane effects, presenting detailed analyses of what is inside the fault, and how that can affect flow through the fault zone.

For membrane seal analysis, several estimation routines exist to predict the effect of the fault; Shale Gouge Ratio (SGR, Fristad et al., 1996, Yielding et al., 1997), Clay Smear Potential (CSP, Bouvier et al., 1989), Shale Smear Factor (SSF, Lindsay et al., 1993). Of these Shale Gouge Ratio (SGR) is the most commonly used. It attempts to predict the shale content at a point in the fault by calculating the average shale content of the host rock in a vertical interval which length is equal to the throw on the fault

Originally the SGR, CSP and SSF were developed to predict the sealing potential of faults in exploration. In its simplest form faults with an SGR value below a threshold value (typically 25%) are assumed to be non-sealing and faults with a higher SGR value are assumed to be sealing. If sufficient data is available, SGR can be calibrated by plotting a fault's SGR value

against the height of the hydrocarbon column it seals. Later studies have expanded the usage of these algorithms to production work-flows. This assumes that SGR is assumed to predict the volumetric shale fraction of the rocks in the fault core, which is used to estimate a permeability.

Several authors have published case studies in which these methods succesfully predicted the hydrological behaviour of the fault (Manzocchi et al., 1999, Harris et al., 2002, Jolley et al., 2007). SGR was used to predict the permeability of the fault zone. With these permeabilities assigned to faults in reservoir flow models, the models reproduced observed production history (history matching). However at present no data is available in the public domain on the overall success rate of these methodologies. Corona et al., 2010 suggest that detailed analysis of juxtaposition relationships may yield more fruitful results and predicting membrane sealing remains very difficult. Another criticism for these work-flows is that they model fault permeability as a smoothly varying property. This is stark contrast to faults exposed at the surface, which vary strongly over short distances (Lunn et al., 2008).

1.3.1.3 Exploration vs production time-scales

When evaluating the effect of faults on fluid flow it is important to consider the time-scale over which fluid flow is of interest. In the hydrocarbon industry two time-scales are relevant; firstly that of the production; the commercial exploitation of the field, which can range from years to decades. Secondly the time-scale of exploration, which entails all processes involved with the accumulation and preservation of the hydrocarbon deposit. This can involve a time span of many millions of years. The effect of a fault on fluid flow can differ for these two time-scales; a fault which is not sealing over geological time can still form a significant baffle over the much shorter time-scales involved with the production of oil and gas (e.g. Childs et al., 2002, Jolley et al., 2007).

1.3.1.4 Multiphase flow

When discussing fluid flow inside hydrocarbon fields, it is important to consider its multiphase nature.. In hydrocarbon fields three different phases can occur: oil, water and gas. Immiscible phases occurring together strongly complicate fluid flow. If only one phase is present the flow of a fluid through a porous medium is determined by the medium's permeability and the fluid's viscosity. Where multiple phases are present at the same time, it is necessary to also know the relative permeability of the medium. The relative permeability provides the permeability for one immiscible phase given the abundance of the other immiscible phase (Fanchi 2006).

For hydrocarbons to enter a water-saturated (fault) rock, it first needs to displace the water from the pores. A fault can act as a seal to hydrocarbons as long as the pressure of the hydrocarbon column in the reservoir is less than the capillary entry pressure of the (fault) rock (Watts, 1987). If the pressure of the hydrocarbon column exceeds the capillary entry pressure, the hydrocarbons start flowing through the fault rocks, even when the pressure drops to below the capillary entry pressure (Fisher et al., 2001). After the fault seal has been breached, the fluid flow is governed by the (relative) permeability.

For a complete understanding of the role of faults in hydrocarbon exploration and production, the multiphase flow properties of fault rocks should also be considered. However this would strongly complicate the flow modelling and laboratory measurements. Therefore this thesis focuses on single phase flow through fault zones.

1.3.2 Flow along faults

The hydrological characteristics of fault zones can also facilitate flow along the fault zone, either along strike or up dip. This can have far reaching consequences for the exploration of oil and gas. Faults can act as pathways for the migration of hydrocarbons into reservoirs. Alternatively, faulting can breach top seals, and act as seal bypass systems (e.g. Weber 1987, Losh 1998, Aydin, 2000, Garden et al., 2001, Boles et al., 2004, Cartwright et al., 2007, Ilg et al., 2012), losing hydrocarbons from the reservoirs. The work-flows discussed previously are unable to predict along fault flow. In addition to applications in the hydrocarbon industry, the ability to predict along-fault flow has potential applications in a variety of fields, e.g. mineral exploration, geothermal energy, radioactive waste disposal and carbon capture and storage.

1.4 Scope of the thesis

Fluid-flow across and along faults can either be studied in the subsurface domain using data from wells and geophysics, or by studying faults in outcrops at the earth's surface. The first approach has the advantage of studying faults under actual hydrocarbon reservoir conditions. Under optimal circumstances the flow of hydrocarbons and water can be monitored in situ, through wells and 4D seismic (e.g. Lygren et al., 2003, Sverdrup et al., 2003, Jolley et al., 2007, Morris et al., 2012). The downside of this approach is that seismic data is not very suitable for imaging fault zone structure or contents. Typically only the offset of (horizontal sedimentary) reflectors is imaged by reflection seismics. Wells can provide a much more detailed picture, but rarely intersect fault zones.

The second approach has the advantage that it provides a much better insight in the internal structure of fault zones. The outcrops can be studied in detail and fault rocks can be sampled for further analysis. The downside is that the fault rocks have been uplifted and exposed to surface processes, potentially altering their properties. In addition information can only be gathered at the exposure surface, limiting the observation to 2.5D. Direct information about the fluid flow characteristics of faults is rarely available at the surface. This information has to be obtained indirectly, by analyzing geochemical alteration produced by paleo-fluid-flow (e.g. Heynekamp et al., 1999, Chan et al., 2000, Garden et al., 2001, Solum et al., 2005, Eichhubl et al., 2009, Solum et al., 2010, Dockrill and Shipton, 2010).

1.4.1 Fault heterogeneity

A particularly challenging aspect of estimating fault properties is their heterogeneity. For a single fault many of its properties (e.g. thickness, permeability, structure) typically vary drastically over short distances. This is nicely illustrated by figure 1.3, which shows a map of Big Hole fault in Utah (A. Bright, unpublished thesis, Lunn et al., 2008), and a graph of the along strike thickness of the fault core. As can be seen on the graph the thickness can change by up to one order of magnitude over distances of just a few meters. Shipton et al., 2002 shows that the thickness variation of the fault core is the most important control on across-fault fluid flow. Lunn et al., 2008 demonstrate that the spatial variability of thickness of Big Hole fault can be adequately described using a semivariogram. Understanding and statistically capturing fault variability is one key objective of this project. Work by Fairley et al., 2004 shows that spatial heterogeneity is also strongly present in along-fault flow. Using a geostatistical analysis

of the temperatures measured in 143 geothermal springs, along a fault in the Alvord basin in Oregon, they show that flow occurs along spatially-discrete pathways. Another example of heterogeneity of along-fault flow is provided in Dockrill and Shipton 2010 and Kampman et al., 2012, which documents the spatially discrete paleo-fluid flow along two faults near Green River, Utah.

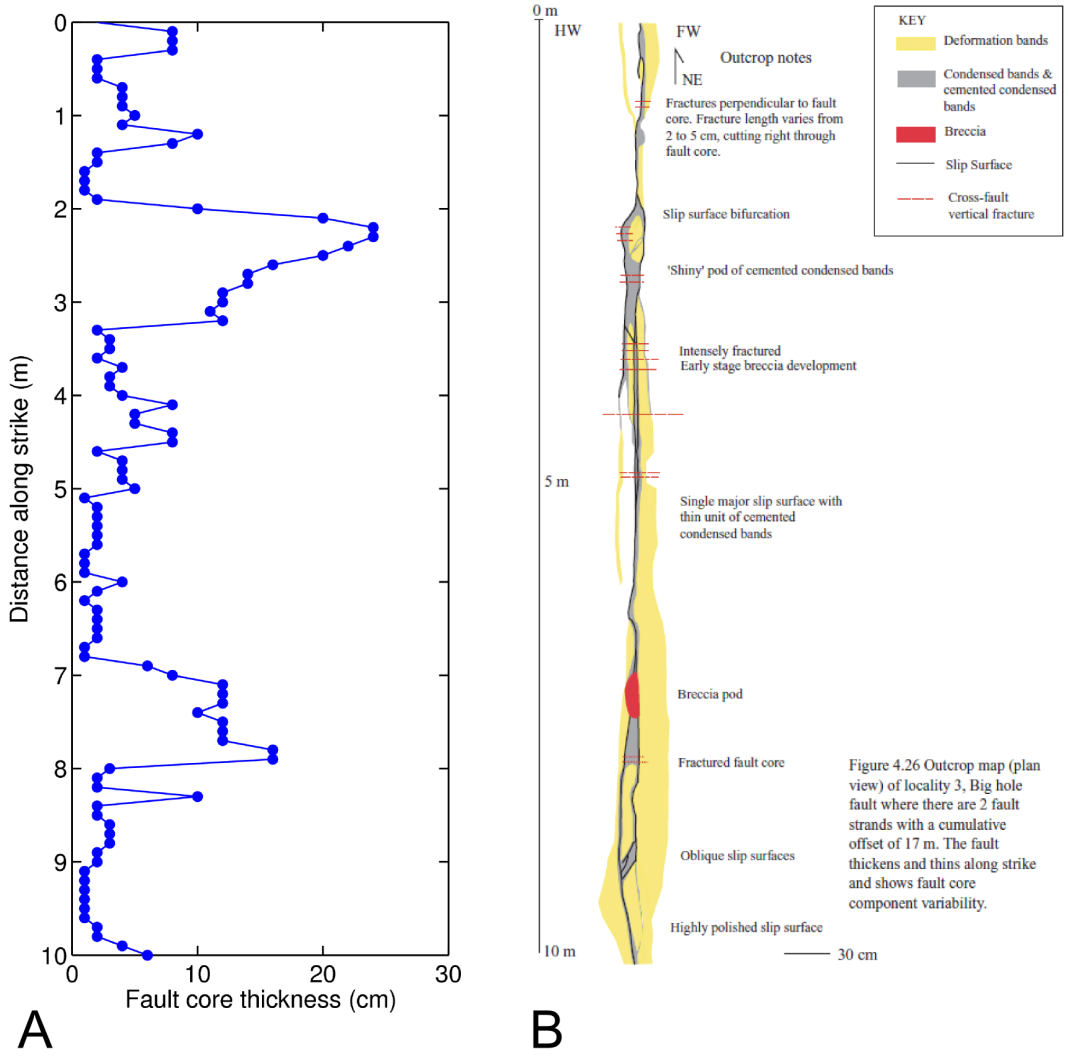

Figure 1.3: Fault core thickness variation at Big Hole Fault, Utah. At this locality the fault has a displacement of 17m. After A. Bright, unpublished thesis. A: Plot of the fault core thickness measurements. B: Map of the fault core.

1.4.2 Approach

This study aims to improve the understanding of fluid flow across and along faults, with an emphasis on the role of heterogeneity. Faults have been studied at 12 exposures, samples have been taken for petrophysical analysis and the gathered data have been used for modelling fluid flow through the fault zones. The study focuses on faults localized in sand-shale sequences. Nearly five months of this PhD project have been spent doing fieldwork. This allowed for

the creation of highly detailed maps of fault zone structure and content. In this thesis these maps are presented, and analyzed using a variety of techniques. Combined with permeability measurements on the sampled fault rocks, the maps serve as the basis for highly detailed modelling of fluid flow along and across fault zones. Analysis of the mapped faults and the modelled fluid flow is used to identify the features that are most important for fluid flow. These Key Flow Controls (KFC), can be used to more efficiently gather data elucidating the relationship between faults and fluid flow. The fault features responsible for along-fault flow will often differ from the features affecting across-fault flow, resulting in the need to collect different key flow controls for different applications.

1.4.3 Similar work

Caine and Forster 1999, define four idealized fault architecture styles based on the fault core damage zone concept. For each style they generate a fracture model using statistical outcrop observations from faults similar to the idealized style. Fluid flow is modelled through the fracture network. The results demonstrate that both the architecture of the fracture network and the aperture of the fractures can have a strong influence on the bulk permeability of the network (up to 3 orders of magnitude due to the architecture variation studied, and 2-3 orders of magnitude due to the fracture apertures modelled here). As both the fault architecture and fracture permeability can change during fault evolution, the authors conclude that the bulk permeability of a fault zone is likely to vary strongly during its evolution.

Shipton et al., 2002 present an analysis of the heterogeneity and permeability of Big Hole fault in Utah. 5 wells have been drilled and cored through the fault zone, at locations where the fault displacement is 8 and 3-5m and the host rock consists of fine grained eolian sandstone. Closely spaced permeability measurements on the cores allow for detailed analysis of the permeability variation in deformation band cluster faults. From this the authors conclude that the most important control of across-fault permeability for this fault is formed by the spatial variability of fault core thickness.

Jourde et al., 2002 present maps of strike slip faults in sandstone, with displacements of 6, 14 and 150m. These maps are used to create detailed 2D flow models. The models represent planar features (deformation bands, joints and slip surfaces) in (decimetre-scale) detail. The fault core itself is assigned a single homogenous permeability. The flow models are used to calculate an upscaled bulk permeability value for the fault zones. Flodin et al., 2004 work with the 14m displacement fault map from Jourde et al., 2002. They use it to investigate ways of upscaling fault bulk permeability. They conclude that large parts of fault architecture can be upscaled, but that planar high permeability features (fractures, slip surfaces) should best be modelled explicitly.

Ahmadov et al., 2007 present further analysis of 6 and 14m fault from Jourde et al., 2002. The maps are used to for flow models which investigate the role of slip surfaces and slip bands. Their results show that small structures can have a large influence (2 orders of magnitude) on the bulk across-fault permeability of the fault zone.

Lunn et al., 2008 present a detailed flow simulation for an exposure of Big Hole fault in Utah. At the studied outcrop, the fault displaces a porous sandstone unit 17 m. The model shows that flow is controlled by small-scale connected high permeability pathways. As these features can not be resolved for faults in the subsurface, they recommend the statistical characterization

of faults on the surface to better understand fluid flow through faults.

The Fault Facies project and the Fault Facies II project (e.g. Fredman et al., 2008 (I), Fredman et al., 2008 (II), Braathen et al., 2009, Fachri et al., 2011) aim to improve the representation of faults in reservoir flow simulators. Rather than a simple planar representation, faults are incorporated as grids (meter-scale cell-size). The flow properties of the grid cells are assigned using a process similar to that of sedimentary facies modelling (Haldorsen and Damsleth, 1990; Damsleth et al., 1992), which is a common hydrocarbon industry workflow for representing sedimentary heterogeneity. First the distribution of several tectonic and host rock facies through the fault zone are modelled stochastically. Calculated kinematic strain is the main parameter used to condition the facies distribution. Further rules for the distribution of the facies are derived from statistics gathered from outcrop analogues. Object-based modelling can be used to incorporate larger features such as sandstone lenses. Subsequently the modelled facies are used to assign permeability values to the fluid flow simulation grid, using a dataset of measured permeabilities.

As demonstrated by the studies discussed here, fluid flow across and along fault zones is strongly affected by fault heterogeneity and connected high permeability pathways. These features will likely never be resolved by geophysical surveys of hydrocarbon reservoirs. This study aims to develop a systematic way to characterize these two factors. By highly detailed (mm-cm scale detail) mapping and modelling of fault zones, it aims to pinpoint the key flow controls. This is more detailed than the previous studies, which typically are performed with dm-m scale detail. Once the key flow controls are identified, these can be collected, to allow large scale statistical characterization of fault zones.

1.4.4 Outline of the thesis

Chapter 2 provides a reference for the methods used for the fieldwork. Chapter 3 presents the data collected during the fieldwork, providing detailed maps of fault zone architecture and statistical observations on fault heterogeneity. Chapter 4 describes the laboratory work performed on samples collected during the fieldwork and the results obtained. The Shale Gouge Ratio is currently the most used tool for predicting fault sealing and permeability. To allow the data in this thesis to be compared to other studies, the SGR values calculated for all outcrops are presented in this chapter. Chapter 6 describes the flow modelling performed using the data collected in the field. Chapter 7 presents a geostatistical analysis of fault heterogeneity. The analysis is used to generate synthetic fault models which are used to demonstrate a probabilistic work-flow for fault permeability prediction. Chapter 8 brings together the results from the previous chapters and highlights the key disparity between faults in the field and the assumptions underlying current fault seal and permeability evaluation methods. A way forward is presented that explicitly considers fault zone architectures.

Chapter 2

Field methodology

2.1 Reconnaissance

Field sites for study for this thesis have been partly selected from published literature, partly by following suggestions from other geologists and partly by reconnaissance of field areas. The reconnaissance was prepared by combining geological maps with remote sensing imagery. Most of this work has been performed using Google Earth, which is a freely available software and data service providing high resolution satellite and aerial imagery draped over a digital terrain model. Maps and other information can be overlain over the existing terrain and viewed in 2.5D. Using these data several locations were selected, where faults were mapped with seismic-scale displacements (>10m) in sand and shale rich sequences, and where the aerial imagery suggested good exposure and accessibility. These locations were explored during the 2009 and 2010 field campaigns. Of the many sites visited, only a few were useful for this thesis, the other sites had to be discarded because of the poor quality of the exposure.

2.2 Grid mapping

If an outcrop surface is approximately planar, it can be mapped in great detail using grid mapping (figure 2.1). A regular grid is created over the surface of the outcrop using brightly coloured string, held in place with nails. Subsequently each grid cell is photographed using a digital camera. A4 or letter sized printouts of the photographs provide an excellent base-map for annotating the structure and components of the fault zone. Optionally, image processing software can be used to increase the brightness of the image before printing to make annotation more readable. The grid provides several advantages; it makes it easier to take detailed photographs of the entire outcrop in an organized manner, the mapping and annotating is aided by the grid as a reference and the rectangular grid allows the photographs to be corrected for perspective during the assembly of the final map.

For outcrops which are not planar enough to allow gridding, photos were taken and interpreted on site. All maps presented in this thesis are the result of careful validation and annotation in the field, rather than later interpretation.

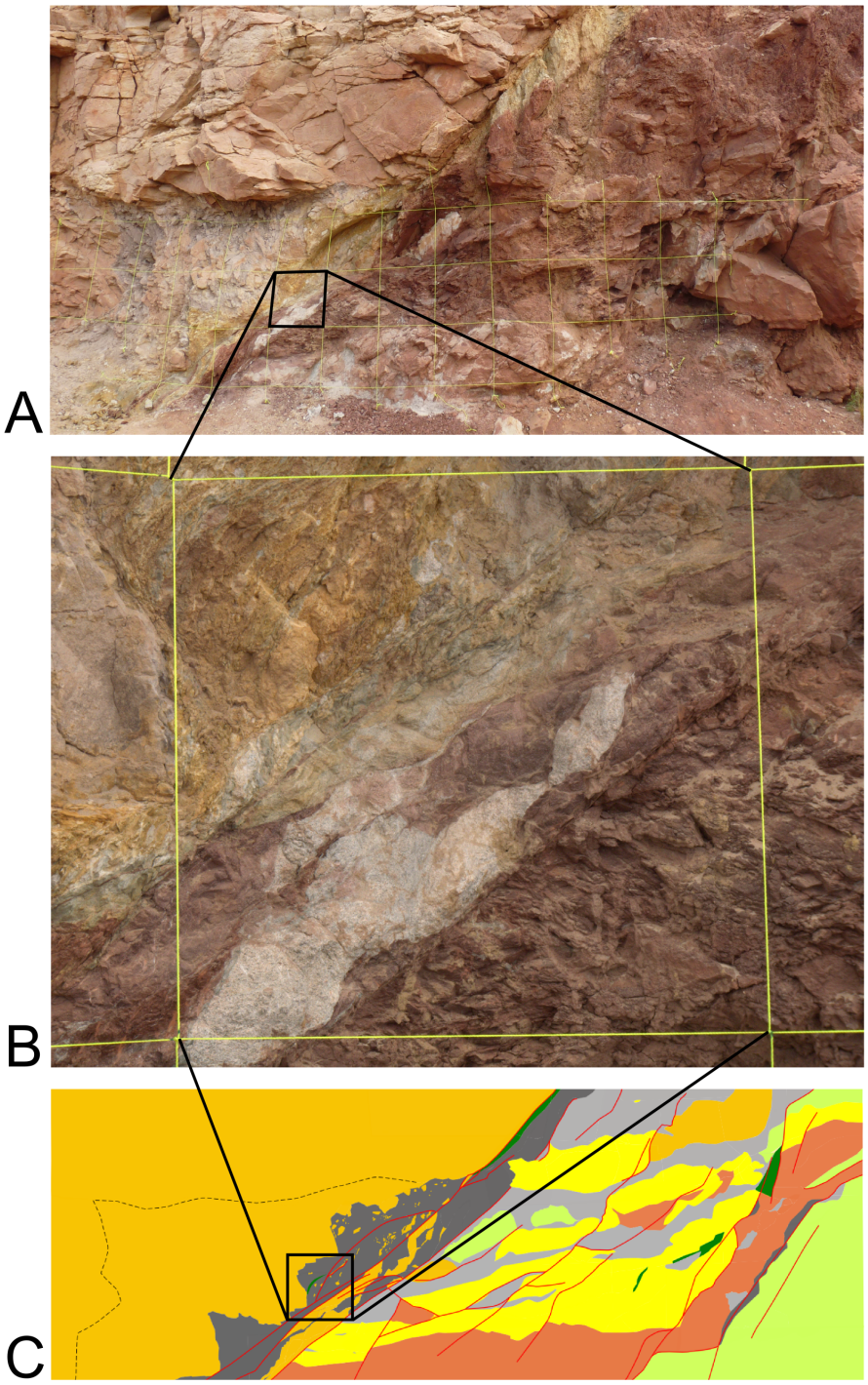

Figure 2.1: Grid mapping of exposure 191SE of the Moab fault. A: overview picture of the outcrop covered by a grid of yellow string. B: Detailed photo of a single grid cell. C: Resulting map of the outcrop.

2.3 Photographic resources

Digital photography has been used extensively during this study. In addition to the mapping and the conventional documenting of interesting features two other photographic techniques

have been deployed.

2.3.1 Gigapans

Gigapans are gigapixel resolution images created by stitching together hundreds of digital photos. The source images are recorded using an ordinary digital camera and a robotised tripod head which facilitates the capture of the structured photo mosaic. The Gigapan device uses servos to pan and tilt a camera and trigger the shutter release button. The resulting collection of digital photographs is stitched semi-automatically using specialized software running on a PC.

The Gigapan images provide a great resource for presentation purposes and reference, several images in this thesis are small crops from Gigapan images.

2.3.2 Multi view stereo reconstruction

Multi view stereo reconstruction (MVSR) is a set of technologies used to build 3D surface models using collections of digital images. The basis is similar to conventional stereo photogrammetry, but thanks to recent advances in computer vision algorithms and computational performance, this can now be applied automatically to large collections of photos. First all the images are compared and the algorithm searches for corresponding features. Using these matching features, the overall geometry of the scene and the camera locations can be reconstructed. Further processing allows the detection of more detailed geometries and the creation of textured surface meshes to capture these geometries.

For this study Autodesk 123D Catch has been used as an MVSR for creating 2.5D models of the studied outcrops. The models have not been used for the data or interpretations presented in this thesis, but are occasionally used for presentation and reference purposes.

2.4 Fracture trace sampling

Fracture networks can strongly impact both the permeability and strength of subsurface rock masses. A variety of methods have been developed to record their main properties. It is generally impossible to record fractures inside a rock mass, leaving only exposed surfaces and or wells to provide information. Therefore basic statistics are gathered on the surface traces. These statistics provide a basic insight into the nature of the fracture network. A full discussion of the relationship between these parameters and the 3D fracture network is beyond the scope of this study.

Linear scanlines are the simplest method of gathering fracture statistics. A linear scanline is laid out along the rock surface. For each fracture intersecting the scanline, the position, orientation, length and other properties such as mineral cement are recorded (figure 2.2 A). The method is quick, and very effective for capturing a set of parallel fractures, where a scanline perpendicular to the set can be used. For rock surfaces with differently orientated fracture traces, the method is strongly hampered by the orientation bias. Fractures parallel to the scanline are much less likely to be sampled than fractures perpendicular to the scanline (Terzaghi, 1965). The collected data can be a summarized as an average fracture trace spacing, or as a frequency.

As most outcrops contain fractures with multiple orientations, circular scanlines (Mauldon et al., 2001) provide a more robust way to collect fracture statistics. This method uses a circular

scanline drawn on the rock surface. Data is collected on the number of fractures intersecting the circle and the number of fracture endpoints inside the circle (figure 2.2 B). In addition orientation and infill data can be collected for the fractures intersecting the circle.

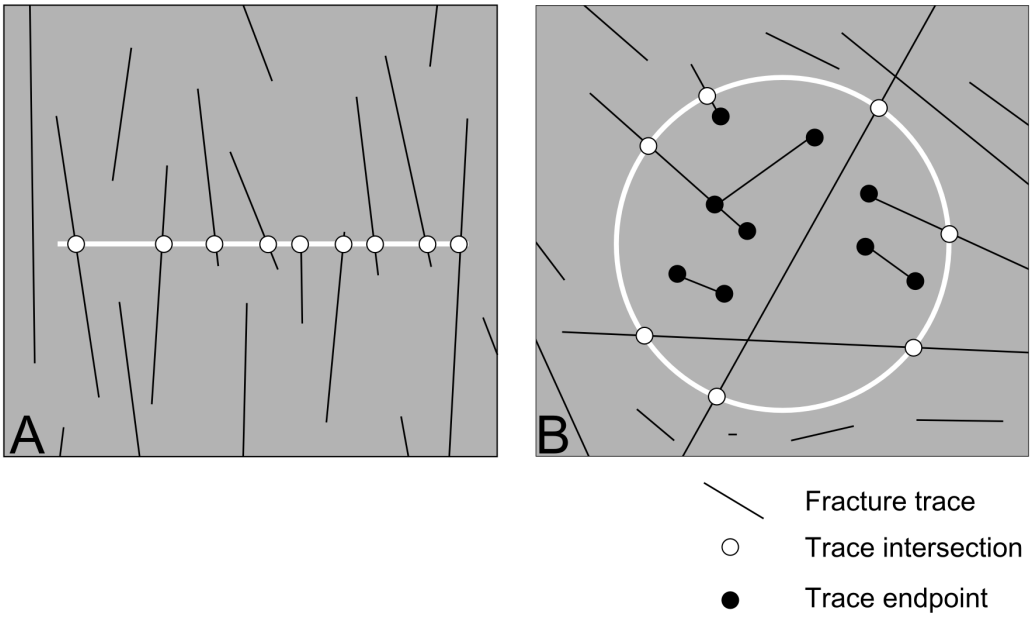

Figure 2.2: Sketch illustrating fracture trace sampling. A: Using a linear scanline. B: Using a circular scanline.

This method reduces the orientation bias in the plane, although fractures parallel to the sampling plane are still under-sampled. Three statistical estimators can be calculated using the number of intersections (n) and the number of endpoints (m) (figure 2.2 B).

Intensity

Trace intensity is comparable to fracture frequency for linear scanline data. It is a measure of fracture abundance, a combination of the number of fractures in the circle and their length.

$$\hat{I} = n/4r$$

Density

The number of fractures present in a sampled area is represented by trace density.

$$\hat{\rho} = \frac{m}{2\pi r^2}$$

Mean trace length

The number of endpoints and intersections can be used to calculate a third important parameter, mean trace length.

^mhu = (pi r / 2) (n/m)

$$\hat{\mu} = \frac{\pi r}{2}\left(\frac{n}{m}\right)$$

Chapter 3

Field observations

Extensive fieldwork was performed to build up a dataset of highly detailed observations on well exposed fault zones. The data collection has focussed on fault zone architecture and highlighting the parts of the fault zone which are the dominant controls on fluid flow both across and along the faults. This chapter describes the outcrops visited and the data gathered from them. For each outcrop the main architectural features are presented. Where available, evidence of past fluid flow is discussed. Architecture and paleofluid flow are analyzed to hightlight key flow controls.

The data were collected on the Colorado plateau in southeast Utah (United States) and the western Sinai Peninsula in Egypt. These locations provide excellent exposures due to the arid climates. In addition their stratigraphy and regional geology are well documented. Only locations from which data were actually used are discussed here, several other locations (Bornholm in Denmark, Crested Butte in Colorado and Girvan in Scotland) were also visited but did not yield sufficient relevant data for this study.

3.1 Faults in the Colorado plateau, Utah

3.1.1 Tectonic history

All faults studied in Utah (figure 3.1) are located on the Colorado plateau. This relatively stable cratonic region is located in between the Basin and Range province and the Rocky mountains (Hintze 1988). Though the Colorado plateau did not experience much deformation during the Nevadan (180-140 Ma) and Sevier (140 – 50 Ma) orogenies, these orogens did act as a source for most of the Mesozoic sediments on the Colorado plateau. From 80-35 Ma, the Laramide orogeny was responsible for the formation of the Rocky mountains, which caused gentle deformation of the Colorado plateau. Most notably it caused the San Rafael Swell, Circle Cliffs uplift and Kaibab uplift (Davis 1999). Igneous activity during the Oligocene manifested itself as both volcanism and the emplacement of large plutons. Since 15Ma Basin and Range extension has affected the Colorado plateau, mainly marked by the formation of three large scale fault systems; the Hurricane, Sevier and Paunsaugunt faults. (Davis 1999). The uplift phase responsible for the present elevation of the Colorado plateau about 2km above sea level is a matter of active debate with little consensus regarding timing or mechanism (Flowers 2010).

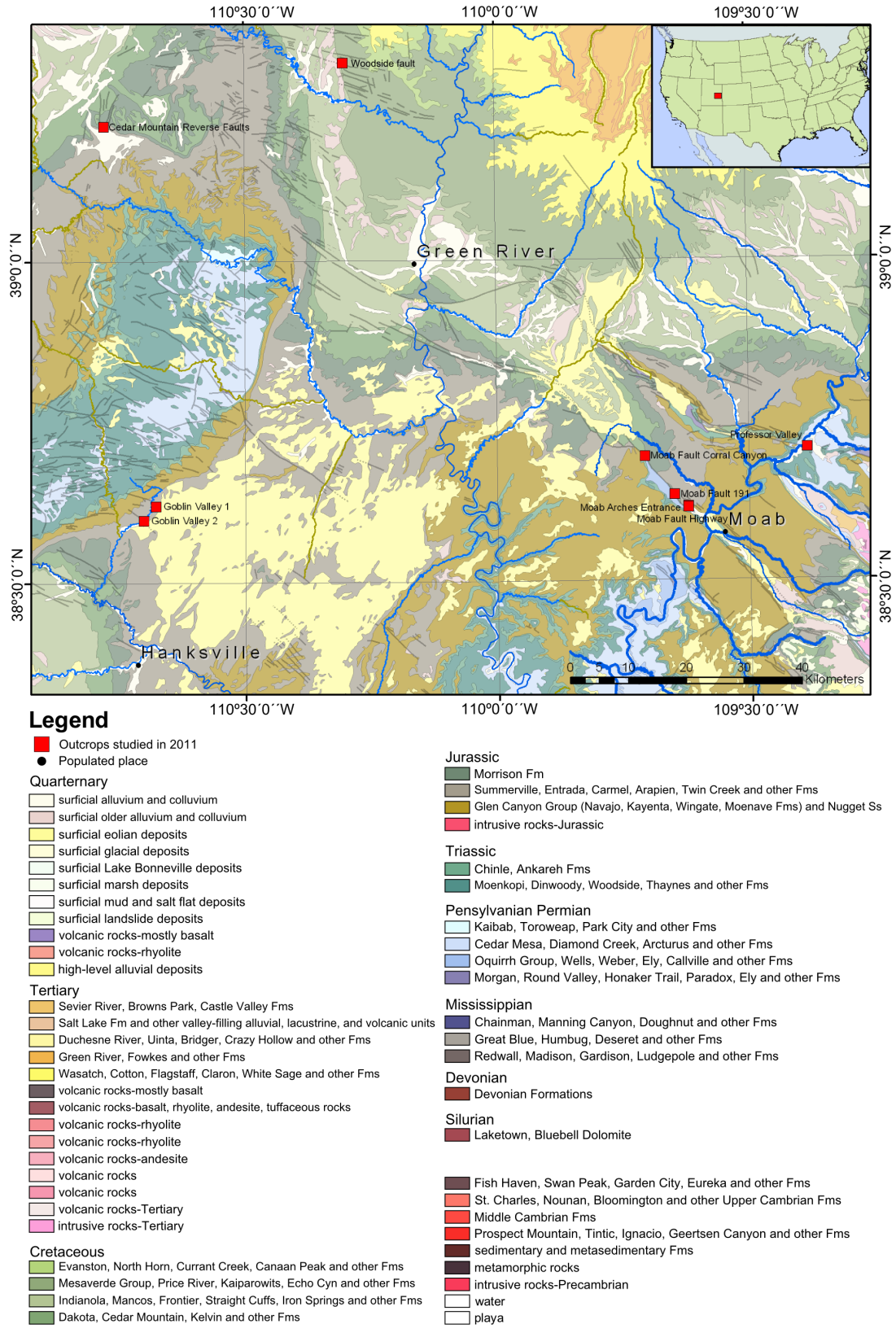

Figure 3.1: Locations of the studied outcrops on geological map (map after Hintze et al., 2000)

3.1.2 Moab Fault

For this study several outcrops of the Moab fault have been mapped in great detail (figure 3.2). This 45 km long normal fault has a maximum offset of 1 km (Foxford et al., 1998), displacing a sedimentary sequence consisting mostly of sandstone, siltstone and shale. A thick evaporate deposit is present at the base of the Paradox basin, below the Moab fault. Movement of this salt is responsible for the formation of this fault and the anticline to the east of it (Doeling et al., 1988). The displacement occurred in two separate phases; the first movement lasted from the Triassic to the mid Jurassic, with the second phase lasting from mid Cretaceous to the Early Tertiary.

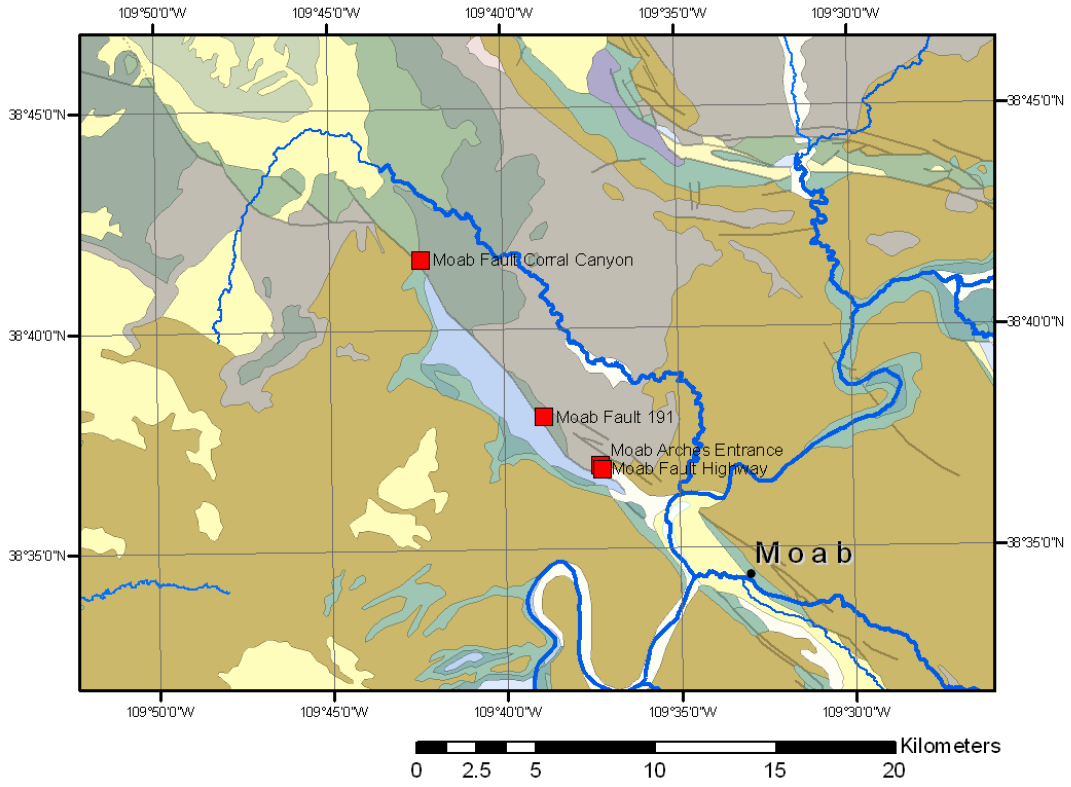

Figure 3.2: Locations of the Moab fault outcrops on geological map (map after Hintze et al., 2000)

Several researchers have studied the Moab fault in relation to fault-related fluid flow. Foxford et al., 1998 studied several outcrops and present these as simple sketches. They note the diversity of fault zone architectures encountered along this fault. From this they conclude that deterministic modelling of fault zone characteristics is unlikely to be successful, and that an empirical approach such as SGR calibrated to known pressure differences is more likely to work.

Davatzes and Aydin 2003 describes the different deformation mechanisms in the sandstone dominated northern parts of the Moab fault. They find that initially faults form by deformation banding. Continued deformation of the deformation band fault cores occurs through jointing and shearing along joints, overprinting the initial clustered deformation band fault core. Davatzes and Aydin 2005 expand upon their previous work by including exposures of the Moab

fault, where shale smear is the dominant fault architecture. Using an extensive set of observations for this part of the Moab fault, they show that the fault zone contents are highly variable, but follow a consistent pattern related to stratigraphy, juxtaposition, displacement and fault geometry. Shale smears occur where the fault displaces thick shale beds, whereas the parts of the fault where only sandstone is involved have developed as deformation band faults with later joint overprinting. Eichhubl et al., 2009 study the same northern section of the Moab fault, focussing on cementation as an indicator of paleo fluid flow. They find cementation to be located in and near joints overprinting deformation band fault core. The most cement occurs where joint density is greatest, which typically occurs at sites of fault interactions, segment intersections and steps.

Yielding 2002 used the sketches from Foxford et al., 1998 to estimate the amount of shaley gouge in each outcrop. He plots these values against SGR values calculated for each outcrop, using a basic v-shale curve estimated from the regional stratigraphy. Yielding finds a reasonably good correlation between these two parameters and uses this as an argument to support the robustness of the Shale Gouge Ratio method.

Chan et al., 2001 observed large scale bleaching of red-brown sandstones in the vicinity of the Moab fault. They argue that the Moab fault must have acted as a conduit for large quantities of hydrocarbons. Water which has become reducing after interacting with the hydrocarbons dissolves red-brown hematite and manganese rich minerals. The dissolved minerals are deposited elsewhere as concretions. The authors have used 40Ar/39Ar dating to determine an age of 20-25 Ma for the iron and manganese rich fluids.

Solum et al., 2005 and Solum et al., 2010 studied the clay mineral composition and geochemistry of the R191 outcrop of the Moab fault (referred to as outcrop 191SE in this study, figure 3). In the 2005 paper they show that the clay mineral assemblages of the fault gouges do not plot on mixing lines for the hanging wall and footwall stratigraphy. From this they argue that significant parts of the clay in the gouge is authigenic. One thing to note is that the mixing model used in the 2005 paper only incorporates samples from the hanging wall and footwall at the outcrop, thereby ignoring the chemistry of all the other displaced stratigraphy. Considering that the displacement at this location is 1 km, this seems a rather significant omission. Despite this, dating of the illite and the microstructure of the illite provide additional support for its neoformation.

The 2010 paper expands the number of outcrops studied and introduces a technique for analysing paleo fluid flow through the fault zone. The paleo fluid flow is demonstrated from the combined strontium and barium enrichment and combined zinc, copper and lead enrichment. The barium and strontium are inferred to result from a Paleocene fluid flow event associated with hydrocarbon migration along the Moab fault. The copper, zinc and lead result from an Oligocene fluid flow event. This event is likely related to igneous activity in the La Sal mountains. This is the same event as the 20-25 Ma fluid flow reported by Chan et al., 2001. For these elements data is available for the entire stratigraphy. All four locations show a relative enrichment in copper, zinc and lead, demonstrating along-fault flow. Authigenic clay growth is only conclusively shown at one location (191SE), with another location (Bartlett wash, not studied in this thesis) possibly affected by authigenic clays and two locations (Corral Canyon and Courthouse Canyon) are shown to be unaffected.

Figure 3.2 shows a basic map of all the outcrops along the Moab fault that I have mapped for this study. The names used here for these outcrops are the same as in Foxford et al.,

1998. Figure 3.3 shows the fault in more detail and uses blue bars to indicate the offset at each exposure. The offsets have been determined by Foxford et al., 1998 from stratigraphic separation. The Moab fault is only well exposed at these discrete exposures, in between the degree of exposure is generally too poor to study the architecture of the fault.

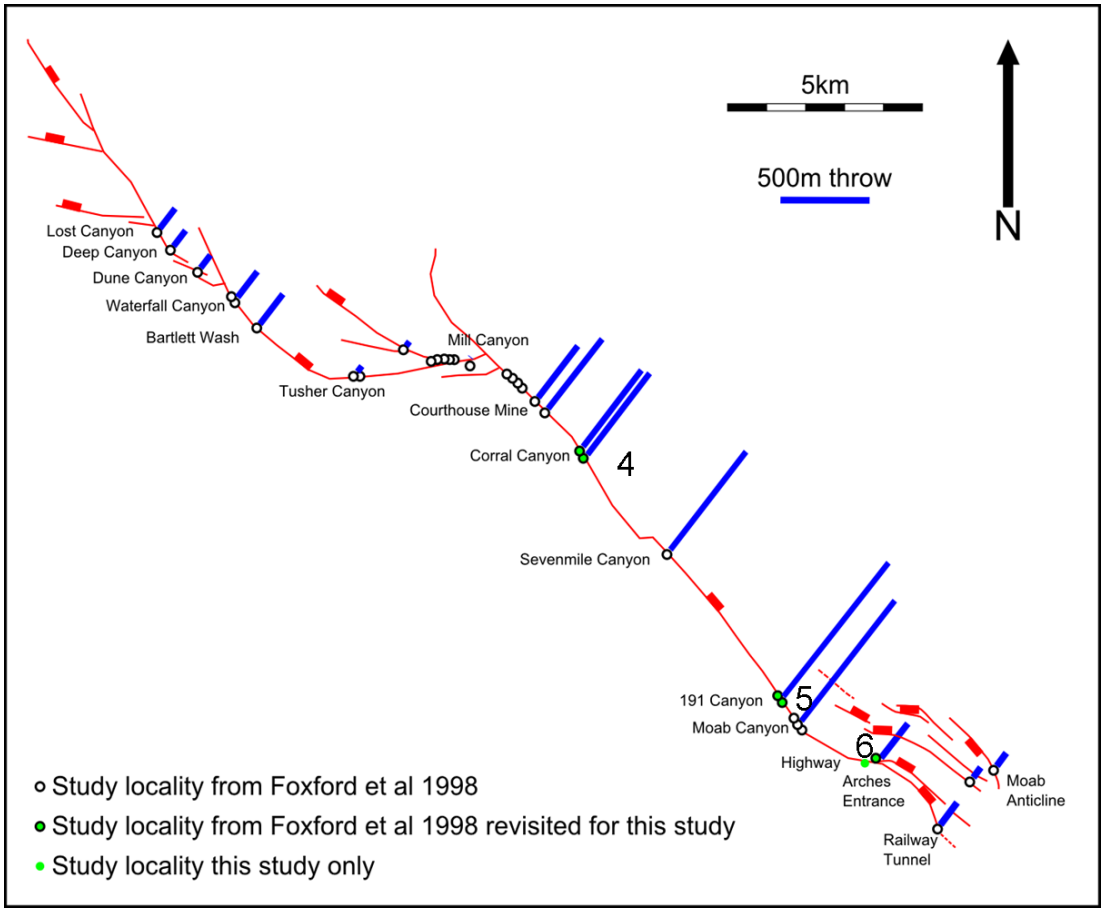

Figure 3.3: Map of the Moab Fault, modified after Foxford et al., 1998. The length of the blue bars indicates the magnitude of throw along the fault.

3.1.2.1 Moab fault outcrop 191

At this location (191 Canyon on figure 3.3) two exposures reveal the inner structure of the Moab fault, the exposures are separated by 60m along strike and 20m vertically. The first exposure (191SE) is found along the old highway 191 (now a bicycle trail). The second exposure can be found by descending the valley 50 m northwards from 191SE, this exposure is referred to as 191NW in this study. The 191 exposures are the sites which have been studied in most detail in this study. At this location the Moab fault reaches its maximum offset of 1km (figure 3.3), placing Permian Honaker trail formation rocks next to Jurassic Salt Wash member rocks.

3.1.2.2 191 SE Architecture

Displacement at this site is distributed over two strands (Figure 3.4A), one with 900m throw and one with 60m throw (Foxford et al., 1998). Data collection has focussed on the large offset

(900 m) strand, this strand has been mapped in detail. The 60m strand is exposed less well and therefore has been sketched instead.

Main strand Figure 3.4C shows the map created for the exposure of the main strand. Most of the data was collected during 2010, but in 2011 an additional area was mapped; this roughly corresponds to the top 1m of this map.

Structure At the NE side of the fault core, the dominant element is formed by a clay rich gouge (figure 3.4E). Small sandstone lenses and clasts occur in this gouge. In the centre of the zone these lenses are elongated and parallel to the fault zone, and they vary in thickness between 5 and 30 cm. Near the hanging wall sandstone, many small (mm – cm scale) sandstone fragments have been incorporated into the gouge. Further evidence for abrasion of the wall rock is visible in the shape of the hanging wall itself, where three triangular wedges of sandstone have been incorporated into the gouge. The process which has acted here seems to be a combination of physical and chemical mechanisms. The wall rock around these triangles is strongly fractured; two perpendicular sets of fractures can be observed. The first set is approximately parallel to bedding and the second set is nearly vertical. In addition the fractured rock appears geochemically altered; it is lighter in colour and less cohesive than the adjacent host rock. The cartoon in figure 3.5 presents a model to explain these observations. Fault movement causes fracturing, which allows fluid flow through these parts. The fluids cause a softening and bleaching of the rock. The softened rock is preferentially incorporated into the gouge, leading to the triangular wedges protruding from the fault wall. Inside the gouge the wall rock fragments are broken down during shearing into smaller clasts. Further movement along the fault would likely repeat the mechanism and incorporate more sandstone into the gouge.

To the SW of the main gouge, a 3m wide zone is visible consisting of large blocks of sandstone and silt. Foxford et al., 1998 suggested this to be part of the gouge, but after careful cleaning and mapping of the outcrop, it becomes clear that this not true. The original 0.5-1m thick sedimentary bedding is clearly visible but offset along multiple slip surfaces. This deformation places low permeability siltstones and shales next to high permeability sandstones. On the SW border this zone is bounded by a minor slip surface with approximately 2m displacement. SW of this boundary the rocks is still fractured but with only minor deformation along slip surfaces.

Figure 3.4D shows a cartoon to summarize the structural observations of the main strand outcrop. Rather than the classic fault core and damage zone model, a three part subdivision can be observed here. The vast majority of the strain has been accommodated in a narrow high strain zone consisting of gouge and strongly deformed sandstone lenses. The three meters of fault rock SW to this zone form a medium strain zone of clearly deformed rocks but with sedimentary beds which can still be distinguished, this zone is separated from the damage zone to the right by a slip surface.

The architecture presented here clearly differs from the interpretation by Foxford et al., 1998. They classify both the high strain and medium strain zone as shaley gouge, with clasts of sandstone floating in the gouge. Following their interpretation, the fault at this location is a 3-5m thick barrier as opposed to the much thinner gouge observed in this study (5 - 30 cm). The different observations presented in this thesis are the result of extensive cleaning and spending several days at each site to map features ranging from mm to m scale.

Paleo fluid flow Several parts of this outcrop show indications of geochemical alteration. In the central high strain zone, strong gradual colour changes near slip surfaces suggest alteration by fluids flowing through the slip surfaces. The geochemical alteration of this gouge is supported by work by Solum et al., 2005 and Solum et al., 2010. The hanging wall contains triangular wedges of damage zone sandstone, affected by fracturing and geochemical alteration, as discussed in section 3.1.2.2. Inside the medium strain zone several beds of a coarse grained sandstone demonstrate alteration by a colour transition from red-brown to white. Figure 3.6 shows a slip surface separating shale and sandstone in the medium strain zone, the coarse grained sandstone above the slip surface shows a gradual colour transition away from the slip surface, suggesting alteration by fluids flowing through the slip surface.

Key flow controls This outcrop is dominated by the main gouge in the high strain zone. For across-fault flow, the thickness variation of this unit is likely to be the key control. In addition to the thickness of the gouge, the presence of sandstone lenses and clasts in the gouge can make it easier for fluids to travel through the high strain zone, but no lenses have been observed which completely breach this gouge. Slip surfaces running through the gouge are all parallel to the orientation of the fault zone. As such they do not form direct pathways through the gouge, but potentially the slip surfaces can link with sandstone lenses in the gouge to provide a pathway across the gouge. .

For along-fault flow through the fault core, the slip surfaces seem to be the most likely key flow controls. Small sandstone lenses could further contribute through flow along fault, but due to their short length (less than 1m), their influence is likely limited. The abundant geochemical alteration in both the gouge, and nearby parts of the fault core and damage zone, suggest that these slip surfaces have been effective at transmitting large volumes of fluids.

Minor strand Figure 3.7 shows a sketch of the architecture of the minor strand, which has accommodated 60m of throw. Due to the more complex geometry and poorer exposure of this outcrop, it was less suitable for accurate mapping. The sketch was created in the field by annotating a digital photo of the outcrop on a tablet PC. It is an accurate portrayal of fault zone contents and structure, but its geometry is distorted by perspective. This makes the sketch unsuitable for flow modelling (Chapter 5).

Structure The fault is dominated by a thick (0.8-1.2m) layer of shale. Inside the shale layer, four distinct components are observed; sandy shale, colour banded shale, blue shale and silt. The boundaries between these lithologies are sharp. The footwall consists of fractured cemented sandstone. The hanging wall consists of fractured sandstone without cementation visible to the naked eye. Close to the fault, the hanging wall sandstone is very damaged, showing brecciation and sandstone fragments inside poorly consolidated sand.

Foxford et al., 1998 described the architecture of this strand as a shaley gouge with entrained sandstone fragments. Solum et al., 2010 describe the composition of the strand as bleached gouge. The observations in this study paint a different picture. Rather than a homogenous gouge, four distinct lithologies are observed. The colour difference between the colour banded shale and the blue shale, could be a result of geochemical alteration, compatible with the bleaching suggested by Solum et al., 2010. Geochemical alteration can not explain the co-occurrence of silt next to shale or sandy shale next to shale. As such this partitioning reflects

the mode of emplacement of the different lithologies into the fault zone. It is possible that the four different lithologies represent an original stratigraphic succession, which has been incorporated into the fault zone as a single shale smear. Or alternatively they could represent different smears amalgamated together inside the fault core.

This lithological separation also shows that internal mixing inside the fault strand is very rare. The only evidence for this is the isolated fragment of colour banded shale inside the sandy shale. In this regard it is also very important to consider the abundance of brecciated sandstone in the hanging wall. If this loose material was available during fault movement, any mixing process would have incorporated it into the shale.

Paleo fluid flow Clear evidence for paleo fluid flow along this strand is scarce. The clearest indication is provided by the thin zone of cementation at the boundary of the hanging wall sandstone and the shale. The sandstone in the footwall is also cemented, potentially indicating the flow of fluids. Solum et al., 2010 suggest that the shale has been bleached, which would have required significant fluid flow. The poor consolidation of the sandstone in the hanging wall is possibly related to fluids weakening the sandstone by partial dissolution. Both the bleaching and the crumbling have not been investigated further during this study.

Key flow controls The key flow control for across-fault flow for this strand is clearly formed by the thick layer of shale. This forms a continuous barrier to flow over the entire exposed length of the outcrop (8m). The observations made on this outcrop suggest that the minor strand is actually a more important barrier to flow than the main strand. The shale smear in the minor strand has a minimum thickness of 80 cm, compared to the 5 cm minimum thickness for the gouge that forms the key flow control in the main strand. This further demonstrates the potential impact of fault architecture.

For along fault flow the damage zone of the strand is the most likely candidate. In both the hanging wall and footwall damage zone cementation indicates fluid flow. For along fault flow the main strand seems the most important, as this part of the outcrop shows more signs of paleo fluid flow

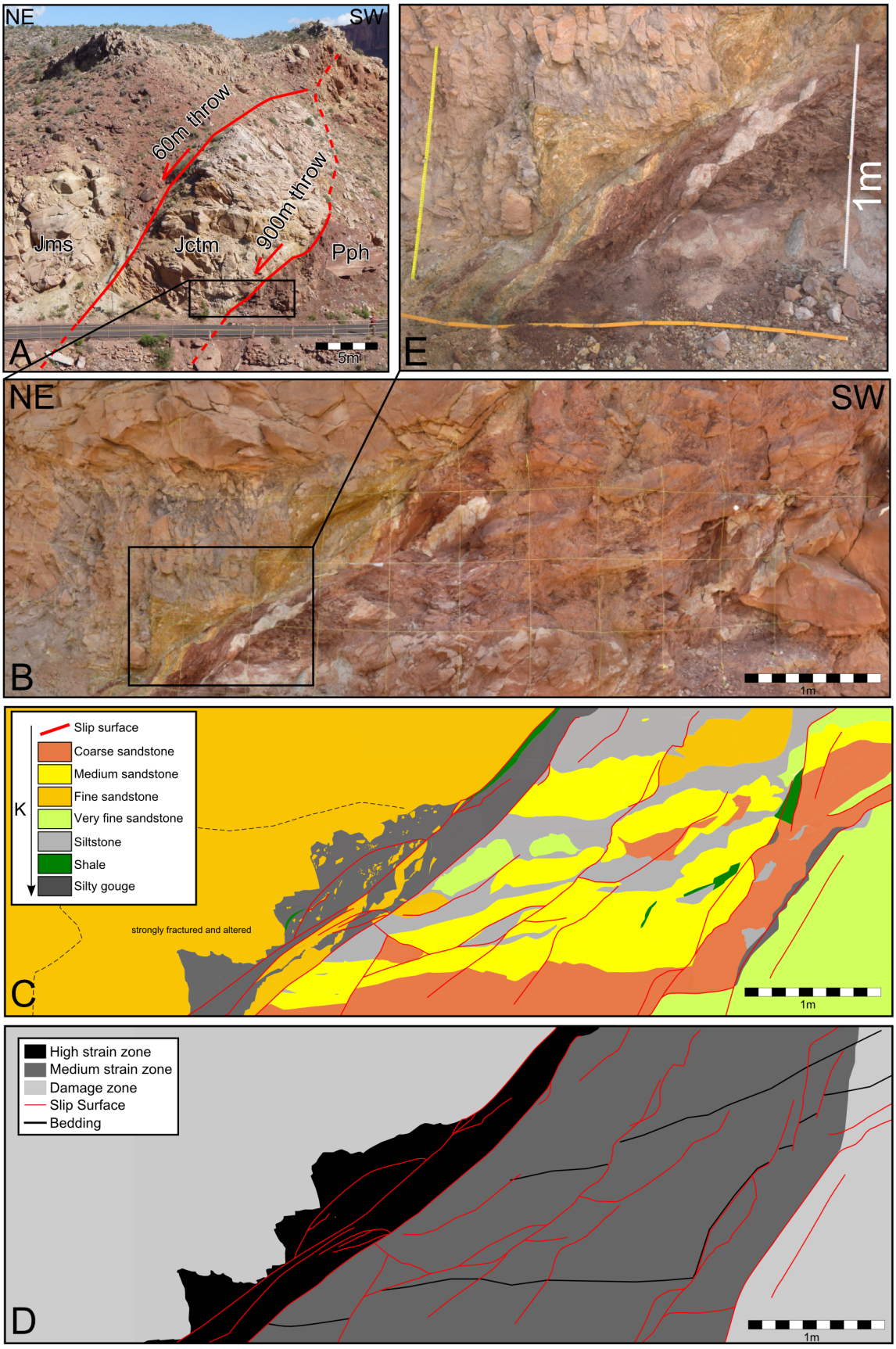

Figure 3.4: Moab fault exposure 191 SE. A: Overview photo of the exposure. Most of the displacement (900m) is accommodated by the main (SW) strand. The minor (NE) strand accommodates a further 60m of displacement. Jms: Salt wash member of the Morrison Formation. Jctm: Moab member of the Curtis Formation. Pph: Honaker Trail Formation. B: Photo of the mapped area. C: Map of fault zone composition. D: Conceptual illustration of the structure of the Moab fault at exposure 191SE. E: Detail photo of the gouge.

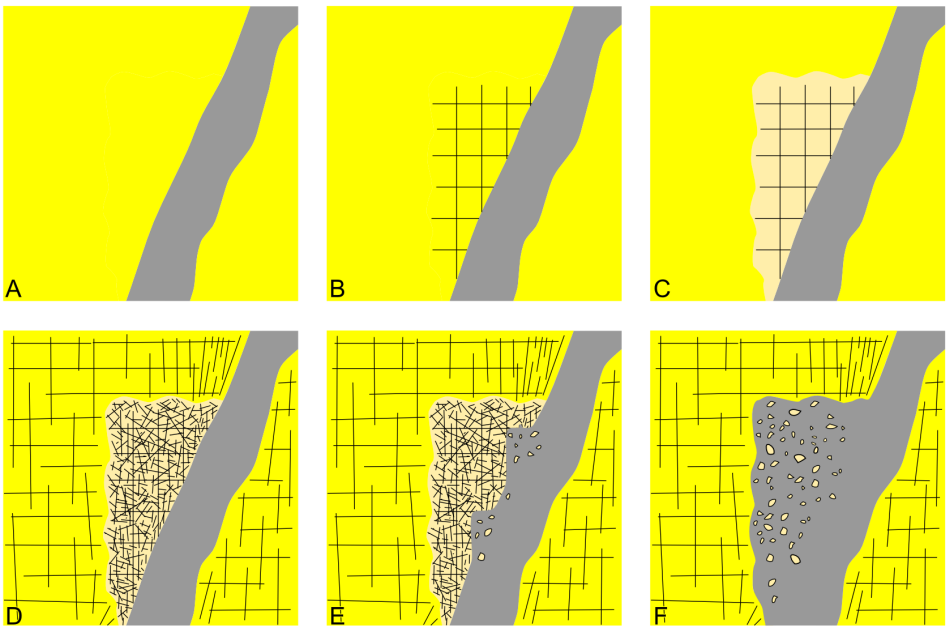

Figure 3.5: Sketch illustrating the sandstone incorporation at Moab fault exposure 191NW. A: Host rock unaffected. B: Fractures form in the damage zone, one set parallel to bedding and set vertical. C: The fractures strongly increase the permeability of the area, abundant fluid flow leads to a geochemical weakening of the sandstone. D: Subsequent deformation strongly affects the weakened rock, leading to strong brecciation. E: Sandstone fragments from the breccia are preferentially incorporated into the gouge. (Current situation). F: Further deformation would incorporate all the weakened sandstone into the gouge.

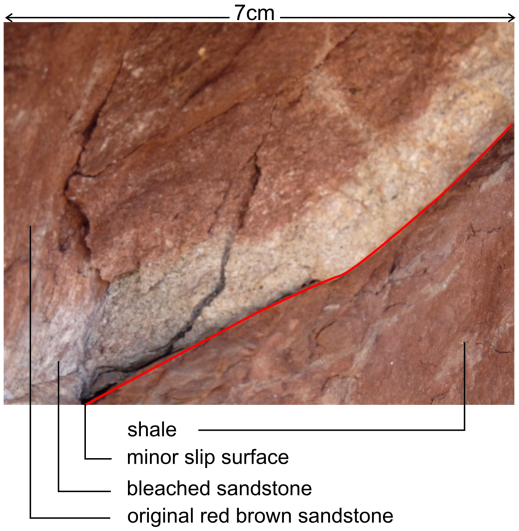

Figure 3.6: Example of geochemical alteration as a paleo fluid flow indicator (Moab fault exposure 191 SE). The originally red brown coarse sandstone has been partially bleached to light grey. The slip surface might have acted as a conduit for reducing fluids. The low permeability shale is not affected.

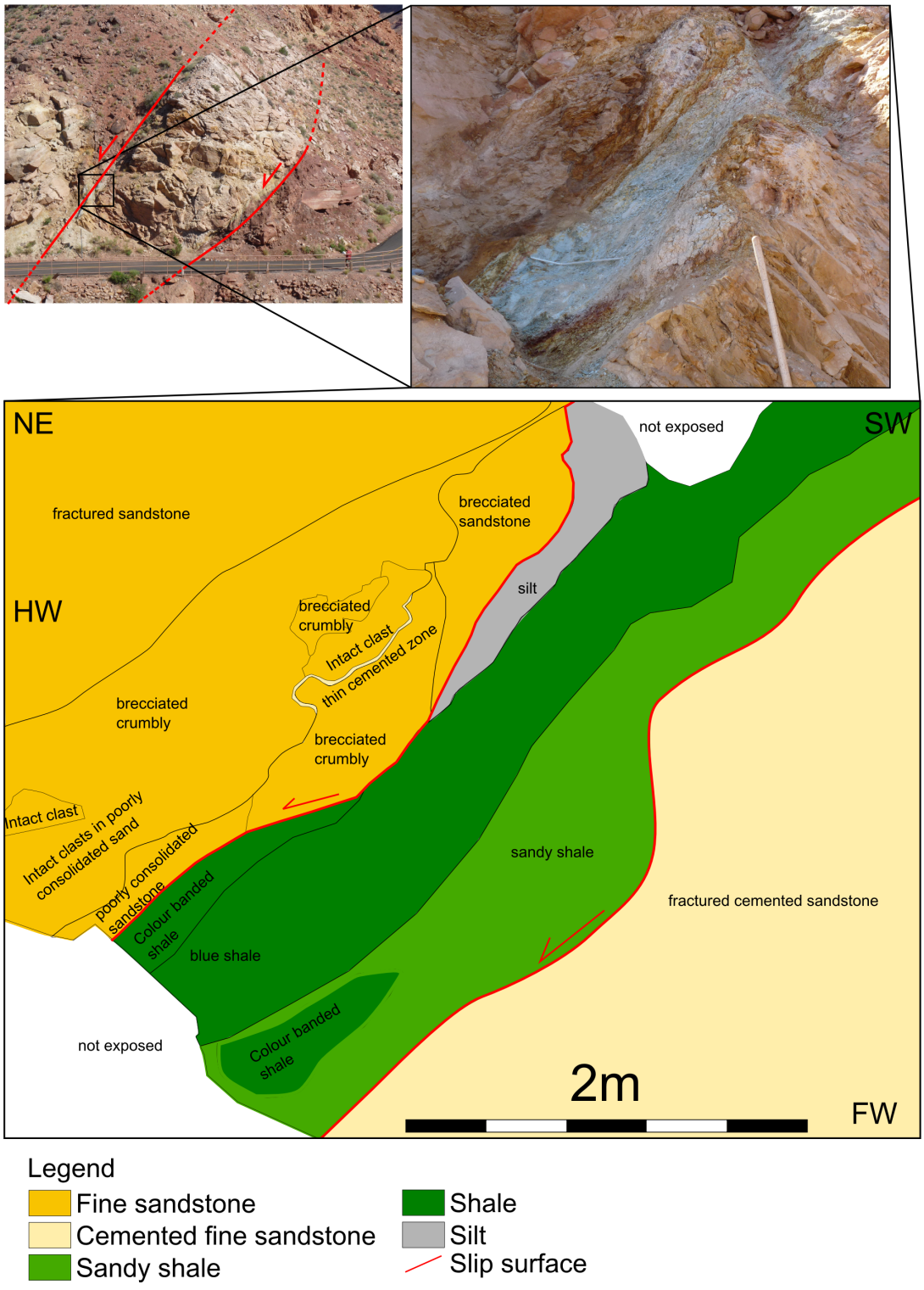

Figure 3.7: Sketch of the minor strand of the Moab fault at exposure 191SE..

3.1.2.3 191 NW architecture

This exposure is located approximately 60 m northwards and 20 m lower than the exposure 191 SE. Foxford et al., 1998 report an offset of 960m for this exposure. At this exposure only the core of the fault is well exposed. The SW edge of this core is poorly exposed as it is almost entirely covered in debris. From the few beds visible and some digging it can be interpreted that the debris covers a relatively undisturbed area. The western boundary of the debris, therefore seems to coincide with a poorly exposed minor fault strand. A similar structure is reported by Foxford et al., 1998. The bulk of the deformation seems to be accommodated by the eastern fault strand which is well exposed. The main (NE) strand has been the focus of this study and has been mapped in detail.

Structure Despite the close proximity to outcrop 191 SE, this exposure displays a rather different architecture (figure 3.8). Rather than a well developed gouge, here the core consists of a complex set of sandstone and siltstone lenses. Siltstone is the abundant component, with sandstone lenses floating in it. The core is crossed by many slip surfaces, most of which (85%) bound the lenses.

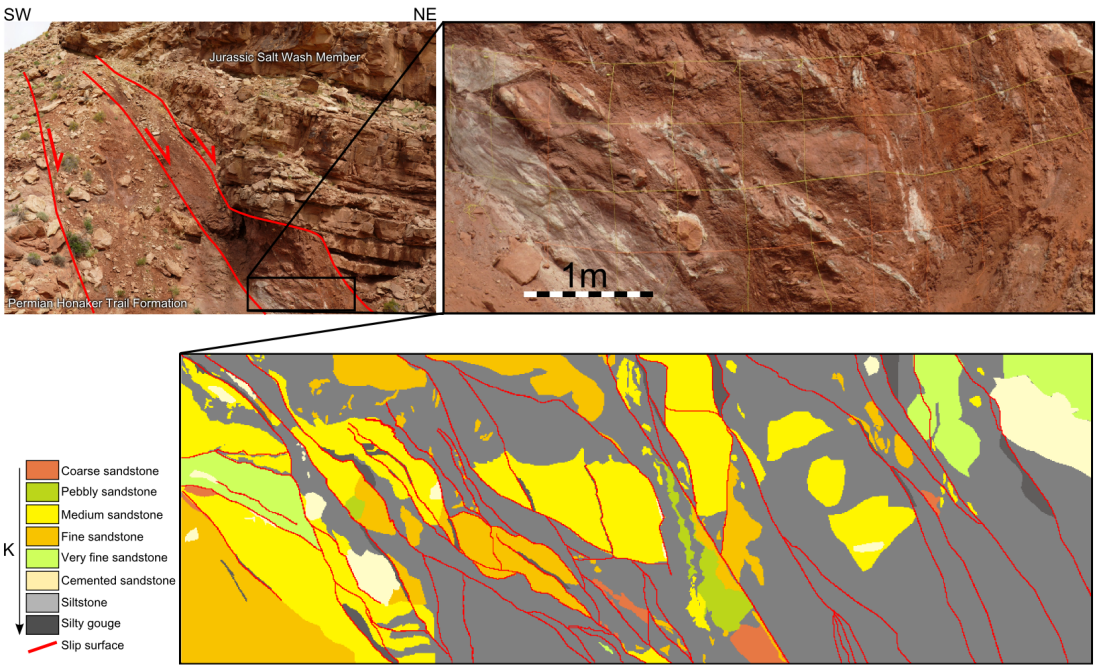

Figure 3.8: Moab fault exposure 191 NW. A: Overview of the exposure. B: Photo of the mapped fault core. C: Map of fault core composition.

The thickness of the core at this outcrop changes from 2 to 6 m over the length exposed (Figure 3.8a). It is clearly visible that the strongest change occurs along a lithological boundary in the hanging wall. The hanging wall here is formed by a sequence of sandstone and siltstone beds. Two models could explain this change. Firstly bedding parallel slip of the top sandstone bed over the siltstone bed could have indented the top sandstone bed into the fault core. Alternatively a minor fault strand or fracture could have developed in the hanging wall parallel to the main fault. Combined slip along this fracture and the top siltstone bed could have transported the hanging wall fragment into the main fault core. Careful observation of this

wedge has revealed no indication for bedding parallel slip. As such the second model seems more likely.

Paleo fluid flow Similarly to outcrop 191 SE the movement of large quantities of fluids through this fault zone can be deduced from geochemical alteration. Most of the alteration in this outcrop is similar to the alteration in the medium strain zone in 191SE. A coarse grained red brown sandstone has been bleached and weakened. Some of the bleaching accentuates pre-existing sedimentary structures like cross bedding, highlighting small scale sedimentary permeability differences in the sandstone. In addition to the bleaching some sandstone lenses have been strongly cemented, forming further indication of abundant fluid flow through this fault zone.

Key flow controls Both the sandstone lenses and slip surfaces could potentially form pathways for fluids to flow across the low permeability silt stone. No single lens or slip surface directly connects the hanging wall sandstones with the footwall sandstones. As both the lenses and the slip surfaces are somewhat parallel to the fault zone, potential pathways across the fault zone can only be formed by connected sandstone lenses and slip surfaces.

3.1.2.4 Arches National Park Entrance exposure

This exposure is located just next to the entrance to the national park, 150m SW of the visitor centre parking centre. As this fault is located inside the national park, it was not possible to collect samples. At this location a little wash cuts through the fault exposure, creating a very three dimensional view of the fault zone. The exposure mainly shows the footwall and the fault zone itself, not much is visible of the hanging wall side. Displacement is partitioned into two separate strands with 250 m and 460 m offset respectively (Foxford et al., 1998). For this study the western strand (460 m offset) has been mapped.

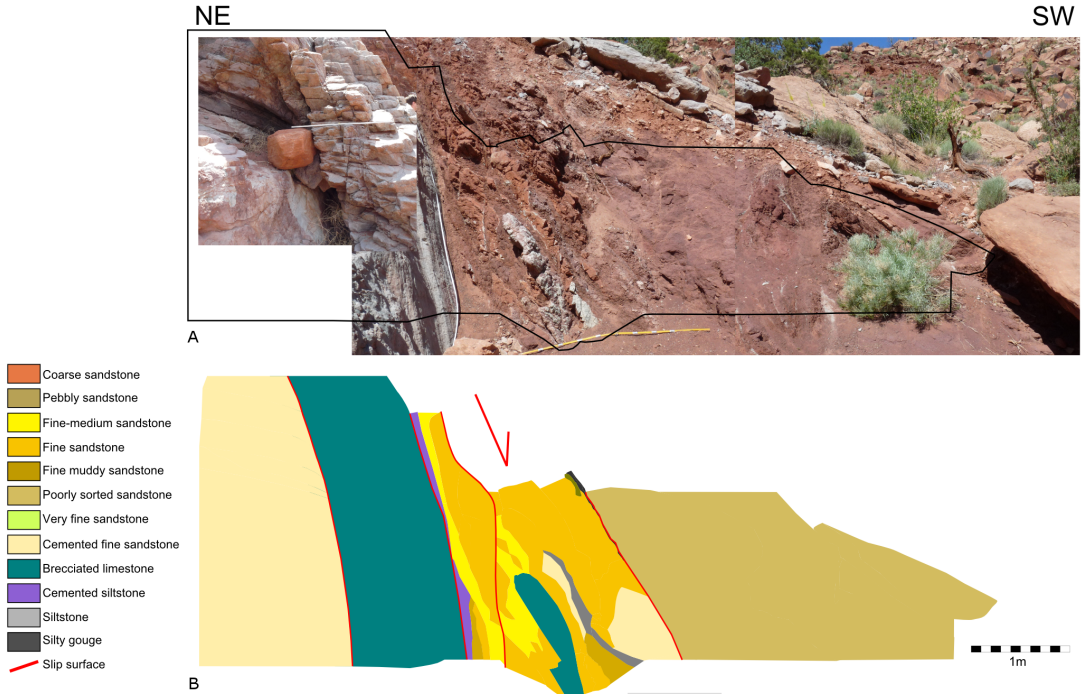

Figure 3.9: Moab fault exposure at the Arches National Park entrance. A: Photo of the outcrop. The black line indicates the outline of the map. B: Map of the fault.

Structure Figure 3.9 shows a map of this exposure. The architecture of this strand is somewhat similar to the 191NW exposure. The central element of this fault zone is formed by a complex set of sandstone, siltstone and shale lenses. These lenses have been strongly sheared and possibly weakened by geochemical alteration, and as such careful observation is required to accurately map this fault. Figure 3.10 shows a detailed sketch from Davatzes and Aydin 2005. In their sketch the bulk of this part of the outcrop consists of shale, with sandstone fragments floating in it. For this study the same area was mapped, investigating every element with a hand lens to verify its composition and grain size. As a consequence the map produced for this thesis reveals a different picture, in which this part of the fault is dominated by fine sandstone. The confusion is probably caused by the occurrence of both dark brown and light coloured material and interpreting these colours to correspond to shale and sandstone respectively. For the map presented in this thesis, I have carefully inspected every mapped feature with a hand lens and in case of doubt verified the grain size by biting on a small fragment.

A 1m thick limestone lens sits to the S of this zone. The limestone lens is intensively

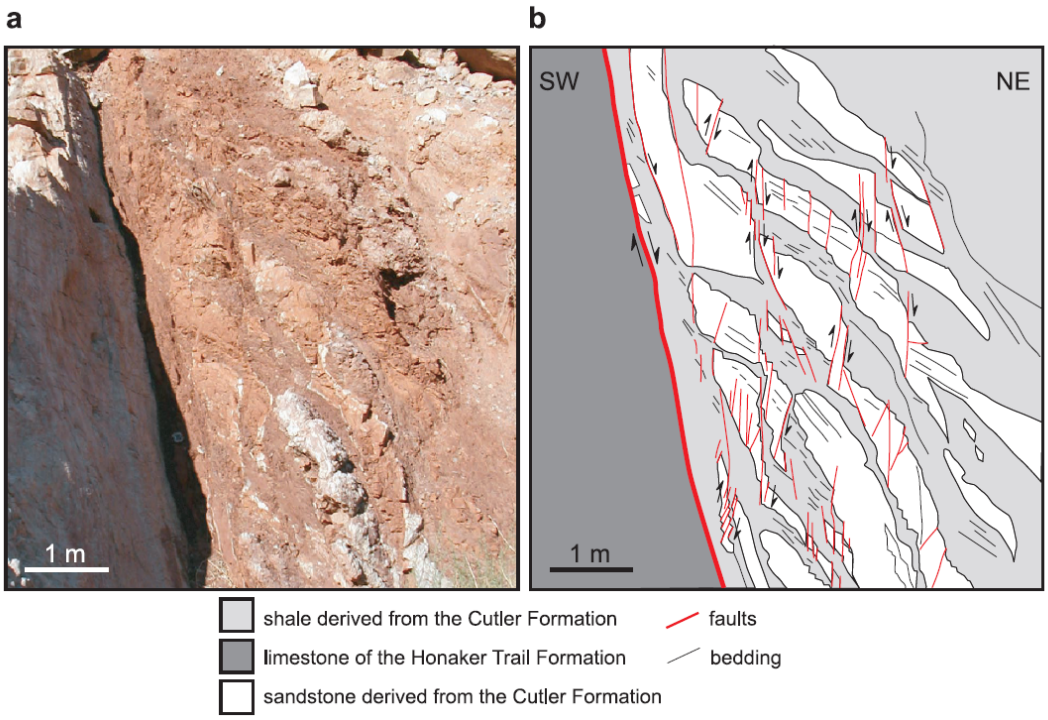

Figure 3.10: Part of the Arches Entrance exposure as interpreted by Davatzes and Aydin 2005. A: Photo of fault core. B: Interpretation. This interpretation differs strongly from the interpretation put forward in this study.

fractured at present. A quick estimate of the fracture density was made using six linear scan lines, yielding a density ranging from 11-31 fractures per meter, with an average of 21 fractures per meter.

Paleo fluid flow Evidence for paleo-fluid-flow is mainly provided by cementation, several lenses inside the fault core are strongly cemented. Some minor lenses are bleached as well, but compared to the other outcrops bleaching is very limited (3% of this outcrop is bleached). Of the fractures counted on the limestone lens, 68% contained mineral cementation. This suggests that the majority of the fractures in this limestone lens existed at depth, and were open to fluids for at least some time. Without samples it is not possible to decide if the cementation is related to along fault fluid flow or to local redistribution of material after pressure solution. The fractures without cementation were probably not present at depth and are perhaps uplift related.

Key flow controls The most important element for fluid flow in this outcrop is the limestone lens. It is continuous over the full length of the outcrop and thicker than the other elements. The thickness of the lens is near constant over the length of the outcrop. However on the larger scale the length of the lens is likely to be limited.

Because it is fractured and the fractured existed and were open for at least some time at depth, its role is complicated. The timing of the fracturing relative to faults history is not known; the fractures could have formed during the emplacement of the lens, or during later fault movement. Barton et al., 1995 have shown that fracture permeability near faults is dependent

on the local stress field. In addition the permeability of the fractures can reduce over time by cementation. As such the role of the limestone lens has probably changed strongly over time. Without fractures, or with fractures closed by over burden pressure or cementation, the limestone lens forms an important barrier to flow. With open fractures, the lens could form an important pathway for along fault flow.

A secondary baffle to across-fault flow is formed by small lenses of shale and siltstone. These lenses are less than 10cm thick and not continuous along the outcrop, so their influence is small.

For along-fault flow both the slip surfaces and the abundant sandstone are the most likely pathways. With an additional pathway formed by the limestone lens, when its fractures are open.

3.1.2.5 Moab fault Corral Canyon

This outcrop is referred to as upper Corral Canyon by Foxford et al., 1998. At this location the fault has an offset of 545m. A detailed map has been created at this exposure (figure 3.11).

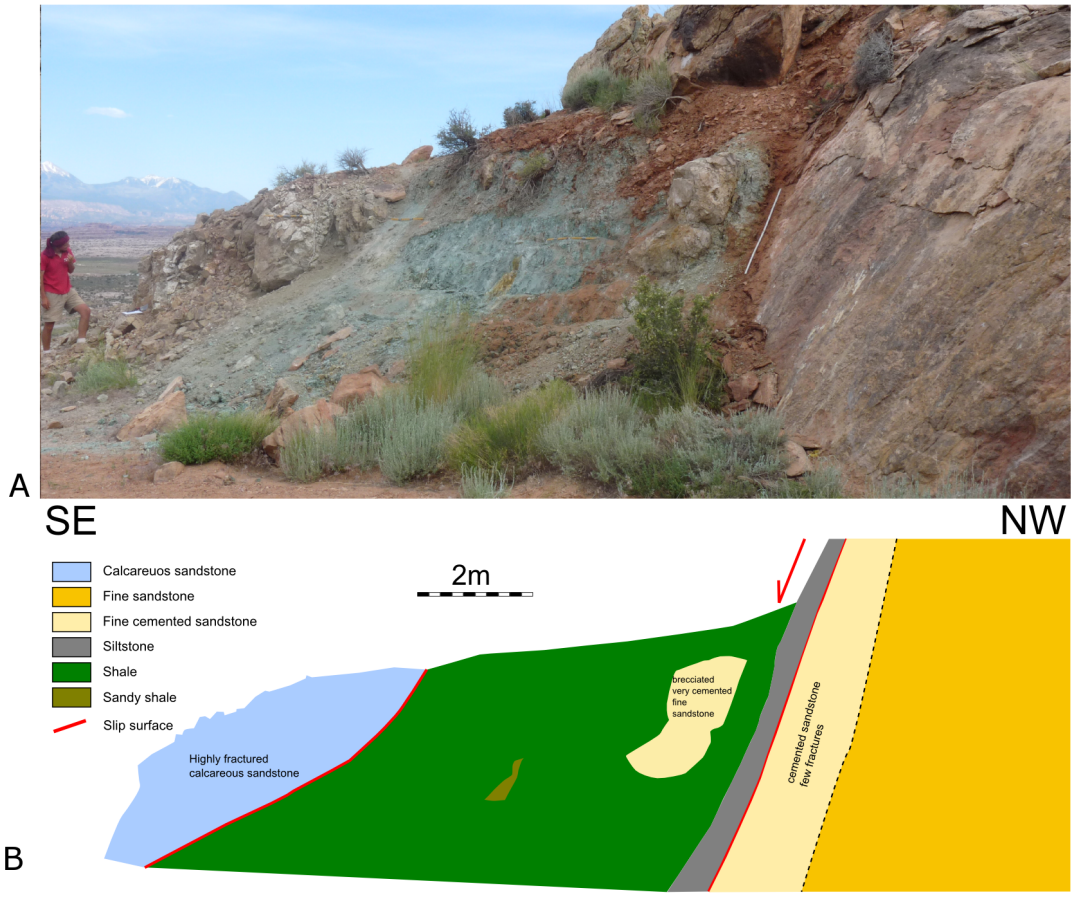

Figure 3.11: Moab fault exposure at Corral Canyon. A: Photo of outcrop. B: Map of outcrop.

Structure The architecture of the Moab fault at this interval is markedly different from the other exposures of the Moab fault. Here the fault core is composed of a thick layer of grey-blue shale, bounded by slip surfaces on both sides. Directly on top of the footwall slip surface there is a 55cm thick layer of silt. At the centre of the shale there is a 40cm long clast of brown sandy shale.

The footwall sandstone is strongly cemented with calcite near the slip surface. The thickness of the cemented zone could not be established as the rock behind the slip surface is not exposed. The cemented sandstone is fractured (figure 3.12). Three circular scan lines (section 2.4) yield fracture densities ranging from 4 to 51 traces per m^2. Part of the fractures (50%, visual estimate) shows staining by iron oxide rich cements. In addition dendritic managnese-oxide cementation is visible, surrounding fractures.

The scarcity of lenses and fragments of other lithologies suggests that this clay has been emplaced predominantly by shale smear. This is also proposed by Davatzes and Aydin 2005. The shale in the fault zone is very similar to the shale which occurs in the Brushy Basin member, which is exposed stratigraphically 30m below the fault exposure. The discrete bodies

Figure 3.12: Fractures in cemented slip surface at Corral Canyon exposure of the Moab fault.

of sandstone, blue-grey shale, brown shale and silt show that there is no grain scale mixing inside the smear, only mixing on a much larger scale.

Paleo fluid flow The iron-oxide and manganese-oxide stained fractures form the main indicators of past fluid flow along the fault at this location. In addition the calcite cementation of the footwall is likely related to fluid flow. Geochemical alteration is not observed in this outcrop; at field scale, the shale in the smear is indistinguishable from the shale rich parts of the Brushy Basin member.

Transect between Corral Canyon and Courthouse mine In between this loacation and the Courthouse mine site from Foxford et al., 1998, the fault has many small exposures. The fault architecture along this transect is fairly constant in style, but very variable in dimension. Over this interval (figure 3.13a) measurements and simple sketches have been collected to document this variation (figure 3.13b). The shale smear is present in all the exposures along the 1.8 km section studied here , but its thickness varies strongly along strike (2 to 24 m). Some sandstone lenses do occur inside the shale, but these are relatively few and isolated; three sandstone lenses were encountered in 9 transects, ranging in size from 0.9 to 2.0 meter wide, due to the limited exposure the length of the lenses could not be determined. No mixing of the sandstone and shale is observed. At all the exposures along the transect the shale smear is present, suggesting that the smear is continuous along strike. There is no information on whether or not the smear is continuous vertically.

Key flow controls The most important barrier for across-fault flow is formed by the shale smear, due to its low permeability and its ductility which makes it unlikely to sustain open fractures for prolonged periods of time. Along the studied transects (figure 3.13) the shale smear seems to be continuous. As the smear consist almost exclusively of shale, with few lenses and no mixing with sand, it should make for a very effective barrier to fluid flow. The effectiveness of shale smears as impermeable barriers to fluid flow over long periods is well established (Weber et al., 1978, Weber, 1987, Faerseth, 2006).

For comparison purposes the Shale Smear Factor (SSF) has been calculated for the mapped exposure. In short the SSF is used to predict if faulting of a single shale bed is likely to produce a continuous shale smear along the fault and therefore seal or a discontinuous non-sealing smear.

It is calculated by dividing fault offset by the thickness of a shale bed. Faults with an SSF value below an empirically derived threshold value are likely to have a continuous shale smear, whereas faults with a greater SSF, are likely to have a discontinuous shale smear. A more comprehensive discussion of the SSF is provided in section 5.3. When calculated using the thickest shale bed (20 m) that can be observed on gamma ray well logs; the SSF is 25. If the SSF is calculated using the entire thickness of the shale-rich Brushy Basin member (100m) the SSF is 5. According to Faerseth, 2006 the threshold SSF value for seismic scale faults is 4, with faults with lower values likely to have continuous shale smears and higher values indicating likely discontinuities. These numbers therefore suggest that the definition of the shale unit can be critical. The latter approach using the entire member thickness seems more appropriate as the sand beds in the Brushy basin member also show fault drag, suggesting the entire stratigraphic unit has been deformed. Throw is not constant along the studied transect, according to Foxford et al., 1998, the throw is 545m at Corral Canyon (SE most part of the transect) and 370m at Courthouse mine (NW most part of transect). Assuming a constant change in throw, throw values have been estimated for each location using linear interpolation. These throw values have been used to calculate the SSF (figure 3.13b), using the thickness of the Brushy Basin member, which is assumed to be constant at 100m. Figure 3.13c presents a plot of the measured shale smear thickness against the calculated SSF values. No correlation is visible between these two variables, suggesting that the thickness variation is not related to the local variation in throw.

The cementation in the footwall should not be ignored as it has a very low permeability. The cementation appears continuous along this part of the fault, but is frequently cut by fractures. The relative timing of the faulting, cementation, fracturing and iron staining is unknown. Without fracturing the cemented sandstone forms a barrier to fluid flow. The iron-oxide and manganese-oxide staining demonstrates that here half of the fractures have been open to fluid flow at one point during the fault's history. This suggests a strong temporal variability for this part of the fault zone. Initially this part of the fault zone started as a high permeability sandstone. The abundant calcite cementation subsequently reduces the permeability of the sandstone near to the fault zone. Cemented sandstone is more likely to form open fractures (Fisher et al., 2003). As such fracturing would increase the permeability of the zone. These open fractures in the calcite cemented sandstone were host to the flow of manganese and iron rich fluids. The iron staining is probably related to the 20-25 Ma fluid flow event described by Chan et al., 2001, and therefore postdates the slip of the Moab fault. The deposition of iron oxide cements in the fractures has subsequenlty reduced the permeability of the zone. The non-cemented/stained fractures probably did not exist at depth and would be uplift related. The permeability of this unit has changed strongly over time, with cementation depending on the pressure, temperature and fluid flow history, and fracture aperture depending on stress state (Barton et al., 1995).

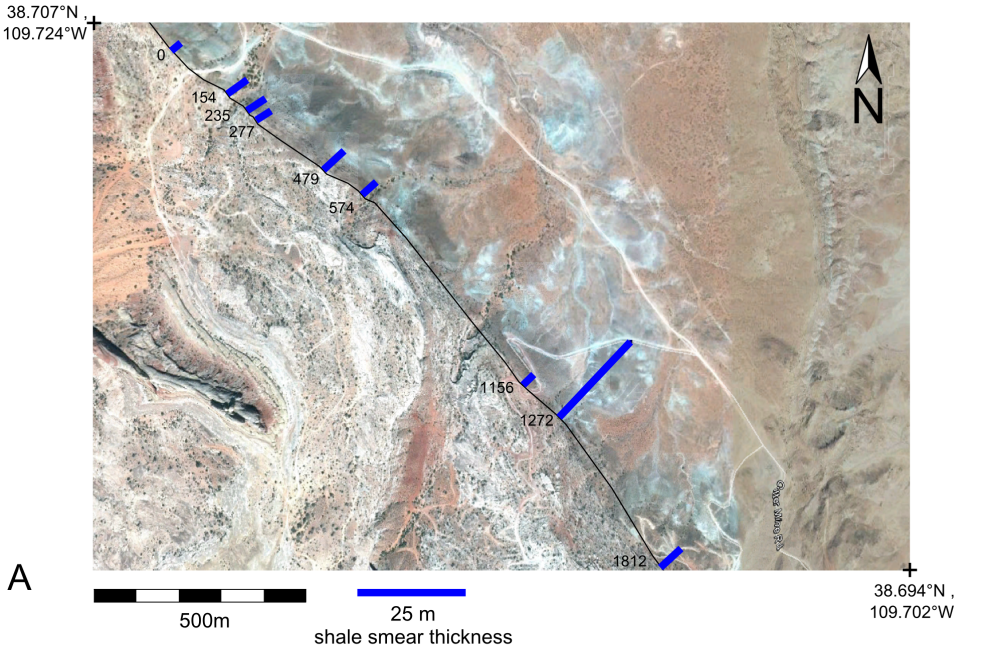

B

Distance along fault (m)	Shale thickness (m)	Throw, estimate (m)	SSF	Sketch FW Shale HW
0	1.9	370	3.7	
154	4.7	385	3.8	
235	3.8	393	3.9	
277	2.6	397	4.0	
479	5.6	416	4.2	
574	3.3	425	4.3	
1156	2.46	482	4.8	
1272	24	493	4.9	
1812*	5.9	545	5.45	

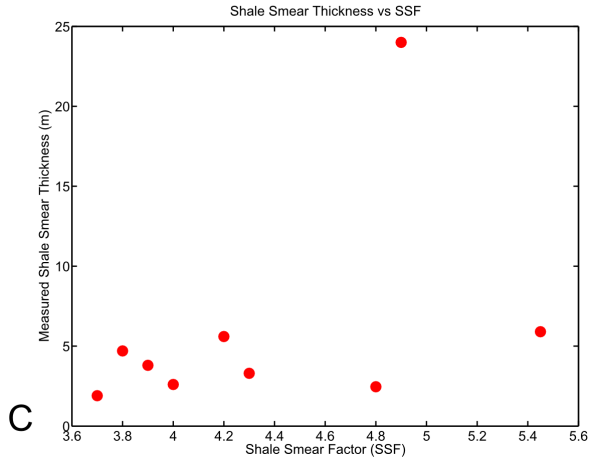

Figure 3.13: Variation of thickness of the shale smear at Corral Canyon. A: Aerial photograph annotated with bars indicating the thickness of the shale smear at each location. The number represents the distance along strike. (imagery from Google Earth). B: Table with simple sketches denoting fault content, shale thickness measurements, estimated throw and SSF values. The throw is interpolated linearly using the values reported in Foxford et al., 1998. C: Plot of the measured shale thickness vs SSF.

3.1.3 San Rafael Swell

Both the Cedar mountain faults and the Goblin Valley faults are located on the San Rafael swell (figure 3.14). This north trending asymmetric anticlinal structure is 120 km long and 60

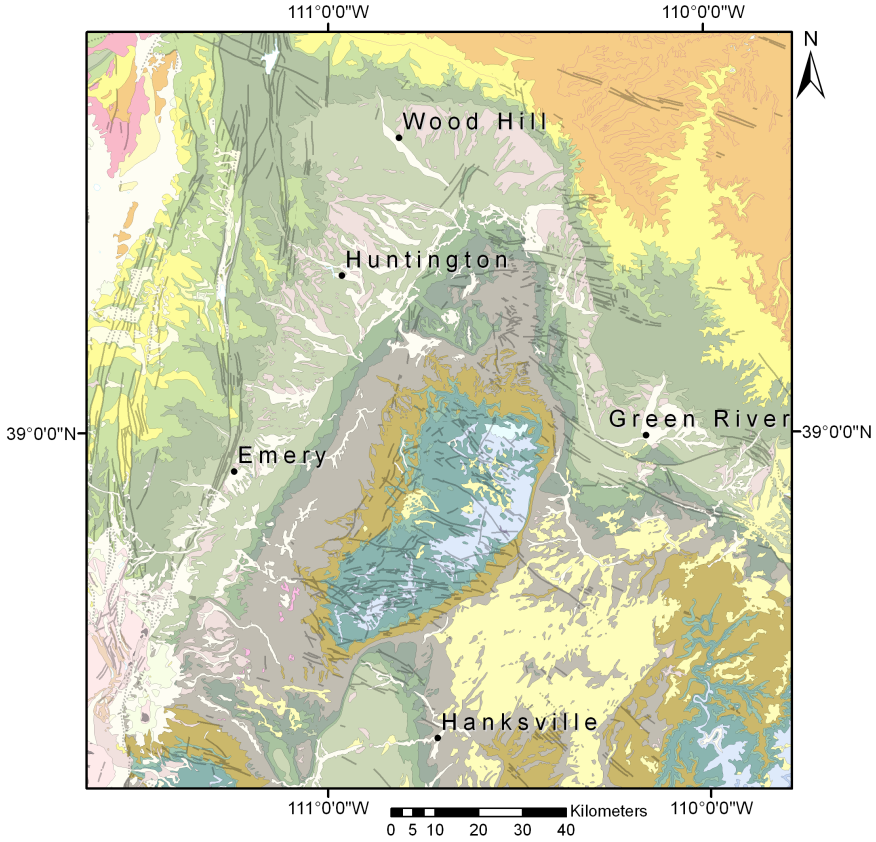

Figure 3.14: A: Geological map of the San Rafael Swell after Hintze et al., 2000.

km wide. The eastern margin is formed by a steep monocline, the western part consists of a much more gently dipping structure. It formed as a consequence of Laramide compression. The San Rafael swell has a long history of exploration and production of resources, most notably hydrocarbons, uranium and gypsum (Gilluly 1929). The Cedar mountain reverse faults are located on this western margin, whereas the Goblin Valley exposures are located just to the east of the eastern margin in the San Rafael dessert.

3.1.3.1 Cedar Mountain reverse faults

Two reverse faults were studied in the Cedar Mountain recreation area near the town of Huntington (figure 3.15a); both are part of the Cedar mountain thrust system. Neuhauser, 1988, interprets these structures to be formed by Sevier orogeny compression, localized here due to the eastward thinning of the shale and evaporate rich Carmel formation below the Cedar Mountain area. Both faults are located in close proximity to each other and cut through similar lithologies (Figure 3.15b). Neuhauser interprets the faults as linked, 700m north of the Ketobe Knob. The faults differ strongly in offset; with 8 m offset recorded for the small fault and 50 m for the large fault. Both faults are discussed in Welch et al., 2009, who used maps of the exposures to test their numerical models for the shearing of shale beds.

Ketobe knob thrust This fault is characterized by its excellent exposure; it is exposed on three perpendicular cliff faces. For this study the east face has been mapped as it is the only face on which both footwall and hanging wall are well exposed (figure 3.16). This fault has a vertical offset of 8 m, and a displacement of 12m. The Ketobe knob thrust is a splay of the main Cedar Mountain thrust. The fault cuts through predominantly fine grained sandstone and siltstones of the Entrada and Curtis formations.

Structure Most of the deformation is accommodated by three discrete slip surfaces. The rock in between the slip surfaces is tilted, sheared and fractured but there is no sign of mixing of sand, shale and silt. The beds in between the outermost slip surfaces are roughly perpendicular to the bedding in the host rock. This tilting of beds in between slip surfaces suggests this structure formed as a fault propagation fold. A thin layer of shaley gouge occurs along the slip surfaces.

Key flow controls Due to the slip being distributed over three main slip surfaces, the sandstones in both hanging wall and footwall are connected by sandstone beds in the fault zone. The main barrier to across-fault flow for this outcrop is formed by the thin (1-10 cm) gouge along the slip surfaces. Unfortunately it was not possible to verify the continuity of this gouge layer in the sand-sand juxtaposition mentioned above, as this part is inaccessible from the ground.

Cedar mountain thrust Roughly 300m north of the Ketobe knob a 4 km long fault is exposed in the same stratigraphy (Entrada and Curtis formations). The Cedar mountain thrust fault has 50 m throw (100m slip) but is less well exposed; mainly the fault core is visible. As the surface of the outcrop is not planar, gridding the outcrop is problematic. Instead photographs were taken at 1m intervals, and the fault was mapped using these photographs (figure 3.17). As a consequence the map is properly scaled, but does include some geometric distortions. The curved nature of the principal slip surface on the map is largely the result of the outcrop geometry rather than a real characteristic of the fault.

Structure The core of this fault consists of a set of small lenses of sandstone, siltstone and shale, fairly similar to the structures encountered in the Moab 191NW and Arches National Park entrance exposures and the Professor Valley fault exposure. One striking difference here is that sandstone is more abundant in this outcrop. The silt and shale lenses are thin (1-20 cm) and not continuous for more than a 0.5-2m.

Paleo fluid flow There is no evidence for significant along-fault flow in the form of geochemical alteration or cementation at this outcrop.

Key flow controls Due to the discontinuous nature of the siltstone in the core, this fault architecture could not act as a long term barrier to flow. As such the key flow control here for across-fault flow is formed by these discontinuities, their frequency and aperture. The slip surfaces might act as potential pathways for fluid flow in the core. But considering that the host rock is made up predominantly of sandstone, it's not likely that the fault core itself acted as a preferred conduit for along fluid flow.

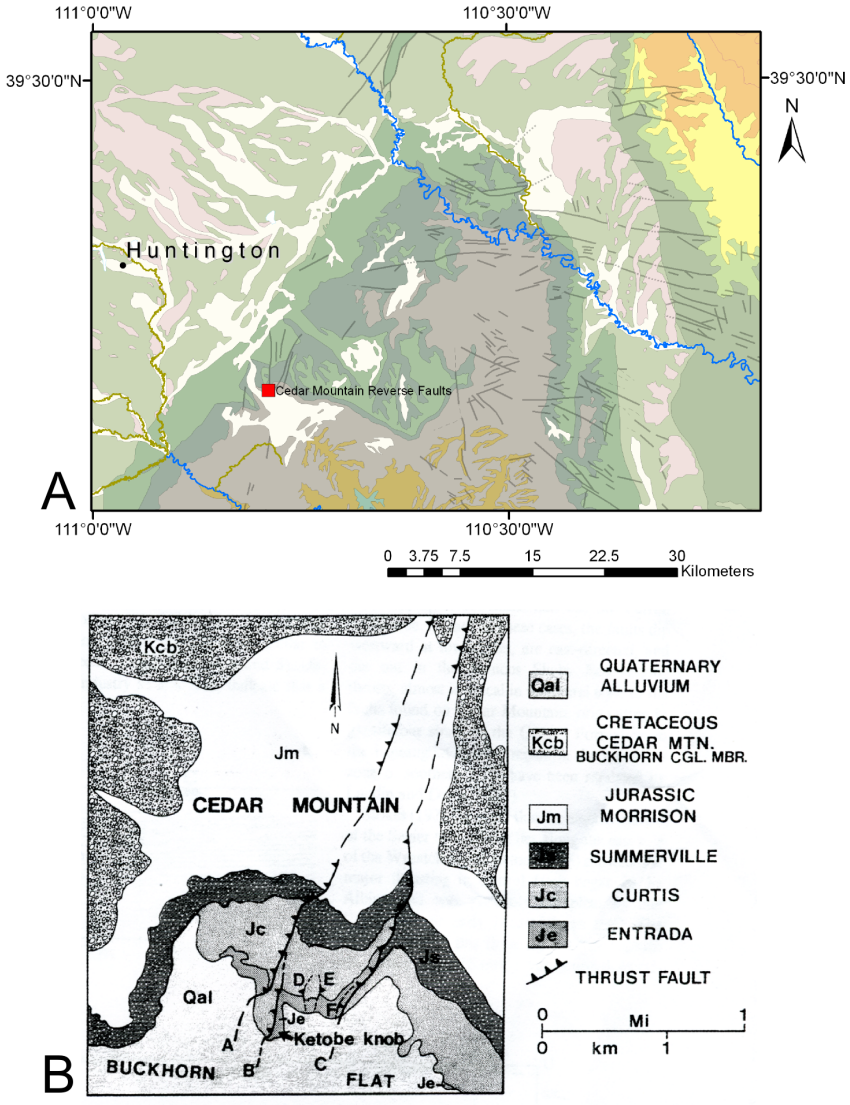

Figure 3.15: A. Location of the Cedar Mountain reverse faults on the geological map. (map after Hintze 2002). B. Detail map of the Cedar Mountain faults. Fault A is the Cedar Mountain Thrust. Fault B is the Ketobe knob thrust. Faults C, D,E and F have not been studied for this thesis. Map from Neuhauser 1988. .

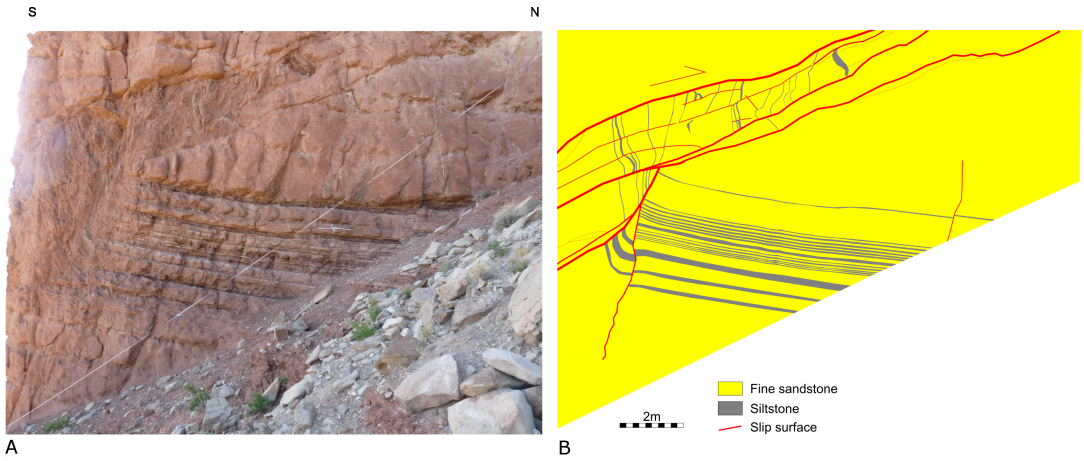

Figure 3.16: Ketob Knob (East face). A: Photo. B: Map of fault zone

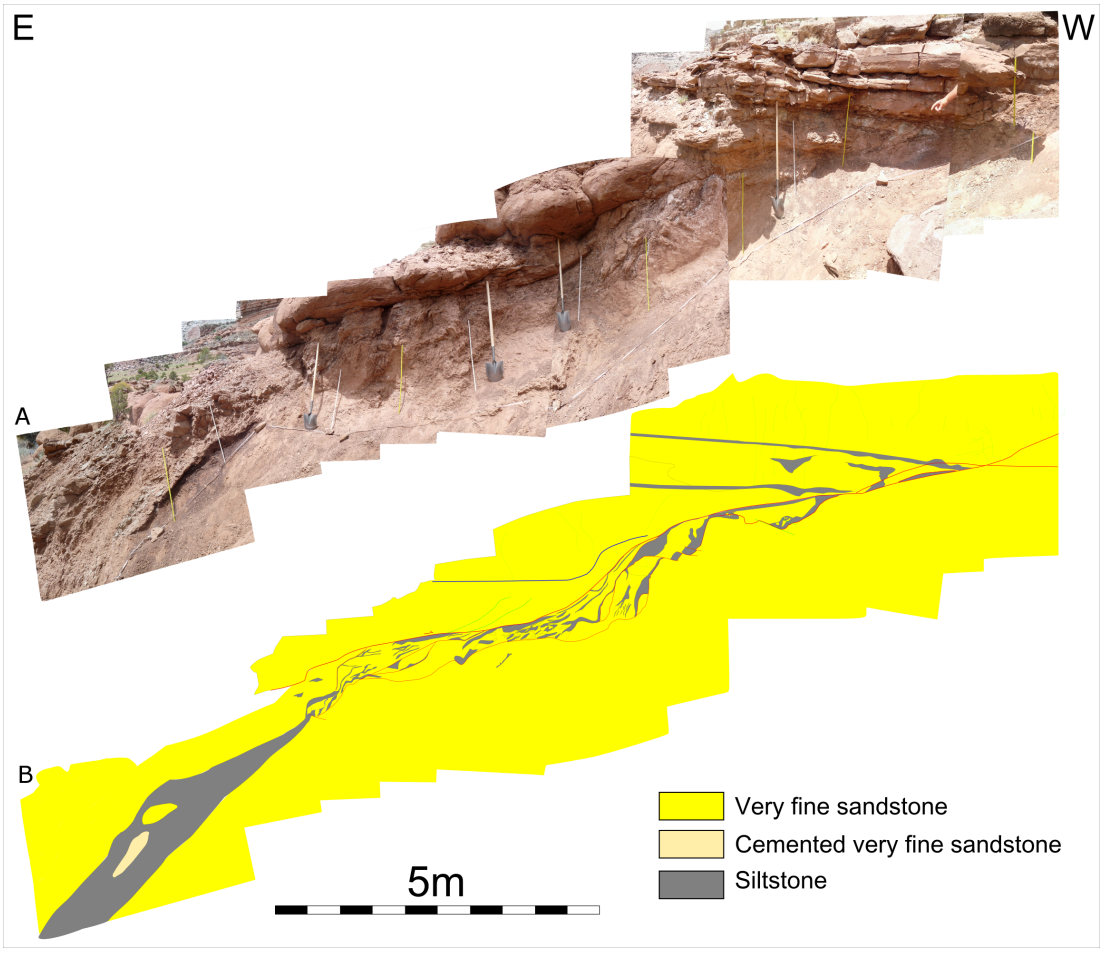

Figure 3.17: Cedar mountain thrust fault. A: Photo montage created using Microsoft Research Image Composit Editor (ICE) . B: Map of the fault zone.

3.1.4 Goblin Valley faults

Near Goblin Valley national park data have been collected from two WNW-ESE trending normal faults (figure 3.18). Both faults have a throw of 4m, and both faults cut a section which consists

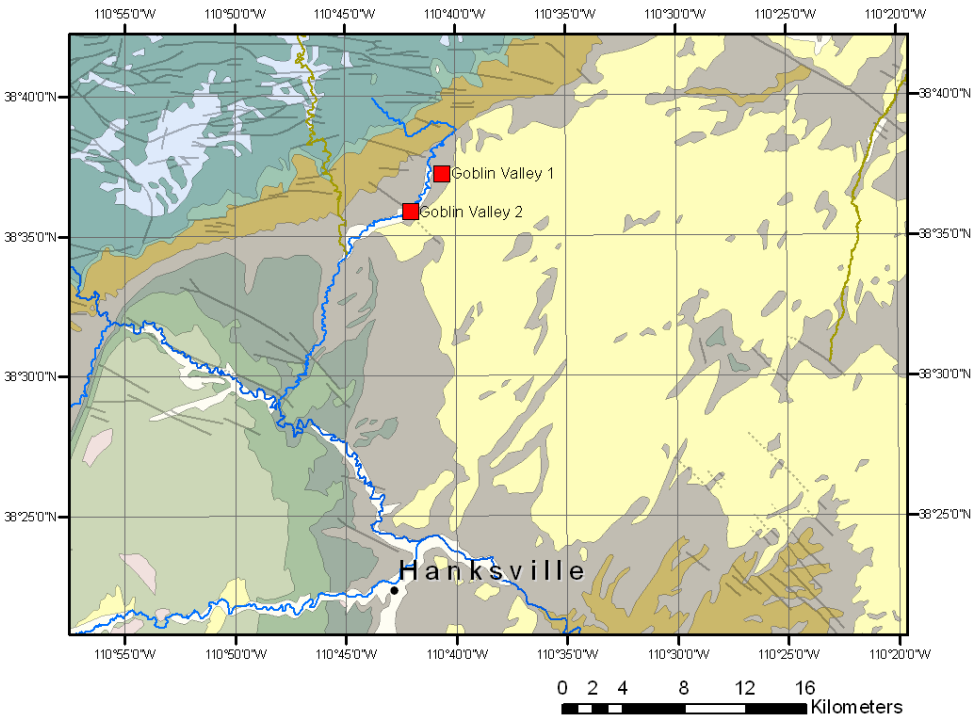

Figure 3.18: Location of the Goblin Valley exposures on the geological map. (map after Hintze 2002)

almost exclusively of porous sandstone and thin shale beds of the Entrada formation.

3.1.4.1 Goblin Valley fault 1

This small displacement normal fault (4.3 m throw) near Buckskin Spring has been previously studied by Aydin 1978 and Bright, 2006 (unpublished thesis), who focussed on the top part where sandstone is juxtaposed against sandstone. Below this level, the fault displaces sandstone with a thin (15 cm) shale bed, this study has focused on the lower part of the fault (figure 3.19).

Structure The shale bed has been smeared, forming a continuous membrane along the fault plane, but the thickness of the smear is strongly heterogeneous. This geometry does not look like the classic smear models, which thin progressively towards the centre until the extension surpasses a threshold value and the smear breaks (Lindsay et al., 1993). Instead the thick patches are bounded by straight segments, suggesting the involvement of planar structures in the host rock such as fractures or deformation bands.

Figure 3.20 presents measurements of the thickness of the shale smear. As the measurements follow the exposure of the shale smear, the 13m long scan line is non linear. The middle segment is horizontal and measures the thickness variation along strike, at a level just above (estimated 10-20cm) the shale bed in the hanging wall. The data shows that there is a strong variation

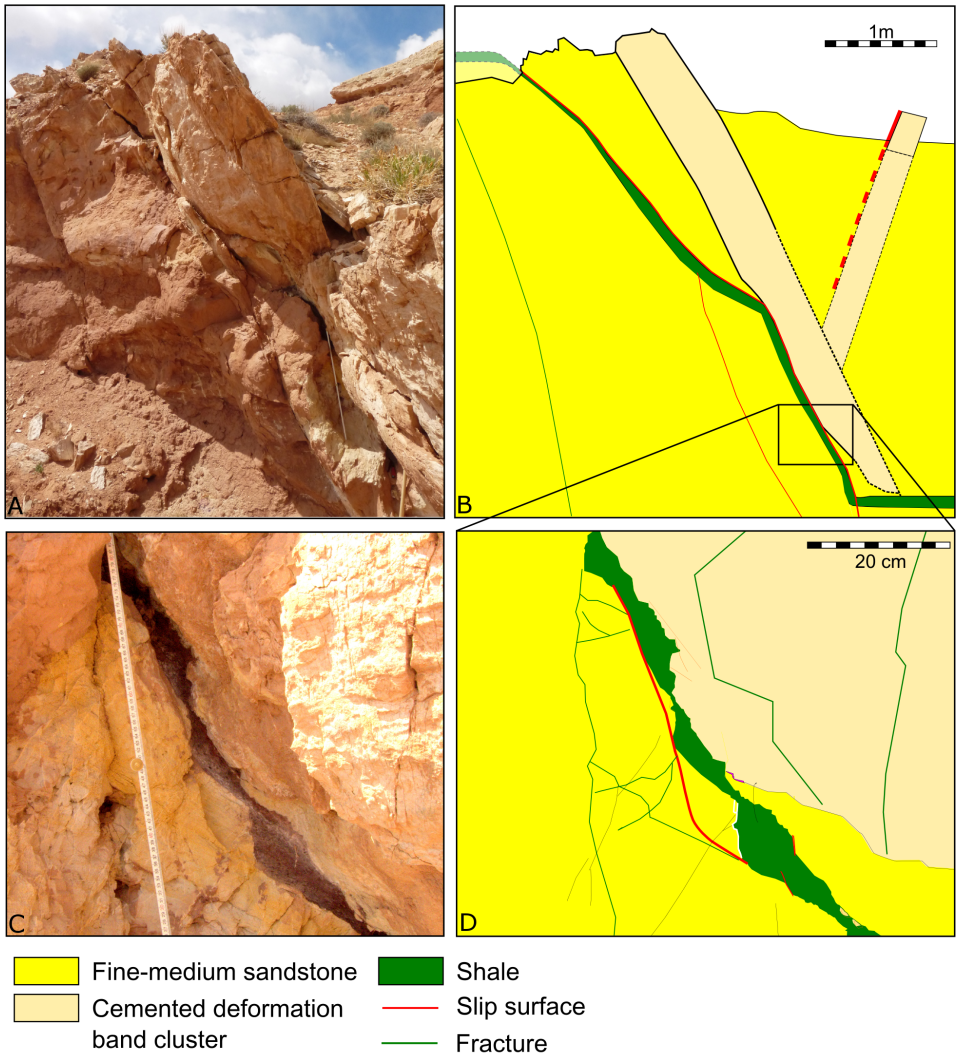

Figure 3.19: Goblin Valley fault 1. A: Overview photo of the shale smear in the NW flank of the exposure. B: Overview sketch. C: Detail photo of the smear. D: Detailed map of the smear.

(nearly 2 orders of magnitude) in the thickness of the shale smear, with the thickness ranging from 0.1 to 9.0 cm.

The NW part of the scan line is near vertical and describes the part of the shale smear mapped in figure 3.19 This again shows a strong variation, similar to the horizontal segment. This very strong thickness variation was also clear in figure 3.19.

The SE part of the scan line is diagonal and combines along strike and up dip variation of shale smear thickness. Again the data shows a strong variation; with thicknesses ranging from 0.3 to 15.0 cm. Part of the variation is caused by an upward trend. This trend most possibly signifies thickening towards the source bed in the foot wall, which has a thickness of 15cm. If this is the case, then the shale smear thickness is asymmetric, as there is no downwards thickening trend towards the source bed in the hanging wall.

On the footwall side a relatively bleached undeformed sandstone lens is located next to the smear. This sandstone lens terminates against the top shale layer. On the hanging wall side the smear is bounded by an approximately 10 - 200 cm thick cemented deformation band cluster,

similar to the fault core studied by Bright. The cemented condensed deformation band cluster is fractured (50 fractures / m2 using a circular scan line). No evidence was found to show that these fractures were open at depth, so they are most likely formed during uplift. Below the shale bed the deformation band cluster does not continue, instead there is sandstone with a low deformation band density.

As the thickness of the cemented condensed deformation band cluster strongly varies, measurements were taken to quantify this variation. Figure 3.21 shows these measurements and photos to illustrate the results. The measurements were taken along the fault at the top of the exposure. Due to the geometry of the exposure, the 14m long scan line is not perfectly horizontal, but goes up by about 1.5m. The measurements show a clear subdivision into two categories. Measurements taken stratigraphically above the shale bed are much larger (80-200cm) than those below the shale bed (10-90cm). This suggests that either the shale bed affects the mode of deformation of the nearby sandstone and therefore the thickness of the deformation band cluster. Or alternatively that the sandstone above and below the shale bed differ and that this lithological difference affects the thickness of the cluster.

Paleo fluid flow There is evidence for paleo-fluid-flow at this exposure. The sandstone lens next to the slip surface has been bleached. As has part of the damage zone in SE part of the exposure. Small linear bleaching patterns in the footwall are interpreted as bleaching by fluids moving through fractures (Figure 3.22). These bleaching patterns affect only a small part of the footwall. The cementation of this structure does not require past fluid flow but is related to local redistribution of quartz as shown by Bright.

Key flow controls In this segment the shale smear would be the main control on across-fault flow, with an additional baffle formed by the cemented deformation band cluster. The shale smear at places gets very thin (1mm), but remains continuous over the length of the outcrop. The shale smear factor (SSF) calculated for this outcrop is 29. Lindsay et al., 1993 suggests that faults with an SSF smaller than 7 are likely to be continuous and faults with an SSF greater than 7 may become incomplete. Faerseth, 2006 shows that for subseismic faults the critical SSF is much harder to define and can range from 1 to 50. This suggests that the processes active in this fault are more complicated than purely smearing of the shale bed.

Just above the mapped area, the shale smear disappears and the zone of cemented condensed deformation bands becomes the key flow control. This illustrates how fault permeability and fault architecture are linked to stratigraphy and juxtaposition.

Based on the bleaching patterns observed at the outcrop, the lens and damage zone are to be the main mechanisms for along fault flow. However these structures do not provide a pathway through the shale bed itself and are therefore only part of the flow network. The bleached halos provide some evidence for flow through a damage zone fracture network. But most damage zone deformation is accommodated by deformation bands rather than fractures. In the fault core the slip surfaces could facilitate fluid flow.

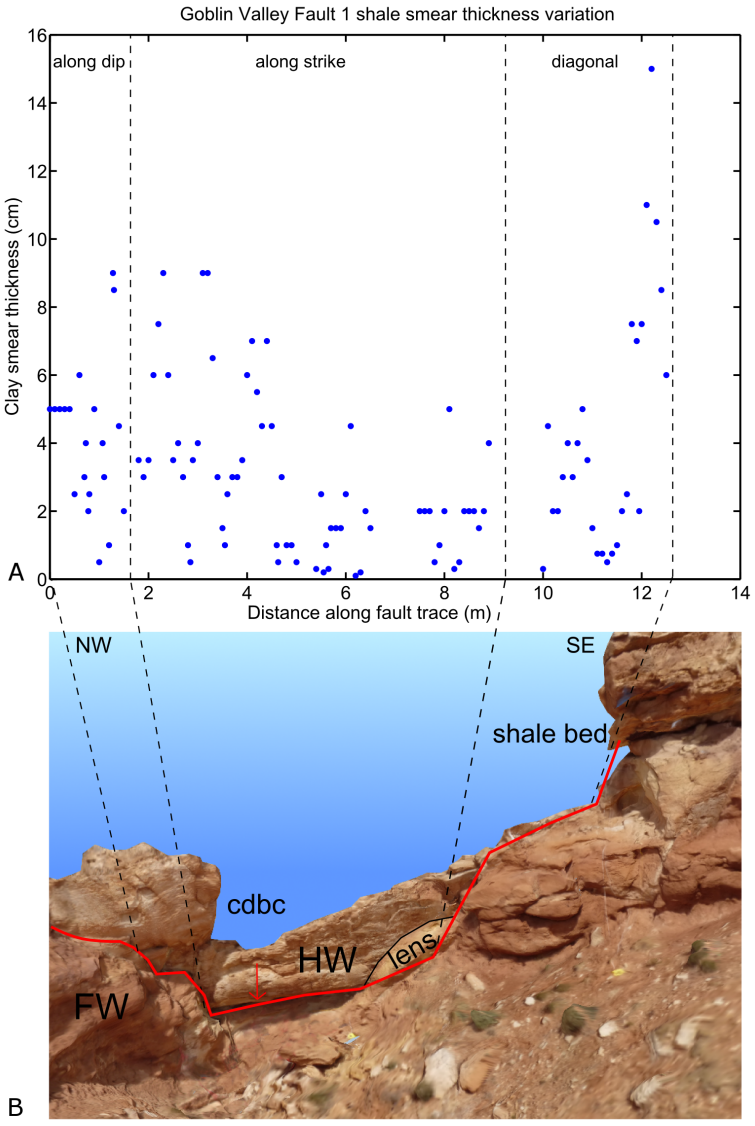

Figure 3.20: Variation of shale smear thickness along the fault trace. A: The graph shows the measured thickness of the shale smear. The transect can be subdivided into three segments. The NW part is the near vertical segment as sketched in figure 3.19. The central segment is near horizontal and as such shows along strike variation. The SE segment goes up diagonally. B: The lower image is an edited synthetic photo composite created using 123D catch. The source bed for the shale smear can be seen in the top right.

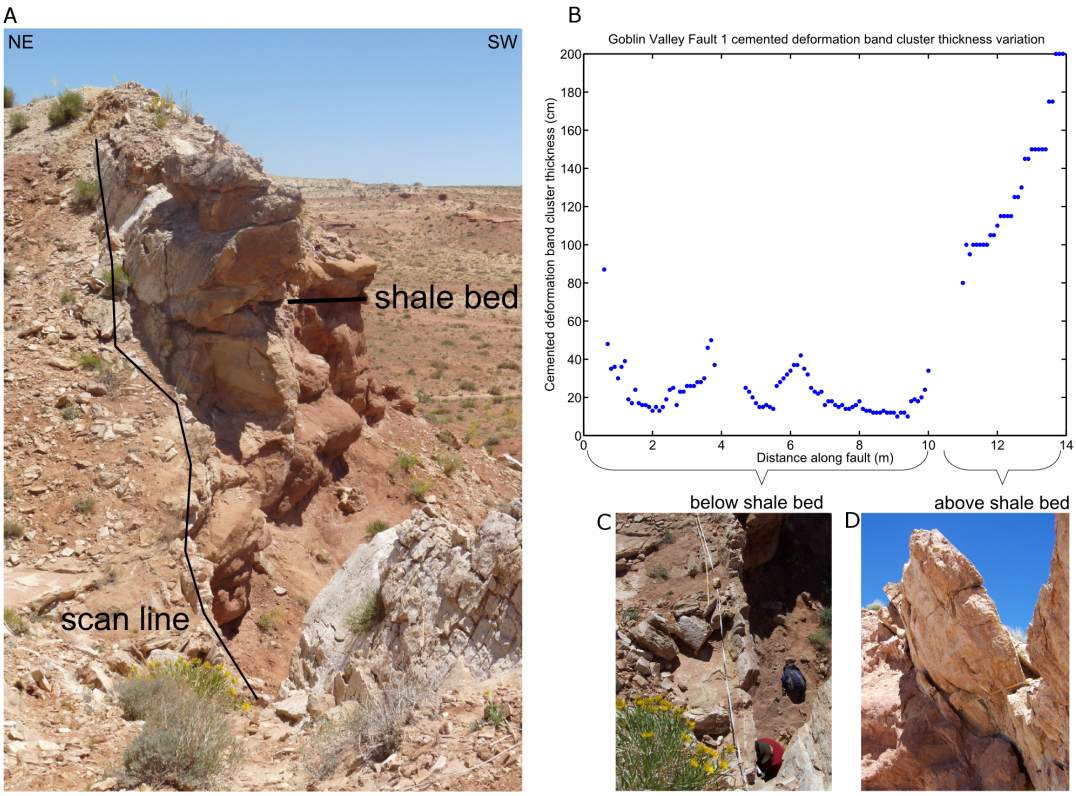

Figure 3.21: Cemented condensed deformation band cluster thickness along the fault variation. A: Photo of the top of the outcrop. The data is collected along the scan line indicated in the picture, starting (0m) at the front of the photo, and ending (14m) at the back. The line is not horizontal, but goes up diagonally. At approximately 11m the scanline crosses the shale source bed. Above this level the condensed deformation band cluster is much thicker than below it. B: Graph of the collected data. C: Photo of the cluster below the shale bed. D: Photo of the cluster above the shale bed.

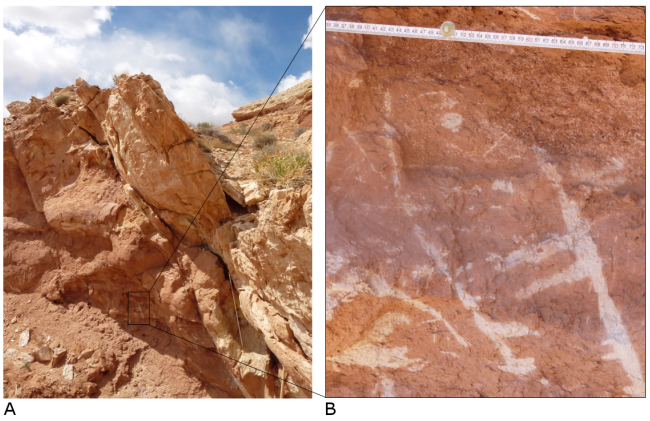

Figure 3.22: Linear bleaching patterns. These patterns are interpreted as bleaching halos around fractures which were open at depth. Currently the fractures are no longer visible, suggesting that they closed after they were no longer critically stressed. A: Overview photo, only a small fraction of the outcrop is bleached. B: Detail photo of bleached fractures.

3.1.4.2 Goblin Valley fault 2

This WNW trending normal fault near Wildhorse Spring was previously mentioned by Fossen and Hesthammer 1997. They have studied deformation bands in nearby sediments. They report a maximum displacement of 6m, at the outcrop studied here, the fault has a throw of 4m. It displaces sandstone, shale and silt beds of the Entrada formation.

In contrast to Goblin Valley fault 1 this fault has not developed a shale smear, instead the fault plane forms a clean cut straight through all the lithologies (figure 3.23). In the outcrop

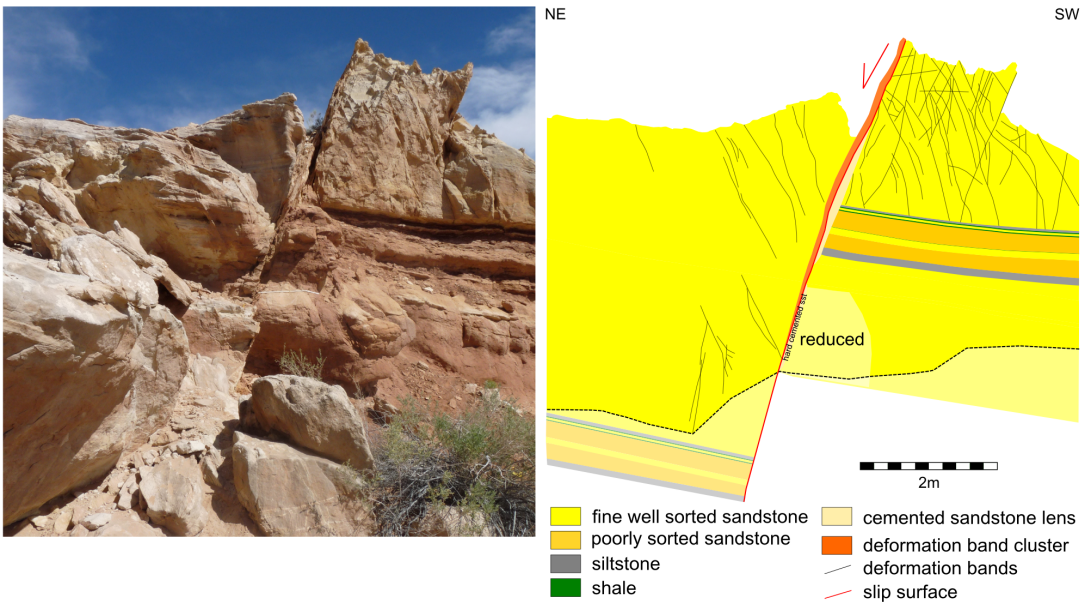

Figure 3.23: Goblin Valley fault 2. A: Photo of studied area. B: Map of fault zone.

two thin (<10 cm) cemented sandstone lenses can be seen parallel to the main slip surface on the SW side. On the NE side of the main slip surface a thin (0-10 cm in the cross section view) deformation band cluster is present. This cluster thins downwards towards the shale, similar to the behaviour of the deformation band cluster at exposure Goblin Valley 1.

Along-strike thickness measurements of the condensed deformation band cluster were collected at the top of the exposure (figure 3.24). The 14m long scan line is near horizontal and fault juxtaposition is constant along the line. The thickness is strongly variable, ranging from 2-30 cm.

Paleo-fluid-flow Evidence for fluid flow through the fault is provided by a reduced/bleached area at the base of the footwall. In addition the cementation of the condensed deformation band clusters is likely the result of local redistribution of quartz, rather than cementation due to fluid migration.

Key flow controls The deformation band cluster and the cemented lenses are the main barriers to fluid flow across the fault. Both are not continuous along the fault on their own, but all structures combined together form a continuous barrier along the exposed part of the fault. For along-fault flow the slip surfaces seem the prime candidate together with the cemented sandstone lenses before they became cemented. As the host rock tends to develop deformation

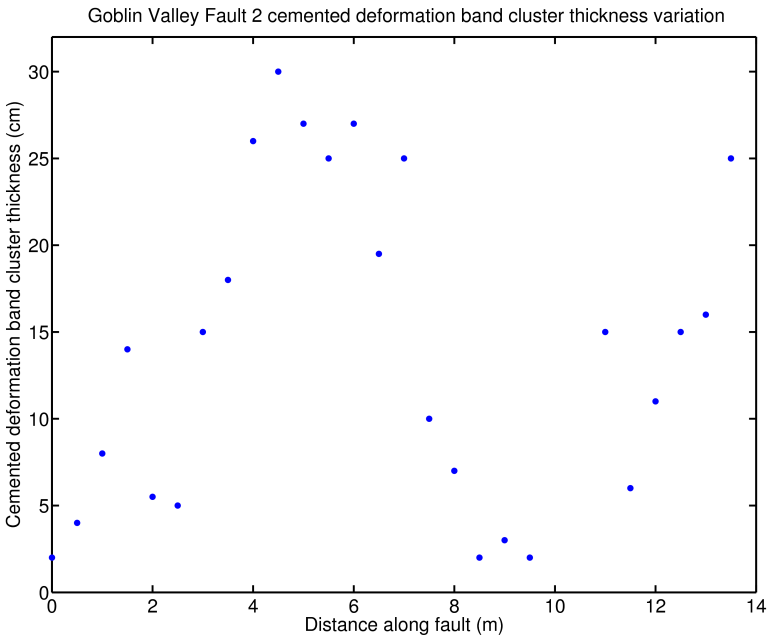

Figure 3.24: Goblin Valley fault 2, thickness variation of the cemented condensed deformation band cluster. Data Collected along a horizontal scan line at the top of the exposure, stratigraphically above the shale and silt beds.

bands rather than fractures, the damage zone is likely to be less important for along-fault fluid flow than for faults in other lithologies.

One possible explanation for the absence of the shale smear might be the slightly different lithologies and their different distribution. At Goblin Valley fault 1 the displaced lithology is formed by sandstone and a single 15cm thick shale bed. At Goblin valley fault 2, the displaced lithology is quite similar but its distribution is different, consisting mostly of sandstone, 26 cm of silt and 6cm of shale distributed over five thin beds. The importance of the shale bed thickness is also incorporated into the SSF algorithm. Table 3.1

unit	thickness (cm)	SSF
silt	6	67
shale	2.5	160
shale	2.5	160
shale	1	400
silt	20	20

Table 3.1: SSF values calculated for Goblin Valley fault 2.

shows the calculated SSF factors for the different beds in this outcrop. These values are very high, and as such SSF predicts that they would not form a continuous smear. Of particular interest is not that there is no continuous smear, but that there is no smear at all. This is in stark contrast with the assumptions behind smearing algorithms. This could possibly be explained by the composition of the 'smearable' material at Goblin Valley fault 2, which consists largely of siltstone, which is less likely to smear due to the absence of ductile clay. It does not explain why the thin shale beds have not smeared.

3.1.5 Professor Valley

At Professor Valley a normal fault with a throw of roughly 30m has been studied. This ENE-WSW trending fault is located along the axis of the similarly trending Cache Valley (figure 3.25). As such its formation is probably similar to the normal faulting in the Cache Valley, which is explained by the collapse of the underlying salt anticline during the Tertiary due to the dissolution of the salt (Graham 2004).

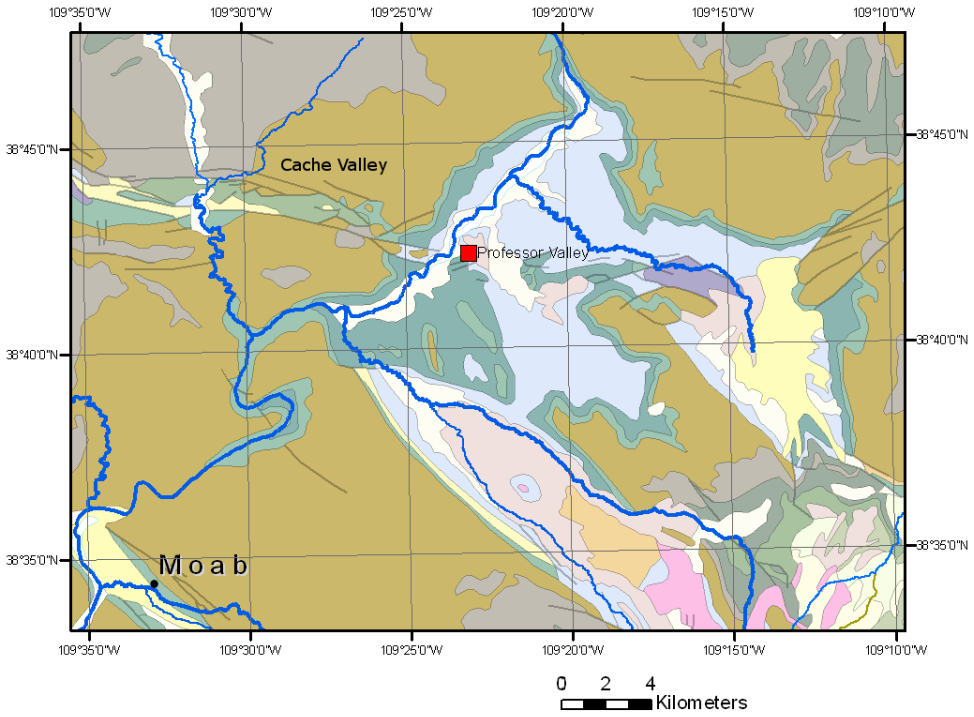

Figure 3.25: Location of the Professor Valley exposure on the geological map. (map after Hintze 2002).

The fault is formed by five strands, of which the main strand juxtaposes a sand dominated sandstone-shale sequence against shale (figure 3.26). This strand has a throw of 30m. It is bounded by a set of lenses composed of sand and shale. There are no signs of mixing of the sand and shale, the original depositional fabric inside the lenses is deformed but still present. Beds inside the lenses have been rotated, sheared and fractured. The westernmost part of the fault zone is formed by a lens of poorly consolidated sand (40 – 80 cm thick). The shale in the hanging wall has accommodated part of the strain; close to the fault bedding is rotated to 60 degrees, in approximately 10 m the bedding dip returns to the regional value of 30 degrees.

Four smaller (m scale displacement) strands are located in the thin bedded sandstone-shale sequence, SE of the main strand. Two of these strands are shown in figure 3.27 a. These are characterized by small displacements (<1m). The minor strand closest to the main strand has been studied here. It has a displacement of 0.5m. Its core is formed by a thin fault gouge of mixed sand, shale and silt. This in clear contrast with the main fault zone where abrasive mixing is not observed. The thickness of the gouge was measured over a short interval (2.5m), the results are shown in figure 3.27c. The gouge thickness shows considerable variation, ranging

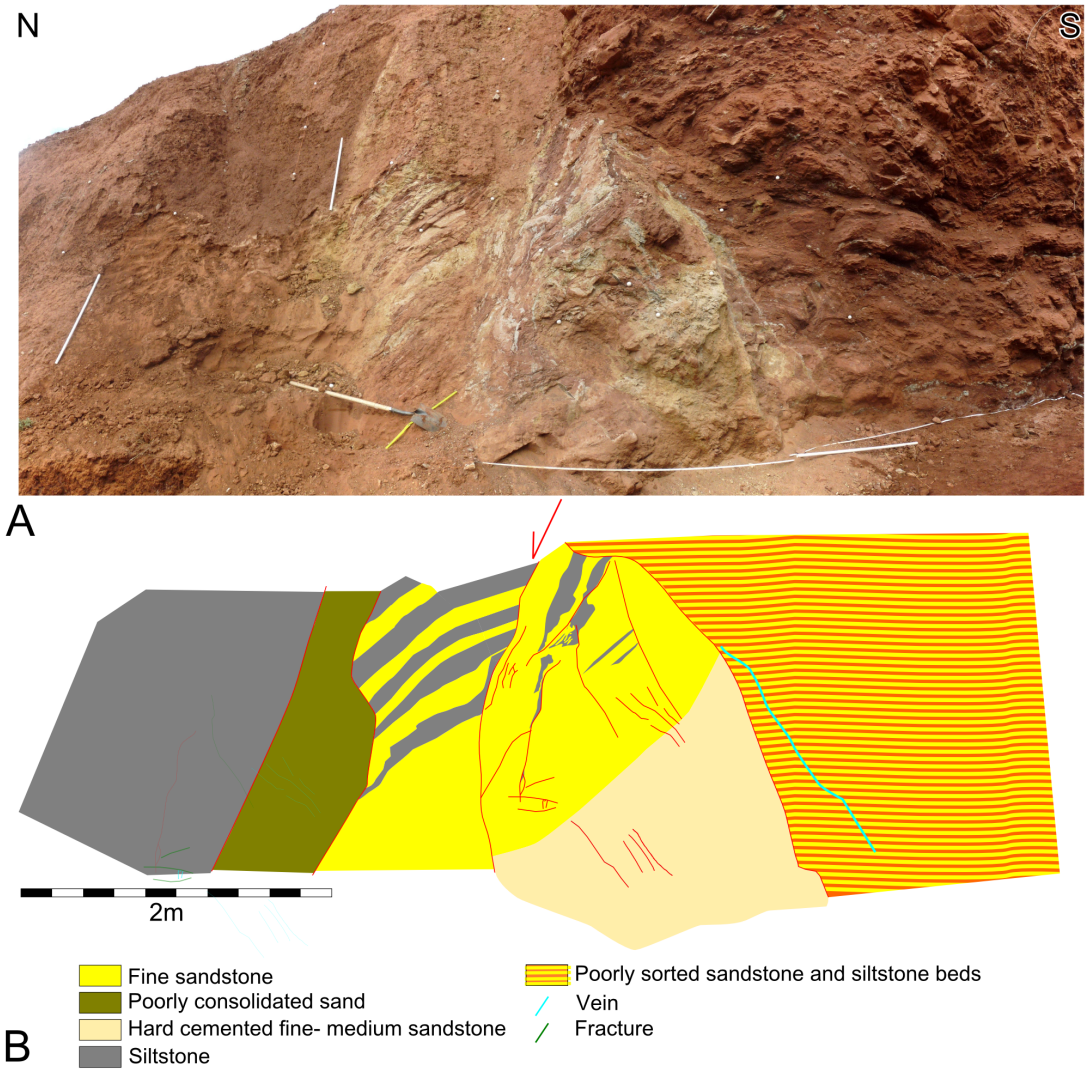

Figure 3.26: Professor Valley fault exposure of main strand (30m throw). A: Photo of mapped exposure. B: Map of fault zone

from 4.5 to 11cm in the studied interval. No trends are apparent in the data set.

Evidence of paleo-fluid flow through the fault zone is provided by cementation and colour changes indicating geochemical alteration. This is primarily observed in the lenses in the fault zone. Additional observations of bleaching are made in the footwall near certain fractures and beds.

For across-fault flow the most important key flow control at this part of the fault is obviously juxtaposition; the thick shale bed forming the hanging wall forms the main barrier to flow. Inside the fault zone itself barriers are formed by cementation and sheared silt beds. But these two elements are not continuous along the fault zone, suggesting that they are of minor importance as barriers to across-fault flow. For along-fault flow the main control is formed by the poorly consolidated sand in the centre. This unit is continuous along the entire length of the exposure. In addition the slip surfaces and sandstone lenses can form potential pathways for fluid flow.

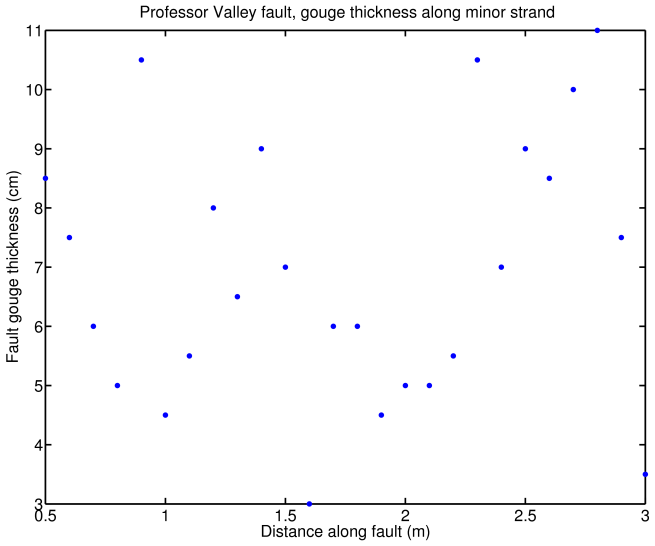

Figure 3.27: Professor Valley minor strands. A: Photo showing the NW most minor strands, 6m SE of main strand. B: Detail photo of the studied minor strand. C: Thickness variation of the gouge of the minor strand. Distance is reported from ground level upwards.

3.1.6 Minor observations Utah

In addition to the mapped outcrops described previously, several other outcrops have been visited but studied in less detail. These outcrops provided interesting insights into fault architecture, but were not suitable for mapping. Here some small but relevant observations are presented. These are not used for the flow modelling in chapter 6, but provide useful insights into the architecture and permeability development of fault zones.

3.1.6.1 Woodside fault

This fault is exposed in the cliffs to the east of the San Rafael Swell, 6.7 km to the NE from Woodside. The exposure is located high up the cliff, making it potentially unsafe, which is why it was not studied in more detail.

Figure 3.28: Woodside fault, displacing a coal seem over ten metre. A: Overview photo. B: Detail photo of the coal smear (Courtesy of C. Wibberley).

The fault has an offset of approximately 10m, displacing sandstones and coal. The coal has been smeared along the fault plane (figure 3.28), similar to the smearing of shale. The smearing potential of coal has been previously mentioned by Faerseth 2006.

3.1.6.2 Moab fault highway exposure

This exposure is located at the bend in the highway 191 north of Moab, 60m south of the Arches National Park entrance exposure. The core of the fault is poorly exposed at this outcrop, but the roadcut offers a magnificent view of the damage zone. The damage zone here contains tens of small (dm to m scale) faults. It has been studied by Ferril et al., 2009, who focus on the geometry of conjugate normal faults. One of these conjugate normal faults is discussed here in more detail.

This fault has a throw of 5m, displacing sandstone and shaley sandstone. The fault is included here because the shaley sandstone has been smeared along the fault. This shows that a wide variety of lithologies can form smears, not only pure shale. Figure 3.29 presents a photo of the smear and measurements of its thickness. The measurements show a strong variation in thickness, ranging form 10 cm to 115cm over the studied interval. There is a clear trend visible,

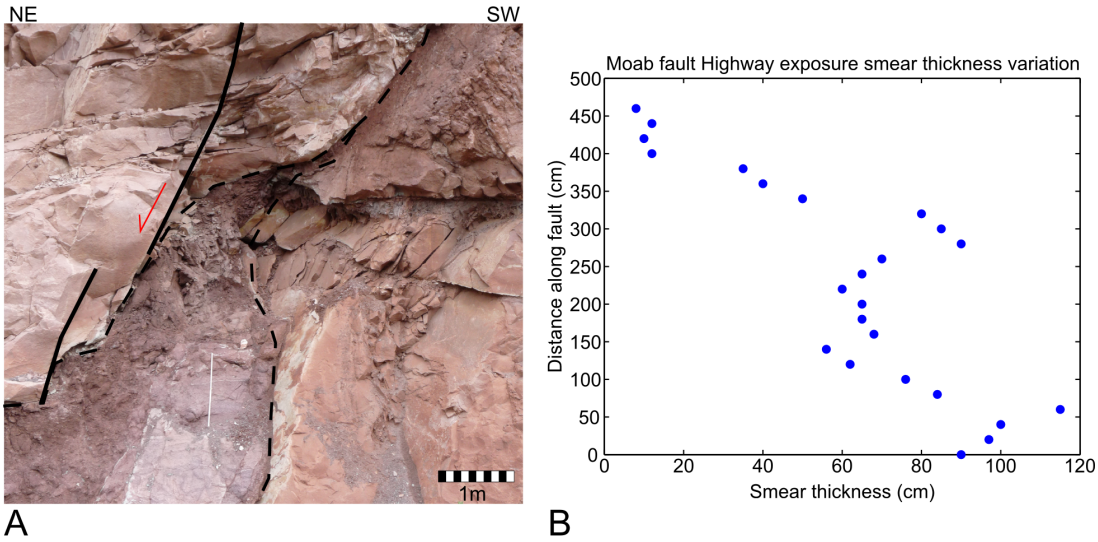

Figure 3.29: Subsidiary fault in the damage zone of the Moab Fault. A: Annotated photo of exposure. B: Graph detailing the thickness variation.

where the smear thins away from the source bed. Additional changes in the thickness can be related to shear along fractures in the sandstone bed.

Sinai desert Egypt

In February 2010 three faults were studied in the Western Sinai desert (figure 3.30) Due to its desert climate, the geology in the area is very well exposed. Towns are located almost exclusively near the coast, but there are many good roads going in land because of the mining activity in the area.

The tectonic history of the area is dominated by the Suez rifting, which is part of the Oligocene to Miocene red sea rifting caused by the separation of the Arabian plate from the African plate (Gawthorpe et al., 2002). Several authors have studied the synrift and postrift sequences exposed in the Hamam Faraun fault block, which is bounded by the Hamam Faraun fault along coastline and the Thal fault in land. In contrast the faults studied for this thesis are located in the pre-rift sediments on the footwall side of the Thal fault (Figure 3.30). Data was gathered from excellent exposures of normal faults in the cretaceous Malha formation whichs form the uppermost part of the Nubian sandstones (Moustafa, 2003). At the studied sites this formation consists of highly porous fluvial sandstones intercalated with kaolinite beds and calcareous shales.

Displacement on these faults ranges from 10 to 100 meters. The fault exposures in the Sinai are fairly large, allowing for the collection of data on the along strike variation of key flow controls. As the host rock stratigraphy is dominated by porous sandstones, typical deformation band dominated fault architectures are encountered. These architectures are similar to those described by Shipton et al., 2005. Key flow controls encountered for these faults are zones of densely clustered deformation bands and dense cementation associated with large slip surfaces. Where shale is present in the host rock, shale smears are encountered.

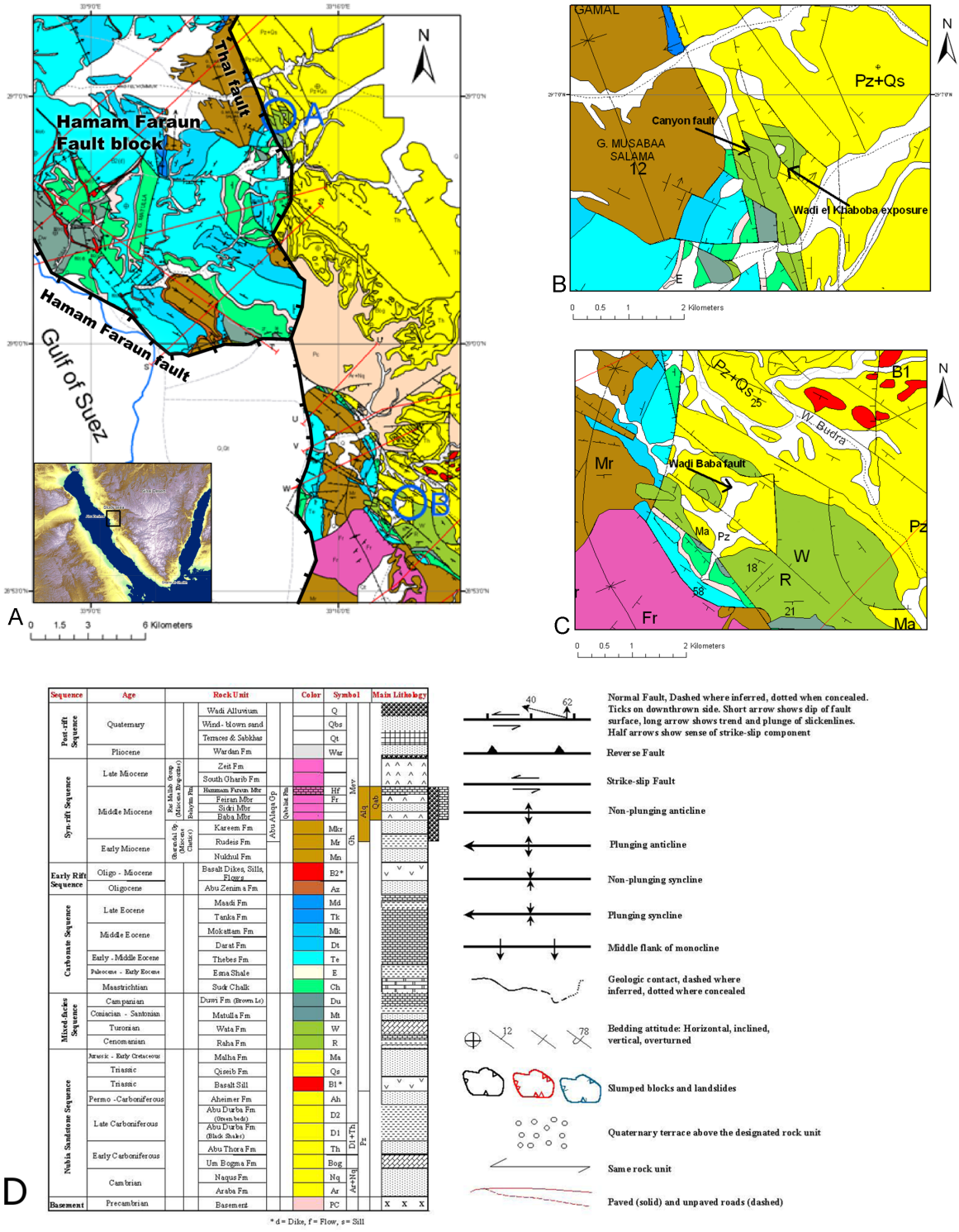

Figure 3.30: Locations of studied areas on geological map. A: Regional geological map, after Moustafa et al. 2003. a: marks the area with the Wadi el Khaboba and Canyon faults. b marks the area with Wadi Baba and Camel fault. B: Detailed map of the area a. C: Detailed map of the area b. D: Legend.

3.1.6.3 Wadi el Khaboba

This location has been previously studied by Rotevatn et al., 2008, who focussed on deformation bands in the damage zones. They describe a type of cataclastic deformation band which has a small slip surface in the centre. This study focuses on the core of this fault (figure 3.31). At this location this fault displaces a sandstone-dominated sequence by 94 m. The host rock is a medium to coarse grained fluvial sandstone, part of the Malha formation. The sandstone is moderately consolidated, with grains that are subrounded. In addition to sandstone the fault displaces a 5 m thick marly sandstone bed.

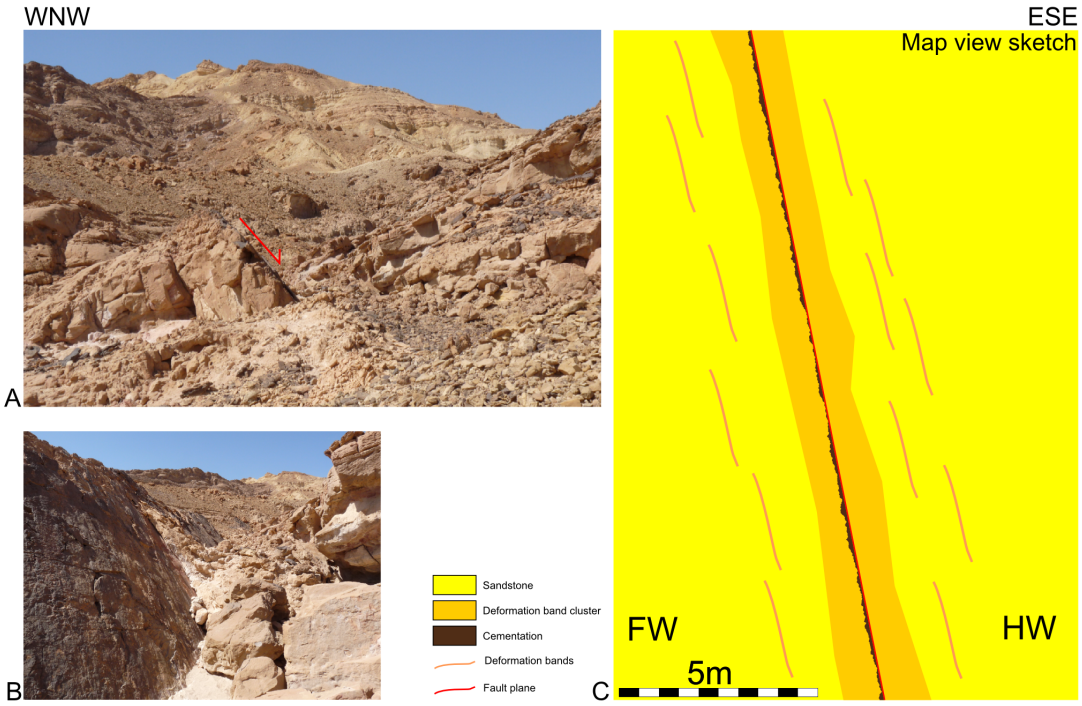

Figure 3.31: Locations of studied areas on geological map. After Moustafa et al. 2003. A: marks the area with the Wadi el Khaboba and Canyon faults. B marks the area with Wadi Baba and

Structure The architecture of this fault is formed by a dense deformation band cluster with a slip surface in the centre. This central slip surface is continuous and approximately planar over the entire studied length of the outcrop. A dense brown-purple cement is present on the main slip surface and continuous into the footwall. The thickness of the cemented zone is variable, following fractures coming from the main slip surface. The cementation overprints cataclasites in the footwall. In addition to the cemented fractures, open fractures also cut the slip surface. The fault has a damage zone dominated by deformation bands and some minor slip surfaces (three encountered along a scan line through the footwall, no data for the hanging wall).

Paleo fluid flow The dense cementation around the slip surface suggests that at some point during the fault's history the slip surface acted as a conduit for fluid flow. This cementation occurs on many major slip surfaces in the region and is dominated by iron and manganese oxides (Tueckmantel et al., 2010). A potential source for the iron and magnesium would be formed by the Carboniferous Um Bogma dolomites (Kora et al., 1994).

Key flow controls In the field, data collection was focussed on the cemented cataclasites as these rocks were most likely the lowest permeability part of the outcrop at present. Data was collected on the thickness of the cemented zone as a key flow control. The thickness of the cemented zone changes strongly over short distances. We have collected data on the thickness variation over a length of 58 m along the strike for the fault. Along the fault, the 58 m transect goes up 6m vertically. The Data was collected at 1 m intervals. The graph (figure 3.32) shows a strong increase in thickness with increasing distance (to the NNW). This can either be indicative of a large scale spatial trend. Or as the scan line also goes up, it can be related to lithological changes of the stratigraphy. Basic geological field observations did not reveal such lithological changes in the field. However more thorough petrophysical inspection of the stratigraphy is needed to decisively rule out this possibility. The thickness variation is analyzed using spatial statistics in the chapter 7.

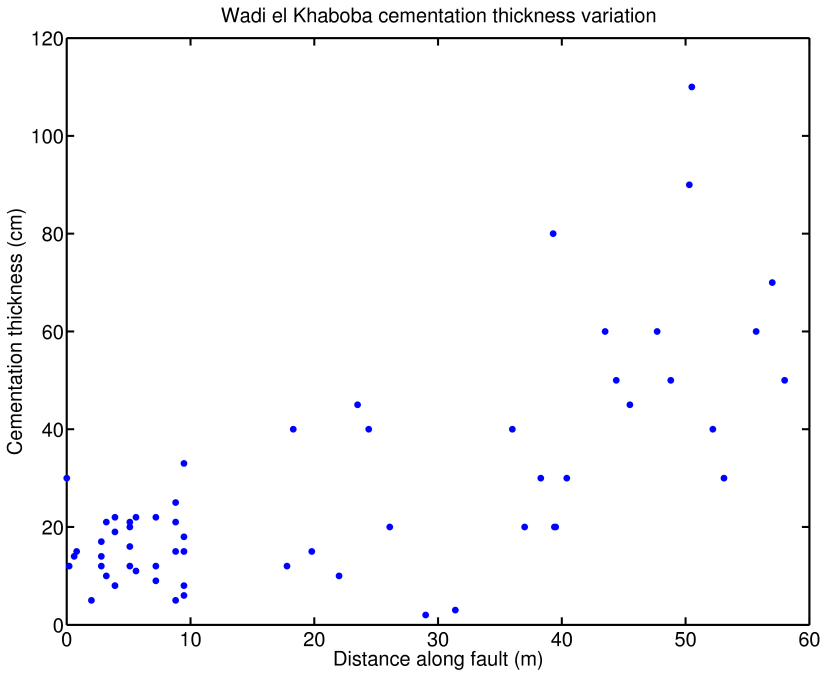

Figure 3.32: Wadi el Khaboba measurements of the thickness of the cemented part of the fault core.

3.1.6.4 Wadi Baba

At this location a fault with a throw of 10m displaces a sandstone-dominated sequence. The sandstone of the Malha formation is similar to the sandstone at Wadi Khaboba; medium- coarse grained, very porous, moderately consolidated subangular grains. In addition to sandstone the top of the sequence contains beds of sandy marl (15%).

Structure This fault is summarized in figure 3.33. The fault architecture is dominated by a dense deformation band cluster with several small anastomosing slip surfaces. No iron oxide cementation was observed a long this fault, unlike Wadi Khaboba.

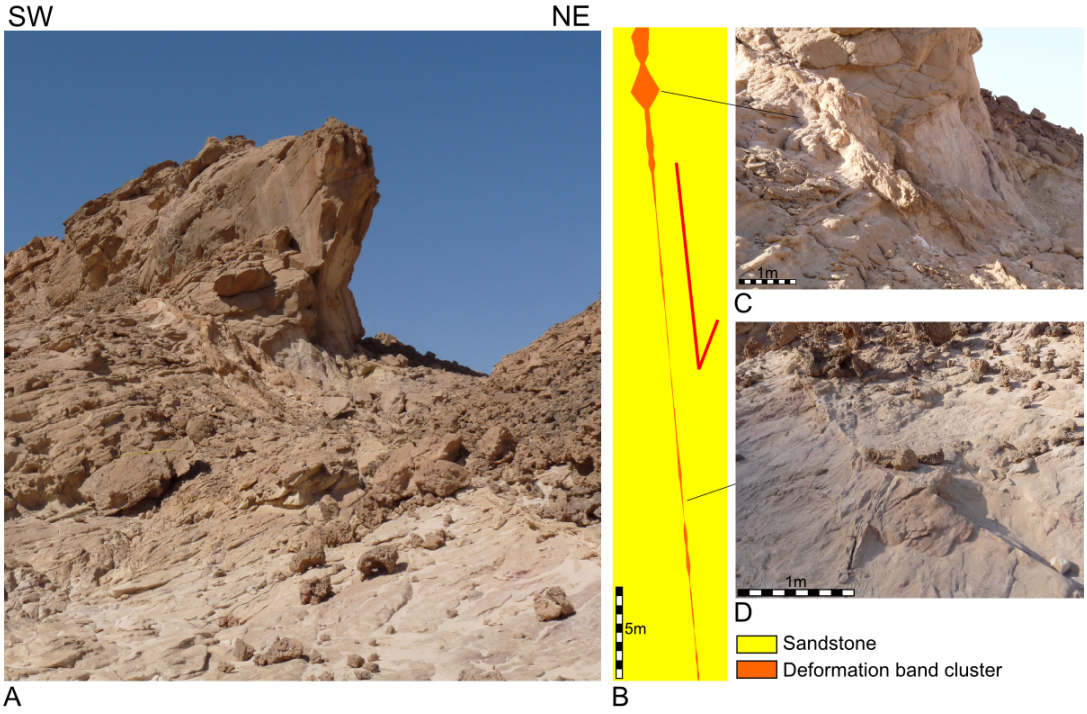

Figure 3.33: Wadi el Khaboba measurements of the thickness of the cemented part of the fault core.

Key flow controls The deformation band cluster is the main fault feature likely to affect fluid flow, forming a baffle to across-fault flow. The thickness of the deformation band cluster has been measured over a length of 35.5m. The scan line is not perfectly along strike, but has an up dip component of 5m. The results of the measurements are shown in figure 3.34. The thickness varies strongly over short distances, ranging from 1 to 160 cm. In addition we see the thickness increase at the top of the scan line (left side of the graph), where the fault intersects more marl-rich intervals. A detailed spatial statistical analysis of the variation is presented in chapter 7.

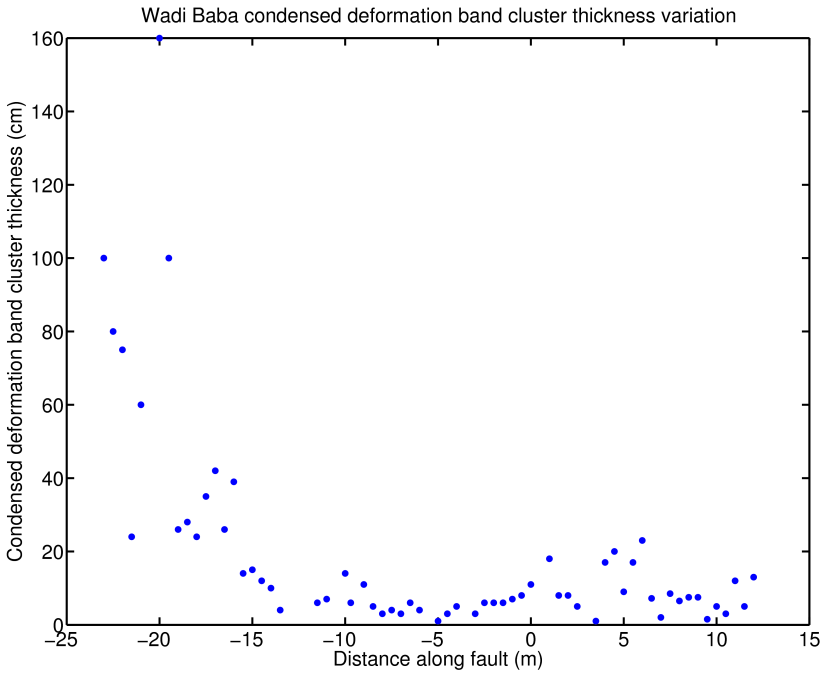

Figure 3.34: Exposure of the Wadi Baba fault. A: Overview photograph. B: Sketch of fault architecture. C: Photo of thickest part of the fault core. D: Photo of the thin part of the fault core.

3.1.6.5 The Canyon fault

At this location a narrow canyon has formed along the fault zone, providing a nice along-strike exposure of the fault core (figure 3.35). The host rock consists of Malha formation sandstones and thin shale beds (15% of the displaced stratigraphy). This fault has a throw of 14m.

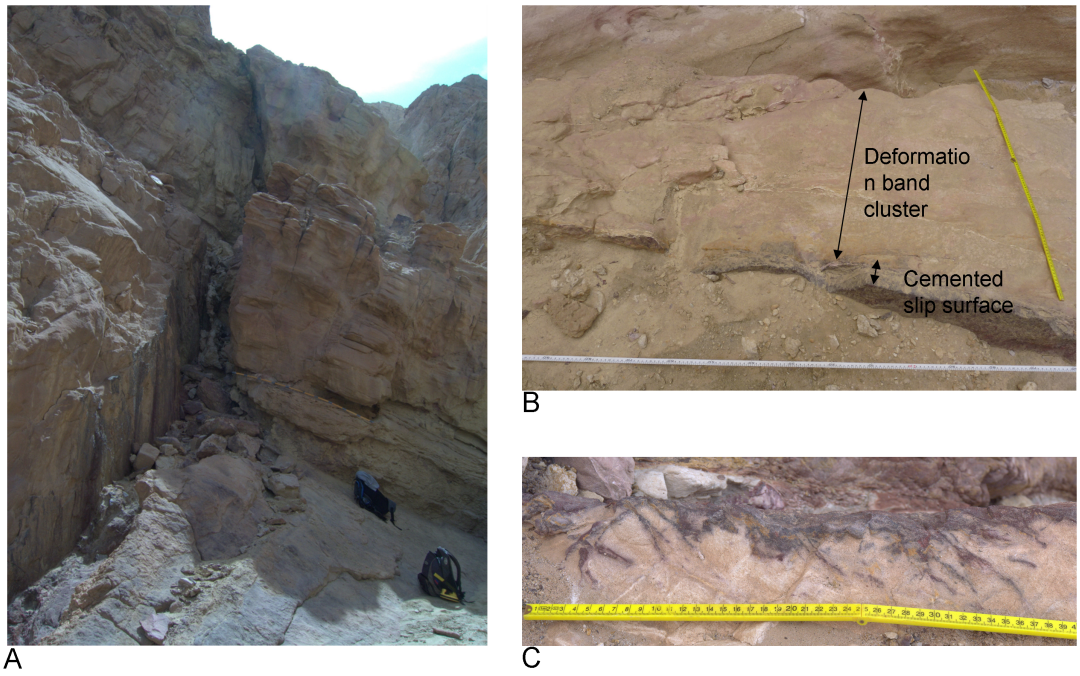

Figure 3.35: Exposure of the Wadi Baba fault. A: Overview photograph. B: Sketch of fault architecture. C: Photo of thickest part of the fault core. D: Photo of the thin part of the fault core.

Structure The architecture of this fault is similar to the Wadi el Khaboba fault. It consists of a deformation band cluster, with a relatively planar central slip surface along which the fault rock is cemented by dense iron and magnesium cementation. Figure 3.35c shows a detailed picture of the cementation. The cementation is continuous along the main slip surface, from which it branches outwards following fractures into the condensed deformation band cluster fault rock.

Key flow controls Similar to Wadi Khaboba, the dense cementation is interpreted as evidence for along-fault flow and as a barrier to across-fault flow. Measurements have been collected of the thickness variation over 20m along strike. The collected measurements are plotted in the graph in figure 3.36. The data is highly heterogeneous, with thicknesses ranging from 1 to 10 cm. This data is further analyzed using spatial statistics in the chapter 7.

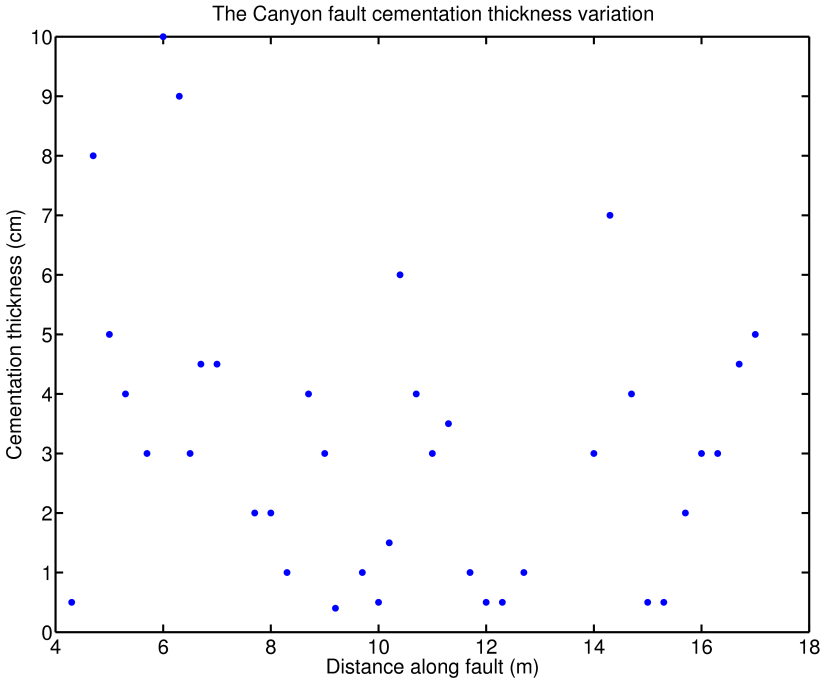

Figure 3.36: The Canyon fault measurements of the thickness of the cemented part of the fault core.

3.2 Summary

The fieldwork has revealed a wide variety of fault architectures. Different exposures of the same fault can be very dissimilar, even when separated only by short distances. The most striking example of this are the two 191 exposures of the Moab fault which have a completely different architecture but are only separated by 60 m along strike. Another good example can be seen at the two Goblin Valley faults. At the upper level these two faults juxtapose sandstone against sandstone, here the fault core is formed by a dense deformation band cluster. Below this level the two faults interact with thin shale beds and the deformation band clusters thin strongly. These two outcrops show that the fault architecture can strongly change along dip. It also highlights the effect of the local stratigraphies juxtaposed on fault architecture.

Heterogeneity of fault zones is central to this thesis, therefore data on the variation of key flow controls has been collected to analyze and quantify this heterogeneity. To gather data on this heterogeneity, it is necessary to define the features of fault architecture which have the strongest effect on fluid flow. For each outcrop in this study, the Key Flow Controls (kfc) have been identified. For across fault flow the key flow control is formed by the continuity and thickness of low permeability material in the fault core (gouge, shale/silt smear, cementation deformation band clusters). The continuity can be affected by gaps in the low permeability material or by breaching of this by sandstone lenses and/or slip surfaces. The key flow control for along fault flow, is typically different than the key flow control for across-fault flow. For most faults in this study, the damage zone fracture network is the most important for along fault flow. For six outcrops, the work shows potential pathways for flow along the fault core (open slip surfaces and sandstone lenses).

The heterogeneity of fault zones is analyzed at locations where key flow control variation could be measured along the fault. The strong along strike thickness variations of the Moab fault at Corral Canyon clearly illustrate such heterogeneity. This is especially interesting as many authors suggest that the thickness of a shale smear can be predicted from the thickness of the source bed and the distance to the source bed (Lindsay et al., 1993, Egholm et al., 2008). For the measured outcrops the variation of these two parameters is very small compared to the observed smear thickness variation (1.9 - 24 m). The outcrops are all at roughly the same distance to the source bed ($\pm$25 m variation, compared to the fault throw of 545m). It is reasonable to assume the thickness of the source bed to be constant over the studied distance (1.3km). To collect data on this variation efficiently, it is necessary to identify which features have the strongest effect on fluid flow through the fault zone. A more in depth analysis of the spatial heterogeneity is presented in chapter 7.

Besides spatial heterogeneity, the field work shows the temporal heterogeneity of fault zones. In 7 out of 13 fault exposures studied here, there is clear evidence for evolution of fault permeability over time. In addition to the initial mechanical processes of faulting, geochemical processes can strongly change the permeability of fault rocks, for example by cementation or the dissolution of cement. Geochemical processes can also change the mechanical properties of fault rocks and thereby affect subsequent deformation. This is very visible at the main strand of the Moab fault at the 191SE exposure, where the fluid weakened damage zone is mechanically incorporated into the fault gouge. The porous sandstones encountered in both southern Utah and the western Sinai commonly accommodate strain as deformation bands, lowering the permeability. Where these porous sandstones have been cemented, they will accommodate such

strain by fracturing instead, increasing the permeability.

Existing workflows for evaluating fault permeability focus almost exclusively on the shale content of the sequences. The work presented here highlights another factor; siltstone. In 6 out of 13 fault exposures silt has been incorporated into the fault core. Inside the fault zone, silt is likely to have similar effects on fault architecture and permeability as shale. Therefore the presence of siltstone in the host rock deserves similar attention as shale in workflows for predicting the permeability of fault zones.

A similar conclusion can be reached for cementation, which is encountered in 8 out of 13 studied fault exposures. Cementation is typically not included in fault permeability prediction studies. Although the cementation is not always continuous on the scale of the outcrop, it can be very important working together with other incomplete barriers such as discontinuous shale smears or deformation band clusters.

Chapter 4

Petrophysical properties of fault rocks

This chapter discusses the analysis of the samples gathered during the fieldwork. For understanding the effects of faults on fluid flow the permeability of the fault rocks needs to be known. Permeabilities have been measured to allow modelling of fluid flow (Chapter 6). The detailed modelling of fluid flow elucidates the effect of fault architecture on fluid flow, and as such provided feedback on fieldwork. Current industry workflows for evaluating fault seal potential and permeability emphasize the role of shale. To compare the data gathered in this study to these workflows two types of analysis are used to constrain the shale volume in the outcrops. Semi-quantitative XRD provides data on the composition of samples. Quantitative map analysis is used to evaluate the volume of shale in the whole outcrop.

4.1 Permeability

4.1.1 Rationale

During the fieldwork samples were collected of the rock types most likely to form a dominant control on bulk fault permeability. Permeability measurements of these fault components are required for flow modelling through the mapped architectures. The measured permeabilities can be assigned to the mapped fault components, generating approximate maps of permeability, which can be used for numerically modelling fluid flow. In addition the measurements augment our qualitative determination of key flow controls with quantitative insight.

Several methods exist for measuring permeability. A popular approach is to measure the permeability of rocks directly on the outcrop using a mini-permeameter. However mini-permeameters are not suitable for measuring the low permeabilities of common fault rocks such as shale smears or cemented sandstones. As such it is necessary to use the more sophisticated techniques available in the laboratory. All porosity and permeability measurements were carried out at the University of Leeds. The University of Leeds laboratory follows the recommended practice for core analysis by the American Petroleum Institute (API RP 40, 1998).

4.1.2 Sampling and sample preparation

Laboratory permeability measurements are typically performed on small cylinders of rock. Obtaining such cores of fault rock turned out to be challenging. Fault zones commonly consist of materials with strongly contrasting competencies, for example very hard cemented sandstone can be found next to very fissile shales. In particular, the more fragile materials are difficult to sample and core without destroying the sample. For this study several methods for sampling fault rocks have been tried, each of which is described below.

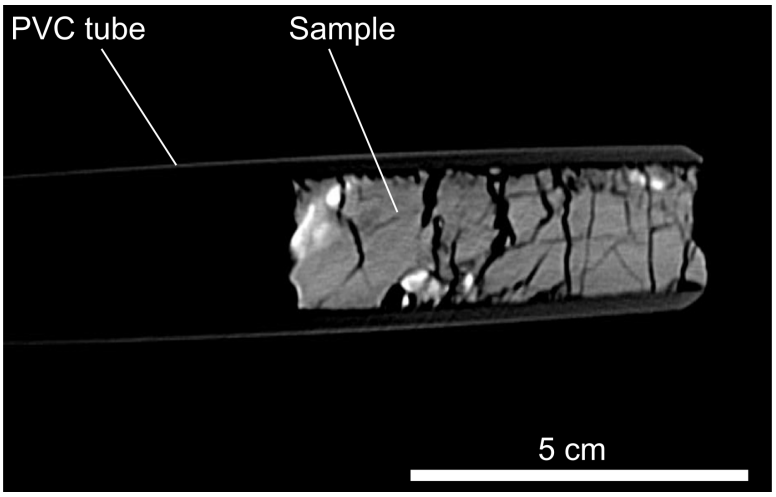

Figure 4.1: CT-scan of core sampled using sharpened PVC tube. The scan clearly shows the strongly damaged nature of the sample.

For soils it is common practice to take samples using a metal tube. The cutting side of the tube is sawed off at an oblique angle and the edge is sharpened on the outside. The tube is hammered into the fault rock, using a rubber hammer and a wooden block to protect the back of the tube. For the fault rocks encountered during this research, this approach did not yield satisfactory results. It was difficult to get the tube sufficiently deep into the rock, to get the tube back out of the rock and to extract the sample out of the tube. No intact samples of adequate dimensions were obtained this way.

A slight modification to the above method was tried by using sharpened PVC tubes. This way samples could be stored and transported inside the tube, preventing further damage. However, subsequent CT-scanning of these samples inside the tubes revealed strong damage to the structure of the samples (figure 4.1). Therefore these samples were discarded for permeability analysis. Any sampling method which involves hammering a tube into the rock damages the sample too much to allow representative permeability measurements. The usage of thin walled tubes for sampling soils is discussed extensively by the American Society for Testing and Materials (ASTM standard D1587). The ASTM recommends against using tubes for sampling hard soils.

Figure 4.2: Examples of cores used. From left to right: cuboid core in resin, standard cylindrical core and cuboid core used for GRI degassibility. Cores are 3.81cm in diameter.

The problems associated with coring fault rocks in the field led me to adopt an approach which relies on coring in the laboratory rather than in the field (figure 4.2). This reduces the sampling challenge in the field to obtaining reasonably large (dm scale) block samples. These block samples are subsequently cored in the laboratory. For cohesive samples a rock coring drill has been used to produce cylindrical cores with a diameter of 3.81 cm (1.5 inch). A rock saw was used to trim the ends so that they are perpendicular to the axis of the core.

Less cohesive samples could not be cored using the drill, as it strongly damages the samples. In this case a rock saw was used to cut the samples into cuboid shaped cores. The rock saw visibly causes less damage to the samples than the coring drill, providing a better chance of creating intact cores from the collected block samples.

The steady state and pulse decay methods for permeability measurements require cylindrical cores. To allow the square cores to be used in the cylindrical core holders, cylindrical cores were created by encasing the samples in resin. Samples are placed inside a cylindrical enclosure into which the resin is cast. The top and bottom sides of the sample are protected by masking tape during the casting. The resin has been previously tested to be effectively impermeable (personal communication Dr. C. Grattoni) and has sufficiently high viscosity not to permeate into the sample. This approach using cuboid cores is less ideal than cylindrical cores as the cross sectional area is smaller and thus the measurements are less accurate. Certain samples were tested using the GRI degassibility method, for this method, cylindrical cores are not necessary and the cuboid cores can be used directly.

As the presence of water inside the pores would affect the gas based permeability measurements, the samples needed to be dried. The samples were dried by placing them in an oven with a temperature of 60^{o}C for one hour. Between drying and measuring, the samples were stored in dry chambers.

Rock permeability often displays anisotropy; therefore the orientation of the core influences the measured permeability. All cores taken for steady state and pulse decay measurements were taken perpendicular to the main fault zone, and therefore represent across-fault permeability. Across fault permeability has a higher priority in this thesis and the phyllosilicate-rich rocks which commonly form a key flow control for across fault flow are also likely to develop

an anisotropic permeability due to fault related fabric development. Faulting-related fabric development in the sandstones is likely less intense than in phyllosilicate rich rocks.

4.1.2.1 Helium expansion porosimetry

The porosity of the samples has been determined using the Boyle's law double cell method. This method uses an apparatus with two chambers connected through a valve. The sample is placed into the first chamber, which is filled with helium gas until the pressure reaches about 15 psi. Pressure is monitored in the chamber, to determine when the helium gas has saturated the sample. By opening the valve, the first chamber vents into the second chamber. Boyle's law states that given constant temperature, the volume of an ideal gas varies inversely with pressure. The pressure change after opening the vent is used to calculate the pore volume of the sample. Combined with the volume of the sample, this provides the porosity of the sample. The sample volume is determined by measuring the sample dimensions using a digital caliper. This procedure does not damage the sample in any way, so that it can be used for further analysis, for example permeability testing.

4.1.3 Permeability analysis

The first two approaches; steady state and pulse decay are quite similar and are performed with the same equipment. The sample is placed inside a core holder (figure 4.3).

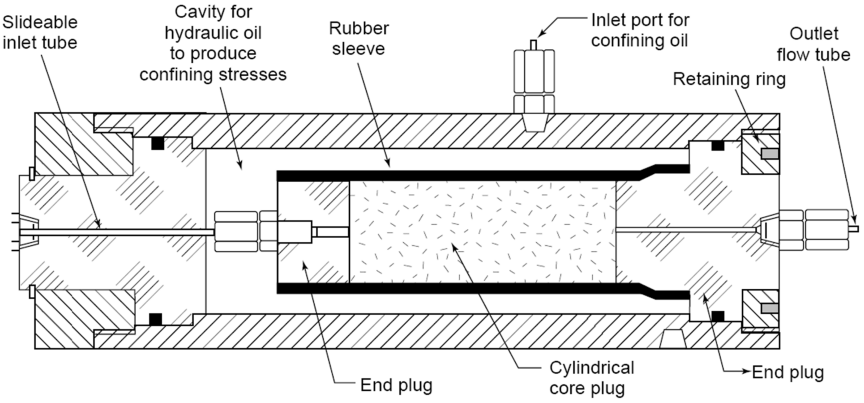

Figure 4.3: Schematic illustration of a high pressure core holder for hydrostatic stress. (After API RP40, 1998)

The core holder allows the sample to be subjected to confining pressures similar to those experienced by the sample before uplift, here the steady state and pulse decay samples have been tested under a hydrostatic confining pressure of 2500 psi. The apparatus applies a controlled pressure difference of helium gas across the flat sides of the sample. Pressure gauges measure the differential gas pressure across the sample and the pressure on the outflow side. Another sensor monitors the flow rate across the sample. All sensor and valves are computer controlled so that permeability measurements can be semi-automated.

4.1.3.1 Axial flow steady state permeametry

This method for measuring permeability works by creating a constant pressure difference across the sample in the core holder. The apparatus cannot instantly apply a constant pressure difference, as the flow of gas through the sample decreases the pressure, which leads to lower flow rates. Depending on the permeability of the sample it takes several minutes to achieve equilibrium (steady state). Once the system is in equilibrium, the pressure difference and the resulting flow rate can be used to calculate the permeability using Darcy's law. As the time required to reach equilibrium increases with decreasing permeability, the method is most suited for samples with a permeability greater than 0.1 mD.

Here, the samples were tested with helium gas. Klinkenberg, 1941 showed that unlike liquids, the permeability for gas depends on the absolute pressure of the gas as well. As a consequence the permeability measurements performed using gas will yield higher values than those made using liquids. Klinkenberg developed a method to correct for this. A set of permeability measurements made at different mean pore pressures can be extrapolated to infinite pore pressure, at which point the permeability corresponds to the liquid permeability. All the steady state permeability estimates reported in this thesis are Klinkenberg corrected values based on measurements with at least three different pore pressures per sample.

4.1.3.2 Axial flow pulse decay permeametry

For samples with a permeability lower than 0.1, pulse decay analysis has been used. Steady state would require a very long time to reach equilibrium for low permeability samples. The pulse decay approach works by creating a high gas pressure in a sealed chamber, the gas exits the chamber through the sample. The pressure change over time in the chamber is monitored and used to calculate the permeability. The method requires the pore volume to be known, for all pulse decay samples this has been determined using helium expansion porosimetry. Pulse decay permeametry allows the Klinkenberg corrected result to be obtained using a single measurement.

4.1.3.3 GRI degassibillity permeametry

This method was developed by the Gas Research Insititute for work on shale cores and cuttings (Luffel et al., 1993). They show that shale is very prone to microfracturing during coring. As such axial flow measurements of shale permeability on cores tend to overestimate the permeability of the shale in the reservoir. Therefore they developed an approach for obtaining the matrix permeability of the sample instead. The GRI approach to measuring permeability works in a similar fashion to the Boyle's law double cell method for porosity. The main difference is that much higher helium pressure is used (150 psi). The pressure is built up in an empty pressure vessel, which is then connected to a pressure vessel containing the sample. The gas will slowly permeate into the sample, during which time the gas pressure inside the vessel is recorded. Due to the very low permeabilities of the samples tested with this method, the test can take several days. From the pressure measurements the permeability of the sample has been determined using reservoir flow simulation software (Petrel) modelling of the sample and the chamber and history matching the pressure decline curve.

4.1.4 Results

Sample	Permeability	Porosity	Fault outcrop	Desciption
Pulse decay				
MB4	0.0004 mD	3.1 %	Moab fault 191 NW	Partly cemented sandstone clast
MD2	0.014 mD	9.3 %	Moab fault Coral Canyon	Slip surface of cemented sandstone
MB1	0.11 mD	5.9 %	Moab fault 191 NW	Cemented siltstone
MC3	0.08 mD	8.1 %	Moab fault Coral Canyon	Sandstone slip surface
CNS4	0.0023 mD	16.9 %	Crow's Nest Spring fault	Cemented calcareous sandstone lens
GRI				
MB2	2.5 pD		Moab fault 191 NW	Blue cemented sandstone lens
MA11	10 pD		Moab fault 191 SE	High strain zone gouge
MA2	5 nD	2.7 %	Moab fault 191 SE	Red brown silt and yellow green sand gouge
MA13	30 pD	2.2 %	Moab fault 191 SE	Stratigraphic silt
MC2B	5 pD	2.2 %	Moab fault Coral Canyon	Blue Clay
Steady State (Klinkenberg corrected)				
CNS7	200 mD	21.9 %	Crow's Nest Spring	FW host rock (Navajo sandstone)
MA7	145 mD	17.8 %	Moab fault 191 SE	Sandstone in partial alteration zone
CNS6	82 mD	16.3 %	Crow's Nest Spring	SW navajo lens
MB5	3.3 mD		Moab fault 191 NW	Altered coarse poorly sorted sandstone
MA8	58 mD		Moab fault 191 SE	Sandstone (HW) 3m outside of alteration zone
MA5B	13 mD		Moab fault 191 SE	Altered fine sandstone
PV06B	1.4 mD	4.5 %	Professor Valley fault	Host rock, sandstone and silt
MD4	49 mD	10.5 %	Moab fault Coral Canyon	HW Calcareous sandstone
CNS8	68.5 mD	31.6 %	Crow's Nest Spring	HW host rock (poorly consolidated Entrada slick rock)

Table 4.1: Permeability and porosity measurements.HW stands for hanging wall, FW for footwall.

Gloyn et al., 1995	permeability
Navajo fine-medium eolian sandstone	200 - 600 mD
Carmel silty shale, siltstone and silty sandstone	1 - 54 mD
Brushy Basin	10 mD
Salt Wash fine - medium sandstones	263-813 mD
Entrada well sorted medium sandstone, very fine - medium sandstone, sandy siltstone	26-1445 mD

Table 4.2: Selected permeability values from Gloyn et al., 1995.

Table 4.1 contains all the measured permeabilities and porosities. The porosities have not been measured for all samples. The measurements were only necessary for those samples tested using pulse-decay. The degassibility method combines measurement of permeability and porosity. For the samples tested using steady-state, porosity was not required, but collected were time allowed. The measured permeabilities range from 200 mD for unfaulted sandstones downto 2.5 pD for a densely cemented sandstone lens. The higher permeability values measured with pulse decay and steady state are comparable to other values measured for similar fault rocks and lithologies in the region. Table 4.2 summarizes a set of measurements reported in Gloyn et al., 1995. Their results tend to be higher, this is likely related to the hydrological nature of their study, which would imply that they have used lower confining pressures. The extremely low values determined with the GRI method clearly stand out. These values are much smaller than those measured using pulse decay in this study, and also much lower than those reported in literature for shale and silt in the study area (table 4.2). The GRI degassibility method measures the matrix permeability of the sample and excludes the effect of (micro-) fractures (Luffel et al., 1993, Quentin Fisher personal communication). Assuming that flow-rates through micro-fractures are much higher than through the matrix, this explains the much lower permeability measurements using the GRI degassibility method.

4.1.5 Discussion

The measurements presented in this chapter are the result of very careful sampling and analysis in an advanced laboratory following industry standard procedures. As such they very accurately represent the permeability of the sampled lithology. One cause of concern is that these samples where taken at the earth's surface and therefore the measured permeability might differ from the permeability of these rocks when the fault was at depth. During uplift the reduction in confining pressure is likely to have induced (micro-) fracturing. In addition changes in fluid chemistry and temperature during uplift can potentially affect fault rock properties.

After uplift the fault rock has experienced some degree of interaction with the atmosphere, hydrosphere and biosphere. Especially clay rich fault gouges were visibly affected by their exposure to the elements. In this study, most fault gouges exposed in outcrops are preferential sites for vegetation and were disrupted by roots. In the arid regions were these outcrops are located, plants tend to develop deep root systems, and as such large volumes of gouge are disturbed by the roots. To take samples, large volumes of material needed to be removed to provide access to fault gouge without roots. All samples presented here are free from roots. The sampled gouges looked undisturbed, but it is not possible to rule out that the gouges have not experienced deformation due to the growth of nearby the root system.

The faults studied here are all located in desert and desert-like environments, where they are subject to strong temperature changes during the day. Frost weathering of fault rocks can potentially contribute to the development of micro-fractures. The irregular precipitation in the studied area can further affect the samples by repeated wetting-drying cycles. In rocks containing swelling clays, this could further contribute to the development of micro-fractures.

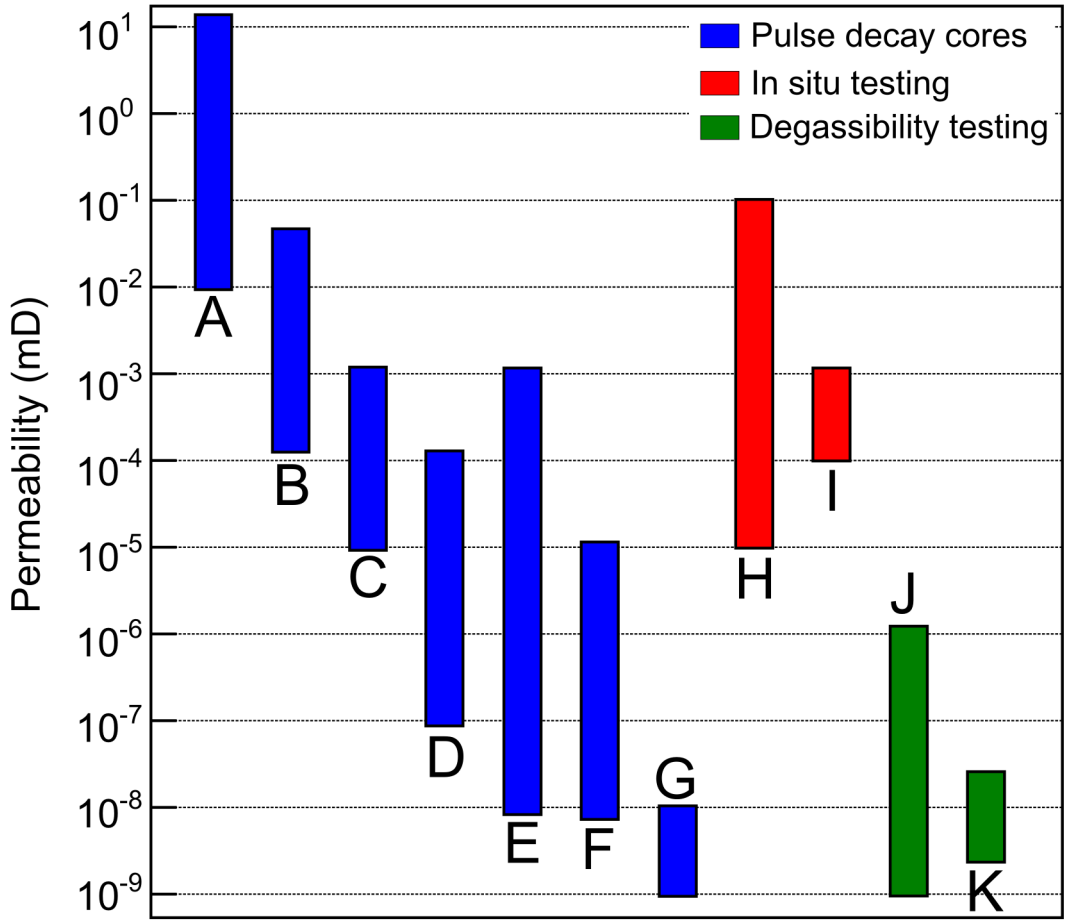

	Source	Description	K (mD)
A	Olsen 1966	Kaolinite cores tested with brine	3e-2 to 30
B	Mesri and Olson 1971	Illite cores tested with brine	2e-4 to 5e-2
C	Mesri and Olson 1971	Smectite cores tested with brine	1e-5 to 3e-4
D	Kwon ea 2004	Illite bearing shale (Wilcox fmt)	3e-7 to 3e-4
E	Brace 1980	Shales range from laboratory cores	1e-8 to 1e-3
F	Neuzil 1994	Compilation of shales and clays	1e-8 to 1
G	Luffel et al., 1993	Cores tested using pulse decay permeability from depth (4km)	2e-9 to 6e-8
H	Brace 1980	Triassic siltstone and mudstone in situ	1e-5 to 1e-1
I	Brace 1980	Pierre shale in situ	1e-4 to 1e-3
J	Luffel et al., 1993	Matrix degassibility (GRI) cores from depth (4km)	2e-9 to 2e-6
K	this study	Clay, silt and gouges	5e-9 to 3e-8

Figure 4.4: Compilation of shale permeability measurements from published literature.

As discussed in section 4.1.4, the GRI degassibility results are much lower than the values reported by Gloyn et al., 1995. Figure 4.4 shows a compilation of shale and silt permeability measurements from published literature. It shows that the picodarcy permeabilities measured

for shales and silts in this study are not unique, but correspond to the very lowest range of the laboratory measurements and are much lower than what is typically measured through wells. The GRI degassibility method measures the matrix permeability of the sample. In contrast axial flow methods measure a combination of the matrix and the micro-fracture network in the sample. The samples used for this study were collected from outcrops and as such will also contain micro fractures formed during uplift, surface exposure and sampling. However that does not mean that some micro fractures were not already present in the rocks at depth. This makes it difficult to approximate the permeability of shales, silt, gouge and cementation under reservoir conditions using surface samples. During axial flow testing the confining pressure is set at a level similar to what the rocks experienced at depth, which closes at least part of the micro-fractures. The permeability measured this way is assumed to be a representative value for the rock's permeability under reservoir conditions. The axial flow measurements in the compilation typically show higher values than the degassibility measurements, suggesting that also under reservoir conditions micro-fractures exist and affect flow. The in situ measurements test a much larger volume of rock (several meters along the well) and show permeability values several orders of magnitude greater than the degassibility measurements. Since the in situ measurements sample a large volume of rock, it can include the effect of both micro- and larger fractures and sedimentary heterogeneities.

Considering all the factors that could potentially affect the permeability of fault rocks in surface exposures, leads to the conclusion that great care is necessary in using samples from these outcrops. Ideally faults would be studied in the subsurface, but this is typically not possible. Sampling fault rocks in wells will provide more reliable estimates of fault rock permeability, but does not yield information on the structure and heterogeneity of the fault zone. Therefore working with faults exposed at the surface is currently the best option, provided that great care is taken in sampling and that the potential uncertainty is considered.

4.2 XRD analysis of sample composition

4.2.1 Rationale

Fault seal analysis and fault permeability studies place a large emphasis on the shale content of the fault rocks. The most commonly used fault seal potential and permeability estimation workflows rely on predicting the shale content of the fault zone from host rock shale content. As such it is interesting to know the actual abundance of shale in the fault zones studied in this thesis. Validation of the clay content and distribution in these outcrops provides insight into the relative merits of different fault seal potential and permeability estimation workflows and may lead to improvements to these approaches. The XRD analysis is a first step in evaluating the clay content of the fault zone. It provides information on the clay content of discrete samples. Hence it is a useful tool for analyzing small structures. To obtain an estimate of the shale content of the whole fault core exposed in the outcrop a quantitative analysis of the digitized maps is performed in the second part of this section.

4.2.2 Theory of XRD analysis

X-ray diffraction analysis relies on the diffraction of x-rays by crystalline substances and how this diffraction differs for different crystalline structures. The analytical procedure works by

illuminating a sample with an x-ray source over a range of different angles. A detector measures the x-ray intensity on the opposite side of the sample.

The XRD analysis produces a plot of the x-ray intensity over the range of source-detector angles expressed as 2ϑ. This spectrum has a different set of peaks for each different mineral. Qualitative XRD uses these spectra to identify the mineral constituents of the sample. For this research I have used the Diffrac.EVA software by Brucker. This software comes with a large database of known spectra for many different substances. Ideally the software would compare the measured spectrum to all known substances. However due to small imperfections in the measurements and the complexity of the sample composition, this tends to favour the identification of compositions which are very unlikely for rocks. For this study an alternative workflow was devised which only searches for a predetermined set of likely components. This selection of candidates is based on published compositions of rocks from the area and rock types commonly observed in the field. The downside of this approach is that rare minerals will be missed. As the objective of this analysis is mainly to determine the ratio of clay to sand, the error introduced this way is likely to be small. Clay minerals tend to have similar spectra, so the exact clay type might be misinterpreted but the total clay fraction would be determined accurately by quantitative XRD. To perform quantitative XRD, first all the components of the sample are identified. Subsequently a mixing model is used to calculate the relative abundance of each component from the area of all the peaks. Due to the compositional complexity of rocks and imperfections in the grain size distribution of the sample, the result is non unique and components need to be selected by the operator based on geological probability. The Diffrac.EVA software uses a simpler workflow and relies on a purely graphical analysis of the spectra. As a result the determined mineral compositions are semi quantitative, with error bars approaching 10-20 percentage points.

4.2.3 Sample preparation

Samples need to be ground to a very fine and consistent grain size. Samples for the XRD analysis were prepared at the XRD laboratory of the University of Edinburgh. Initial grinding is performed manually using a pestle and mortar. Subsequently the sample is ground using a McCrone micronizing mill, which produces a homogenous grain size. Platy minerals such as clay, tend to settle in a preferential orientation. As the intensity of the peak in the spectrum depends on the crystallographic orientation of the sample, a preferred orientation will cause an unwanted bias for quantitative XRD analysis. This can be counteracted by ensuring a random orientation of all the mineral grains. Here we follow the approach developed by Hillier 1999. His spray drier technique works by randomizing the grain orientation in a water based suspension. Droplets of the suspension are sprayed into a heated chamber, where the water evaporates before the droplets reach the base of the chamber. At the base the resulting spherules of randomized grains are collected on a sheet of paper. These spherules are used for the XRD analysis.

The XRD analysis itself was performed at the University of Strathclyde Advanced Materials Research Laboratory using a Bruker D8 Advance with Davinci (2010) X-Ray Diffractometer. Samples were analyzed over 2ϑ angles of 5^{o} to 70^{o} with a stepsize of 0.02^{o}. Each sample was analyzed for 1 minute, using a CuK alpha source with a 40KV voltage and 40mA current. No internal standards were included in the samples. These settings were recommended by the lab technician.

4.2.4 Results

Table 4.3 presents a summary of the measured compositions. For this summary all the clay minerals have been grouped together into clays, limestone and dolomite have been grouped as carbonates and feldspars, micas and oxides have been grouped as other. One thing that becomes clear from this analysis is that a simple binary composition model consisting of only clay and quartz does not accurately describe our observations.

In particular, calcite and dolomite are commonly observed in this data set. However the validity of these results needs to be questioned, as the clay values seem very low, especially those for the corral canyon samples. These samples consist of pure shale and hence should contain mostly clay. Comparison with the quantitative XRD analysis of the shale gouge at the 191SE exposure of the Moab fault by Solum et al., 2010 also reveals a strong discrepancy. For this gouge, they report a clay content of 59%, much larger than the maximum value of 16% obtained here. This provides enough reason to strongly question the value of the results obtained here. Most likely the semi-quantitative XRD algorithm provided by the DIFFRAC.EVA software performs less well than quantitative XRD algorithms available in other software. In addition the analysis time was probably too short. Srodon et al., 2001 recommends an analysis time of 2s per timestep for best results, which yields a total analysis time of 110 minutes, much longer than the 1 minute used here.

Fault outcrop	description	Clay	Quartz	Carbonate	other	sample name
Cedar Mountain Thrust	Fine sandstone and silt	0	55	28	16	CMB2D
Cedar Mountain Thrust	sandstone	0	60	26	12	CMB3A
Cedar Mountain Thrust	Fine sst from slightly harder bed	6	53	19	22	CMB6
Moab 191 SE	gouge	0	51	0	50	MA1A
Moab 191 SE	Sandstone > gouge transition zone	10	46	10	34	MA5B
Moab 191 SE	Sandstone > gouge transition zone	16	40	0	44	MA6
Moab 191 SE	gouge	7	50	1	40	MA11
Moab 191 NW	Coarse sandstone (not altered)	15	63	10	12	MB5B
Moab Corral Canyon	shale smear (blue)	33	53	0	14	MC2B
Moab Corral Canyon host rock	shale donor brushy basin	44	55	0	0	GCBB
Professor Valley	Altered sandtstone	8	60	6	25	PV4

Table 4.3: Summary of the semi-quantitative XRD sample analysis. The clay fraction comprises all the clay minerals, carbonates consists of limestone and dolomite, the other group encompasses feldspars, micas and oxides.

4.2.5 Future work

The usefulness of the results presented here is clearly limited by their poor accuracy. One way to improve this would be to use better software which provides quantitative XRD analysis rather than the semi-quantitative workflow in the DIFFRAC.EVA software used here. Further improvements can likely be made by re-running the analysis using longer running times and the inclusion of an internal standard.

4.3 Quantitative map analysis

4.3.1 Rationale

Whereas the XRD analysis of samples can provide the composition of small fault components such as fault gouges, this does not necessarily represent the composition of the whole fault core.

In this section another approach is explored which aims to provide a shale fraction for the entire outcrop. This approach uses the detailed maps of the outcrops made in the field. For each map the area covered by the different lithologies is determined.

4.3.2 Method

As the maps also contain parts of the host rock, selection is made of the fault core. As the term fault core can lead to some confusion, here it is defined as the area in between the outermost slip surfaces. This area is selected using a raster based image manipulation program (Gimp). Subsequently this image is further analyzed using a Matlab function written for this purpose by the author (analyzemap.m).

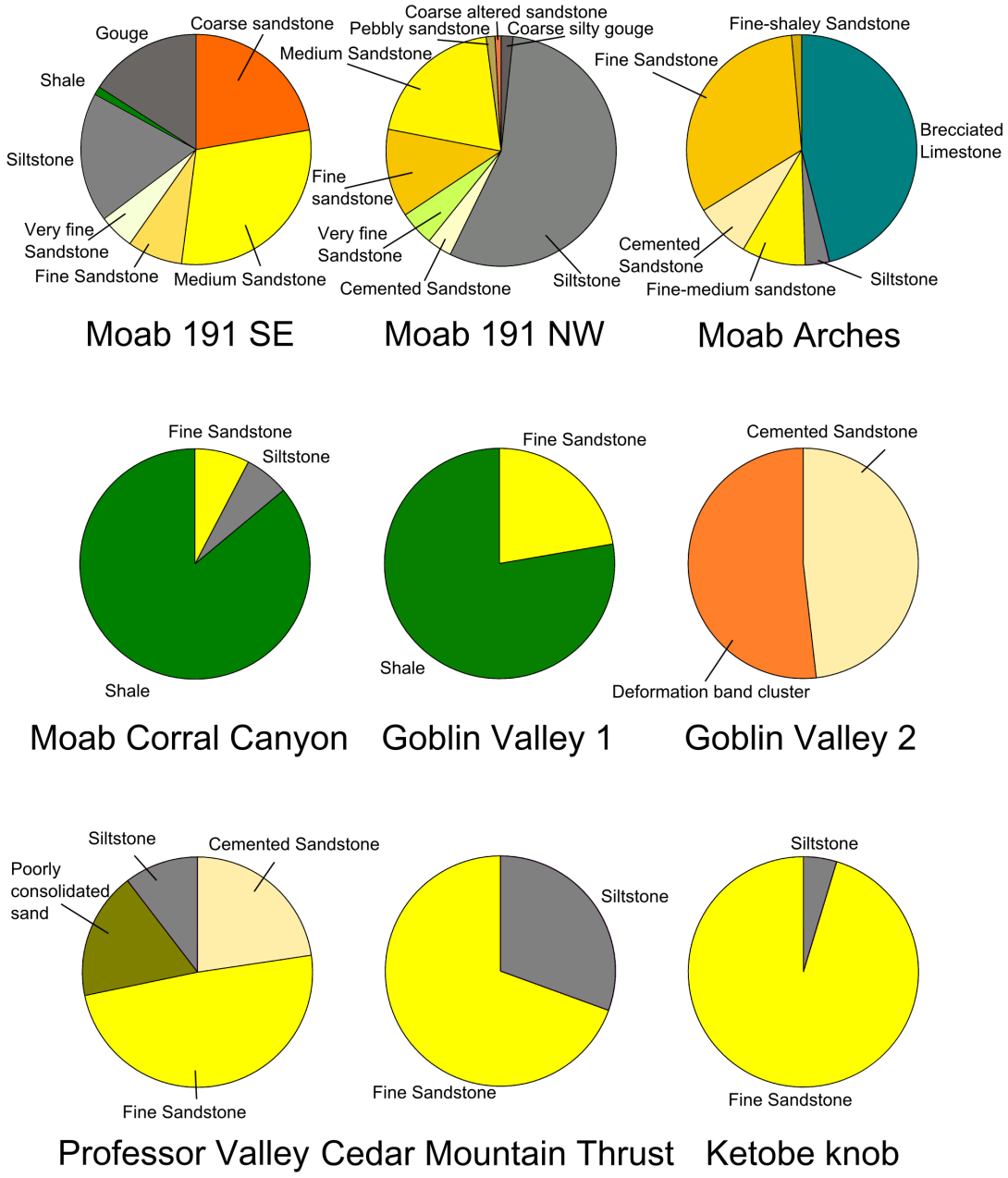

Figure 4.5: Compilation of pie charts representing the composition of the outcrops.

4.3.3 Results

The results are presented in figure 4.5. The composition of each mapped fault core is presented in a pie chart, with colours corresponding to the colours used in the maps. These pie charts present all mapped components, e.g. sandstones with different grain sizes are presented separately. The Shale gouge ratio assumes sandstone and shale as the only lithologies. For a proper comparison with algorithms like SGR the data here are summarized by grouping the lithologies into sandstone and shale. Figure 4.6A shows a cross-plot of SGR against the shale content of the mapped fault cores. As shale is absent in most outcrops, this leads to a very poor correlation. Figure 4.6B shows a cross-plot of SGR against the mapped shale and silt. Siltstone is normally not incorporated in SGR, but as it has been very abundant in the outcrops in Utah, it is included here as a separate category. The siltstone here has been observed to show a similar behaviour as shale, frequently occurring in gouges, lenses and smears. This plot still does not display a great correlation, but presents a far better representation of the outcrops in which both shale and silt can act as barriers. Goblin Valley 1 and Corral Canyon show a much higher shale content than expected on the basis of SGR. This is very reasonable, as these fault architectures are dominated by shale smearing, which leads to a fault core consisting almost entirely of shale. The value for the Moab fault exposure 191NW is probably higher than it should be, as the map does not cover the entire width of the fault zone, if the exposure had allowed mapping of a larger area, the map would probably have contained 10-30% more sandstone.

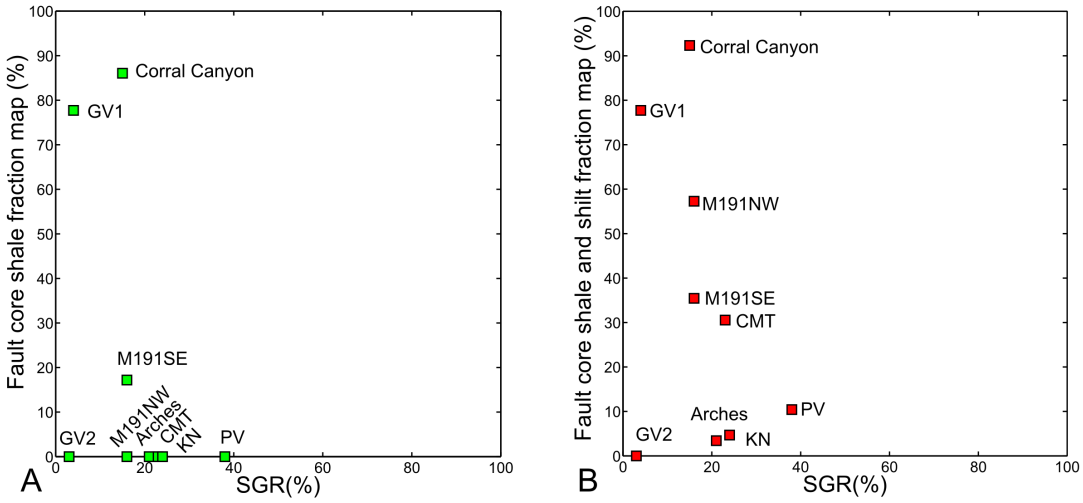

Figure 4.6: Results of quantitative map analysis compared to SGR values calculated for each outcrop. A: Plot of the outcrop shale volume against SGR. B: Plot of combined outcrop shale and silt volume against SGR.

Chapter 5

Applying common algorithms for fault seal and permeability estimation to the field sites

Being able to spend several months studying fault outcrops in the field in all their glorious detail is very much a luxury only available to PhD students. For industrial applications of structural geology direct access to faults is rarely ever available, instead fault properties need to be determined using well and geophysical data. Fault offset and seismic scale geometry is typically determined using seismic data, whereas well logs and cores are used to determine the stratigraphy. Two common methods for estimating fault seal potential and permeability are the Shale Gouge Ratio and the Shale Smear Potential. In this chapter these parameters are calculated for the outcrops discussed in this thesis.

5.1 Shale Gouge Ratio

5.1.1 Introduction

Shale Gouge Ratio (SGR) is a commonly used parameter in fault seal analysis. It is a measure of the volumetric shale content of the host rock along which a part of the fault has moved past. Faults with a high SGR value are deemed more likely to seal or baffle fluid flow than faults with a low SGR value. Determining the SGR values of these outcrops allows for a better comparison with hydrocarbon industry cases.

Two different approaches have been used for caculating the SGR values. For faults in Utah, SGR values were calculated using well log data provided by the Utah State Department of Natural Resources. For the faults in the Sinai these data are not available in the public domain, and as such SGR values are estimates based on field observations. The well log based values for the faults in Utah provide a significant advantage, as previously published SGR values for outcrops along the Moab fault (Foxford et al., 1998 and Clarke et al., 2005) are based on the published stratigraphy (Doeling 1988) and approximated shale volumes. SGR values based on V-shale well log data allow for a better comparrison with hydrocarbon industry data.

5.1.2 Data sources

For the outcrops in Utah at least one well log based SGR value is provided. For the faults in the Sinai field based estimates are used. For smaller faults in Utah a field based estimate is also provided for greater accuracy. Well logs are available online from the Utah State Department of Natural Resources. These are provided as scans of the original paper logs, as most of the wells in this area have been drilled between 1950 and 1970. Gamma ray logs are the only reliable V-shale estimators commonly available in this data set.

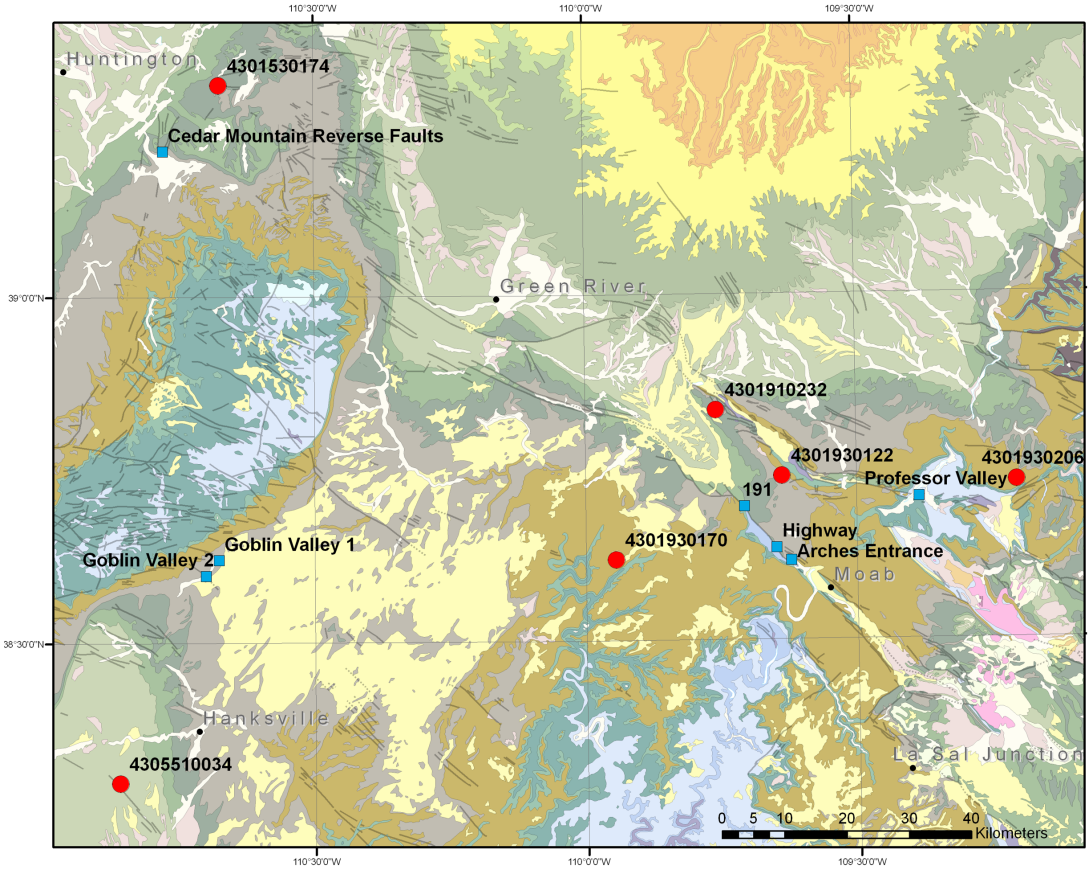

Figure 5.1: Location of outcrops (blue squares) and wells (red squares) used for calculating SGR, plotted on geological map by Hintze et al., 2000. Legend for geology can be found in figure C.

Figure 5.1 shows a map of outcrops and well locations used in this study. For each outcrop the nearest wells providing complete coverage of the faulted stratigraphy have been selected. The Moab fault is located in an area with very strong lateral stratigraphic thickness variation caused by subsurface salt movement during sediment deposition (Matthews 2004). Over distances of less than 2km, the Pensylvanian, Permian and Triassic units can triple in thickness. The strongest variation occurs in the hanging wall of the Moab fault, the footwall stratigraphy is relatively unaffected (Doelling 1988).

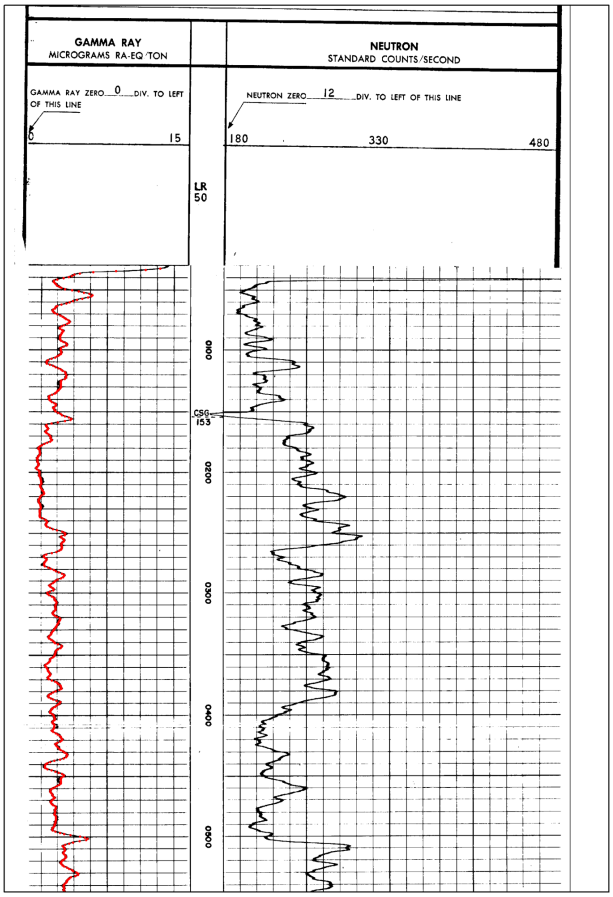

Figure 5.2: Digitization of well logs. This figure shows the scan of well 4301910232 with the digitized log (red dots) superimposed on it.

Figure 5.2 shows the top part of a scanned paper log. To be able to use the log the data has to be digitized. Whenever the quality of the scan permits the log has been digitized by automated image analysis. This image analysis is performed using a set of Matlab functions developed by the author. A short overview of these functions is listed in appendix C. The resulting log values were carefully compared to the original well log image and corrected where necessary. Lower quality log images had to be digitized by manual tracing using GIS software.

For the derivation of V-shale from gamma ray logs the procedure is followed as outlined in both Serra 1986 and Asquith & Krygowski 2004. First the Index Gamma Ray (Igr) is calculated by normalizing the gamma ray log values:

$$I_{gr} = \frac{GR_{log} - GR_{min}}{GR_{max} - GR_{min}} \tag{5.1}$$

Subsequently the Index Gamma Rays is transformed into V-shale by using the Larionov (1969) function for rocks older then Tertiary. This function acts on values between 0 and 1, it slightly lowers intermediate values and has the largest effect on Igr values near 0.5.

$$Vshale = 0.33\,(22\,I_{gr}{-}1) \tag{5.2}$$

The resulting V-shale curves are shown in figure 5.3 combined with formation top well picks from the Utah State Department of Natural resources. No correction for borehole effects has

been applied as calliper logs are not available for the well used in this study. This is not likely to have a significant effect on the final SGR value.

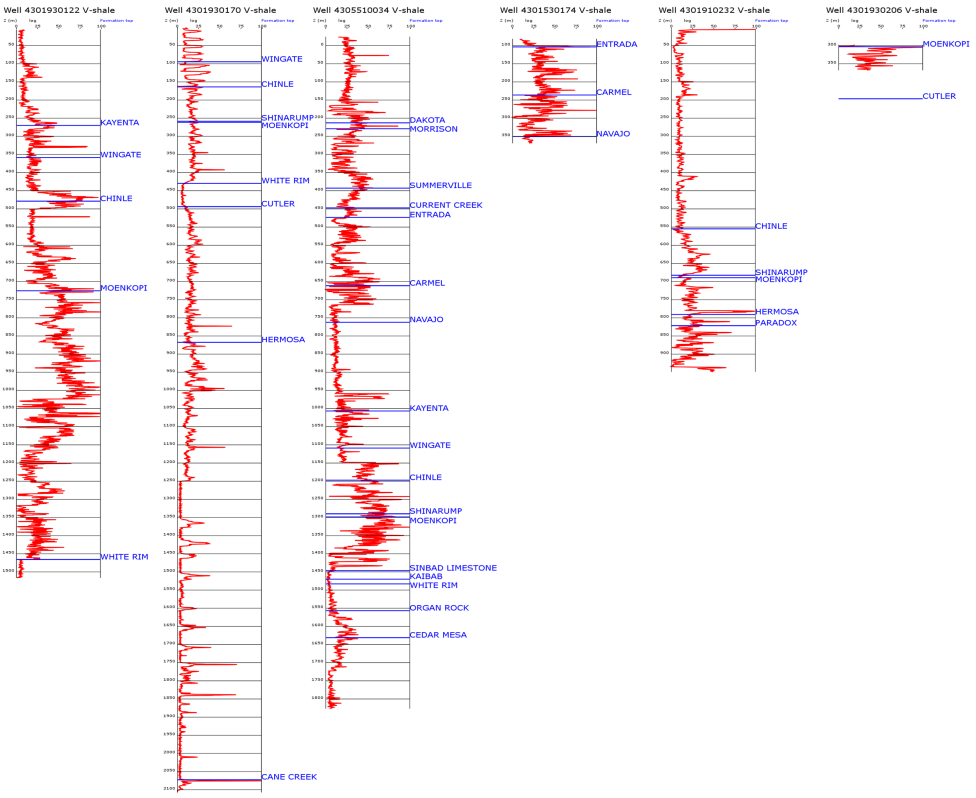

Figure 5.3: V-shale logs created using by digitizing the scans, calculating the index gamma ray and Larionov 1969 correction for rocks older than Tertiary.

5.1.3 SGR Calculation

Figure 5.4 illustrates the common procedure for calculating the Shale Gouge Ratio. SGR is the average shale content of all the beds along which a point on the fault plane has moved past. As such it is often calculated as a bed thickness weighted average shale content of the host rock. For this thesis the SGR is calculated using gamma ray well log data. To simplifiy the SGR calculation, the log is resampled to a regular sampling interval. To prevent data loss a sufficiently small sampling interval is selected. The SGR is then calculated as the average value of all the v-shale values inside the fault's stratigraphic separation. The calculation is performed using Matlab, with functions developed for this thesis by the author. An overview of these functions is provided in apendix X. Field based SGR estimates are made by measuring the thickness of sand and shale beds in the host rock of the outcrop, and estimating their shale content by eye. These data are combined to calculate the SGR.

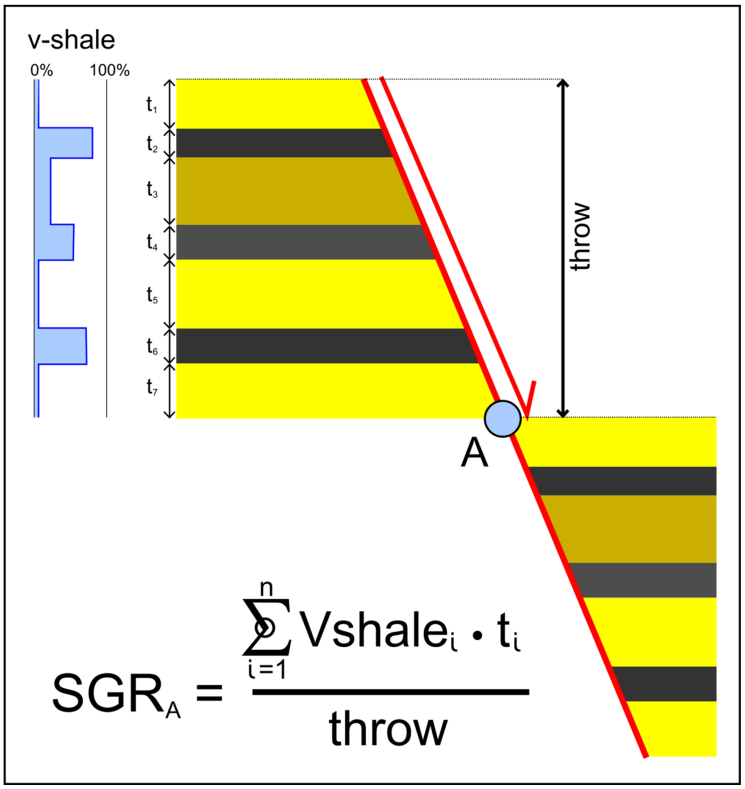

Figure 5.4: SGR calculation theory. SGR is defined as the bed thickness weighted average shale content of all the beds along which a point A on the fault plane has moved past.

5.1.4 SGR values

Table 5.1 shows the resulting SGR values. For most outcrops two values have been calculated. Considering the strong stratigraphic thickness variations in the region, the nearest well based estimate is likely the most accurate. As such for each estimate the distance between the well and the outcrop is reported. For the synsedimentary Moab fault estimates from both footwall and hanging wall are reported whenever possible. For the two faults near Goblin valley a field based estimate is also reported. These faults have a very small throw (4m), for which the complete stratigraphy is known, allowing a simple yet reliable SGR calculation. In this case the field based estimate is likely more accurate than the well based estimate as it is impossible to accurately locate such a small throw interval on the log from a well at relatively great distance (36 and 39 km).

Outcrop	Data source	SGR (%)	Fault position	Distance of well from outcrop (km)
Outcrop Highway 191	Well 4301910232 gamma ray	**15**	HW	25
	Well 4301930170 gamma ray	16	FW	28
Outcrop Arches Entrance W. strand	Well 4301930122 gamma ray	**21**	HW	14
	Well 4301910232 gamma ray	24	HW	27
	Well 4301930170 gamma ray	22	FW	29
Outcrop Arches Entrance E. strand	Well 4301910232 gamma ray	**14**	HW	27
Upper Corral Canyon	Well 4301910232 gamma ray	**15**	HW	16
Ketobe knob	Well 4301530174 gamma ray	**23**		14
Cedar Mountain Thrust	Well 4301530174 gamma ray	**24**		14
Goblin Valley fault 1	Well 4305510034 gamma ray	8		39
	Field observation	**4**		0
Goblin Valley fault 2	Well 4305510034 gamma ray	8		36
	Field observation	**5**		0
Professor Valley	Well 4301930206 gamma ray	**38**		16
Wadi Baba	Field observation	**3**		
Wadi Khaboba Synthetic	Field observation	**5**		
The Canyon Synthetic	Field observation	**15**		

Table 5.1: Calculated SGR values. All well log based estimates are calculated from gamma ray logs corrected with 'Larionov 1969 for older rocks'. The first four outcrops are part of the synsedimentary Moab fault, therefore the well's location in either footwall or hanging wall has been indicated by the abbreviations 'FW' and 'HW' respectively. The SGR estimates deemed most accurate are shown in bold.

These SGR values for outcrops along the Moab faults are significantly different from those reported in literature (Yielding 2002 and Clarke et al., 2005). A true comparison is not possible as these authors do not provide the exact location of their SGR estimates. In general the values in this thesis are 5-15% lower than those previously published. Both publications only used estimates of V-shale, which are prone to error. Yielding used the stratigraphic triangle diagram from Foxford et al., 1998 which assigns sandstone dominated formations a v-shale value of 0% and mudstone dominated formations a v-shale value of 100%. Similarly Clarke et al., 2005 used the published stratigraphy (Doelling 1988) and approximated the argillaceous fraction of the units in the field. The argillaceous fraction differs from true v-shale as it also contains the silt fraction, which probably explains why their estimates are higher then those presented here. These well log based SGR values should allow for a better comparison with hydrocarbon industry cases than the field based estimates.

5.2 SGR based fault permeability

Faults are commonly incorporated into reservoir simulation models by using transmissibility multipliers. A transmissibility multiplier is assigned to the boundary between two adjacent grid cells. Its value is calculated such that multiplying it with the cell to cell transmissibility mimics the insertion of a thin cell (with the required thickness and permeability) in between the two cells. This rather simplistic approach of using transmissibility multipliers is used often as it is computationally more feasible than incorporating the actual fault zone using grid cells. The downside of the transmissibility multipliers approach is that they only act on the flow across the fault zone, it is therefore impossible to implement faults as conduits or conduit-barrier systems this way.

5.2.1 Fault transmissibility multipliers

Faults are commonly incorporated into reservoir simulation models by using transmissibility multipliers. A transmissibility multiplier is assigned to the boundary between two adjacent grid cells. Its value is calculated such that multiplying it with the cell to cell transmissibility mimics the insertion of a thin cell (with the required thickness and permeability) in between the two cells. This rather simplistic approach using transmissibility multipliers is used often as it is computationally more feasible than incorporating the actual fault zone using grid cells. The downside of the transmissibility multipliers approach is that they only act on the flow across the fault zone, it is therefore impossible to implement faults as conduits or conduit-barrier systems this way.

5.2.2 Manzocchi et al., 1999 work-flow

The work by Manzocchi et al., 1999 introduced a method to use the Shale gouge ratio in hydrocarbon production work-flows. Rather than making a binary subdivision between sealing and non sealing faults; they assume that the SGR value predicts the volumetric shale content of the fault zone. Subsequently this approach assumes that this shale content is the main control on the permeability of the fault zone, using the empirically derived equation:

$$\log k_f = -4SGR - \frac{1}{4}\log(D)\,(1 - SGR)^5 \tag{5.3}$$

This permeability value is combined with the thickness of the fault zone which is estimated using fault width vs. displacement ratios. The estimated fault width and permeability are combined into a transmissibility multiplier.

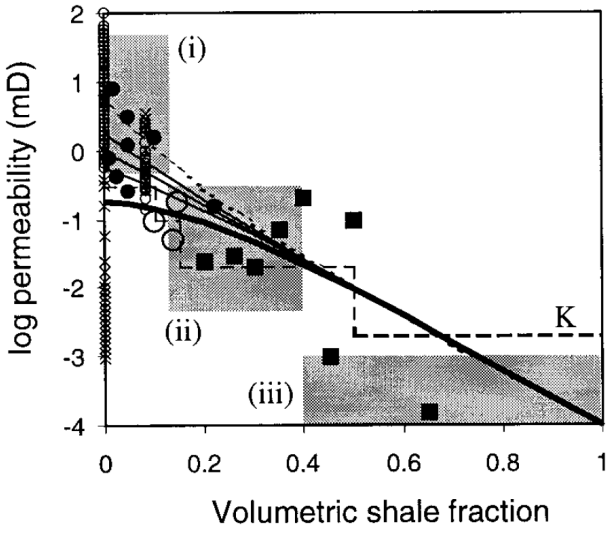

Figure 5.5: Manzocchi et al., 1999 relationship between volumetric shale fraction and permeability. Data from Gibson 1998 and Antonelli and Aydin 1994. Filled circles: Cataclastic deformation bands ; Filled squares: clay gouge; Open circles: solution deformation bands; crosses : slip surfaces. They grey boxes summarize the measurements for cores from the Sleipner field by Ottessen Ellevset et al., 1998. The set of lines depict the fitted function, the different lines represent different fault displacement values.

Figure 5.5 illustrates the volumetric shale fraction to permeability algorithm presented by

Manzocchi et al., 1999 and the data on which it is based. As can be seen on the figure there is a wide scatter of the data around the fitted curve. The data set exists of permeability measurements on a wide range of small fault structures, including deformation bands and shale smear, both of which are examples of faults incompatible with the notion of homogeneous mixing of shale and sand in the fault zone, which underlies the algorithm.

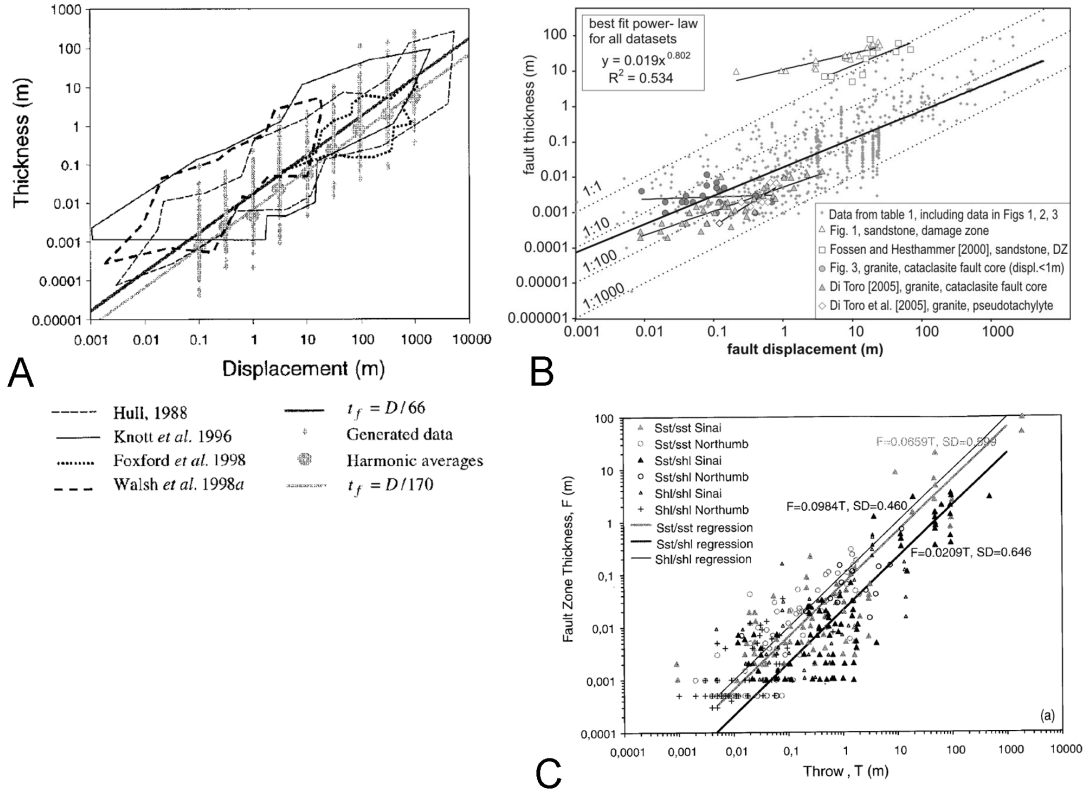

Figure 5.6: Data compilations on fault thickness vs displacement. A: Manzocchi et al, 1999 B: Shipton et al., 2006, C: Sperrevik et al., 2002.

Figure 5.6 shows three data compilations on the relationship between fault displacement and thickness. Although on the log-log scale a linear trend is visible on both graphs, it is also very clear that the data displays a wide spread (up to four orders of magnitude) around these trends. In addition data compilations are often critiqued, as many authors do not clearly define the fault thickness they have measured, suggesting that this dataset contains both measurements of the fault core and of the damage zone (Shipton et al., 2006). The data analysis in the synthetic fault section of this chapter shows that fault thickness distributions are often skewed towards smaller values. This implies that the average thickness of a fault zone is not the most relevant statistic to collect. Typically the minimum thickness has a stronger influence on across-fault bulk permeability. Considering this and the strong spatial variation of fault thickness these observations should ideally include several descriptors including the arithmetic average, the minimum and maximum value, variogram and the length of the sampling window.

5.2.3 Sperrevik et al., 2002 work-flow

Sperrevik et al., 2002 suggest a similar work flow as Manzocchi et al., 1999. The shale gouge ratio is assumed to correspond to the amount of shale in the fault zone. This shale content is used to to estimate permeability. The permeability is combined with a fault thickness into a fault transmissibility multiplier. Sperrevik et al. suggest a slightly different fault thickness estimation routine, besides displacement it is also dependant on shale content, with thickness decreasing with increasing shale content:

$$F = T(0.06V_f^2 - 0.12V_f + 0.0659) \tag{5.4}$$

With:
F : fault thickness estimate
T : throw
Vf : volumetric shale fraction

Where Manzocchi et al., 1999 based their permeability algorithm on a collection of measurements from various publications, Sperrevik et al., have used samples from faults in silliciclastic sequences from cores from hydrocarbon fields in the North Sea and Norwegian Shelf.

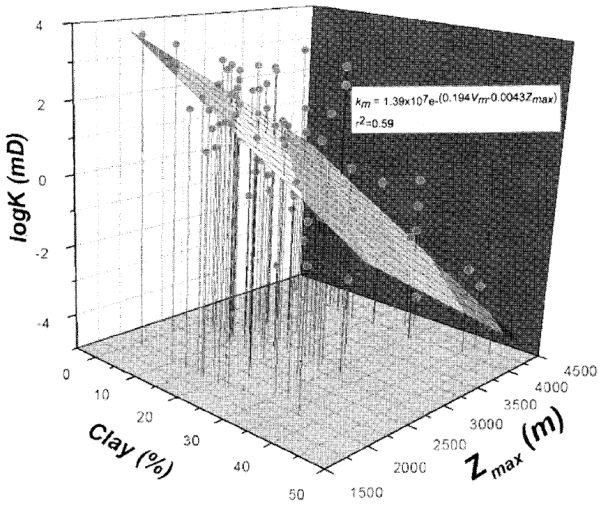

Figure 5.7: Sperrevik et al., 2002 3D plot of log fault permeability against the volumetric clay fraction and maximum burial depth.

Figure 5.7 displays the data set used by Sperrevik et al., 2002. The samples are of faults with displacements in the millimetre and centimetre range. It is questionable if the permeability of such small structures is representative for the permeability of the core of larger (seismic scale) faults. Despite this, the Sperrevik study is frequently cited and included in most fault analysis software and is therefore included in this comparison. In addition to the volumetric shale fraction, their algorithm also incorporates the maximum burial depth and the depth at time of faulting.

$$k_f = a_1 \exp\left\{-\left[a_2 V_f + a_3 z_{max} + (a_4 z_f - a_5)(1 - v_f)^7\right]\right\} \tag{5.5}$$

With:

a1 = 80000; a2 = 19.4 ; a3 = 0.00403 ; a4 = 0.0055; a5 = 12.5
zf : burial depth during faulting.
zmax: maximum burial depth.
vf: volumetric shale fraction.

5.2.4 Revil and Cathles 1999 based permeability

Revil and Cathles present an robust model for the permeability of sand and clay mixtures. Their work is not aimed at directly at fault gouges, but at a wide range of applications in hydrology and hydrocarbon production. The model is derrived from theoretical considerations and subsequently tested against both natural and artifical mixtures of sand and clay. It provides an extensive discussion on what controls the permeability of sand-clay mixtures.

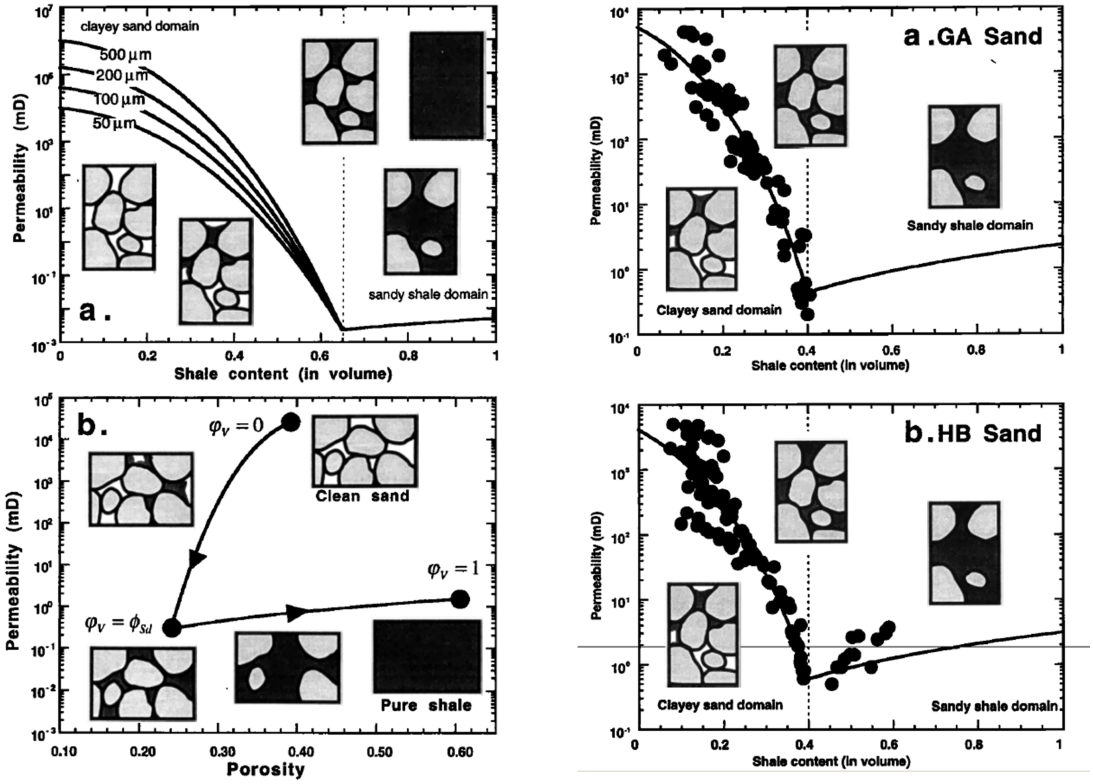

Figure 5.8: Revil and Cathles 1999, figures illustrating the relationship between permeability and content for sand clay mixtures. Dots represent the measured permeabilities of sand-shale mixtures.

Their work demonstrates the importance of critical shale content; permeability decreases with increasing clay content (equation 5.6), until the clay content reaches the critical shale content, after which permeability slightly increases (equation 5.7. The critical shale content is equal to the porosity of the sand used. As such their method produces a very different clay content vs permeability relationship as either Manzocchi et al., 1999 or Sperrevik et al., 2002. Obviously the downside of using a method for non faulted material means that the potential mechanical effect of faulting (e.g. grain crushing, fabric development) are not reflected in the final permeability.

One advantage for this work is that the permeability of the host rock materials can be accounted for in the mixed permeability. The permeability values used as input for the MODFLOW modelling have a strong effect on the final modelled bulk permeability. By using the modelling permeabilities in the SGR based algorithm, any anomalies due to the permeabilities used are mitigated. Any differences between the SGR based permeability and the modelled bulk permeability must therefore be a consequence of the fault architecture and heterogeneity.

Clayey sand domain:

$$k = k_{sd}\left[1 - \varphi_v\left(\frac{1-\phi_{sh}}{\phi_{sd}}\right)\right] \qquad {}^{3m_{cs}}\ \varphi_{\mathbf{v}} < \phi_{sd} \tag{5.6}$$

Sandy clay domain:

$$k = k_{sh}\,(\varphi v)\,m_{sd\,x} \qquad \varphi_v > \phi_{sd} \tag{5.7}$$

5.2.5 Calculations

The different fault permeabilities are calculated using a Microsoft Excel spreadsheet. The Manzocchi et al., 1999 calculation is relatively straightforward, using only the SGR and fault displacement. The Sperrevik et al., 2002 calculation requires two additional parameters; depth at the time of faulting and maximum burial depth. These data has been collected from the published literature and can be found in the database in appendix A. Obviously the quality of these data varies per fault and introduces some uncertainty. For the Revil and Cathles 1999 approach the critical shale content needs to be known. For a simple mixture of one type of sand and one type of clay; the porosity of the sand can be used for this. For the faults studied here sandstones with different porosities are mixed. In addition the grain size distribution of the sand in a fault zone is likely affected by mechanical action as well. Since these parameters are unknown for the hypothetical uniform fault gouges that are modelled here, these parameters are chosen the same for all faults. For the sand permeability a value of 500 mD is used; for the shale permeability $1{\cdot}10^{-6}$ is used and for the porosity of the sand 25 % is used. This results in a simplified SGR to permeability algorithm, which ignores many of the subtleties presented in Revil and Cathles 1999, but is still a useful addition to the comparison as the curve has a very different shape than Manzocchi et al., 1999 and Sperrevik 2002.

5.3 Shale Smear Factor

5.3.1 Description

The Shale Smear Factor (SSF) provides another common method of evaluating the sealing potential of faults in sand shale sequences. The SSF was first defined by Lindsay et al., 1993, it is relevant for faults where shale beds have been smeared out along the fault plane. Whether or not such a fault is sealing depends on the continuity of the shale smear. The SSF helps assess the likeliness of continuous shale smears along the fault plane. The SSF assumes that a bed can be sheared up to a certain distance before it breaks. This maximum distance is proportional to the thickness of the shale bed. The SSF is calculated using:

$$SSF = \frac{Throw}{Shale\,bed\,thickness} \tag{5.8}$$

Lindsay et al., 1993 studied a set of 80 faults in a Westphalian sandstone shale sequence with throws less than 15 meters. They show that for the faults they have studied, smears with an SSF of <7 tend to be continuous and faults with an SSF > 7 tend to be broken.

5.3.2 Calculation

Of the fault outcrops in this study, two show shale smearing as the dominant process. For these two faults the SSF has been calculated. For Goblin Valley fault 1 the calculation is straightforward, as a single 20cm thick shale bed is down thrown 4m, resulting in a SSF of 20.

The situation is less straightforward at the Coral Canyon exposure of the Moab fault. According to the gamma ray well log the thickest shale bed is 20m. This bed is part of the shale dominated brushy basin member, which itself is 100m thick. When calculated using the thickest shale bed (20 m) from the gamma ray logs; the SSF becomes 25. If the SSF is calculated using the entire thickness of the Brushy Basin member the SSF becomes 5. According to cross sections in Davatzes and Aydin 2005 the entire Brushy basin member is involved in the smearing. In addition the thickness measurements of the shale smear in this study show a maximum measured thickness of 24m, which suggests that the stratigraphic unit involved in the smearing is much thicker than 20m.

5.3.3 Conclusion

In this chapter two conventional estimators of fault zone hydrology have been calculated. The Shale Gouge Ratio is calculated as the average shale content of a faulted rock sequence. In this study most SGR value have been calculated from gamma-ray well logs available from the Utah State Department of Natural Resources. Where such logs are not available or suitable, the SGR has been estimated from the lithology recorded at the outcrop.

The SGR value can be used in a variety of ways. In the simplest application, the value is used to predict which faults are likely to be impermeable (sealing) over long (exploration) timescales and which faults are not. Other workflows assume that the SGR predicts the shale content of the fault gouge and that this fault gouge is a dominant and continuous element in the fault core. Following these assumptions, the permeability of the fault gouge can be calculated from the predicted composition. In this chapter the fault core permeability has been predicted from the SGR value using three different algorithms (Manzocchi et al., 1999, Revil and Cathles 1999 and Sperrevik et al., 2002).

The Shale Smear Factor assumes that faulting causes shale beds to be smeared along the fault zone. The SSF is used to predict if a fault develops a continuous shale smear along the fault plane, or a partial broken shale smear. The SSF has been calculated for two faults in this study.

Chapter 6 presents bulk permeability estimates of fault permeability, modelled using the data collected from outcrops. It compares those bulk permeability values with the SGR-based values calculated here.

Chapter 6

Flow models

The detailed maps of fault zone architecture and composition have been used as the basis for numerical modelling of fluid flow. This modelling investigates where fluids traverse fault zones, and how different fault architectures affect the length and shape of the fluid pathways. In addition to showing where fluids flow, it can show how easily fluids flow through the fault zones. Therefore providing a way of upscaling permeabilities measured from outcrop samples to a bulk value for the entire mapped fault zone.

6.1 Modelling software

The flow modelling is performed using MODFLOW2000 (Harbaugh et al., 2000). The MODFLOW software simulates fluid flow through porous media. It is the de facto standard for groundwater hydrology modelling. Fluid flow is modelled in a regular grid using the ground water flow equation:

$$\frac{\delta}{\delta x}\left(K_{xx}\frac{\delta h}{\delta x}\right)+\frac{\delta}{\delta y}\left(K_{yy}\frac{\delta h}{\delta y}\right)+\frac{\delta}{\delta z}\left(K_{zz}\frac{\delta h}{\delta z}\right)+W=S_s\frac{\delta h}{\delta t} \tag{6.1}$$

In this equation Kxx, Kyy and Kzz are the hydraulic conductivity in the x, y and z direction respectively. h is the hydraulic head, a way of expressing fluid pressure as the height of a column of that fluid above an arbitrary level. W represents sources and sinks of water in the model. S_s is the specific storage of the material t represents time. Units are not predefined in MODFLOW, so users can choose these to their preference, as long as the units are mutually consistent.

Equation 6.1 is solved for pressure, using a finite difference approach. The groundwater flow equation is a partial differential equation derived from Darcy's law combined with conservation of mass. Darcy's law is a constitutive equation relating flow rates through porous media to properties of the medium and fluid (Eggen 1996). Flow rates are proportional to the pressure gradient, the cross sectional area perpendicular to flow and the permeability of the porous medium. Flow rates are inversely proportional to the viscosity of the fluid and the length of the path traversed by the fluid. Darcy's law is often written as:

$$Q=\frac{-kA}{\mu}\frac{P_a-P_b}{L} \tag{6.2}$$

Here Q is the flow rate, k represents the permeability, A is the cross sectional area perpendicular to the direction of flow, P_b and P_a are the fluid pressure on both ends a and b, of the volume under consideration, L is the distance between a and b, μ is the viscosity of the fluid.

The hydraulic conductivity used in MODFLOW is related directly to permeability by the equation:

$$K = k\rho g/\mu \tag{6.3}$$

Where K stands for hydraulic conductivity, k represents permeability, ρ is density, g for gravitational acceleration and μ is viscosity.

The aim of the flow modelling is to understand the interplay between fault architecture and fluid flow, allowing the identification of the key features of fault zone architecture that control flow. For this purpose MODFLOW is excellent as it is technology which has proven itself in many studies, it is easy to use and adapt and freely available.

One caveat is that MODFLOW is a single phase flow simulator. Perfectly emulating the complex multiphase flow of oil, gas and brine through highly complicated fault rock assemblages is beyond the scope of this study. Besides the need for using different software, data of the relative permeabilities of all the rock units would be required. Considering the combined effects of uplift, diagenesis, weathering and sampling it is questionable if the relative permeabilities of samples taken from fault outcrops are representative for faults at depth.

6.2 Model generation

The fault maps created in the field are assembled and digitized in vector-based illustration software (Inkscape). For the modelling, maps are carefully edited so that they contain features affecting flow; outlines are removed, leaving colour representing the lithology. To use these vector maps in MODFLOW, they need to be converted into rectangular raster images. The colour of each pixel in the resulting raster image is used to automatically assign a permeability value to each grid cell in the model. This conversion is performed using ImageMagick as it allows the rasterization without anti-aliasing (AA). AA is a computer graphics technique that optimizes line drawings for use on electronic displays; sharp colour transitions are slightly smoothed to prevent edges looking jagged. For the modelling in this study this is undesirable as it introduces intermediate colours not reflecting the mapped geology.

After conversion to raster format, the image is stored in Graphics Interchangeable Format (.GIF), which is a compressed 8 bit palette-based raster file format. The advantage of using a palette-based format is that every pixel is assigned only a single number. These numbers typically start at zero and count upwards, making it relatively straightforward to map colours to permeability values.

Slip surfaces and fractures are included in the flow models by using grid-based representations. These features are thinner than the grid cells used to represent them, this needs to be addressed. Decreasing the size of the grid cells is usually not an option here as the overall model size would become too large to be modelled in MODFLOW using ordinary PC hardware. Instead the permeability value of the slip surfaces is upscaled to accommodate for the size of the grid cells used to represent them. The upscaling is performed by running a small high resolution simulation which has the size of one grid cell in the final model. In this high resolution model

the feature of interest has the appropriate size. For simple geometries analytical solutions exist to average permeability.

For simplicity, anisotropy in the upscaled permeability is ignored. Properly accounting for anisotropy would require the assignment of anisotropy, based on the local orientation of the slip surface. This is technically feasible, but labour intensive and not likely to strongly improve the modelling for the purpose of this study.

Slip surfaces and open fractures are included as zones of connected grid cells, one cell wide or high. For diagonal parts it is ensured that slip surface grid cells are connected by a top, bottom, left or right face because corner contacts do not allow fluid flow in MODFLOW. This involved development of a new MATLAB function '*fixslipsurfaces.m*' to automatically enforce these criteria. However manual checking of the slip surface geometry is still recommended. These checks are most easily performed using a pixel-based image editor, such as GIMP.

MODFLOW expects its input data as a set of strictly formatted ASCII files. Several tools exist to facilitate the creation of these files. Here mfLab is used (Olsthoorn, 2012); a MATLAB based solution developed at Delft University of Technology. The user defines models in the MATLAB language by writing scripts of MATLAB commands; mfLab uses these to generate input files for MODFLOW. This approach offers several benefits over Graphical User Interface based tools. Models can be modified by copying the files and just changing one or more commands. In addition it allows for full automation, for example easily generating many flow models from synthetic realizations for fault geometries (chapter 7). For this study an mfLab and MATLAB based work-flow has been developed which can largely automate the model building and analysis whilst still retaining full user control.

6.2.1 The permeability of slip surfaces

From the maps it becomes apparent that slip surfaces are a common feature in the seismic scale faults mapped in this study. Because of their length and continuity they have the potential to form a strong control on bulk fault permeability. As such it is necessary to understand their permeability structure and how this varies spatially, temporally and in different rock types. Direct measurement of slip surface permeability is nearly impossible due to the difficulty of taking an intact sample containing a slip surface. In addition the present day permeability of the slip surface in the outcrop does not necessarily relate to the permeability history of the same slip surface at depth. Matthai et al., 1998 have succeeded in measuring the permeability perpendicular to slip surfaces in sandstones in Utah, yielding permeabilities ranging from 1 to 0.001 mD. As they have used a probe permeameter, this is at the lower limit of what can be measured, so slip surface permeability in sandstones could actually be smaller.

Measurements for slip surfaces in other lithologies are not available. Instead the role of slip surfaces is investigated here by modelling different scenarios of slip surface permeability. The first scenario assumes that slip surfaces have no effect on fluid flow. The second scenario assumes a high permeability for all the slip surfaces. For these a permeability of 100.000 mD is used, which corresponds to a fracture with a constant 1 mm aperture (Matthai et al., 1998). The third scenario assumes that all slip surfaces have a low permeability. For slip surfaces in high permeability sandstones, a permeability value of 0.001 mD is used as suggested by Matthai et al., 1998. Slip surfaces in silt, shale and cemented lithologies are assumed to consist of the same lithology and are assigned the same permeability value as their host lithology. The actual

value used in the model is calculated by upscaling a 1mm thick slip surface to the size of the grid cell.

Subsequently the modelling results are compared with the distribution of geochemical alteration mapped at the outcrops. It is assumed that zones of geochemical alteration correspond to areas that have experienced high flow rates at depth. The mapping of alteration is based mostly on observed colour changes, where red brown sandstones and siltstones have been bleached. Other observed forms of paleofluid flow indicators include cementation and mineral veins.

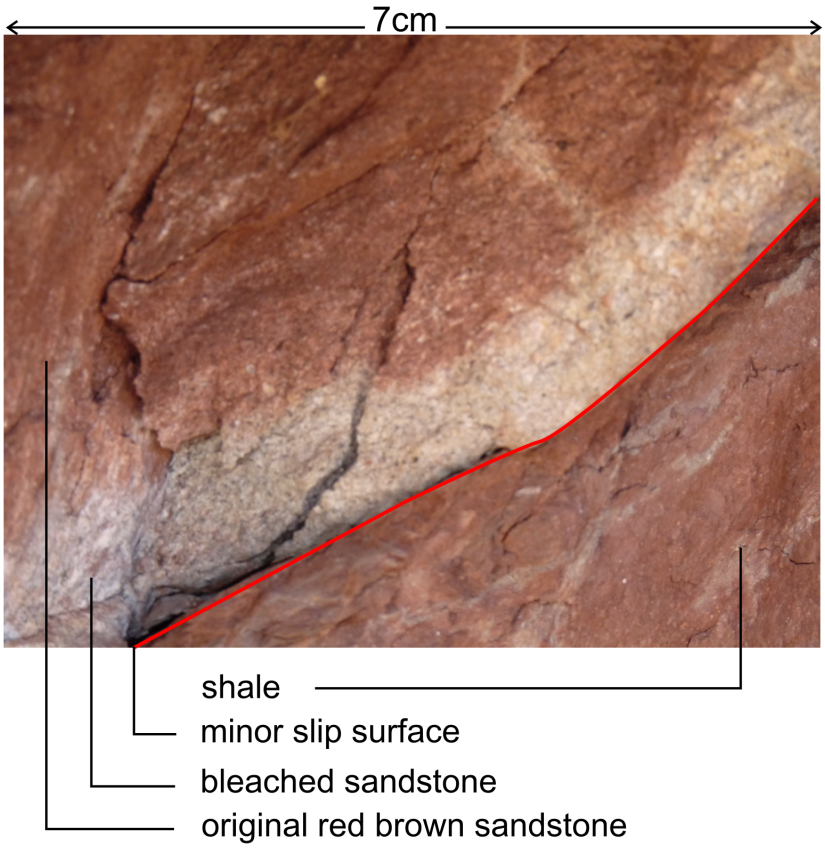

Figure 6.1: Example of geochemical alteration as a paleo fluid flow indicator (Moab fault exposure 191 SE). The originally red brown coarse sandstone has been partially bleached to light grey. The slip surface might have acted as a conduit for reducing fluids. The low permeability shale is not affected.

Figure 6.1 shows an example from Moab fault exposure 191 SE, where a red sandstone is bleached above a slip surface, and below the slip surface the less permeable shale is not bleached. Solum et al., 2010 suggests two main regional episodes of fluid migration based on work by Morrison and Parry, 1986, Nuccio and Condon, 1996, Chan et al., 2000, Chan et al., 2001 and Garden et al., 2001. Of these the first episode that occurred around 49-62 Ma is associated with reduction of iron oxide and thus the bleaching of red sandstones. The second phase of fluid flow consisted of Cu, Pb and Zn rich fluids probably related to igneous activity in the La Sal mountains. This second phase is associated with mineralization but is not with bleaching in the literature. Reported ages for this second phase range from 29.7 Ma to 20 Ma (Nelson et al., 1992, Solum et al., 2010, Chan et al., 2001). As such the alteration observed

in the Moab fault is likely related to the first phase, and as such provides information on the fluid flow through the fault at that time. The Moab fault was active from the Triassic until at least early Tertiary (Foxford et al., 1998). Solum et al., 2005 suggests that the Moab fault was reactivated around 60 Ma. Therefore the alteration likely provides information on fluid flow through the Moab fault in it's final or near final form, but well before uplift, as the Paradox basin in this area reached maximum burial around 39 Ma (Nuccio and Condon, 1996).

In this study the likeliness of the different modelled scenarios is evaluated, by comparing regions of high flow rates with areas showing geochemical alteration. It is assumed that these regions have experienced high flow rates during the 49-62 Ma episode of fluid flow. In this way, the slip surfaces can be selected that were most likely high permeability features during the episode of bleaching fluid migration.

6.2.2 Modelling rationale

The primary goal for the modelling study is to improve understanding of how fluids flow through fault zones. Developing insight into this will allow researchers to collect more relevant data on fault zone properties. The approach also provides an estimate of the bulk permeability of mapped area of the fault zone. The modelling allows the permeability values measured on small samples to be up-scaled to the entire outcrop, with an approach that honours much of the geological information available. This way bulk fault permeability estimates can be obtained which are more realistic than those obtained from traditional work-flows.

Obviously the accuracy of the bulk permeability estimates is limited because of several reasons. First the models are limited to two dimensions, features which are not connected on the maps might very well be connected in the third dimension and barriers which appear intact on the map might be breached in unexposed parts of the fault zone. Secondly as the studied faults are at the surface, exhumation and surface processes could have affected the permeability of the sample. I try to negate these effects by using unweathered samples (section 4.1.2) and testing their permeability under confining pressure where possible (section 4.1.3).

6.2.3 Modelling set-up

This study only uses static flow models; i.e. fluid flow under constant conditions. A constant hydraulic head gradient is applied to two opposing boundaries. For across-fault flow (figure 6.2 A) the hydraulic gradient is applied along the entire height of the model. If the orientation of the fault deviates strongly from vertical, the model is rotated so the fault becomes approximately vertical. The (single phase) modelling does not include any gravitational effects, so the rotation does not affect the results. For example for flow across a (near) vertical fault, a constant hydraulic head of 1m is assigned to the leftmost column of grid cells, and a value of 0 m is assigned to the rightmost column, leading to flow from left to right. For the purposes of this study, the actual magnitude of the hydraulic gradient does not matter, it does not affect the pathways of the flow or the bulk permeability. As discussed in the introduction, one of the most important controls on reservoir-scale across-fault flow is formed by juxtaposition of permeable rocks against impermeable rocks. As this process is well understood, it is not the focus of the study, which focusses on fluid flow in the fault core itself. For most of the models presented here the effect of juxtaposition (on an outcrop scale) is minimal. Only at the Professor Valley outcrop it is significant and therefore is accounted for in the modelling.

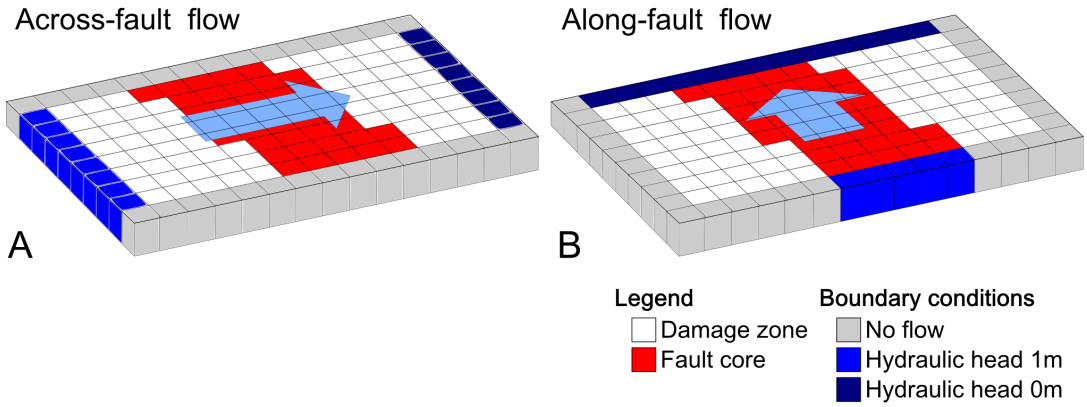

Figure 6.2: Setup of the flow models for across-fault flow and along-fault flow. Colours show a simplified geometry of the fault and boundary conditions. A: Across- fault flow, for the across-fault flow models a hydraulic head of 1m is applied to cells on the leftmost column, and a 0m hydraulic head is applied to cells in the rightmost column. This leads to flow from left to right. A no-flow condition is applied to the top and bottom row, preventing fluid flow out of the model. B: Along-fault flow, for along-fault flow, the model is setup to focus flow into the fault core at the base. On the top, flow is allowed to exit through both fault core and damage zone.

For the along-fault flow (figure 6.2 B) the aim is to model fluid moving upward through the fault core. To enforce this scenario, a no flow condition is assigned to the damage zone at the base of the model, on the top of the model flow is permitted everywhere. The flow/no flow boundary conditions are visualized in the figures using black bars for flow and grey bars for no flow. This set-up is chosen to model upward flow through actual fault core rather than fluid focussed in the damage zone. A fault zone providing a pathway through a stratigraphic seal would be one way of focussing fluid flow in the core rather than the damage zone (Cartwright et al., 2007). The abundant geochemical alteration inside many fault cores suggests that flow along the core of the fault is important, both from a hydrocarbon exploration and production perspective and the effect this fluid can have on fault rocks and as such fault architecture.

6.2.4 Permeability values

As discussed in section 4.1.5, there are several difficulties in using surface measurements for representing fault rock permeability at depth. Rocks exposed at the surface are likely to have been affected by uplift, weathering and vegetation. In addition sampling can affect the permeability of the sample. This affects predominantly the low permeability rock types (shale, silt, gouge, cementation). A small micro-fracture can strongly affect the overall permeability of these samples. The high permeability rock types are less likely to be strongly affected by this, as a micro-fracture is less likely to be a significant pathway compared to the existing pore network. It is unclear how many micro-fractures exist under reservoir conditions. To account for this uncertainty two sets of permeabilities are used for the modelling.

Both sets use the same permeability values for the high-medium permeabilities. For the low permeability units (fault gouges, shale, silt, cementation), the first set (Degassibility and

Axial Flow permeability Measurements, DAFM) uses the permeability values determined in this study using GRI degassibility for shales, gouges, siltstones and cementation. For other lithologies (sandstones, condensed deformation band clusters) axial flow measurements have been used. As such the set represents corresponds to a scenario where all micro-fractures are nonexistent at depth. For the second set (Literature and Axial Flow permeability Measurements, LAFM), the degassibility measurements have been replaced with values in the same range as the in situ measurements from the literature (chapter 4.1.5). This corresponds to a scenario where micro-fractures do occur at depth and strongly affect the permeability of low permeability lithologies. These two sets of permeabilities illustrate the uncertainty in permeability of shale and other low permeability lithologies under reservoir conditions.

6.2.5 Limitations of 2D modelling

For this study two-dimensional maps have been used as the basis of the modelling. This is brings up a common problem in field geology; field geologists can only work with what is exposed at the surface. No geophysical techniques exist which could have provided anywhere near the level of detail, in three dimensions. The use of LIDAR for this study has been considered. LIDAR produces three dimensional data, but only for the surface. Due to the complexity and heterogeneity of fault zones, very little scope exists for extrapolating such 2.5D data to true 3D models of the fault zone contents. The only realistic option for performing a study with this spatial resolution in 3D would be excavate successive slices across the fault zone, map each slice and interpolate these to obtain 3D geometry. Since many of the outcrops in this study are of great scientific and educational value, this is clearly impossible here. As such; a choice has to be made between a detailed study in two dimensions and a low resolution geophysical study in three dimensions.

It is very well possible that structures which do not connect on the outcrop surface, would connect a short distance into the rock and vice versa. Similarly many structures show strong changes in thickness over short distances. The present high-resolution two dimensional work strongly demonstrates the importance of small scale features and heterogeneity. It would have been impossible to show this at a larger scale. Therefore the current two dimensional study presents the best option for evaluating the role of heterogeneity and fault architecture. Nonetheless the reader should keep in mind that three dimensional heterogeneity could affect the models and bulk permeability values presented in this study.

6.3 Model visualization

The results can be visualized in several ways. A common approach is to display the hydraulic head as a contoured or colour graded map. This is useful, but not ideal as it is hard to combine this type of map with other information. A more practical approach involves streamlines, which represent flow rates and direction rather than pressure. The streamlines represent the path a fluid particle would follow from one side of the fault to the other side. Spacing of the streamlines corresponds to the local flow rates; closely spaced streamlines denote high flow rates. Streamline maps can easily be plotted on top of maps of rock properties such as lithology, permeability or geochemical alteration.

6.4 Results

For all the modelled faults appendix B provides a complete set of figures detailing the set-up and results for each modelled scenario. This includes a map of the hydraulic head and maps with streamlines superposed on fault geology maps. In addition a bar chart shows the relative flow distribution per unit and another bar chart provides the flow rates per unit per grid cell. Figures are provided for each modelled scenario and set of permeabilities. For three faults the distribution of geochemical alteration has been mapped, for these faults the appendix contains an extra figure combining the geology, geochemical alteration and the modelled streamlines. In this chapter the most interesting features of the flow models are highlighted, to show the key flow controls for different faults. For Moab fault exposure 191SE and 191NW figures for all modelled scenario are included in this chapter, for the other exposures only the figure for the scenario where slip surfaces have no effect is included in the chapter itself. Figures for the other scenarios are available in appendix B. This is done to constrain the size of this chapter.

In this chapter only figures for LAFM data are included as this provides for the most realistic models. The tables in this chapter with the modelled bulk permeability values include both LAFM and DAFM data. Appendix B includes figures for both LAFM and DAFM models.

6.4.1 Moab Fault site 191NW

Figure 6.3 shows the map for outcrop 191NW of the Moab fault. At this location the Moab fault has a throw of 1km. For this fault three different scenarios have been modelled, for which the results are shown in figure 6.4 to 6.6.

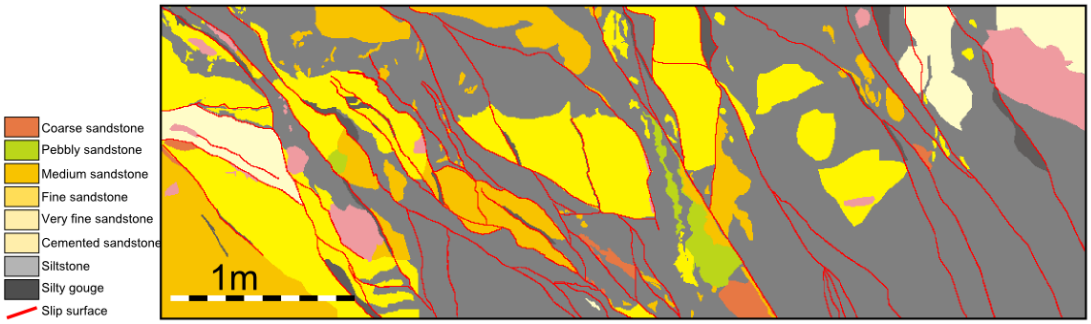

Figure 6.3: Figure illustrating the mapping of Moab fault exposure 191NW.

The streamlines show that fluid flow is highly focussed into connected high permeability features. For along-fault flow fluids are concentrated into the central sandstone lenses connecting both sides of the model, if open slip surfaces are available, these are used as well. For across-fault flow no single sandstone lens or slip surface is available to facilitate flow across the low permeability siltstone. As a consequence the streamlines link up connected sandstone lenses and/or open slip surfaces and traverse the siltstone where this is thinnest. The across-fault thickness of the silt-dominated core part of the fault is 3.4 m, the sandstone lenses reduce the length of the minimum pathway through the silt to 1.3 m, with open slip surfaces this further reduces to 0.3 m. As a consequence these high permeability features form the key flow control for this outcrop. Rather than their size or adundance, the connectedness of these features is the most influentual on flow.

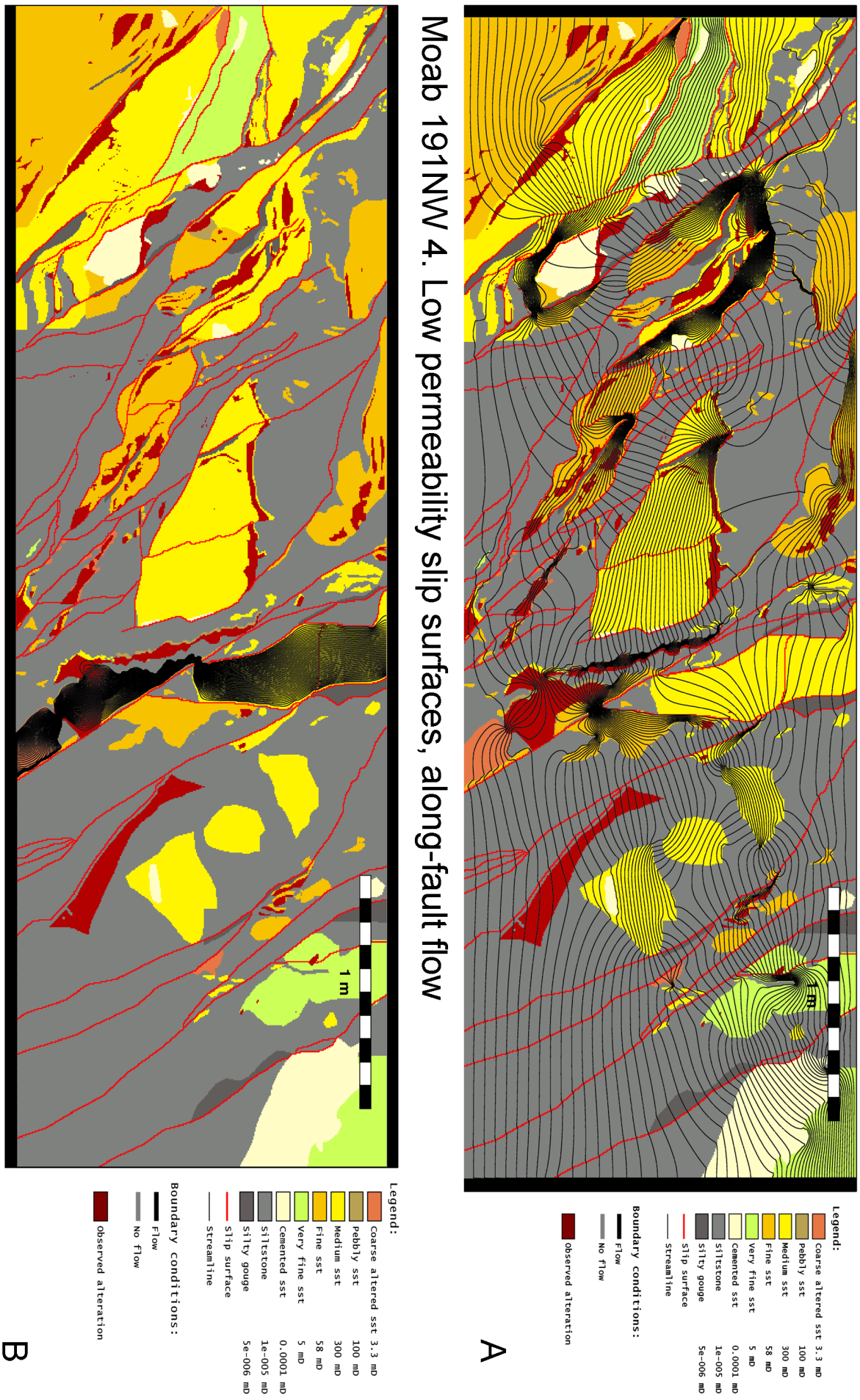

Figure 6.4: Moab fault exposure 191NW. Low permeability slip surfaces. A: Across-fault flow. B: Along-fault flow.

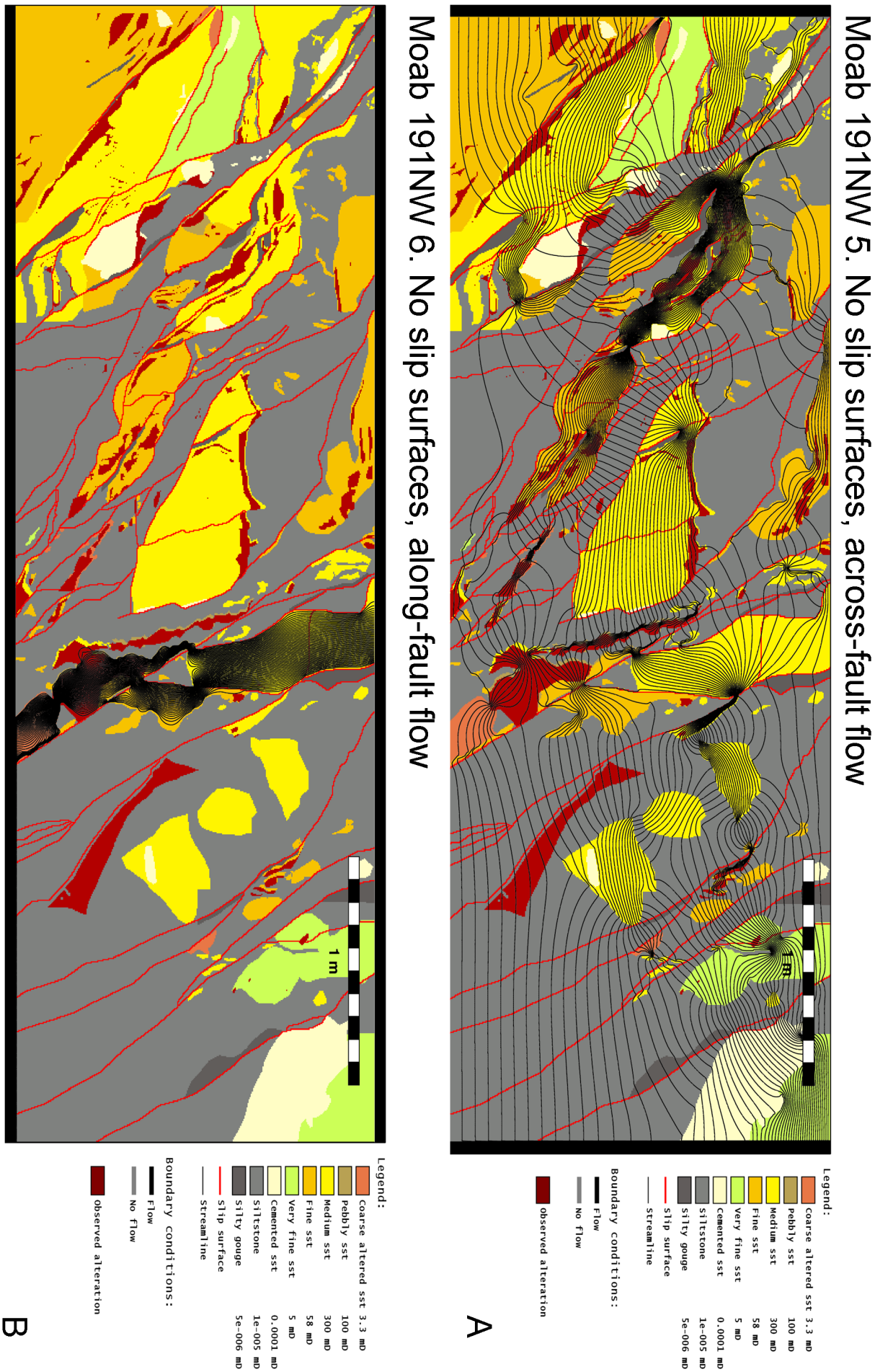

Figure 6.5: Moab fault exposure 191NW. Slip surfaces have no effect. A: Across-fault flow. B: Along-fault flow.

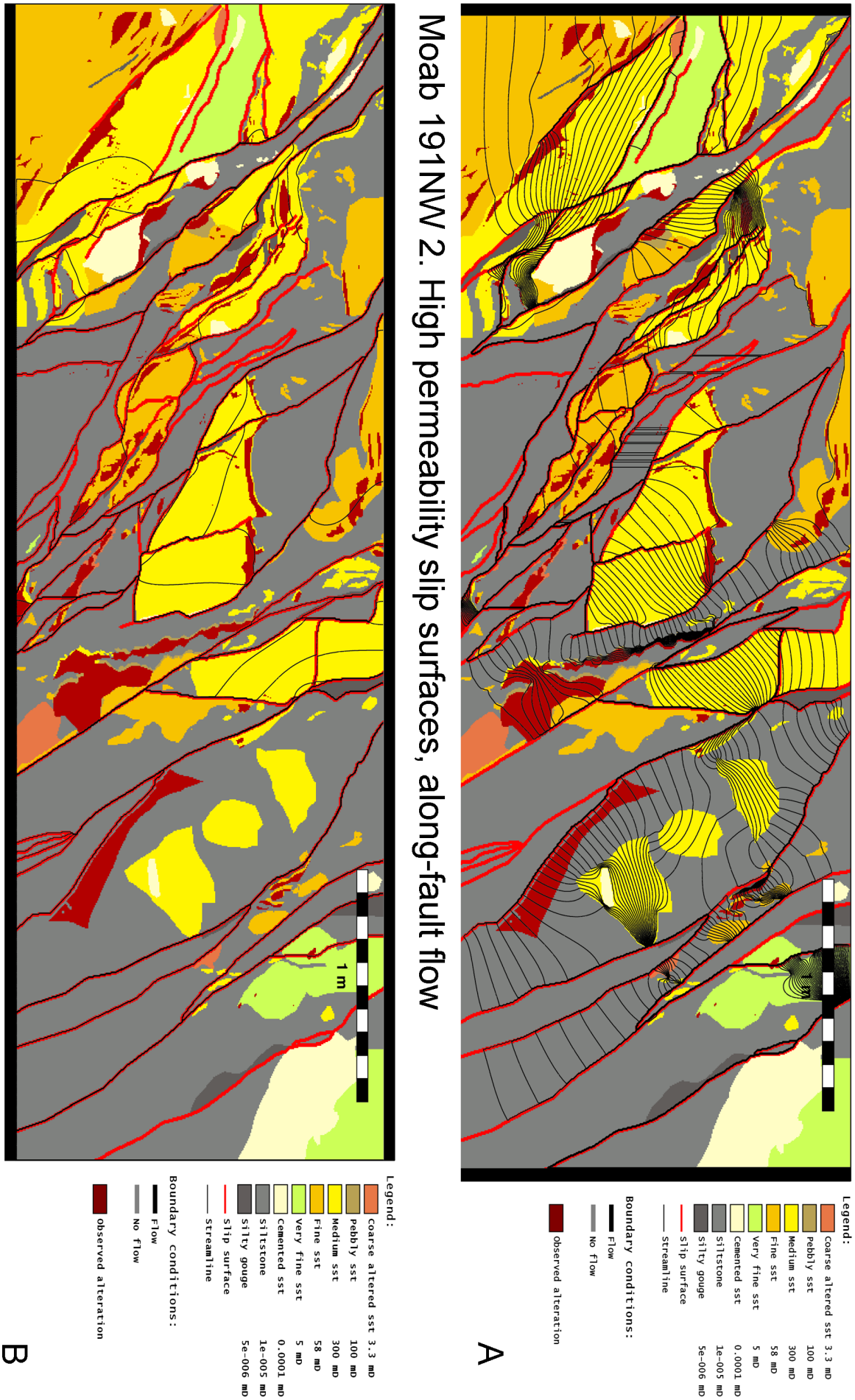

Figure 6.6: Moab fault exposure 191NW. High permeability slip surfaces. A: Across-fault flow. B: Along-fault flow.

Scenario	Bulk permeability (using LAFM)		Bulk permeability (using DAFM)	
	across-fault	along-fault	across-fault	along-fault
Low permeability slip surfaces	2.1e-5	9.6e-3	6.7e-8	9.5e-3
Slip surfaces have no effect	3.4e-5	6.1e-1	9.2e-8	6.1e-1
High permeability slip surfaces	1.4e-4	2.1e+2	-	2.1e+2

Table 6.1: Modelled bulk permeabilities (in mD) summarized for the 191 NW exposure of the Moab fault. The DAFM models use very low permeability values measured using GRI degassibility for shales, silts, gouges and cementation and Axial Flow measurements for sandstones. The LAFM models discard the degassibility measurements in favour of typical in situ shale and silt permeabilities from the literature. The difference between the two sets is discussed in section section 6.2.4.

Table 6.1 summarizes the bulk permeabilities calculated for the different slip surface permeability scenarios. It shows that the slip surface permeability can strongly affect the bulk permeability. For across-fault flow for the LAFM data, the no slip surfaces scenario results in a higher bulk permeability than the low permeability slip surfaces, and the high permeability scenario even has a modelled bulk permeability an order of magnitude higher than the scenario where slip surfaces have no effect. The difference between slip surfaces having no effect and low permeability slip surfaces is small, as most slip surfaces are located in the low permeability siltstone. Flowrates through the silt is already low, so the effect of the slip surfaces here is small. For the DAFM data the difference between the open slip surfaces and the other two scenarios is even more pronounced, spanning seven orders of magnitude. With the very low DAFM permeabilities for the silt, the inclusion of high permeability pathways across the fault has a very striking effect.

For along-fault flow the effect of open slip surfaces is much more pronounced, with this scenario having a bulk permeability two orders of magnitude higher than the scenario where slip surfaces have no effect, and five orders of magnitude higher than the scenario with low permeability slip surfaces. Overall the inclusion of slip surfaces as high permeability features increases the heterogeneity of the model by forming even more localized pathways for flow to traverse through the low permeability siltstone which forms a dominant barrier at the core of this fault. In addition the slip surfaces can link up other high permeability features like sandstone lenses. For the along-fault flow models the difference between the two permeability sets LAFM and DAFM is small, flow is focussed in sandstone lenses and slip surfaces for which the permeability is the same for both sets.

The modelled scenarios demonstrate that the slip surfaces can potentially have a pronounced effect on the bulk permeability of the fault zone, it is therefore necessary to understand their permeability and ideally its spatial and temporal variability. Here the geochemical alteration pattern is used to elucidate the role of slip surfaces. Figure 6.7 to 6.9 show the streamlines plotted on a map combining the geology and the geochemical alteration, for the three slip surface scenarios (no effect, low permeability, high permeability). By comparing altered areas with regions of high flow rates (closely spaced streamlines), the likelihood of each scenario is tested. None of the three scenarios completely explains the observed alteration pattern. The majority of the altered areas fit with the model without slip surfaces or low permeability slip surfaces. However a few altered areas are clearly best explained by the high slip surface

Scenario	Bulk permeability (using LAFM)		Bulk permeability (using DAFM)	
	across-fault	along-fault	across-fault	along-fault
Low permeability slip surfaces	2.1e-5	9.6e-3	6.7e-8	9.5e-3
Slip surfaces have no effect	3.4e-5	6.1e-1	9.2e-8	6.1e-1
High permeability slip surfaces	1.4e-4	2.1e+2	-	2.1e+2
Calibrated slip surfaces	4.3e-5	3.7e+1	1.2e-7	3.7e+1

Table 6.2: Modelled bulk permeabilities (in mD) using the calibrated slip surfaces scenario, summarized for the 191 NW exposure of the Moab fault. The DAFM models use very low permeability values measured using GRI degassibility for shales, silts, gouges and cementation and Axial Flow measurements for sandstones. The LAFM models discard the degassibility measurements in favour of typical in situ shale and silt permeabilities from the literature. The difference between the two sets is discussed in section section 6.2.4..

permeability model. The alteration-calibrated slip surfaces are summarized in a map in figure 6.10, where colours are used to indicate the scenario most appropriate for each slip surface. This map is used for a final flow model, where slip surface permeabilities are assigned on the basis of the calibration above. The resulting model is presented in figure 6.11. This model has a bulk permeability of 4.3.10-5 mD for across-fault flow and 37 mD for along-fault flow (table 6.2). This represents the an estimate of bulk permeability for the fault at the time the alteration was formed, which as discussed in section 6.2.1 is after the last fault movement, near maximum burial.

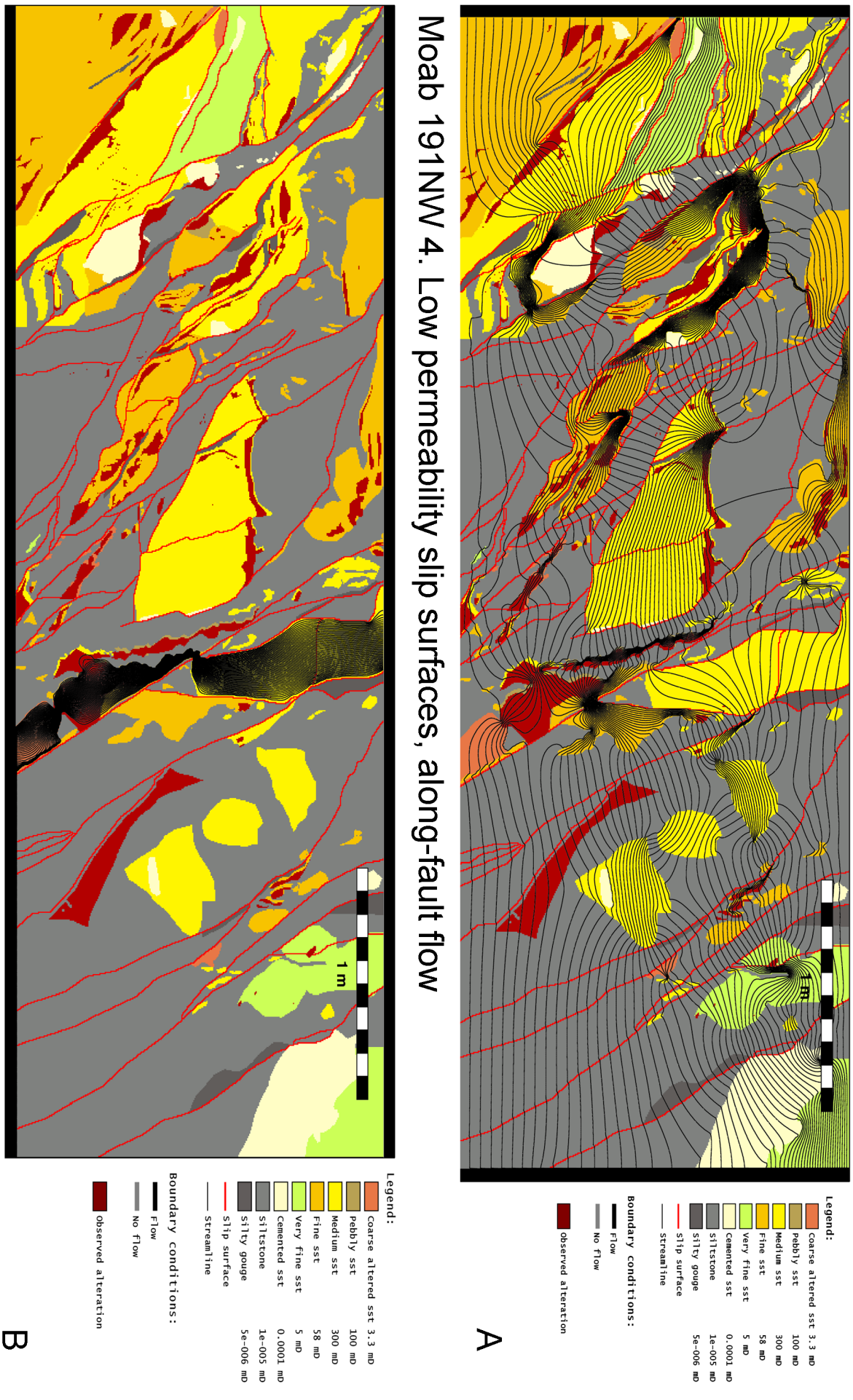

Figure 6.7: Moab fault exposure 191NW, geochemical alteration included. Low permeability slip surfaces. A: Across-fault flow. B: Along-fault flow.

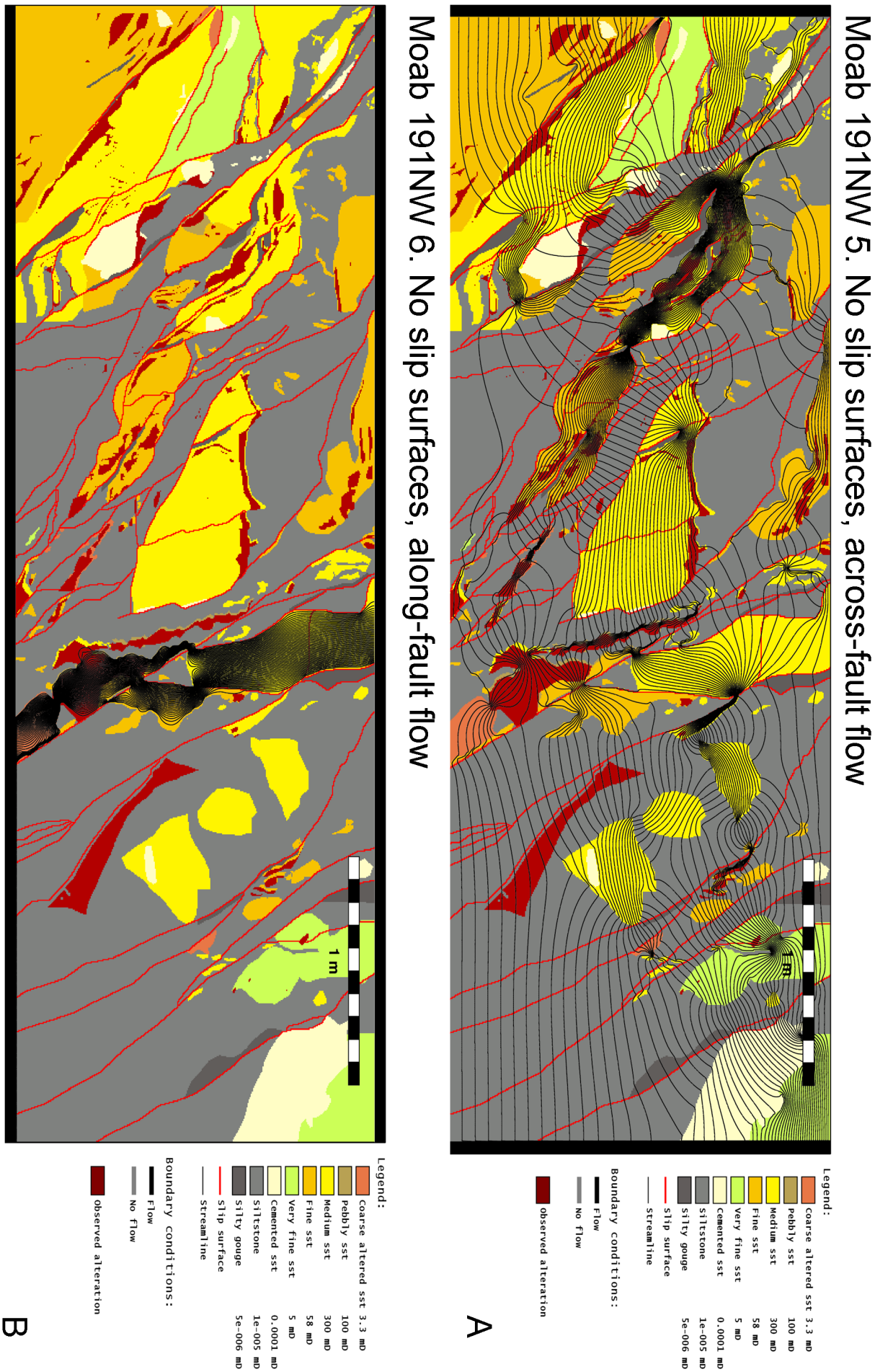

Figure 6.8: Moab fault exposure 191NW, geochemical alteration included. Slip surfaces have no effect. A: Across-fault flow. B: Along-fault flow.

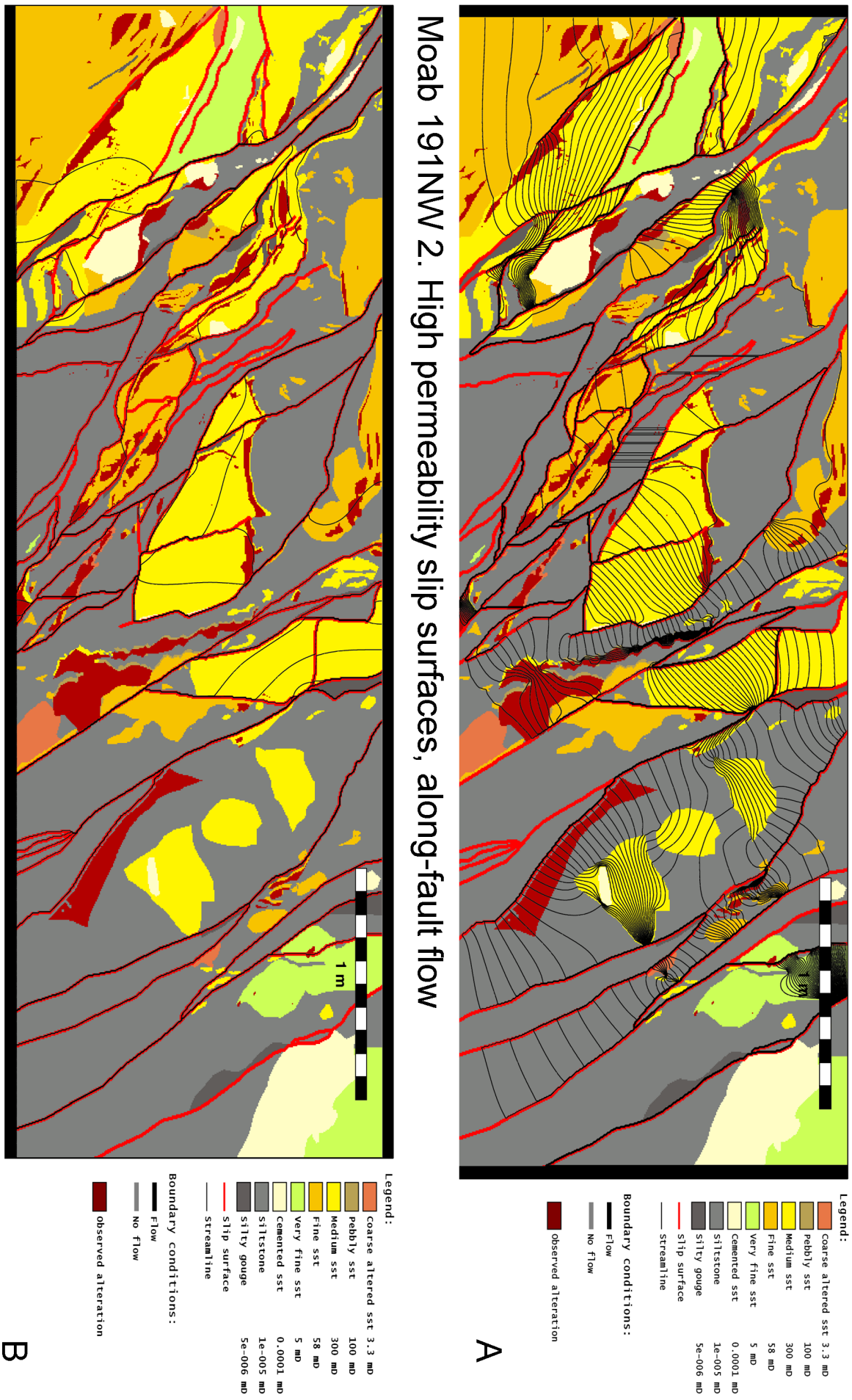

Figure 6.9: Moab fault exposure 191NW, geochemical alteration included. High permeability slip surfaces. A: Across-fault flow. B: Along-fault flow.

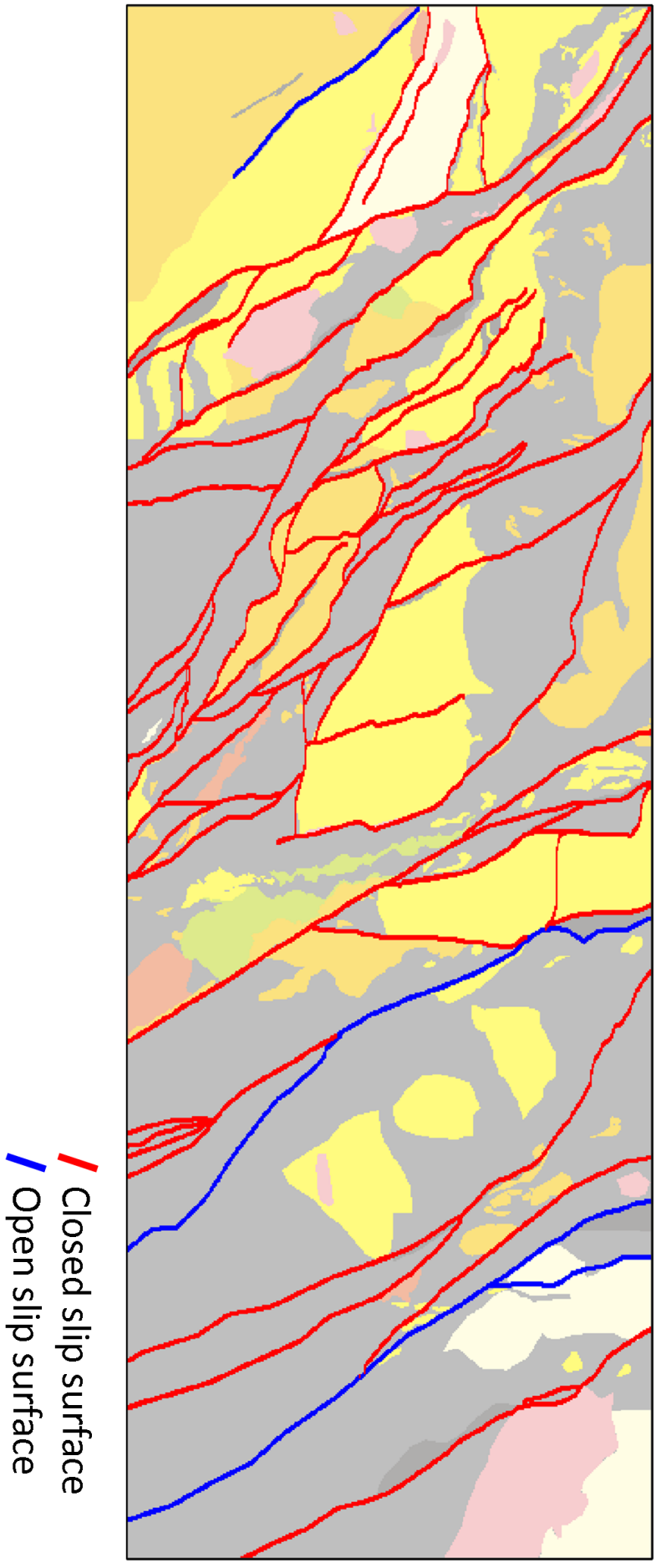

Figure 6.10: Moab fault exposure 191NW. Map indicating which slip surfaces were likely open at the time the geochemical alteration was occuring.

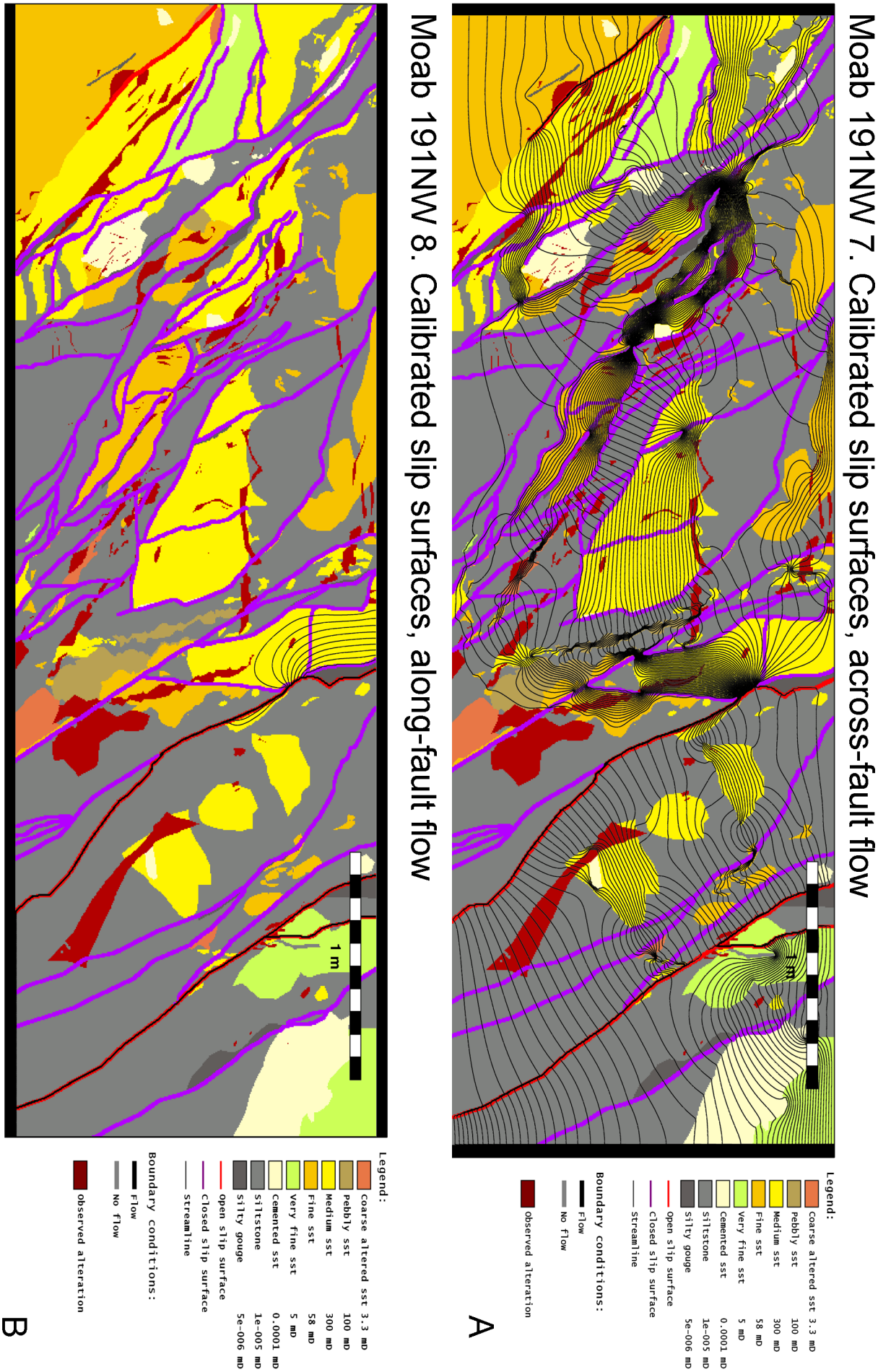

Figure 6.11: Moab fault exposure 191NW, geochemical alteration included. Calibrated slip surface permeability. A: Across-fault flow. B: Along-fault flow.

6.4.2 Moab Fault site 191SE

This locality is located 50m southwards along strike and 10 m higher stratigraphically than the 191NW site. As such it displaces the same stratigraphy and fault offset is similar (1km), a small difference is that a small part of it (60m) is accommodated by a second strand (Foxford et al., 1998). Despite the geographical proximity, this outcrop displays a very different fault architecture and the modelling yields a different bulk permeability. Figure 6.12 through 6.14 show the modelled scenarios for this exposure. The main difference from the 191NW exposure is that this outcrop is dominated by a narrow shale and silt gouge, in between the relatively intact sand and silt sequence. The potential role of slip surfaces has been investigated by modelling three different scenarios; high permeability slip surfaces, low permeability slip surfaces and a scenario where slip surfaces have no effect. These models have been calibrated using the geochemical alteration pattern observed in the outcrop to establish which slip surfaces have likely been open at some point during the fault's history. Figure 6.15 illustrates which slip surfaces were most likely open, and figure 6.16 shows the resulting flow model. The range of bulk permeability for all modelled scenarios is given in table 6.3.

Scenario	Bulk permeability (using LAFM)		Bulk permeability (using DAFM)	
	across-fault	along-fault	across-fault	along-fault
Low permeability slip surfaces	7.8e-5	2.6e-1	8.5e-6	2.6e-1
Slip surfaces have no effect	1.1e-4	6.9e-1	7.8e-5	6.9e-1
High permeability slip surfaces	4.6e+1	3.7e+1	4.6e+1	3.7e+1
Calibrated slip surfaces	1.1e+1	2.9e+1	1.1e+1	2.9e+1

Table 6.3: Modelled bulk permeabilities (in mD) for the 191 SE exposure of the Moab Fault. The DAFM models use very low permeability values measured using GRI degassibility for shales, silts, gouges and cementation and Axial Flow measurements for sandstones. The LAFM models discard the degassibility measurements in favour of typical in situ shale and silt permeabilities from the literature. The difference between the two sets is discussed in paragraph section 6.2.4.

The main control on across-fault fluid flow is the thickness of the low permeability gouge and the streamlines can be seen to converge in the thinnest part of this zone. In this exposure the thickness of the gouge is controlled by both the walls and the occurence of sandstone lenses.

For along-fault flow both the hanging wall damage zone and open slip surfaces show large flow rates. In the model the hanging wall is favoured over the footwall, but this is an artefact of the modelling since the modelled section of the hanging wall does not contain any low permeability beds unlike the footwall. In the low permeability gouge of this fault, geochemical alteration is observable and its distribution is closely linked to the occurrence of slip surfaces, which suggests that these slip surfaces were open to fluid flow for some time. This is clearly supported by the modelling, which also shows that open slip surfaces through this gouge are likely to experience large flow rates both for the along-fault and across-fault scenarios. Similarly modelled scenarios without open slip surfaces do not explain the observed alteration in the gouge.

The low flow rates through the altered coarse sandstone seem counter-intuitive, since the alteration has been used here to infer high flow rates. Here the 4D nature of fault permeability

causes the complication. The measured permeability of the altered sandstone has been used, which is fairly low, most likely as a consequence of the alteration.

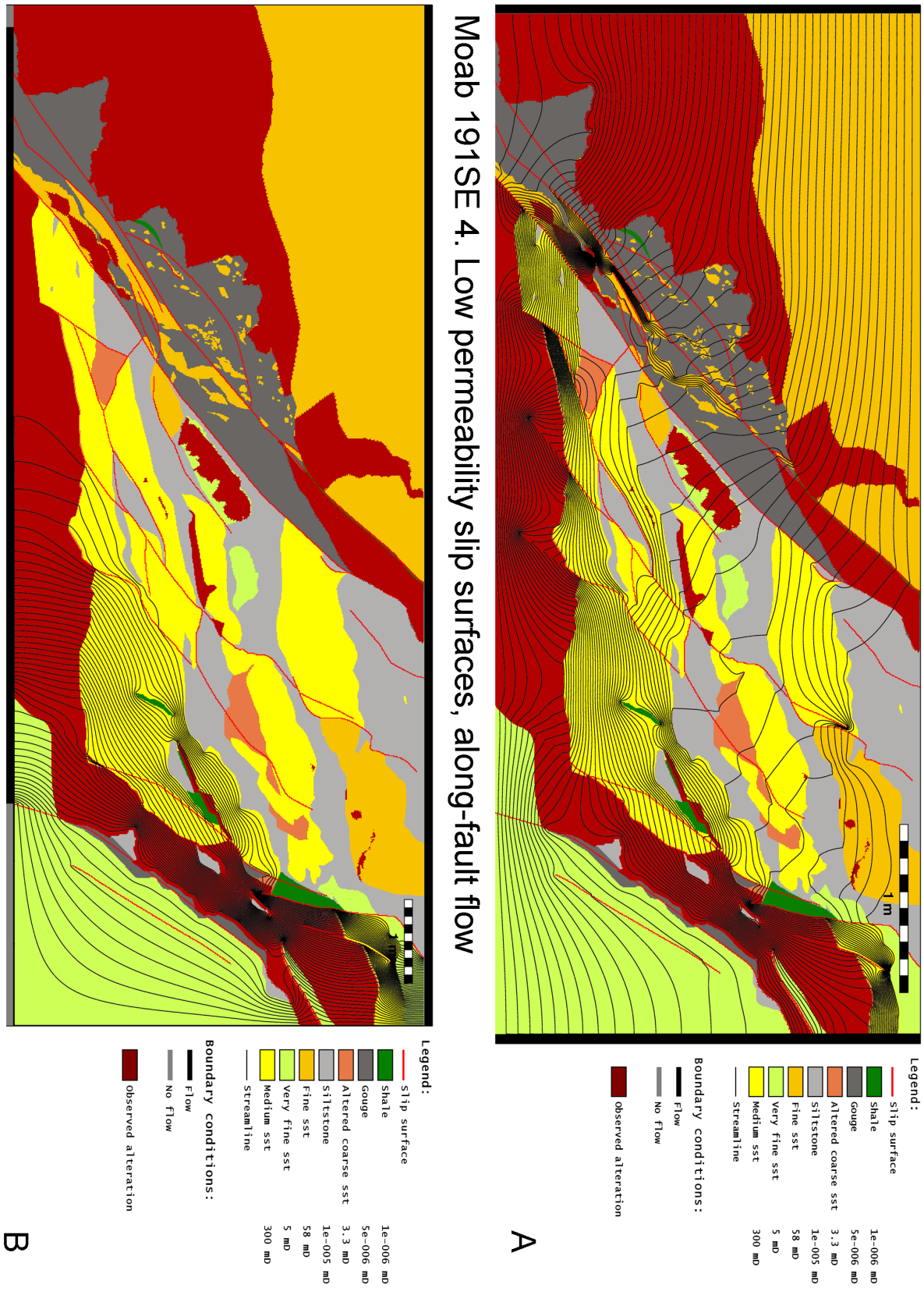

Figure 6.12: Moab fault exposure 191SE. Low permeability slip surfaces. A: Across-fault flow. B: Along-fault flow.

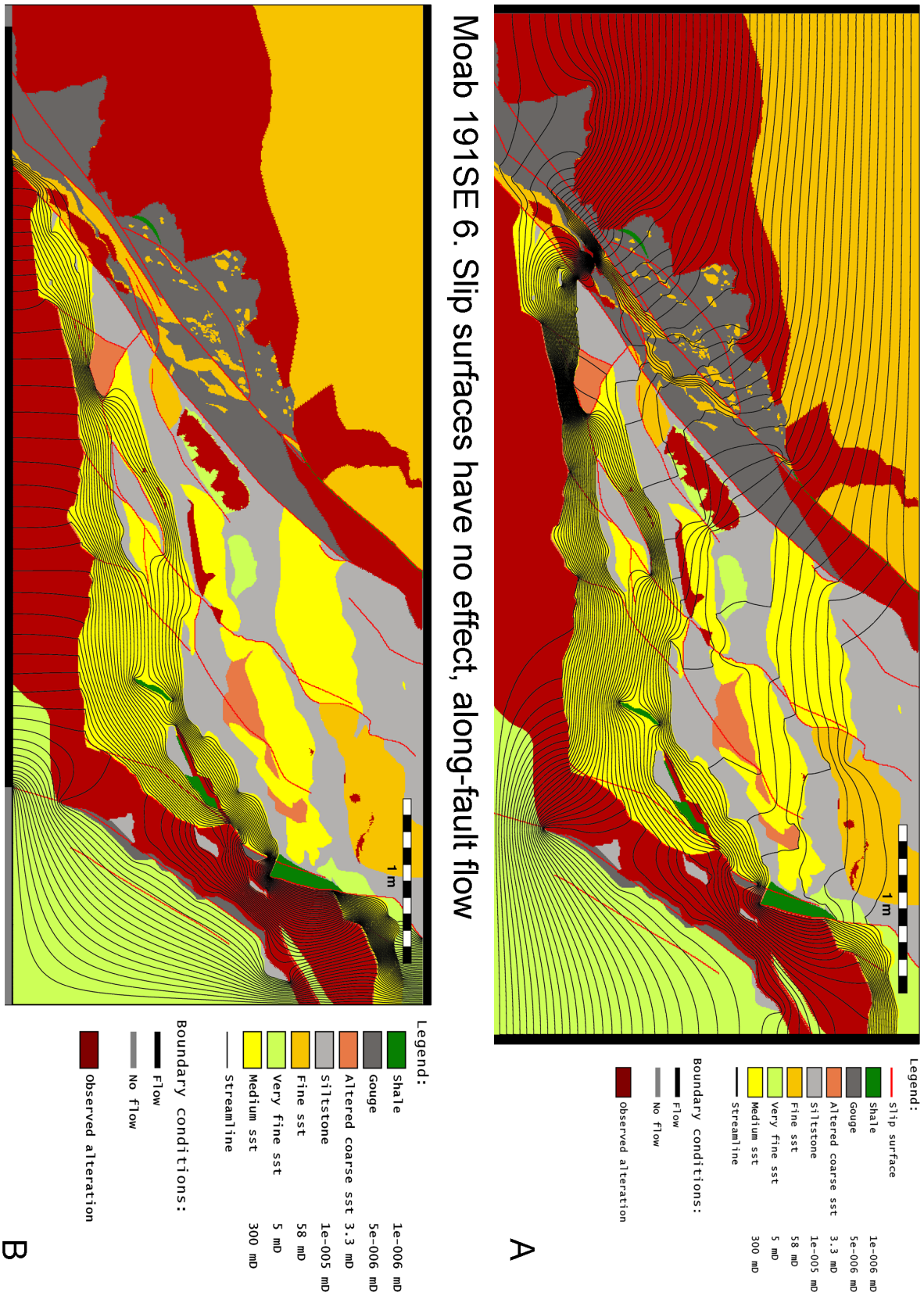

Figure 6.13: Moab fault exposure 191SE. Slip surfaces have no effect. A: Across-fault flow. B: Along-fault flow.

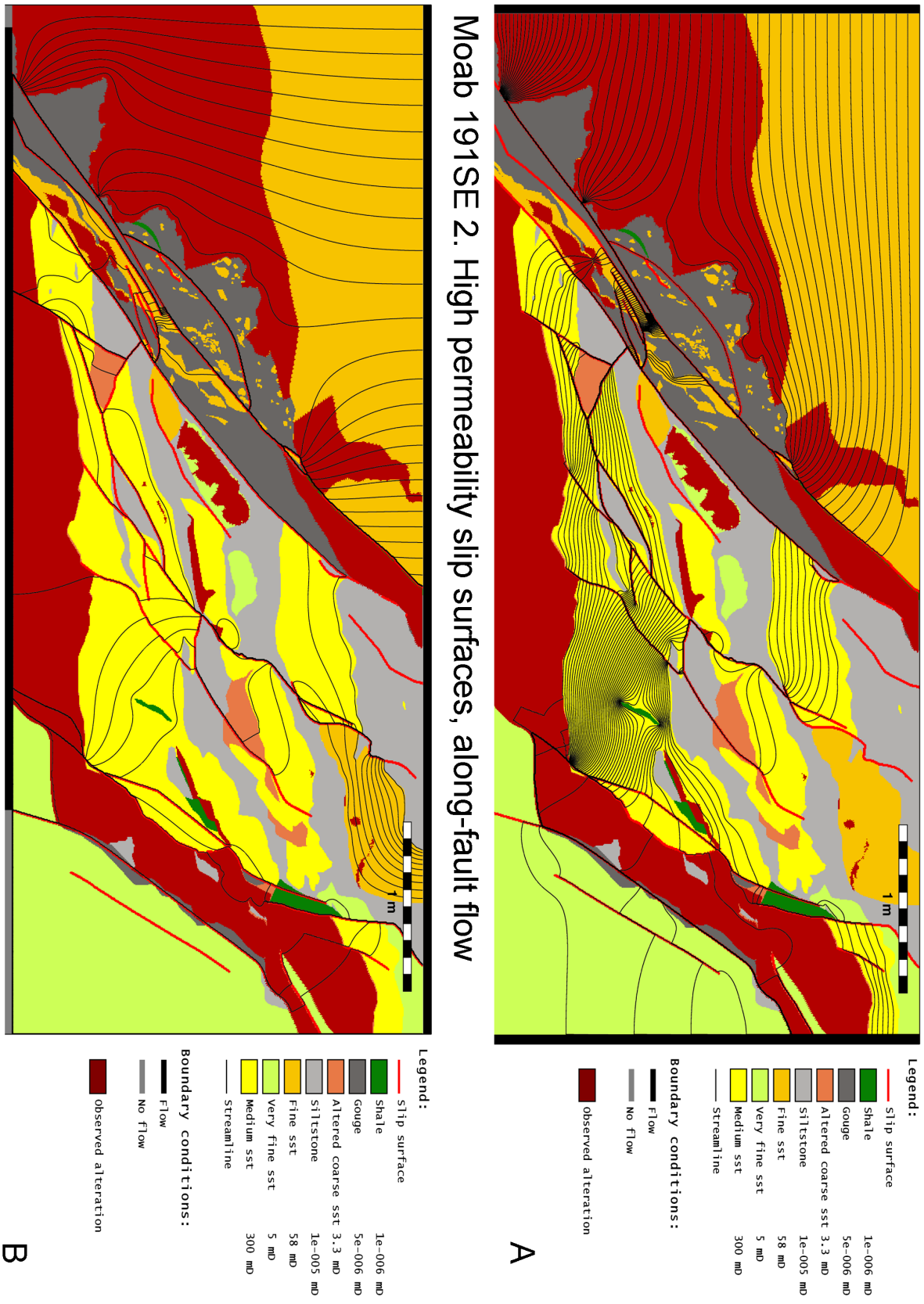

Figure 6.14: Moab fault exposure 191SE. High permeability slip surfaces. A: Across-fault flow. B: Along-fault flow.

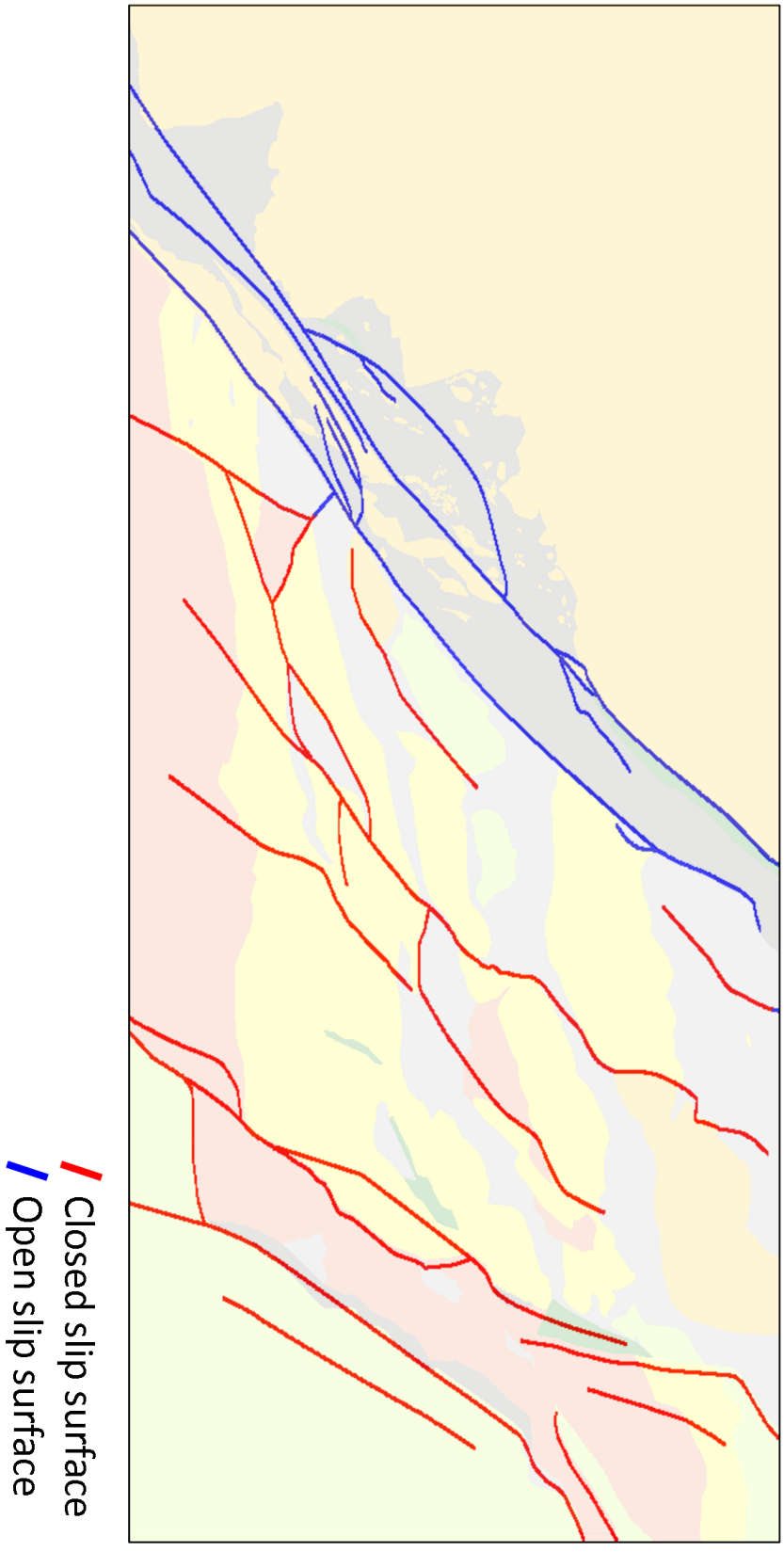

Figure 6.15: Moab fault exposure 191SE. Map indicating which slip surfaces were likely open for some time during the fault's geological history.

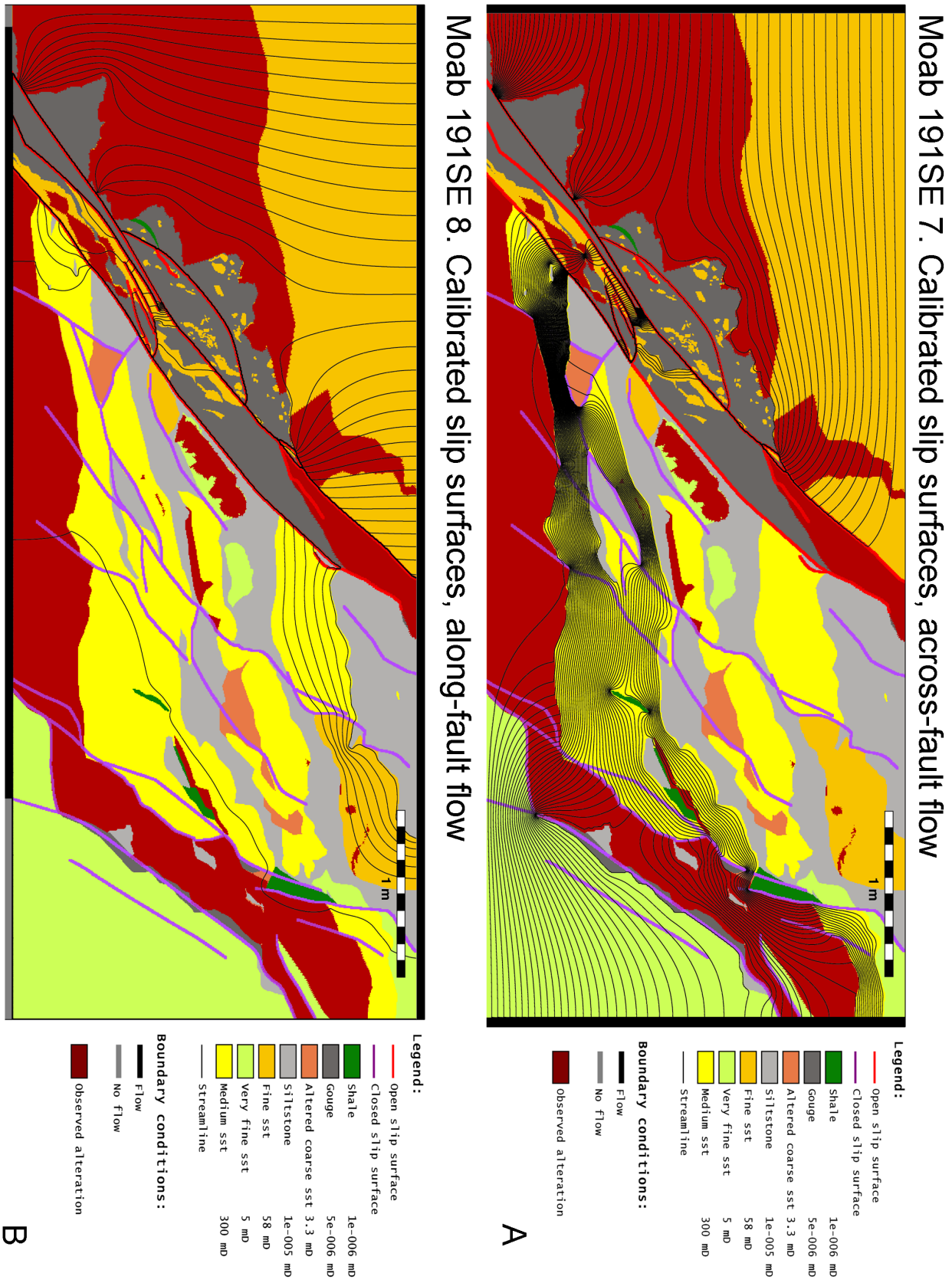

Figure 6.16: Moab fault exposure 191SE, geochemical alteration included. Calibrated slip surface permeability. A: Across-fault flow. B: Along-fault flow.

6.4.3 Moab fault Corral Canyon exposure

At this outcrop the Moab fault displays a much simpler architecture. A thick smear of shale and silt in the centre of the fault forms the main barrier to fluid flow. The central smear is separated from the hanging wall and footwall by two single slip surfaces. Inside the central smear a sandstone lens occurs. Cementation in the footwall forms an additional barrier. The cemented sandstone contains cemented fractures (section 3.1.2.5), this fracturing is not included in the model to simplify the modelling. The fractures have been open for a finite timespan, during which their permeability depended on the stress state and the progression of cementation. In addition the permeability of the fracture network is largely defined by 3D connectivity, for which both the data and modelling capability are lacking.

Scenario	Bulk permeability (using LAFM)		Bulk permeability (using DAFM)	
	across-fault	along-fault	across-fault	along-fault
Low permeability slip surfaces	2.0e-6	1.5e-4	8.0e-9	3.3e-8
Slip surfaces have no effect	2.0e-6	1.5e-4	7.0e-9	3.1e-8
High permeability slip surfaces	2.0e-6	5.6e+0	7.0e-9	5.6e+0

Table 6.4: Modelled bulk permeabilities (in mD) summarized for the Corral Canyon exposure of the Moab fault. The DAFM models use very low permeability values measured using GRI degassibility for shales, silts, gouges and cementation and Axial Flow measurements for sandstones. The LAFM models discard the degassibility measurements in favour of typical in situ shale and silt permeabilities from the literature. The difference between the two sets is discussed in section section 6.2.4.

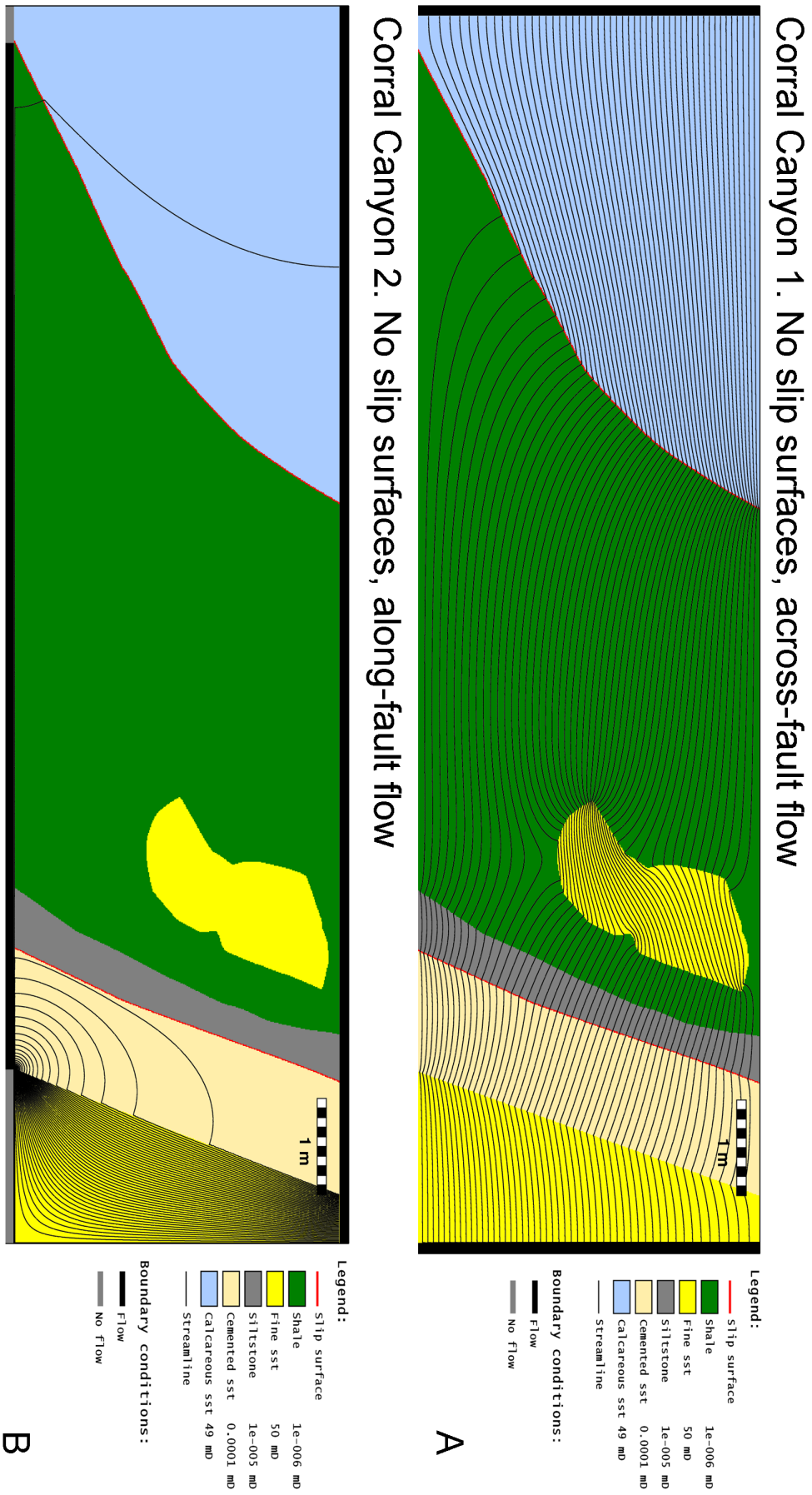

Figure 6.17: Moab fault exposure Corral Canyon. Modelled scenario assuming slip surfaces have no effect on flow. A: Across-fault flow. B: Along-fault flow.

As a consequence of the relatively simple architecture at this site, the modelled fluid flow is fairly straightforward (fig 6.17). Across-fault flow is almost homogeneous, flow rates are higher near the top since the shale smear is thinner there. The sandstone lens inside the smear has higher flow rates than the surrounding shale. Additional modelling shows that the presence of the sandstone lens increases the bulk permeability by 15% compared to a similar model without such a lens.

The modelling shows that for this outcrop the key flow control for across-fault flow, is formed by the continuity and thickness of the shale smear. The cementation observed here can further reduce the across-fault permeability but for this exposure the cemented sandstone is a lot thinner than the shale smear.

For along fault flow the fault core provides very few pathways. The shale smear, the silt and the cementation are all very low permeability. Fluid flow will primarily occur in the damage zone fracture network and sandstone protolith. The occurrence of open slip surfaces is the only way to localize high flow rates in the fault core itself. In the model fluid is injected into the low permeability fault core. From the injection point it follows the shortest path to the high permeability damage zone and host rock. As a consequence all modelled fluid travels through at least some low permeability shale and or cemented sandstone, resulting in a low bulk permeability value (1.5×10^{-4} mD, table 6.4). In the scenario with open slip surfaces, these provide an alternative high permeability pathway, giving a higher bulk permeability (5.6 mD, table 6.4). If fluids are travelling exclusively through the damage zone or the sandstone protolith, the bulk permeability will be much higher.

The observed geochemical alteration is formed by the calcite cementation on the footwall side. Unfortunately this does not provide an unambiguous answer to the question whether along-fault flow is concentrated in the damage zone or in open slip surfaces. As such it is clear that fluids have flowed along the Moab fault at this exposure, but it is impossible to assign a single key flow control for along-fault flow.

The relative simplicity of the fault architecture at outcrop scale of this fault limits the role of small scale heterogeneity in the model. As discussed in section 3.1.2.5, the architecture of this part of the fault is fairly constant, but the thickness of the shale smear is quite variable along strike (figure 6.18).

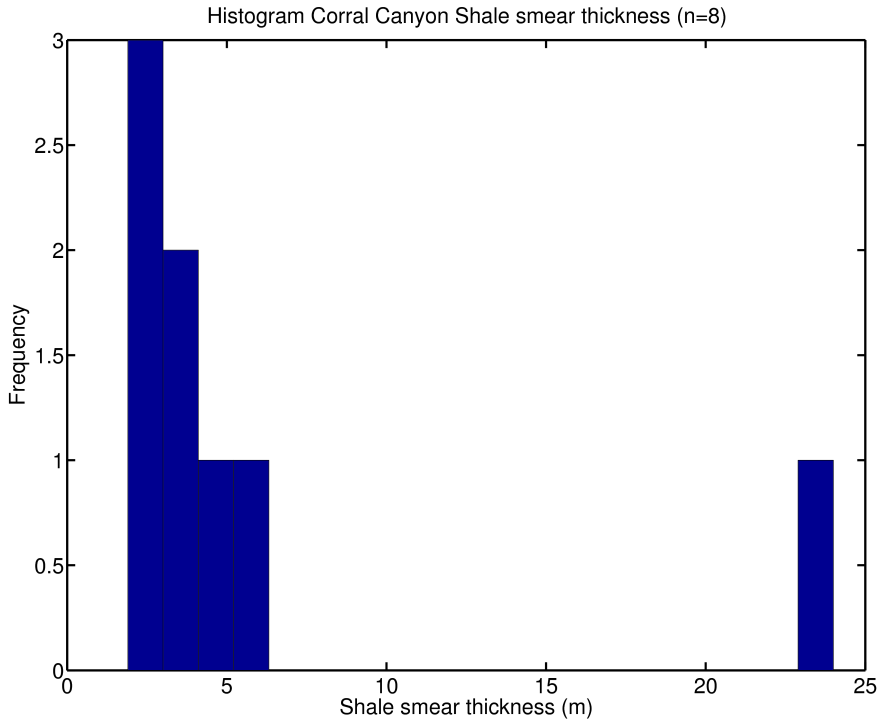

Figure 6.18: Moab fault exposure Corral Canyon. Histogram of shale smear thickness measured along a 1.3 km long transect.

To show the effect of this thickness variation, the bulk permeability is not useful, as this does not depend on the thickness of the shale smear. Instead the fault hydraulic resistance (effective thickness x bulk permeability) is a more appropriate measure for the effect on flow. As this is linearly related to the thickness and the bulk permeability will be roughly constant, the distribution of the fault hydraulic resistance will closely resemble the distribution of the shale thickness.

6.4.4 Moab fault Arches Entrance

At this location, displacement of the Moab fault is partitioned into two separate strands with 250 m and 460 m of offset respectively (Foxford et al., 1998). Here the western strand (460m offset) has been mapped and modelled. This fault is dominated by a thick carbonate lens and a complex zone of sand, silt and shale lenses, cut by several slip surfaces.

For across-fault flow the streamline maps show that flow rates are highest where the combined thickness of the low permeability units (limestone, siltstone, gouge, cemented sandstone) is least. As such the key flow control for across-fault flow are the discontinuities in the low permeability units. The slip surfaces are all parallel to the fault and do not link up, which strongly limits their influence, especially since discontinuities in the low permeability units are abundant. For along-fault flow the sandstone lenses in the fault zone show the highest flow rates. If open slip surfaces are included in the model, this further increases the along-fault permeability.

Scenario	Bulk permeability (using LAFM)		Bulk permeability (using DAFM)	
	across-fault	along-fault	across-fault	along-fault
Low permeability slip surfaces	7.0e-3	5.3e+0	7.0e-3	5.3e+0
Slip surfaces have no effect	6.9e-3	5.6e+0	6.9e-3	5.6e+0
High permeability slip surfaces	7.2e-3	3.7e+1	7.2e-3	3.7e+1

Table 6.5: Modelled bulk permeabilities (in mD) summarized for the Arches entrance exposure of the Moab fault. The DAFM models use very low permeability values measured using GRI degassibility for shales, silts, gouges and cementation and Axial Flow measurements for sandstones. The LAFM models discard the degassibility measurements in favour of typical in situ shale and silt permeabilities from the literature. The difference between the two sets is discussed in section 6.2.4.

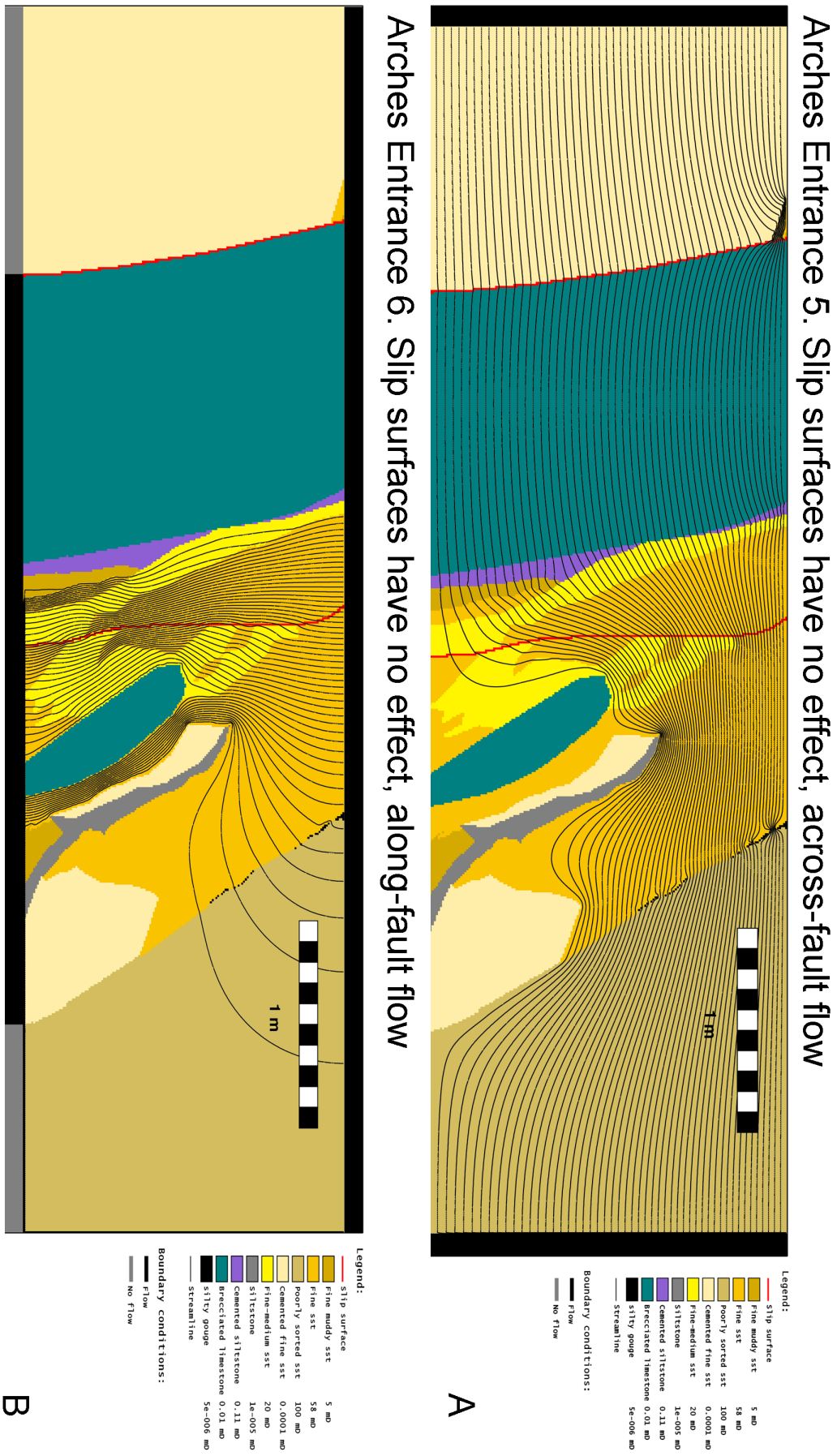

Figure 6.19: Model for the Moab fault Arches National Park Entrance exposure. Modelled scenario assuming slip surfaces have no effect on flow. A: Across-fault flow. B: Along-fault flow.

As discussed in section 3.1.2.4, the map used here differs from the sketch published in Davatzes and Aydin 2005. They interpret the zone NE of the limestone lens to consist of shale with poorly connected sandstone lenses. The Davatzes and Aydin 2005 sketch, contains much more shale and much less sandstone. Models using the Davatzes and Aydin 2005 sketch would yield lower bulk permeabilities. The effect would be most pronounced on the along-fault models, where flow strongly relies on connected sandstone features, which are absent in the Davatzes and Aydin 2005 sketch. For across-fault flow the effect would be smaller as this is dominated by the thick limestone lens which is the same in both interpretations. As discussed in section 3.1.2.4, the map presented in this thesis is the result of careful investigation of all mapped features with a handlens and even tasting if necessary.

6.4.5 Professor Valley

This fault with an offset of 30 m juxtaposes a thin bedded sandstone and silt sequence against a thick siltstone deposit. The juxtaposition against siltstone makes an effective barrier to flow across the fault. Figure 6.20 shows a flow model for flow through the fault zone and the neighbouring host rock. For the calculation of the bulk permeability values (table 6.6), the fault has been isolated from the host rock, so that the permeability represents that of the zone itself and not the combination of fault and juxtaposition.

The fault zone itself consists of sheared silt and sandstone beds, cemented sandstone and a zone of poorly consolidated sand. For this fault the silt and cemented sandstone form the major obstacles to across-fault flow. As a considerable pathway of connected sandstone is available across the fault zone, the fault zone itself does not form a strong barrier.

For along-fault flow the abundance of sandstone provides several pathways. The long lens of poorly consolidated sand forms the most important key flow control. For this outcrop the potential effect of the slip surfaces on bulk permeability is fairly small, as it falls within one to two orders of magnitude. The effect is rather limited as the slip surfaces are located in permeable sandstone, unlike many of the other exposures where slip surfaces breach low permeability barriers, leading to a very pronounced effect.

Scenario	Bulk permeability (using LAFM)		Bulk permeability (using DAFM)	
	across-fault	along-fault	across-fault	along-fault
Low permeability slip surfaces	2.2e-2	1.0e+2	6.9e-5	1.0e+2
Slip surfaces have no effect	2.9e+1	1.2e+2	6.9e-5	1.2e+2
High permeability slip surfaces	3.3e+1	1.9e+2	6.9e-5	1.9e+2

Table 6.6: Modelled bulk permeabilities (in mD) summarized for the Professor Valley fault exposure. The DAFM models use very low permeability values measured using GRI degassibility for shales, silts, gouges and cementation and Axial Flow measurements for sandstones. The LAFM models discard the degassibility measurements in favour of typical in situ shale and silt permeabilities from the literature. The difference between the two sets is discussed in section 6.2.4.

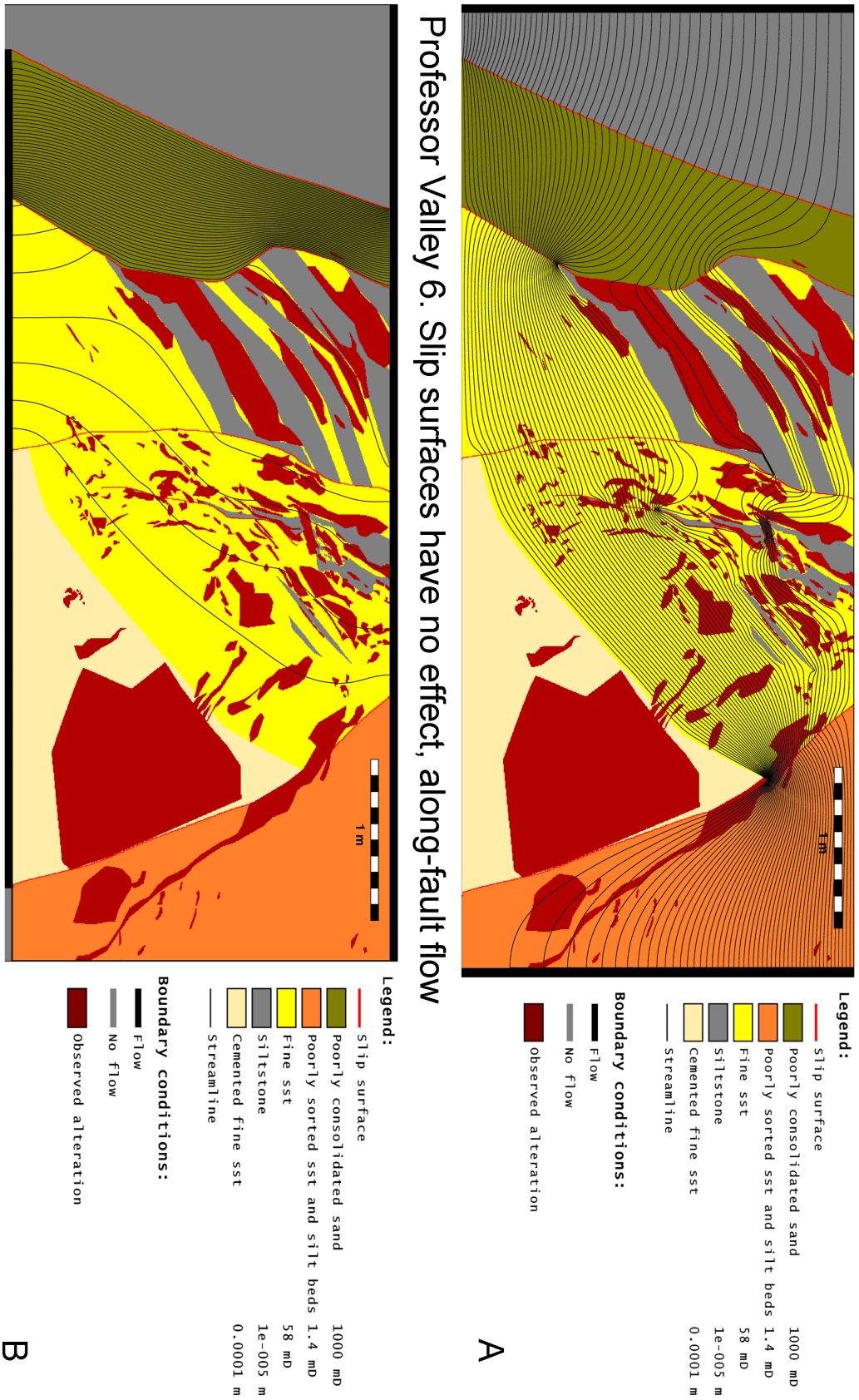

Figure 6.20: Model for the Professor valley fault. Modelled scenario assuming slip surfaces have no effect on flow. A: Across-fault flow. B: Along-fault flow.

6.4.6 Goblin Valley fault 1

At this site a small displacement fault (4m) juxtaposes sandstone against sandstone and displaces a thin shale bed. The shale bed has been smeared along the fault plane, but the thickness of the smear is strongly variable. Another barrier for across-fault flow is formed by a zone of dense cementation and cataclasites. Due to the complicated shape of the outcrop, only a small section could be used for the modelling. The section used is indicated in figure 6.21. Table 6.7 summarizes the modelled bulk permeabilities and figure 6.22 shows one of the models. The modelling confirms that for this outcrop the smear is the main control on across-fault flow. In the model flow rates are highest across the thinnest parts of the smear. The cementation has a more limited effect on fluid flow patterns. Slip surfaces barely affect across-fault flow since no slip surfaces cross the low permeability units.

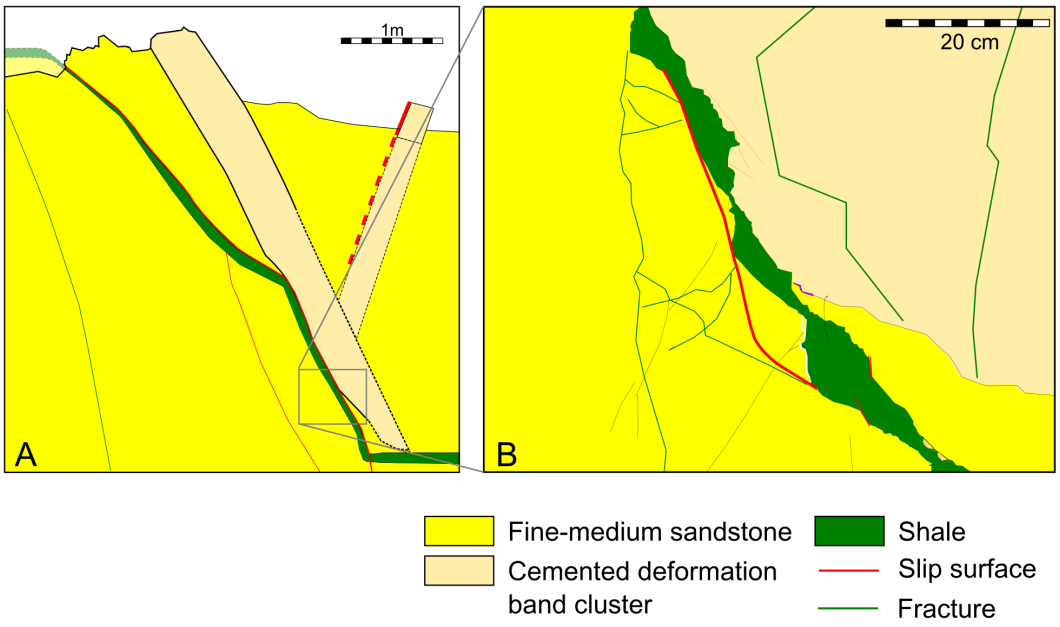

Figure 6.21: Illustration of outcrop Goblin Valley 1 . A: Overview sketch of the (NW flank of) exposure. B: Map of the outcrop used for modelling.

This model studies flow across the shale smear; it is only relevant for a limited stratigraphic interval in between the shale bed in the footwall and the hanging wall. All other flow could bypass the shale smear and flow through the higher permeability sandstone dominated parts of the fault. Slip surfaces might have more influence as they could breach the stratigraphic seal, allowing flow around the smear. In this outcrop that is not the case as the slip surface does not breach the top bed.

For along-fault flow the model shows that the damage zone is the most important here, no continuous sandstone lenses or slip surfaces are present inside the fault zone. As such almost all the flow circumvents the fault core and is deflected into the damage zone.

Scenario	Bulk permeability (using LAFM)		Bulk permeability (using DAFM)	
	across-fault	along-fault	across-fault	along-fault
Low permeability slip surfaces	1.3e-5	8.1e-4	7.3e-8	5.3e-1
Slip surfaces have no effect	1.3e-5	8.1e-4	7.3e-8	5.3e-1
High permeability slip surfaces	1.3e-5	8.1e-4	7.3e-8	5.3e-1

Table 6.7: Modelled bulk permeabilities (in mD) summarized for the Goblin Valley fault 1 exposure. The DAFM models use very low permeability values measured using GRI degassibility for shales, silts, gouges and cementation and Axial Flow measurements for sandstones. The LAFM models discard the degassibility measurements in favour of typical in situ shale and silt permeabilities from the literature. The difference between the two sets is discussed in section 6.2.4.

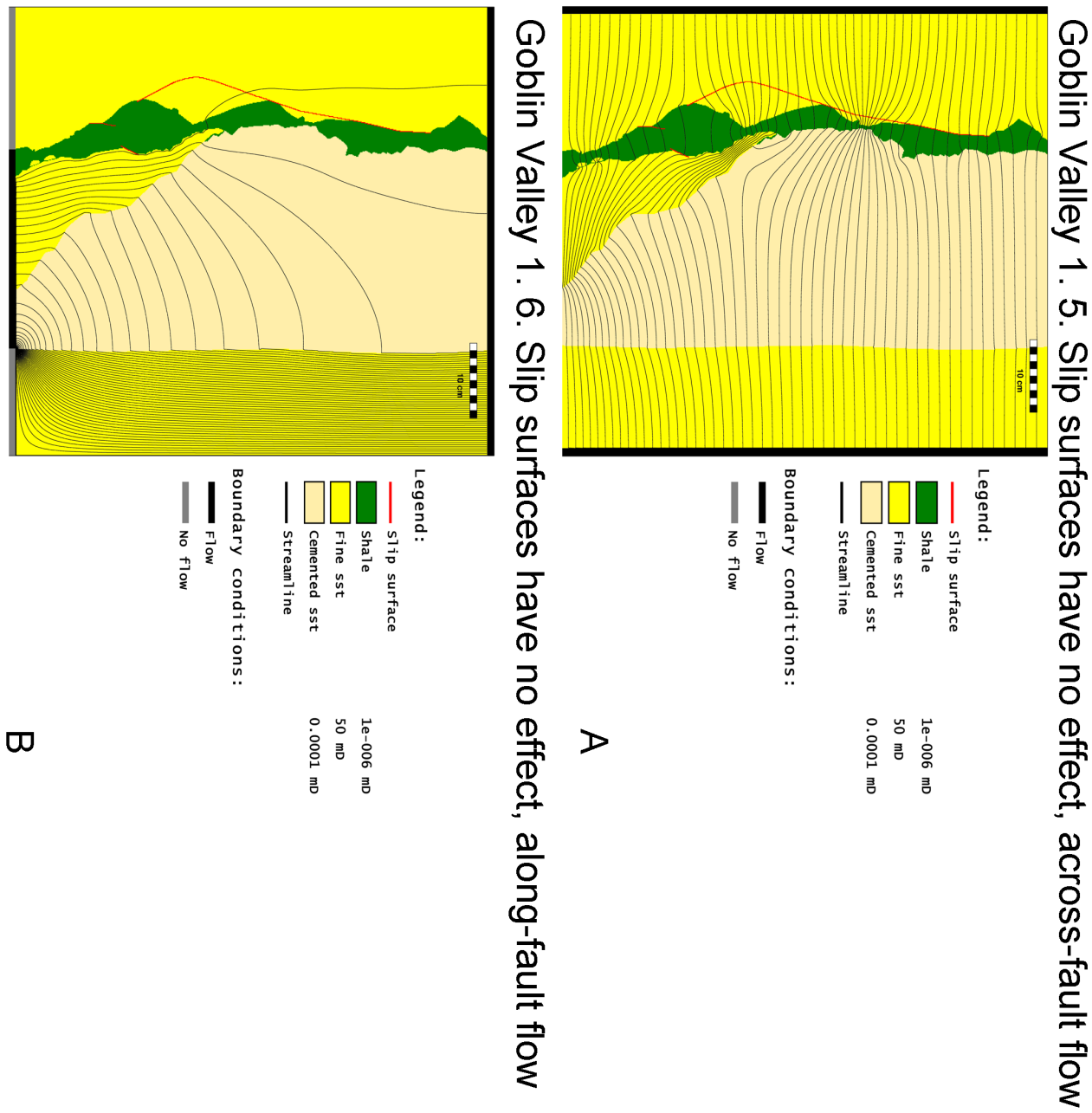

Figure 6.22: Model for Goblin Valley fault 1. Modelled scenario assuming slip surfaces have no effect on flow. A: Across-fault flow. B: Along-fault flow.

6.4.7 Goblin Valley Fault 2

This fault forms an interesting contrast to Goblin Valley Fault 1 It has a similar offset (4m) and displaces a comparable amount of silt and shale, however the architecture is quite different because the silt and shale has not been smeared in this fault. In addition deformation bands are a prominent feature in this fault zone so they have been included in the flow simulations. The main low permeability features in this fault are a deformation band cluster and a zone of cemented sandstone adjacent to the slip surface. In the footwall a shale beds forms another constraint on flow in the model. Figure 6.23 present the resulting model and table 6.8 lists the

modelled bulk permeabilities.

The modelling shows that for across-fault flow the cemented sandstone lenses form the main barrier; where these cemented lenses are absent flow rates are highest. For the along-fault flow the highest flow rates are seen in the hanging wall, however this is an artefact of the modelling, which only includes the shale bed in the footwall. The shale bed is not exposed in the hanging wall of the mapped rock face, and as such not included in the model. It can be seen elsewhere in the outcrop. This results in a model with a barrier for along-fault flow in the footwall, but not in the hanging wall. In reality this barrier obviously exists in both hanging wall and footwall and flow will be more balanced between footwall and hanging wall. An additional model has been made which extends the map and includes this shale bed roughly where it would be expected, the fault core itself is simply extended kept similar in structure as it is at the base of the model (figure 6.24). Modelling fluid flow along the fault in this extended model yields upward fluid flow first avoiding the shale bed in the hanging wall by travelling through the footwall. Once the fluid is above the hanging wall shale bed, it traverses across the fault core where the cemented sandstone is thinnest into the hanging wall to bypass the shale bed in the footwall. This last model seems to fit reasonably well with the observed bleaching of the sandstone in the footwall. Although in that case similar bleaching would be expected in the hanging wall where the fluids cross the fault zone. In addition the cementation near the slip surfaces also supports the flow of fluids up dip along the fault. The concentration of this cementation near the slip surfaces rather than over the otherwise permeable sandstone, suggests that the slip surfaces were open to fluid flow.

Scenario	Bulk permeability (using LAFM)		Bulk permeability (using DAFM)	
	across-fault	along-fault	across-fault	along-fault
Low permeability slip surfaces	3.3e-3	3.6e+1	3.1e-3	3.6e+1
Slip surfaces have no effect	2.1e-2	3.6e+1	2.1e-2	3.7e+1
High permeability slip surfaces	2.8e-1	9.1e+1	2.8e-1	9.1e+1

Table 6.8: Modelled bulk permeabilities (in mD) summarized for the Goblin Valley fault 2 exposure. The DAFM models use very low permeability values measured using GRI degassibility for shales, silts, gouges and cementation and Axial Flow measurements for sandstones. The LAFM models discard the degassibility measurements in favour of typical in situ shale and silt permeabilities from the literature. The difference between the two sets is discussed in section 6.2.4.

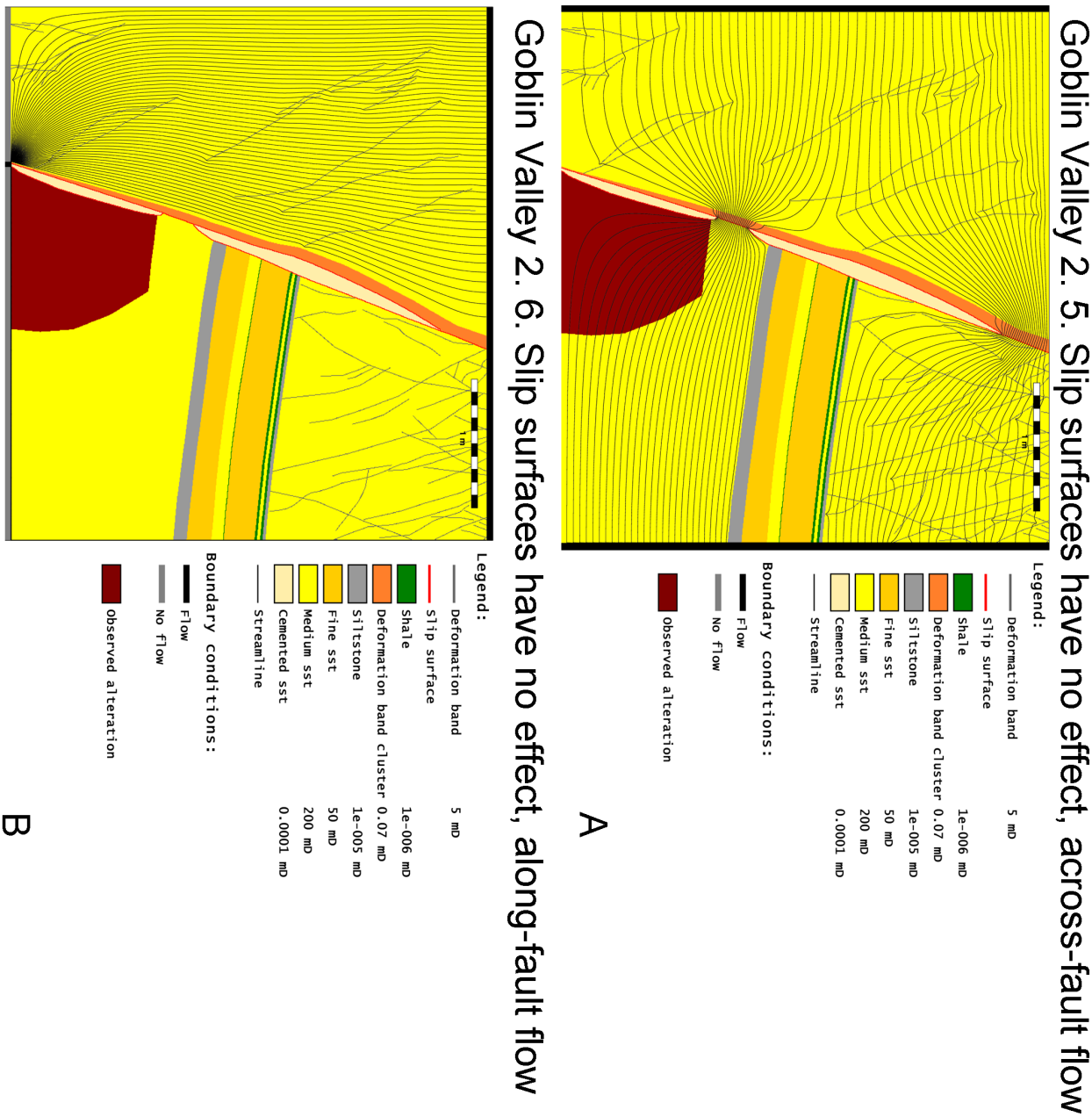

Figure 6.23: Model for Goblin Valley fault 2. Modelled scenario assuming slip surfaces have no effect on flow. A: Across-fault flow. B: Along-fault flow.

Figure 6.24: Extended model for Goblin Valley fault 2 for along-fault flow. The area below the dashed line is inferred. A: Scenario where slip surfaces do not affect fluid flow. B: Scenario where slip surfaces have a high permeability.

6.4.8 Cedar Mountain Thrust

This reverse fault has a vertical offset of 50 m. Its fault core consists of sandstone and siltstone lenses. None of the siltstone lenses are continuous along the fault, resulting in many gaps where footwall sandstone is in direct contact with hangingwall sandstone. Figure 6.25 presents the results and table 6.9 summarizes the modelled bulk permeabilities. The main control on fluid flow is formed by the small silt lenses, or more accurately the many discontinuities between them. The modelling shows that the fluids can easily traverse the fault. For models without slip surfaces, the bulk permeability of the fault approaches that of the sand. Since the slip surfaces are abundant and continuous along the entire exposure, there chosen permeability strongly affects the bulk permeability for the other scenarios. No alteration is observed to further calibrate these models.

Along-fault flow is mostly accommodated by the sandstone in the fault core and damage zone. Inclusion of high permeability slip surfaces can strongly increase the along-fault bulk permeability because the slip surfaces are continuous along the entire fault zone.

Scenario	Bulk permeability (using LAFM)		Bulk permeability (using DAFM)	
	across-fault	along-fault	across-fault	along-fault
Low permeability slip surfaces	3.5e-2	3.9e-3	3.5e-2	2.7e-4
Slip surfaces have no effect	3.0e+1	3.7e+1	3.0e+1	3.7e+1
High permeability slip surfaces	9.1e+1	1.4e+2	9.1e+1	1.4e+2

Table 6.9: Modelled bulk permeabilities (in mD) summarized for the Cedar Mountain Thrust exposure. The DAFM models use very low permeability values measured using GRI degassibility for shales, silts, gouges and cementation and Axial Flow measurements for sandstones. The LAFM models discard the degassibility measurements in favour of typical in situ shale and silt permeabilities from the literature. The difference between the two sets is discussed in section 6.2.4.

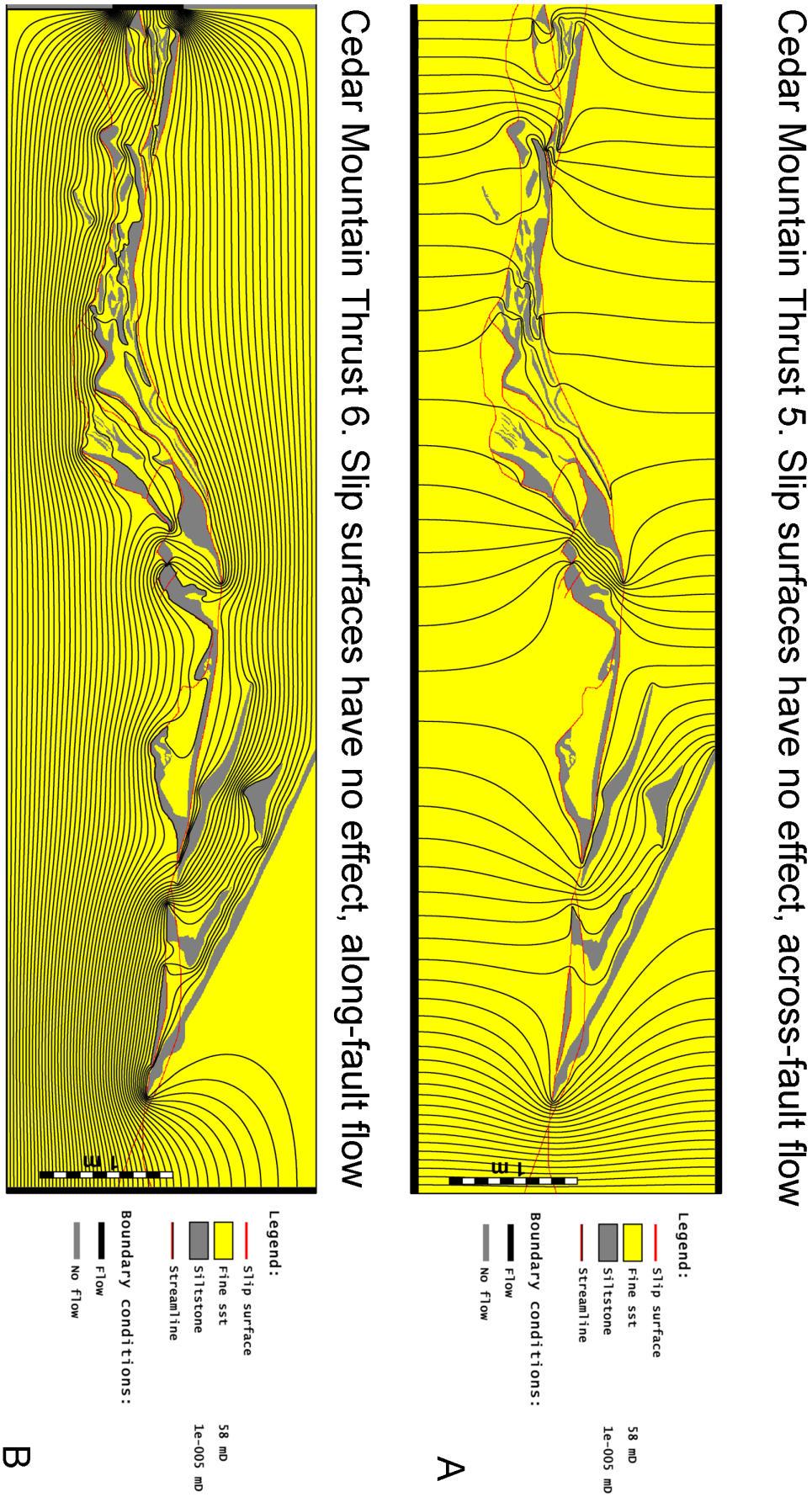

Figure 6.25: Model for Cedar Mountain Thrust. Scenario assuming slip surfaces have no effect on flow. A: Across-fault flow. B: Along-fault flow.

6.4.9 Ketobe Knob

This small reverse fault has a vertical offset of 8 m. Its structure is dominated by a set of roughly parallel slip surfaces with continuous gouges (1-10 cm thick) developed along them. In between the slip surfaces, the rocks have been strongly rotated and sheared. Figure 6.26 shows the resulting model, and table 6.10 summarizes the bulk permeability.

The key flow controls for this fault are formed by the fault gouges along the slip surfaces. This is not immediately obvious from the streamline pattern, because in the model the thickness of slip surfaces is continuous along the full extend of the map. Detailed along-strike variation data on the thickness variation of these gouges could not be measured due to accessibility. As a consequence the modelled flow is likely less heterogeneous than it should be. In between the slip surfaces the tilted siltstone beds compartmentalize flow, adding a further source for flow complexity. For this outcrop, it is clear that the gouge lined slip surfaces act as low permeability barriers. Although it is possible that the slip surfaces have also had a high permeability for flow along them, resulting in a strong anisotropy of the slip surface permeability. No evidence for flow along the slip surfaces has been observed, so only the low slip surface permeability scenario has been modelled. The permeability of these gouges has not been determined experimentally, as due to the thinness and fragile nature of the gouges, it is practically impossible to obtain an intact sample. Instead it is assumed to be in the same order of magnitude as the gouge permeability measured at Moab 191SE.

Scenario	Bulk permeability (using LAFM)		Bulk permeability (using DAFM)	
	across-fault	along-fault	across-fault	along-fault
Low permeability slip surfaces	3.1e-5	1.4e-4	3.9e-8	5.9e-7

Table 6.10: Modelled bulk permeabilities (in mD) summarized for the Ketobe knob exposure. The DAFM models use very low permeability values measured using GRI degassibility for shales, silts, gouges and cementation and Axial Flow measurements for sandstones. The LAFM models discard the degassibility measurements in favour of typical in situ shale and silt permeabilities from the literature. The difference between the two sets is discussed in section 6.2.4.

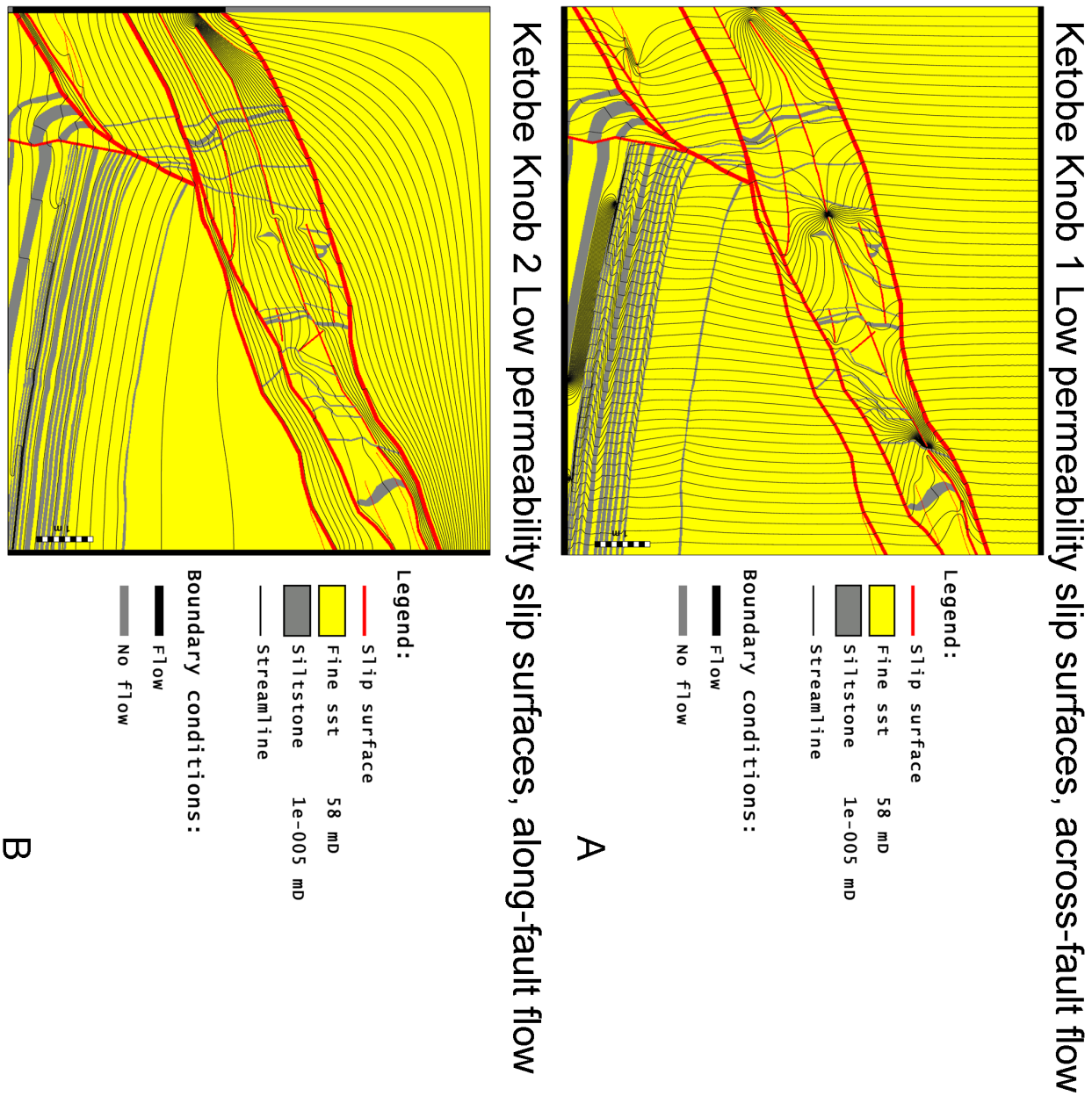

Figure 6.26: Model for Ketobe knob exposure. Scenario assuming slip surfaces have no effect on flow. A: Across-fault flow. B: Along-fault flow.

6.4.10 Summary flow models

The fault outcrops studied in this research typically display complex architectures and strong heterogeneity along both strike and dip. The modelling in this chapter provides insight into how fluids traverse such architectures. All the fault zones studied here consist of materials with strongly contrasting permeability values. Low permeability materials (shale, silt, gouge, cementation, deformation band clusters) form potential barriers to flow. Many outcrops also show high permeability features inside these low permeability barriers, most notably discontinuities in the barrier unit, sandstone lenses and potentially slip surfaces. Evidence from paleo-fluid flow indicators shows that many slip surfaces have had high permeabilities for at least some

duration while the fault was at depth. Where these features form connected pathways across both sides of the fault, they become sites of high fluid flow rates and can strongly increase the bulk permeability of the fault for across fault flow. The along fault flow modelling focuses on flow through the fault core. Several outcrops studied here (Moab 191NW, Moab 191SE, Moab fault Arches entrance, Professor Valley and Ketobe Knob) contain sandstone lenses that can facilitate fluid inside the fault core. In addition open slip surfaces can act as pathways for fluid flow through the fault core. The focus on upwards flow through the core of the fault zone is mostly relevant for bypassing stratigraphic barriers to flow. In other scenarios high permeability host rocks and the damage zone fracture network are more likely candidates for high volumes of fluid flow.

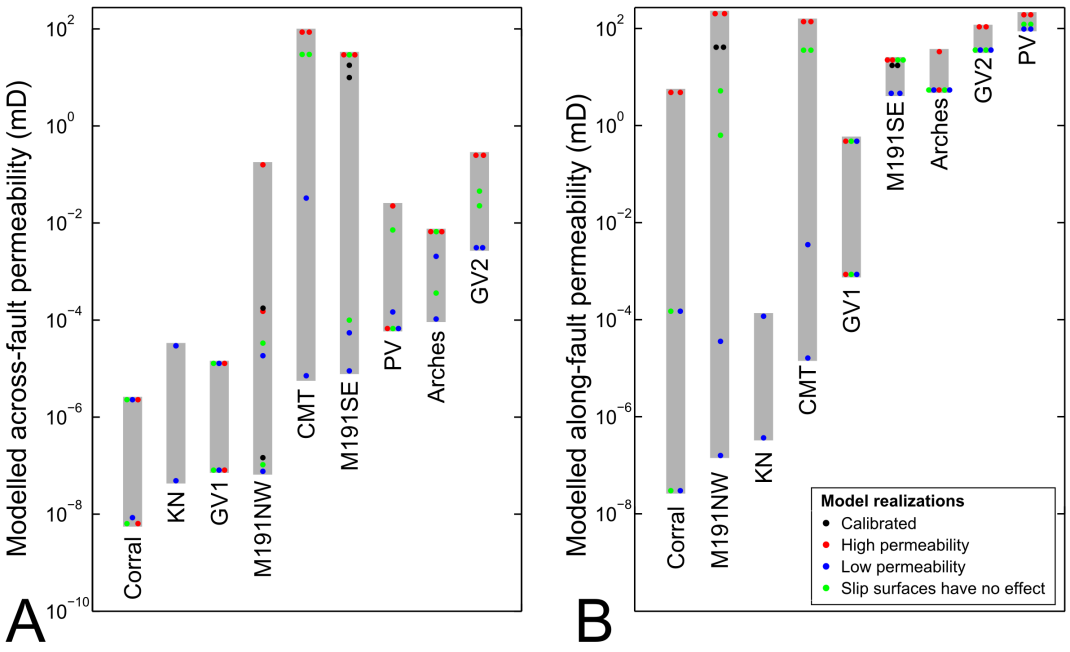

Figure 6.27: Compilation of all modelled bulk permeabilities for all scenarios and both LAFM and DAFM permeability sets. The grey bars denote the rangeof the modelled permeability values, the coloured dots represent the modelled values. The bars are ordered from lowest minimum bulk permeability to highest minimum permeability. A: Across-fault flow. B: Along-fault flow.

A secondary result from the modelling work are estimates of the fault bulk permeabilities. Figure 6.27 shows an overview of all the modelled bulk permeabilities. The grey areas indicate the range of all the modelled scenarios and permeability sets. This illustrates both the uncertainty in subsurface flow conditions and the scope for temporal variability in bulk permeability. The differences between the two permeability scenarios typically cause two to four orders of magnitude in variation for across-fault flow. Mostly because the low permeability lithologies (shale, silt, gouge) are most strongly affected by the different methodologies. Fault zones where open slip surfaces can contribute to a connected pathway across the fault can expect another permeability variation up to four orders of magnitude. Purely looking at the Moab fault, ten orders of magnitude variation can be observed for the lowest value (Corral Canyon low permeability slip surfaces DAFM permeability) and the highest value (Moab 191 SE, high permeability slip surfaces, LAFM permeability). These two outcrops are separated 8.6 km hori-

zontally and 110 m vertically. At these two outcrops, the displacement affects different parts of the stratigraphy, resulting in very different fault architectures. The thick shale smear at Corral canyon has the lowest modelled bulk permeability of all models. At Moab 191SE the gouge is very thin (minimum thickness 5 cm) and the architecture contains many sandstone lenses and slip surfaces, yielding a wide range of variability in the modelled bulk permeabilities for the different scenarios. This work demonstrates that it is very difficult to predict the permeability of a fault zone. The amount of low permeability material (e.g. shale) in the fault core has limited predictive power. The continuity of the low permeability material has a much greater control on the bulk permeability. In addition it is important to consider the presence of open fractures and slip surfaces, as these can strongly affect the permeability of the fault zone. This introduces a strong potential for temporal variation in fault permeability. Fault architecture, geological history and stress conditions form important controls on fault bulk permeability.

6.5 Comparison to SGR-based work-flows

In addition to the insight in how fluids traverse fault zones, the models provide another interesting form of information, the modelled flow can be used to calculate the upscaled bulk permeability. As discussed in the introduction, there are several limitations to this calculation: the models are 2D, permeabilities are measured at the surface, fault permeability at depth is likely to change over time and be stress-dependent. Despite the shortcomings discussed in the introduction, the work-flow presented here yields a dataset relevant to hydrocarbon industry workflows. It combines the real structure of seismic scale faults with permeability measurements of real seismic scale faults. Existing work-flows focus on simplified geometries and permeabilities of sub-seismic faults. This data is mostly relevant to hydrocarbon production scenarios and as such should be compared to existing industry work flows for implementing faults into reservoir models.

6.5.1 Bulk permeability and SGR

Figure 6.28 shows cross-plots of the modelled bulk permeability values and the shale gouge ratio values (section 5.2). Separate plots have been made for across-fault flow and along-fault flow and the two sets of sample permeabilities used as input. Typically SGR is not assumed to be a useful predictor of along-fault permeability, but a few studies have attempted to use it that way (e.g. Rudolph et al., 2010), so it is included here for comparison purposes. The different slip surface permeability scenarios modelled are included to provide a range of the possible fault permeabilities, depending on geological evolution and the stress state. Colour coding is used to differentiate between the different models.

From the plots it becomes apparent that the modelled bulk permeabilities span a large range (8-10 orders of magnitude). None of the four graphs suggests a simple relationship between these modelled faults and the shale gouge ratio. This seems counter-intuitive because at least a basic relationship between shale gouge ratio and bulk fault permeability would seem likely; faults developing in more shale rich host rocks are more likely to incorporate low permeability shale into their fault rocks. In addition several studies have successfully used SGR to estimate fault permeability in faulted hydrocarbon reservoirs and achieve a good history match (Manzocchi et al., 1999, Yielding 2002, Sperrevik 2002, Harris and Yielding 2002). As such the lack of

correlation between SGR and bulk permeability here needs a thorough explanation.

First of all it is likely that besides shale content, several other variables can affect the bulk permeability, e.g. displacement, burial depth, fault architecture, cementation, other lithologies than sand and shale. Another possible problem is the extent of the fault maps; only a few meters along each fault are mapped. As such heterogeneity of the fault zone has to be considered; the bulk permeability of an outcrop scale model could very well deviate from the bulk permeability of the same fault on a reservoir model scale. As discussed previously the mapping and modelling is performed in two dimensions. In three dimensions there are possibly more connected pathways across low permeability barriers, potentially increasing the bulk permeability.

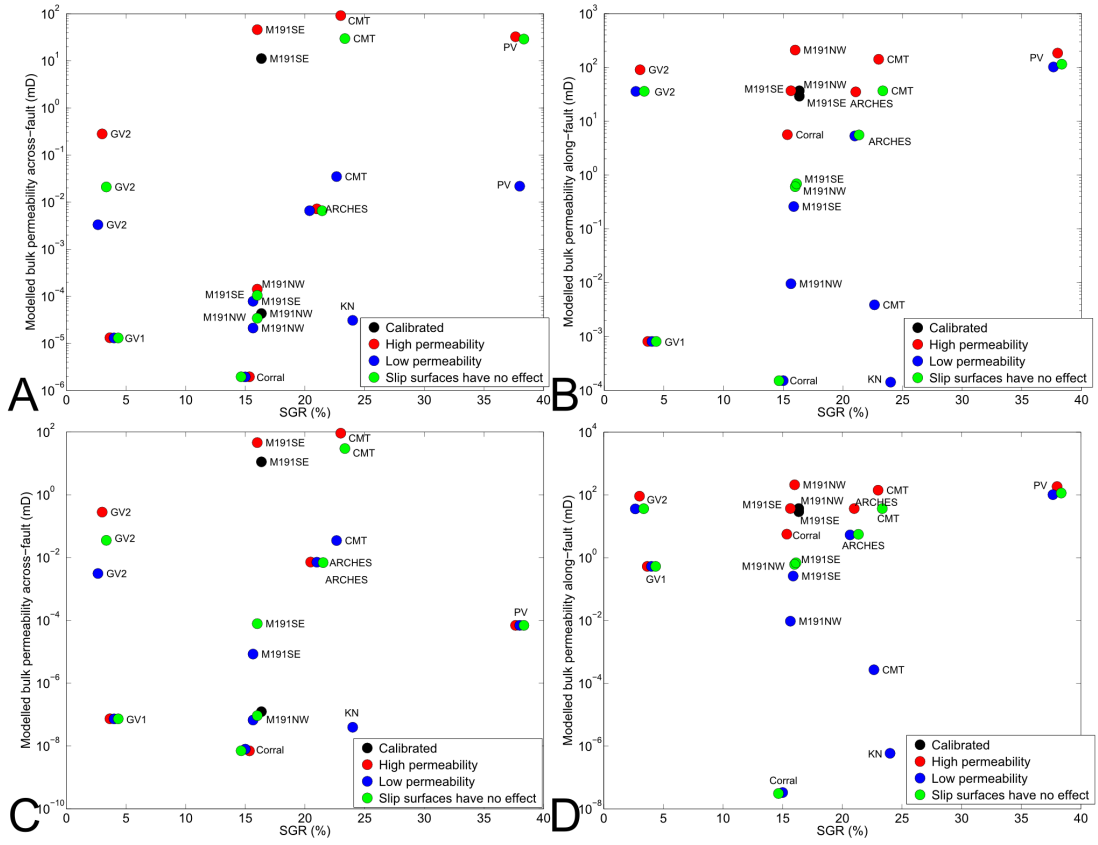

Figure 6.28: Cross-plots of modelled bulk permeability vs SGR. A: Across-fault permeabilities modelled using LAFM permeability sets. B: Along-fault permeabilities modelled using LAFM permeability sets. C: Across-fault permeabilities modelled using DAFM permeability sets. D: Along-fault permeabilities modelled using DAFM permeability sets. The difference between the two sets of permeability values are explained in section 6.2.4. Where necessary data-points for each fault have been moved apart slightly in the x-direction, this is done for visibility.

The current data set clearly demonstrates that SGR is not the only controlling parameter on bulk permeability. This does not rule out that host rock shale content is an (important) control, but if it is, it is so together with other parameters, such as burial depth, displacement, reactivation, host rock consolidation state, porosity, bedding thickness, fluid flow through the fault zone, pressure and temperature history. The following sections explore industry workflows which combine SGR other parameters thought to control fault permeability and thickness and as such could be expected to better explain the variation in bulk permeability.

6.5.2 Bulk permeability and SGR permeability estimates using Manzocchi et al., 1999

Figure 6.29 show cross-plots of the modelled permeability against the fault permeability predicted by the Manzocchi et al., 1999 algorithm (section 5.2.2). Both along and across-fault permeability plots are included here, however the Manzocchi et al., 1999 algorithm is not designed for along-fault flow. This algorithm relates fault permeability to both the volumetric shale fraction of the fault zone and fault displacement. Including both SGR and fault displacement might improve the correlation between fault permeability estimates and the modelled bulk permeabilities. However the plots do not show a clear relationship between the two fault permeabilities. The same factors responsible for the poor correlation with SGR alone are likely to be part of the explanation for the poor correlation here.

In addition the Manzocchi et al., 1999 work-flow assumes the volumetric shale content of the fault zone to be equal to SGR. This appears not to be true for the faults studied here as discussed in section section 4.2 and section 4.3. Such a relationship would make sense for fault cores in which sand and shale from the wall rock is incorporated in equal measure and mixed homogeneously. As shown in the chapter 3, no such architecture has been observed on any of these faults.

The comparison here focuses exclusively on the fault permeability algorithm of Manzocchi et al., 1999, whereas their transmissibility multipliers approach also uses an estimate of fault thickness. The combined effect of fault thickness and permeability is further explored in section 6.5.5, to allow for a more reallistic comparrison.

Besides the poor correlation there is a strong difference in the range of variation of both data sets. The modelled bulk permeabilities span eight to ten orders of magnitude, even in the scenarios where slip surfaces have no effect, whereas the Manzocchi permeabilities are limited to two orders of magnitude. A first explanation is that the Manzocchi et al., 1999 SGR to permeability algorithm only estimates a limited range of permeabilities for the SGR values in this study; in the SGR 0 to 40% range the Manzocchi algorithm suggests a permeability drop spanning only two orders of magnitude. This is in strong contrast with both the modelled bulk permeabilities in this study (chapter 6).

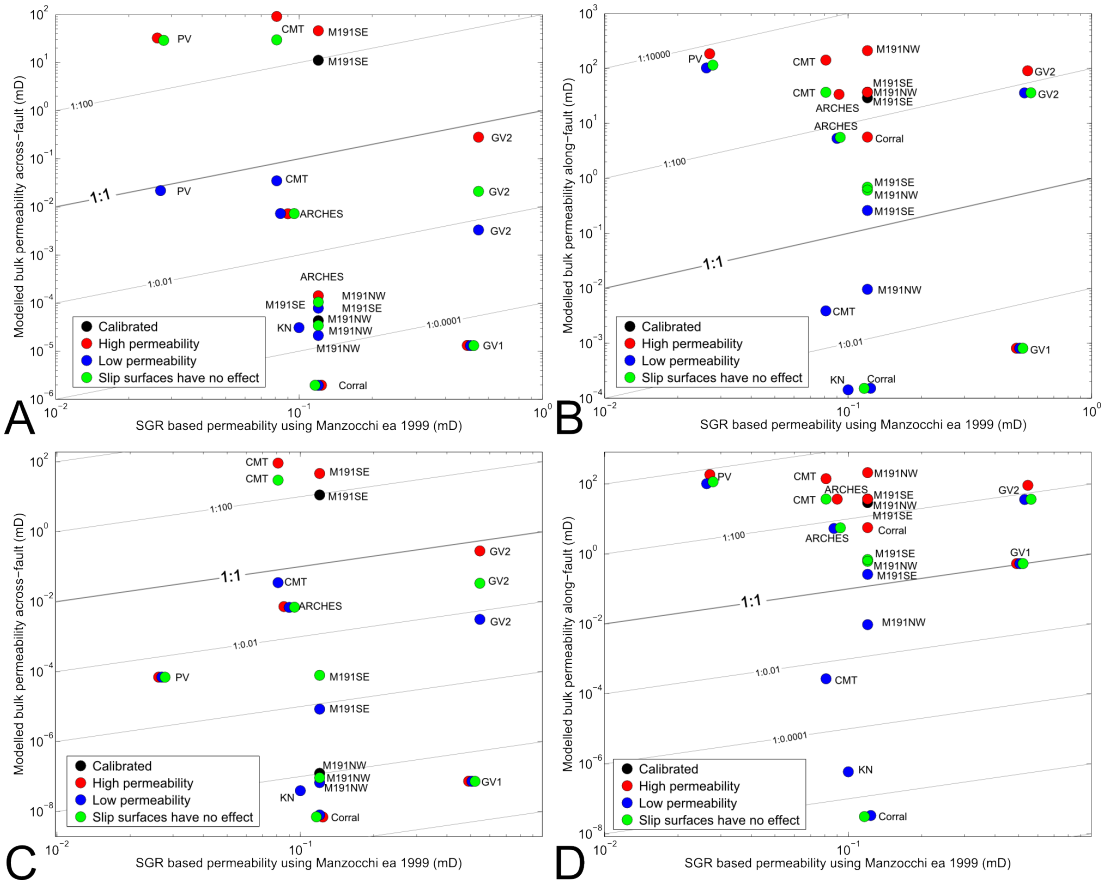

Figure 6.29: Cross-plots of modelled bulk permeability vs fault core permeability predicted using the algorithm from Manzocchi et al., 1999. A: Across-fault permeabilities modelled using LAFM permeability sets. B: Along-fault permeabilities modelled using LAFM permeability sets. C: Across-fault permeabilities modelled using DAFM permeability sets. D: Along-fault permeabilities modelled using DAFM permeability sets. The difference between the two sets of permeability values are explained in section 6.2.4. Where necessary data-points for each fault have been moved apart slightly in the x-direction, this is done for visibility.

6.5.3 Bulk permeability and SGR permeability estimates using Sperrevik et al., 2002

Cross-plots of the modelled bulk permeability and permeabilities predicted using the algorithm from Sperrevik et al., 2002 (section 5.2.3) are shown in figure 6.30. Both across and along-fault permeability plots are provided with the caveat that the Sperrevik et al., 2002 approach does not aim to model along-fault flow, it is included purely for comparison purposes. For this algorithm the volumetric shale fraction, depth during faulting and maximum burial depth are used to estimate fault permeability. Again no relationship is apparent from the cross plots. With seven orders of magnitude, the variation in permeability predicted by the Sperrevik algorithm, is almost as wide as the range of the modelled permeabilities. The Sperrevik permeabilities are mostly higher than the modelled bulk permeabilities. This is interesting as in their own study Sperrevik et al., report that when applied to an existing reservoir flow simulation model, their transmissibility multipliers are one to two orders higher than needed to obtain a good history match. Sperrevik et al., suggest that the difference could be explained by relative permeability

rather than single phase flow.

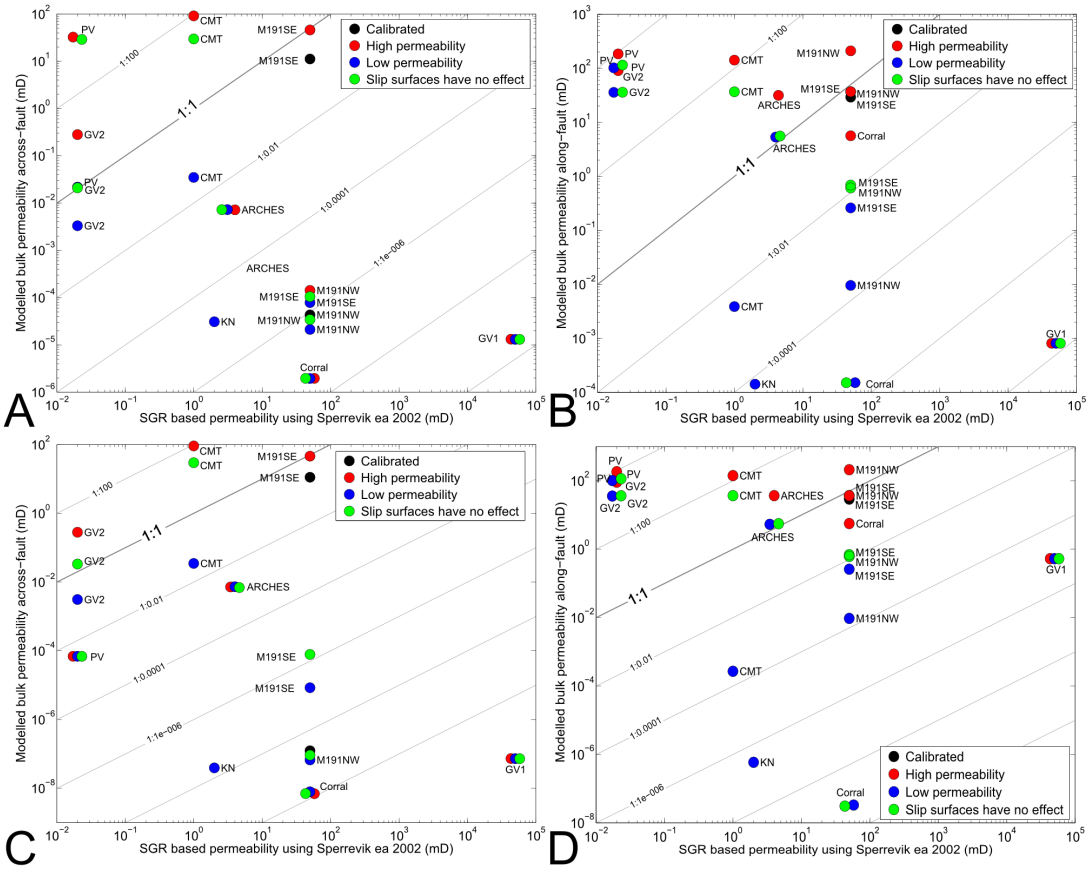

Figure 6.30: Cross-plots of modelled bulk permeability vs fault core permeability predicted using the algorithm from Sperrevik et al., 2002. A: Across-fault permeabilities modelled using LAFM permeability sets. B: Along-fault permeabilities modelled using LAFM permeability sets. C: Across-fault permeabilities modelled using DAFM permeability sets. D: Along-fault permeabilities modelled using DAFM permeability sets. The difference between the two sets of permeability values are explained in section 6.2.4. Where necessary data-points for each fault have been moved apart slightly in the x-direction, this is done for visibility.

6.5.4 Bulk permeability SGR permeability estimates using Revil and Cathles 1999

Cross-plots of the modelled bulk permeabilities and the SGR-based estimates calculated using the simplified relationship based on Revil and Cathles 1999 (section 5.2.4) are shown in figure 6.31. Again these figures do not show a simple relationship between the modelled and the predicted bulk permeability. The ranges of variation of both data sets are the same. This is a logical effect of the use of the same permeability extremes (up to$1x10^{2}$ for sandstones and $1x10^{-6}$ for shales and gouges in the LAFM models and 10e-9 in the DAFM models). Despite the similar ranges, the modelled data-points are typically far removed from the line where the estimates and modelled values are equal. The reasons for this will be discussed further in the conclusion section.

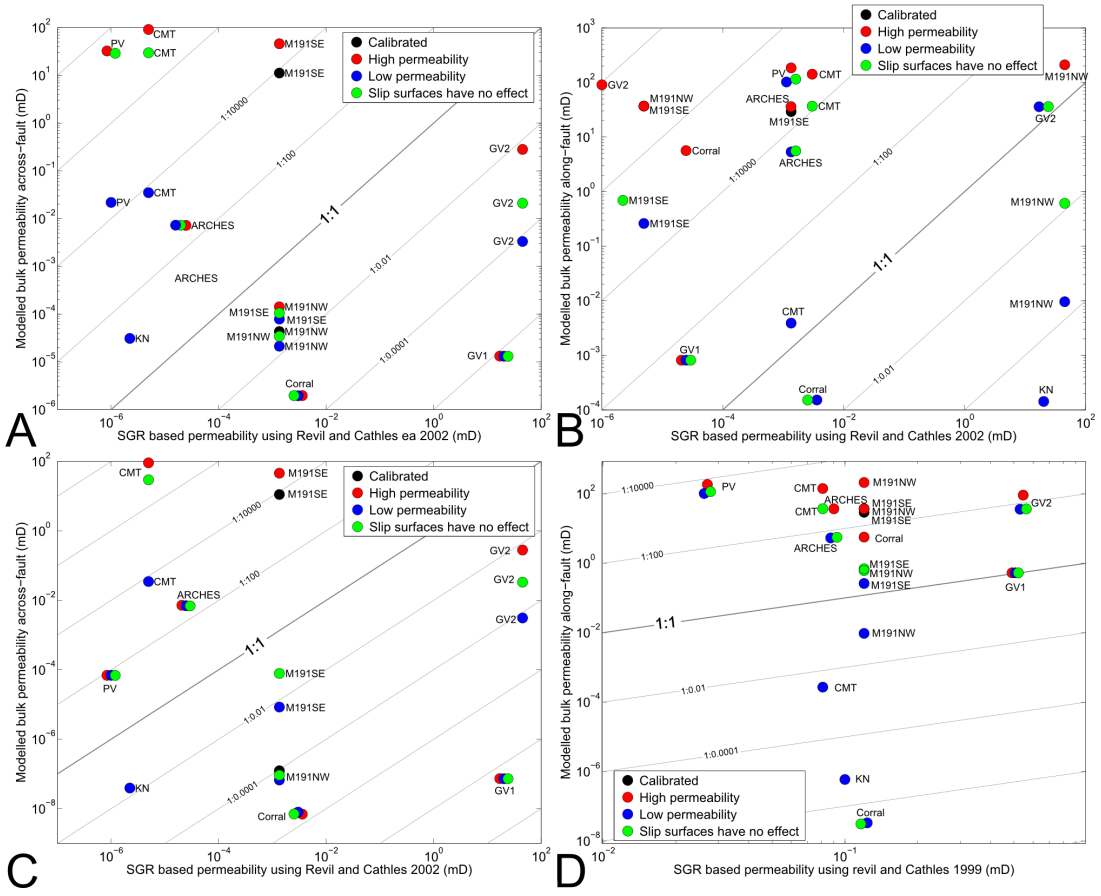

Figure 6.31: Cross-plots of modelled bulk permeability vs fault core permeability predicted using the algorithm based on Revil and Cathles. A: Across-fault permeabilities modelled using LAFM permeability sets. B: Along-fault permeabilities modelled using LAFM permeability sets. C: Across-fault permeabilities modelled using DAFM permeability sets. D: Along-fault permeabilities modelled using DAFM permeability sets. The difference between the two sets of permeability values are explained in section 6.2.4. Where necessary data-points for each fault have been moved apart slightly in the x-direction, this is done for visibility.

6.5.5 Fault hydraulic resistance

In the previous sections modelled fault bulk permeabilities have been compared to SGR-based predictions of permeability. For the actual effect on subsurface fluid flow the length of the pathway across the fault needs to be considered as well. As discussed in the chapter on architecture, there are several problems with defining fault thickness. Still despite the oversimplification it is useful to include fault thickness into the comparison. In the work-flows of Manzocchi et al., 1999 and Sperrevik 2002, fault permeability is combined with an estimate of fault thickness into fault transmissibility multipliers. Since the value of fault transmissibility multipliers also depends on the geometry and permeability of the model grid, they are not practical for comparison purposes. Instead a simpler measure is introduced here, fault hydraulic resistance, similar to fault resistance in Bense, 2004.

Fault hydraulic resistance:

$$Rf = Tf/kf \tag{6.4}$$

Rf fault hydraulic resistance
Tf thickness of the fault zone
kf permeability of the fault zone

The fault resistance is calculated for the same work-flows discussed above. From each work-flow both the permeability and thickness estimation routines are used. For the modelled bulk permeability, the average thickness measured on the maps is used. The Revil and Cathles 1999 based approach does not have a fault thickness algorithm, so here the Manzocchi et al., 1999 relationship is used.

Figure 6.32 shows the fault thicknesses as predicted by these two algorithms plotted against the measured thicknesses. Considering the strong heterogeneity of fault zone, it is no surprise that the predictions and measurements do not show a one to one correlation. The figure shows that the estimates deviate from this ideal by upto 1.5 orders of magnitude. Generally the Sperrevik algorithm tends to produce overestimates for large displacements (100 – 1000s of meters), where as the Manzocchi algorithm tends to produce strong under estimates at smaller displacements. Together these observations suggest that fault thickness is not linearly related to displacement. Faulkner et al., 2010 report a similar observation for damage zones, they show that the growth of macrofracture damage zones decreases after fault displacement exceeds approximately 100 m.

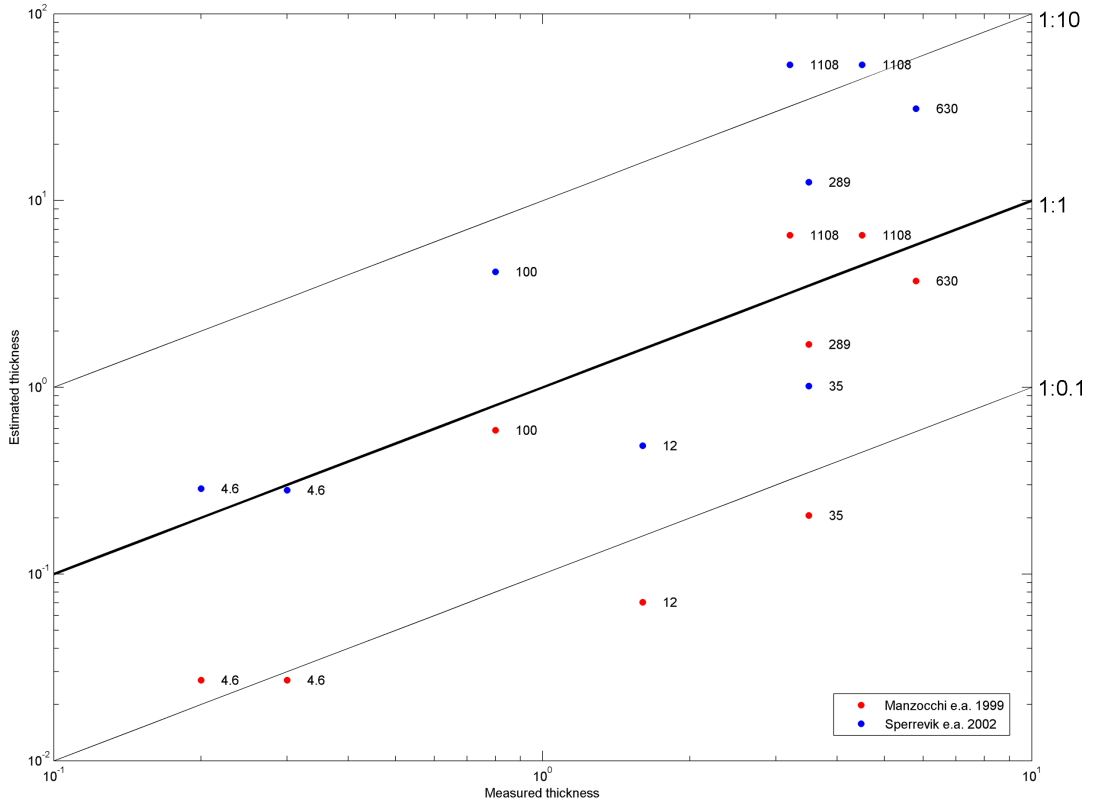

Figure 6.32: Fault thickness predictions plotted against measured thicknesses. Red points are estimated using the algorithm from Manzocchi et al., 1999, blue points are estimated using the algorithm from Sperrevik et al., 2002. The numbers give fault displacement at each site.

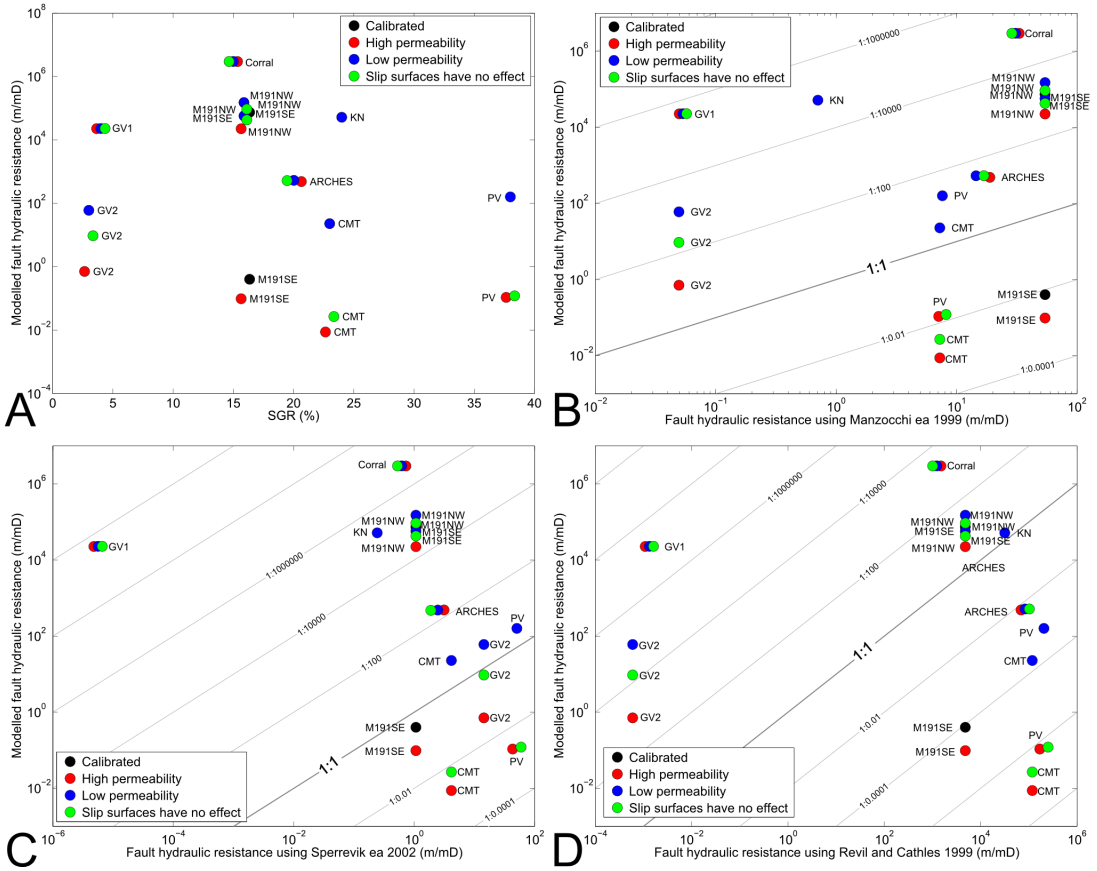

Figure 6.33: Fault hydraulic resistance (FHR) cross-plots using LAFM permeability data for across-fault flow. A: model based FHR vs SGR. B: model based FHR vs Manzocchi ea 1999 based FHR. C: model based FHR vs Sperrevik ea 2002 based FHR. D: model based FHR vs Revil and Cathles 1999 based FHR. Where necessary data-points for each fault have been moved apart slightly in the x-direction, this is done for visibility.

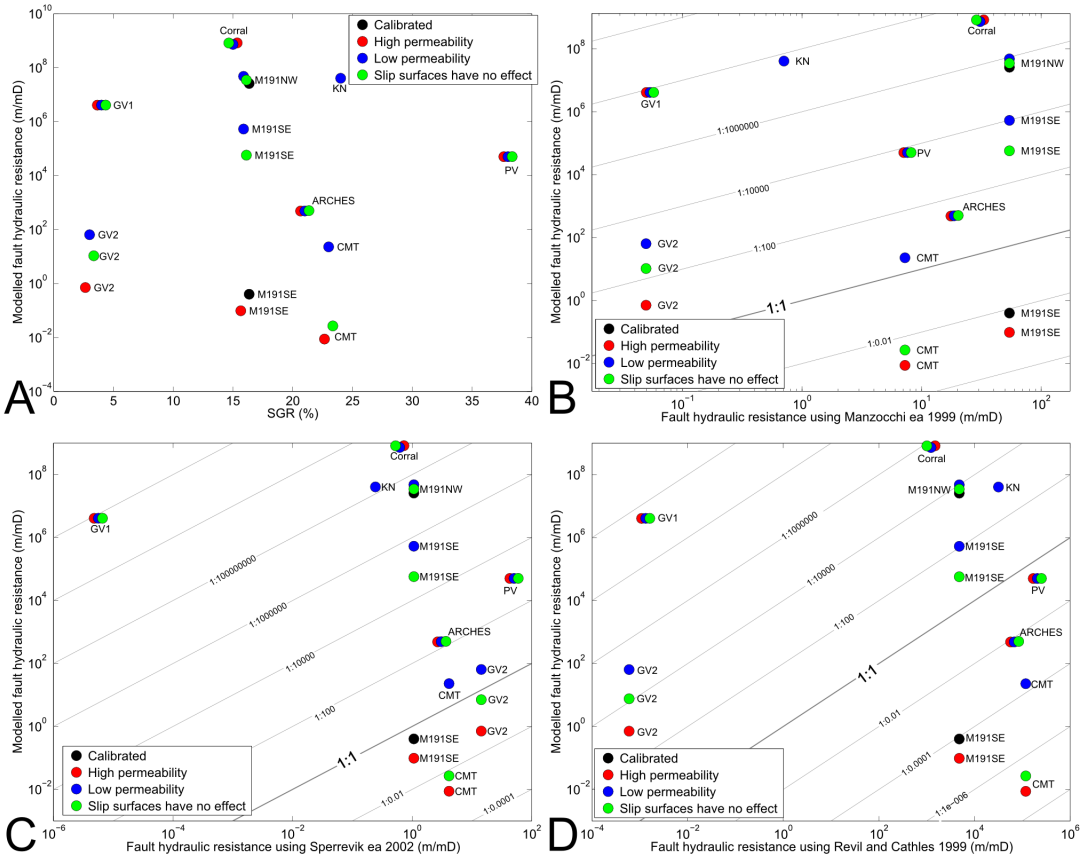

Figure 6.34: Fault hydraulic resistance (FHR) cross-plots using DAFM permeability data for across-fault flow. A: model based FHR vs SGR. B: model based FHR vs Manzocchi ea 1999 based FHR. C: model based FHR vs Sperrevik ea 2002 based FHR. D: model based FHR vs Revil and Cathles 1999 based FHR. Where necessary data-points for each fault have been moved apart slightly in the x-direction, this is done for visibility.

Figure 6.33a shows a cross plot of the model based resistance of the modelled faults against SGR for across-fault flow using the LAFM permeability data. This plot was made to evaluate a basic relationship between SGR and modelled fault hydraulic resistance. It shows a very wide range of resistances and no clear relationship with SGR.

Figures 6.33b through 6.33d show cross-plots of modelled fault hydraulic resistance vs. SGR-based fault hydraulic resistance predictions using respectively the Manzocchi et al., 1999, Sperrevik et al., 2002 and Revil and Cathles 1999 based approaches. As such these plots compare the modelled and predicted magnitude of the fault's ability to baffle fluid flow. None of the three plots reveals a clear relationship between the modelled and the predicted resistance. The difference between the two values can span upto 12 orders of magnitude. Some of the scatter is caused by the inclusion of the different scenarios in a single figure, but except for the 191SE outcrop of the Moab fault this variance is much smaller than the variance between the different exposures.

6.5.6 Conclusions

This chapter presents a basic workflow for 2D modelling of fluid flow through detailed maps of faulted outcrops. The modelling method developed here allows for rapid development of fluid

flow models from field data. Digitized maps of outcrops form the basis of the model. Any image can be used as long as the colour value of each pixel can be meaningfully assigned a permeability value. Currently the method does require the geologist to perform a quality check and have a basic understanding of fluid flow modelling. Large parts of the current workflow are implemented in code, allowing for further automation. As geologists often gather large amounts of data in a graphical format (maps, cross sections, sketches), automated workflows to further analyze these data have great potential.

In this chapter the flow modelling has been used to analyse how fluids could flow through fault zones, using the outcrops mapped for this study. Wherever possible the observed geochemical alteration has been used to compare the models with past fluid flow through the fault zone. The models provide insight in how fluids traverse fault zones. For across-fault flow, all the faults have low permeability material in the core, formed by shale and silt smears, fault gouge, cementation, dense deformation band clusters or a combination of these. If these low permeability features are continuous along the entire length of the outcrop, they can strongly baffle fluid flow across the fault. In addition to holes in the low permeability barriers, pathways across the barriers can be formed by connected high permeability features such as sandstone lenses and open slip surfaces. Such features experience high flow rates in the model, and often show signs of geochemical alteration in the outcrop.

The observed fault architectures do not show mixing of sand, shale and silt, instead the majority of fault core components consist of discrete sandstone, shale or silt. This is reflected in the modelling, fluid flow rates are determined predominantly by fault architecture. The amount of shale is less important than the distribution of shale in the fault zone. In addition other materials such as silt and coal can form barriers to flow. Other processes such as cementation and the formation of condensed deformation band clusters can strongly reduce fault permeability. As a consequence the modelled bulk permeabilities do not correlate with mixing algorithms such as SGR, or permeabilities estimated using SGR.

For along-fault flow the models show high flow rates in the damage zone as well as in connected high permeability features (e.g. sandstone lenses and open slip surfaces) in the fault core itself if these are present. The geochemical alteration observed at many outcrops support the past occurrence of high flow rates through connected high permeability features in the fault core, suggesting that these are important for flow through fault zones. One place where this is likely important is where faults intersect low permeability stratigraphic units such as top seals over hydrocarbon deposits.

Chapter 7

Synthetic fault zones

For the faults studied in the Sinai statistics have been gathered for the key flow controls instead of the detailed maps as made for faults in Utah. These sites are characterized by good along strike exposures and relatively simple fault architectures. The collected statistics consist of closely spaced along strike measurements of the thickness of the cemented zone surrounding the slip surface. Variogram analysis can be used to show that there is a spatial control on the thickness variation for some of these faults. Therefore statistical techniques can be used to generate synthetic realizations of this type of fault. These realizations are random but their thickness variation is similar to the measured faults. The synthetic realizations are subsequently used in this study to explore uncertainty in the thickness of these faults. With this not only bulk permeabilities can be calculated, but also its expected variability. In addition to data gathered in the Sinai desert this modelling is also applied to data gathered by Aileen Bright for Big Hole fault in Utah (A. Bright unpublished PhD thesis).

7.1 Variogram analysis

The concept of the semivariogram was initially developed by Georges Matheron expanding upon work by Danie Krige (Matheron 1965). The semivariogram (commonly shortened to variogram) is used to describe spatial covariation between a set of point observations. There are two types of variograms; the experimental variogram which is calculated from a dataset and the theoretical variogram which is a simplified mathematical model used to describe the experimental variogram.

The calculation of the experimental semivariogram requires several steps. For each possible pair of two data points in the dataset, the interpoint distance and squared difference in value is calculated. Subsequently a set of interpoint distance classes (bins) is defined. For each bin the half the average squared difference in value (semivariance) is calculated. The variogram is a graph of the semivariance plotted at the centres of the bins. As a high number of interpoint distances is necessary to produce a representative variogram, the size of each bin is often adapted to host a minimum number of distances and the edges of bins can be made to overlap if necessary. As the shape of the experimental variogram can sometimes vary strongly with different bin configurations, a geostatistical analysis should explore several different configurations, and verify consistent results. For this study a set of MATLAB functions have been developed by the author. Performing the analysis with MATLAB allows the analyst to combine experimental

variograms for many different bin configurations in a single figure, making it easy to verify the consistency of the experimental variogram.

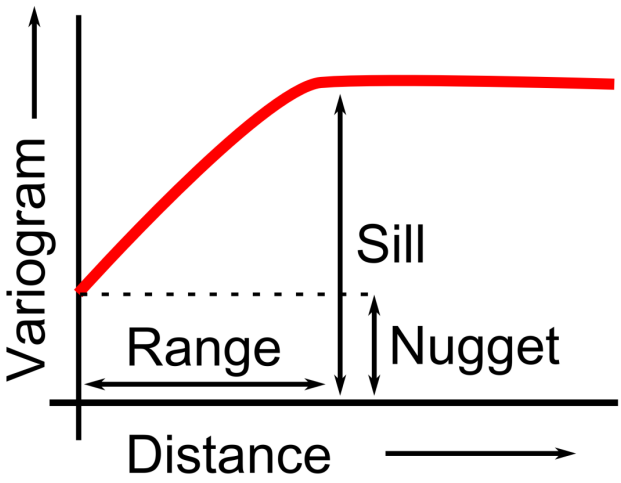

Figure 7.1: Sketch illustrating the basic components of the Variogram.

Figure 7.1 shows a theoretical variogram. Three parts of the variogram can be defined. The range indicates the maximum distance of spatial covariation. For estimation purposes the range represents the maximum distance away from the estimated site for points to be relevant for the estimation. For fault thickness data the range roughly corresponds to typical length of thick and thin patches. The sill is the values of the variogram past the range. At distances greater than the range, there is no significant spatial component to the variation and the sill should approximate the variance of the whole data set. The nugget is the value of the variogram as it approaches zero. Many variograms have no nugget, where is does occur it represents variation for which there is no spatial component at the scale of sampling. This can either represent spatial variation at a scale smaller than spacing of the measurements or a measurement error.

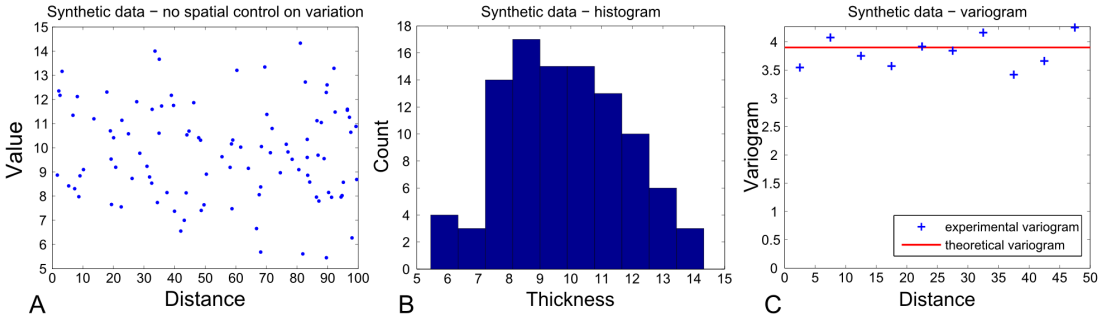

Figure 7.2: Synthetic demonstration data. Normally distributed random numbers, mean = 10, variance = 4. No spatial control on variation. A: plot of data. B: Histogram of data. C: Variogram of data.

Figure 7.2a shows a synthetic data set to illustrate the variogram analysis of fault properties. In this case there is no spatial correlation in the data. The data consists of random numbers normally distributed around a mean of 10 and with a variance of 2. The experimental variogram (figure 7.2c) for this data is approximately horizontal, with values dispersed around the

variance value of 2. If larger bins are chosen the variogram values will more closely approximate the variance. This represents a data set caused by a process where variance is not spatially controlled.

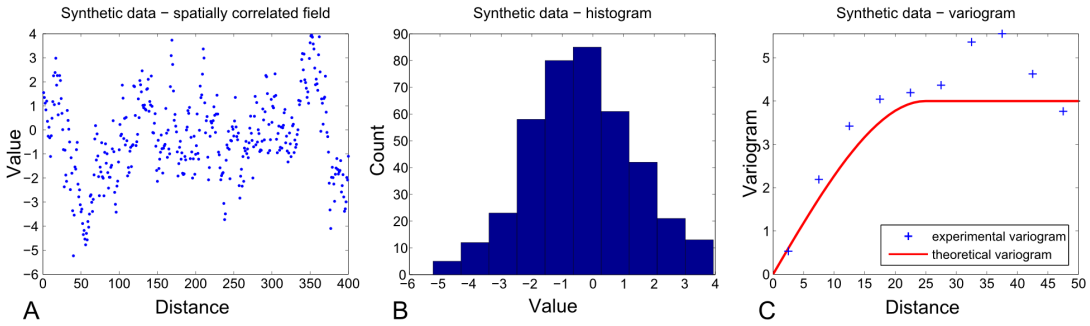

Figure 7.3: Synthetic demonstration data. Spatially correlated random field created with the LUSIM algorithm in SGEMS (Stanford Geostatistical Modelling software, Remy et al., 2009). A: plot of data. B: Histogram of data. C: Variogram of data.

Figure 7.3a shows a synthetic data set which does have a strong spatial component to its variation; in the scatter plot this is visible as nearby points have similar values. Here the experimental variogram (figure 7.3c) resembles the theoretical variogram; rising from zero to the sill value at the range.

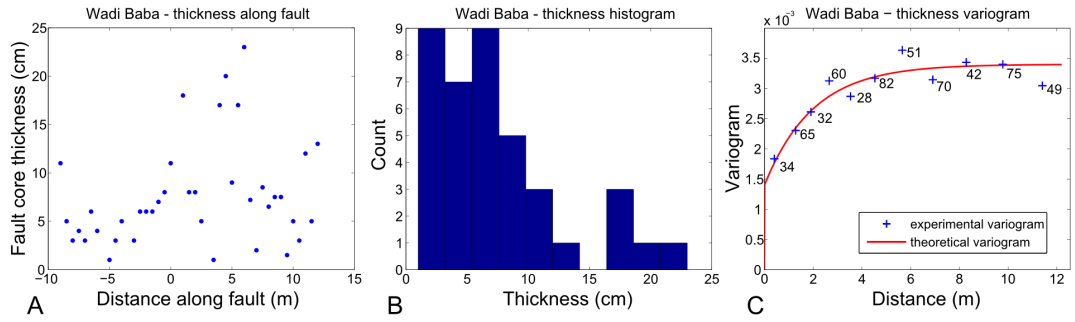

Figure 7.4: Wadi Baba fault core thickness variation. A: plot of thickness along strike. B: Histogram of thickness. C: Experimental and fitted theoretical variogram of thickness.

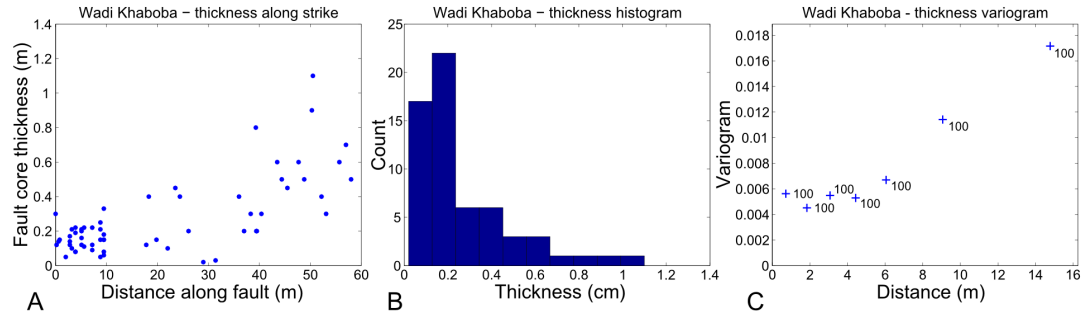

Figure 7.5: Wadi Khaboba fault core thickness variation. A: plot of thickness along strike. B: Histogram of thickness. C: Experimental variogram of thickness.

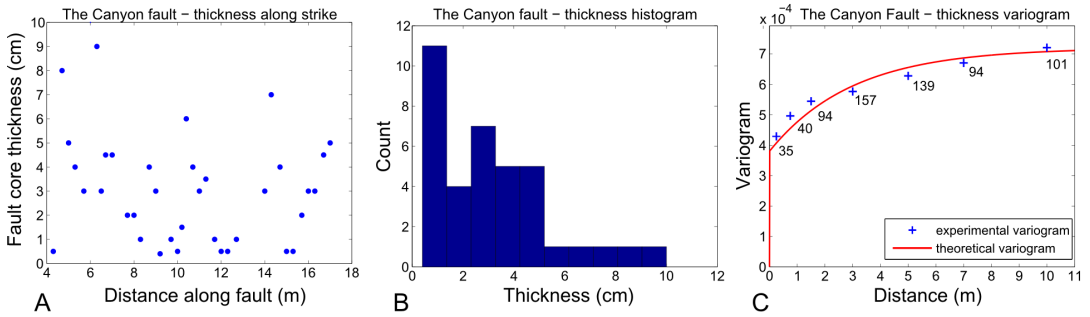

Figure 7.6: The Canyon fault core thickness variation. A: plot of thickness along strike. B: Histogram of thickness. C: Experimental and fitted theoretical variogram (exponential + nugget) of thickness. The numbers indicate the number of pairs per bin.

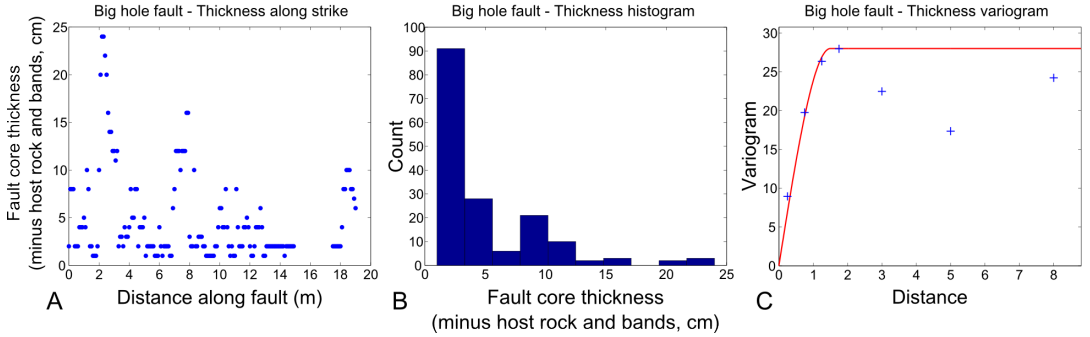

Figure 7.7: Big hole fault fault core thickness variation (data from Aileen Bright – unpublished thesis). A: plot of thickness along strike. B: Histogram of thickness. C: Experimental variogram of thickness.

Figure 7.4 to 7.7 show the along strike thickness data for the Big Hole fault (in Utah), collected by A. Bright (unpublished PhD thesis), the Wadi Baba, the Wadi Khaboba and the Canyon faults in the Sinai desert. These are deformation band faults in porous sandstone. In addition to condensed deformation band fault core, the Wadi Khaboba fault and the Canyon fault, are strongly cemented near the slip surface. This cementation has also affected the zone of condensed deformation bands. The data for these faults consists of the thickness of the cemented zone, whereas the data for Big Hole fault and Wadi Baba represents only the thickness of the deformation bands zone. The b figures show the histograms for these data sets. The c figures present the variograms for the same data. From the histograms it becomes apparent that the thickness distributions of all these faults are strongly skewed towards smaller values. From the variograms it can be seen that all these faults except for the Wadi Khaboba fault have some spatial component to their variation at the scale of sampling. However except for the Big Hole fault, the variograms for all faults have a nugget. The presence of a nugget indicates either measurement error or that there is spatial variation at a scale smaller than the sampling interval. Here the second is the case, as significant errors for thickness measurements are very unlikely. The variation of the cementation of the Egyptian faults has a shorter range than the pure condensed deformation band core at Big Hole fault, the small scale variability of the cementation is controlled by small fractures, around which the cementation is thicker. Figure7.8 shows a variogram for thickness variation at a more detailed level for the Canyon fault, obtained by taking measurements from a photograph. At this scale (25cm) the variogram is much better developed, with a much smaller sill.

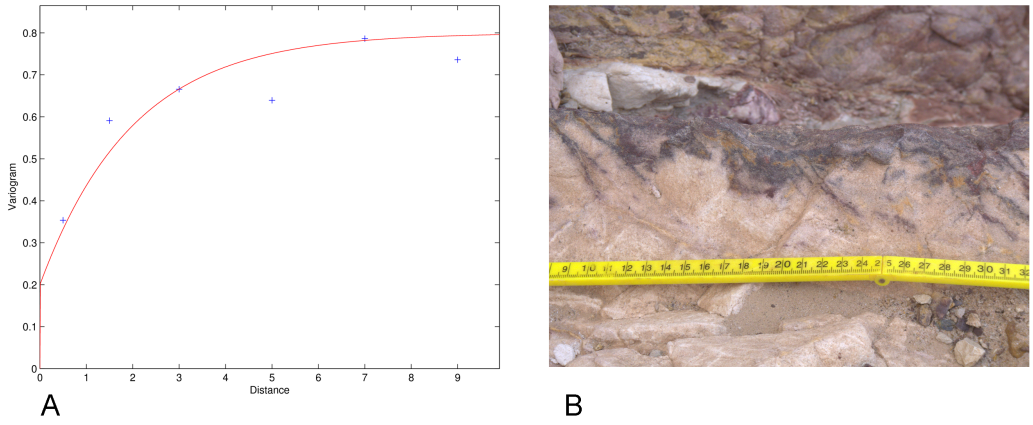

Figure 7.8: The Canyon fault core detailed thickness variation. A: Experimental and fitted theoretical variogram (exponential + nugget) of thickness. B: Photograph of slip surface and cementation, used for the measurements.

7.2 Geostatistical simulation

The data presented here can be used to create synthetic fault thickness data. The synthetic data will have a similar distribution and similar spatial covariation. A well known procedure for generating spatial variables is sequential Gaussian simulation (Isaaks 1990). Sequential Gaussian simulation requires that the input data adhere to a Gaussian distribution. The histograms in figures 7.4 to 7.7 clearly demonstrate that the fault data in this study is not normally dis-

tributed. This can be solved by pre processing the data into a normally distributed variable, perform the simulation and subsequently post process the data into the original distribution. The pre and post processing makes it difficult to match the variograms of the input data. So instead a process called Direct Simulation (DSSIM, Soares 2001) is used. DSSIM deals well with non Gaussian input data, allowing the creation of synthetic thickness data which has approximately the same distribution and variogram as the input data. The DSSIM algorithm can be summarized as follows (Soares 2001):

1. Randomly select a grid node to be simulated
2. Use the kriging equation to estimate the local mean and variance at this grid node. Both input data and previously simulated nodes are used for the kriging.
3. The local kriging mean and variance are used to select an interval of the cumulative distribution function (cdf) of the input data.
4. From this interval of the cdf a value is randomly selected and assigned to the grid node.
5. Repeat with another random grid node until all nodes are simulated.

For this study the Stanford Geostatistical Modelling Software (SGEMS) package is used to perform the spatial simulation (Remy et al., 2009). The variogram analysis is performed using a set of Matlab functions, offering greater flexibility for the variogram modelling than the SGEMS package. The procedure is demonstrated here by generating 400 synthetic realizations using the properties of the Wadi Baba thickness data.

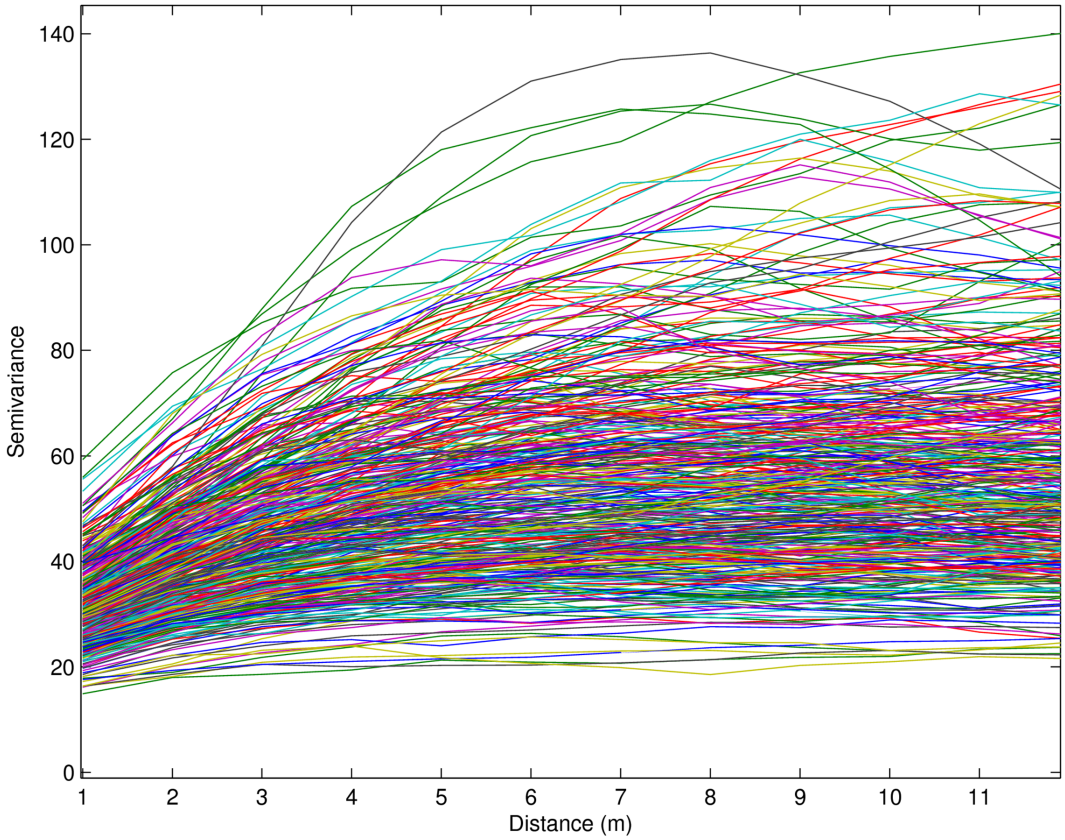

Figure 7.9: Wadi Baba, variograms for 400 synthetic realizations.

Figure 7.9 shows the experimental variograms for a set of 400 synthetic realizations as differently coloured lines. From this figure it is clear that the DSSIM algorithm tends to produce results which roughly reproduce the shape of the input variogram, but with quite a lot of scatter in the sill and nugget (upto 300% deviation for both parameters). For further analysis those realizations are selected which best approximate the input variogram (deviations upto 25%). This reduces the original 400 realizations to 49.

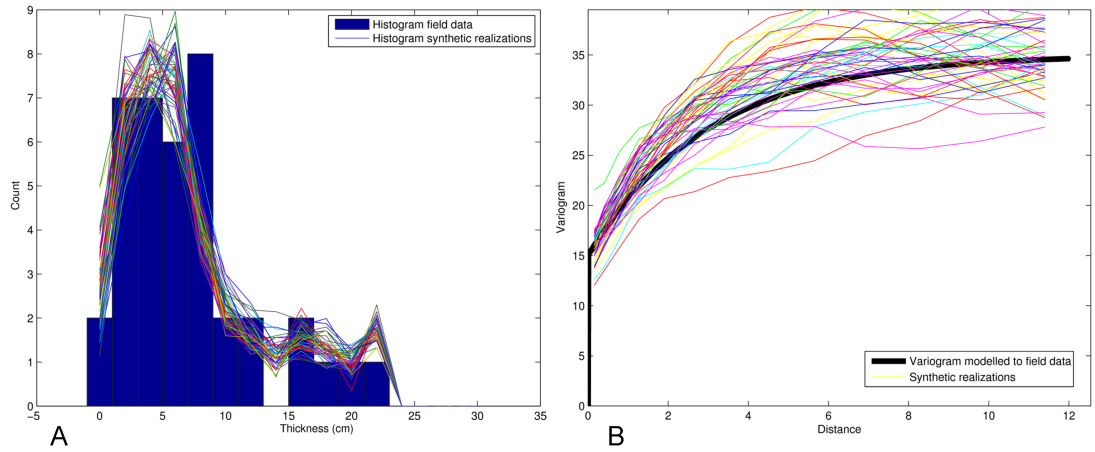

Figure 7.10: Wadi Baba selected synthetic realizations. A: Histograms of synthetic realizations (lines) on top of histogram of field measurements (bars). B: Variograms of synthetic realizations (coloured lines) and variogram modelled to field measurements (black line).

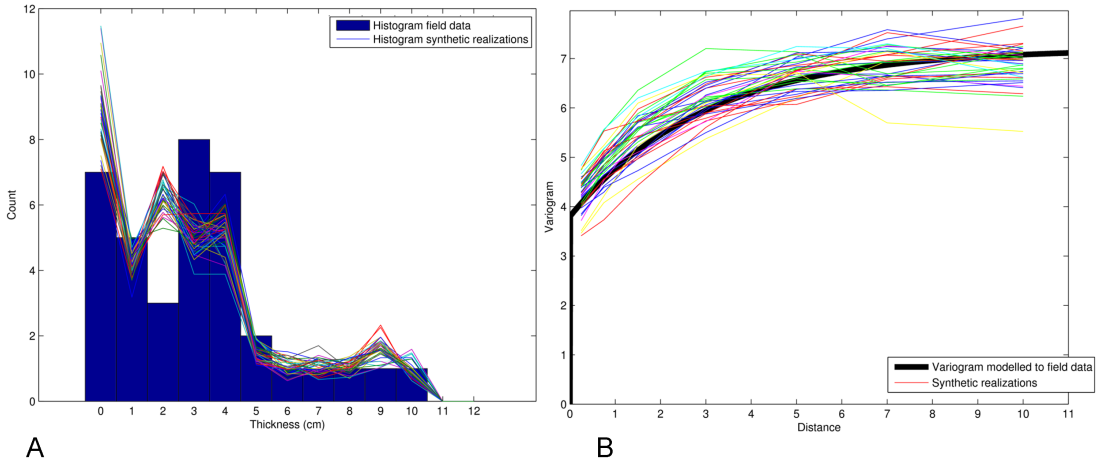

Figure 7.11: The Canyon fault selected synthetic realizations. A: Histograms of synthetic realizations (lines) on top of histogram of field measurements (bars). B: Variograms of synthetic realizations (coloured lines) and variogram modelled to field measurements (black line).

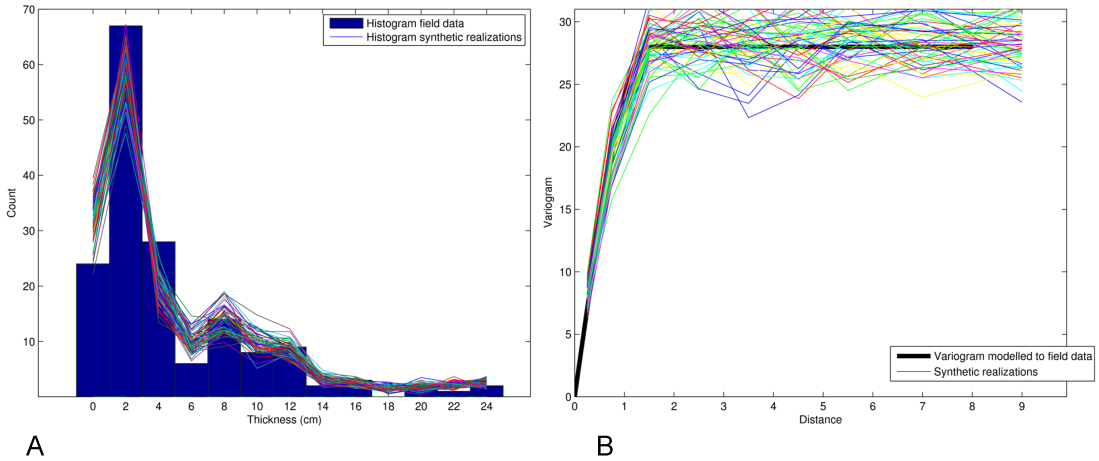

Figure 7.12: Big hole fault selected synthetic realizations. A: Histograms of synthetic realizations (lines) on top of histogram of field measurements (bars). B: Variograms of synthetic realizations (coloured lines) and variogram modelled to field measurements (black line).

Figure 7.10b shows the variograms of the 49 realizations selected for further analysis. There is still some scatter in the sill but overall the shape of the variogram is well reproduced. Figure 7.10a shows the histograms for the synthetic realizations, which closely match the histogram of the input data. Similar realizations were created for the Canyon fault (Figure 7.11) and Big Hole fault (Figure 7.12).

7.2.1 Synthetic fault models for flow modelling

Using these synthetic thickness distributions simple synthetic fault models can be made. A Matlab function (*faultmaker.m*) was devised for this purpose. It creates maps of a homogeneous permeable sandstone host rock with a fault running through the middle. The fault is straight and symmetric, it consists of a single low permeability fault rock. For the faults in Egypt a permeability value of 0.1 mD is used after measurements in similar fault rocks for the South Baba fault (Tueckmantel et al., 2010). For the core of Big Hole fault a value of 1 mD is used, which represents the lower end of fault rocks measured by A. Bright (unpublished thesis). The thickness of the fault is matched to the synthetic realizations.

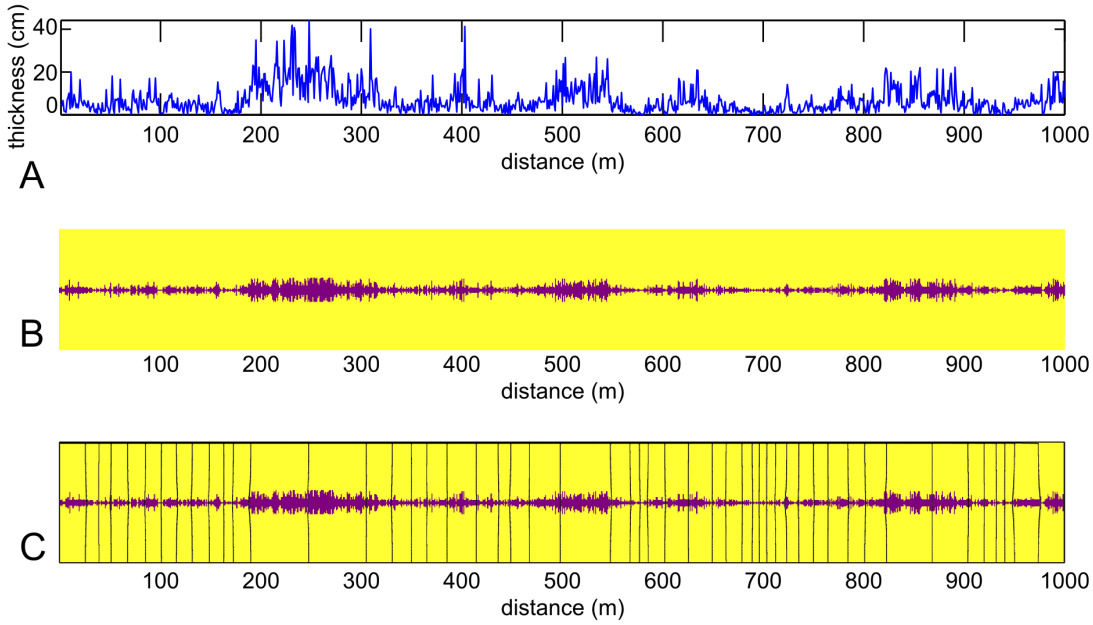

Figure 7.13: Example of a synthetic fault generated from a synthetic thickness realization. A: Graph of the synthetic thickness along strike data. B: Synthetic map used as input for the model, yellow denotes high permeability undeformed sandstone, and purple is low permeability fault rock. C: Streamlines from flow model of synthetic map. High flow (dense streamline spacing) occur where the fault core is thinnest.

Figure 7.13 shows one synthetic fault model for the Wadi Baba data. All fault models are 100m long with grid cells 10cm long and 1 cm in the fault perpendicular direction. A Matlab function *modelmaker.m* takes a set of synthetic realizations and automatically generates mflab models for the number of realizations it contains.

7.2.2 Results and conclusion

For each realization the bulk permeability is determined by modelling using MODFLOW. The histograms in figures 7.14 to 7.16 show the modelled distribution of these bulk permeabilities. It can be seen that the spread in modelled bulk permeabilities is fairly small. This can be explained by the length of the modelled fault (100m) is many times the length of the range of the variograms used (2m for Big Hole Fault and 6m for both Sinai faults). As such the variation is largely averaged out by the modelling. Shorter fault models (10-20m) would show a much more pronounced heterogeneity in the modelled permeabilities. The use of much longer synthetic realizations is necessary to validate the reproduction of the variogram by the modelling. The limited variation in modelled bulk permeability for 100m long faults is probably not representative for natural fault systems. The field data is only sufficient for small scale (1-20m) variation. Over longer distances different heterogeneities tend to occur, for example relay structures and changes in fault geometry related to lithological changes or interaction with other faults (e.g. Childs et al., 2009). Figure 7.17 illustrates this concept of multi-scale fault heterogeneity. Proper quantification of fault heterogeneity at all relevant scales is beyond the scope of this thesis as it will require a very large dataset on many well exposed fault zones. Unfortunately faults which are well exposed over distance of more than a few meters are rare. Despite several weeks of this PhD project spend on reconnaissance using geological maps, remote sensing data, fieldwork and consulting other geologists, only one such exposure was found during this project but only near the end of the project.

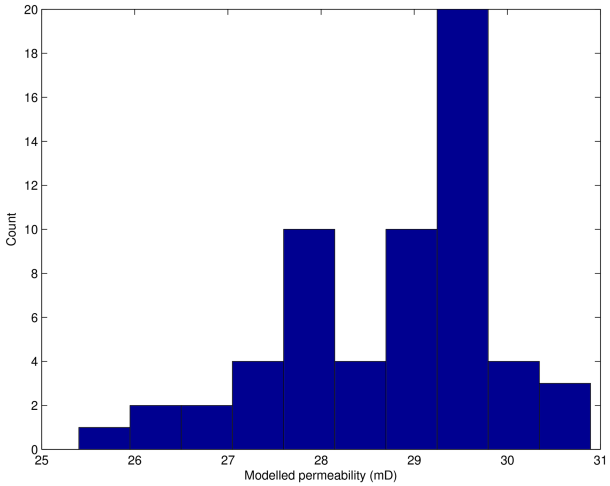

Figure 7.14: Big hole fault histogram of modelled bulk permeabilities using 49 synthetic realizations.

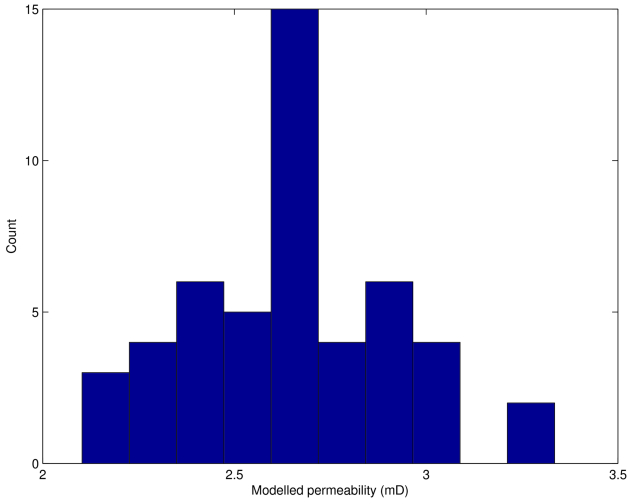

Figure 7.15: Wadi Baba fault histogram of modelled bulk permeabilities using 49 synthetic realizations.

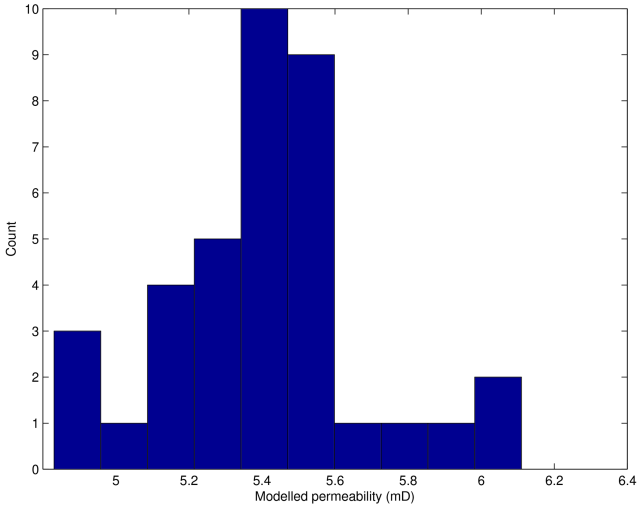

Figure 7.16: The Canyon fault histogram of modelled bulk permeabilities using 49 synthetic realizations.

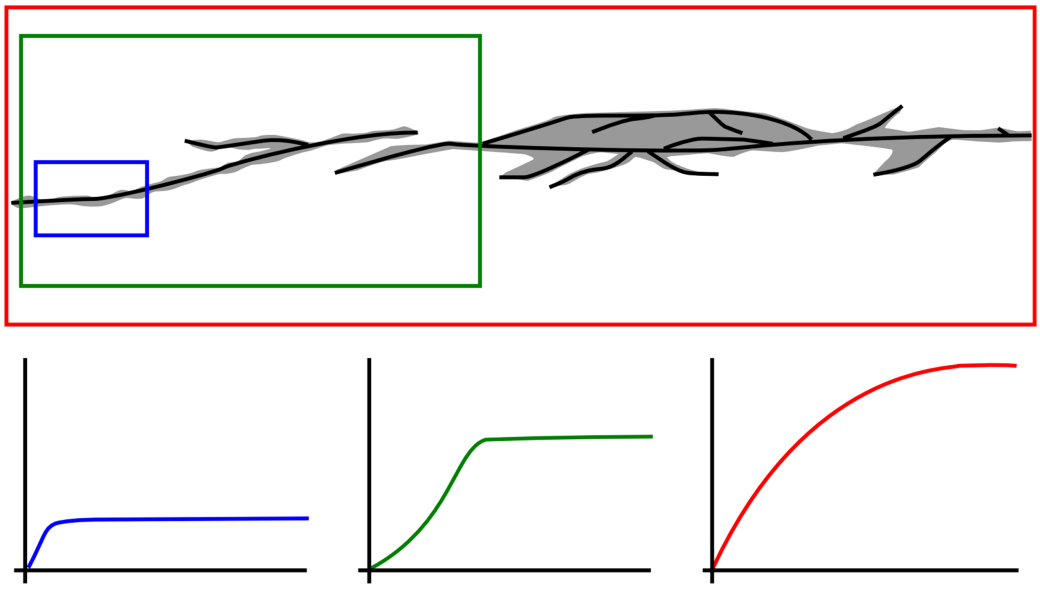

Figure 7.17: Sketch illustrating the different heterogeneities at different scales. At different scales different processes are responsible for the variability. As such the heterogeneity will be characterized by different statistics at different scales. For each scale a different variogram best represents the spatial heterogeneity.

Chapter 8

Discussion

8.1 Results from this study compared to established workflows

In this study a variety of faults in sand-shale sequences has been studied, revealing an almost equally great variety in fault architectural styles. This makes it difficult to come up with a simple predictive rule for the structure, content and permeability of fault zones. As such it is necessary to reassess the existing predictors for fault seal and fault permeability. The existing predictors can be subdivided into two different approaches underlain by different assumptions about fault architecture. First there is the SGR algorithm, which assumes faults to be dominated by a gouge of mixed sand and shale. Secondly there is a group of predictors based on shale smearing, which assumes discrete bodies of shale extending from the host rock into the fault zone.

8.1.1 Shale Gouge Ratio algorithm architecture

Although initially coined as a probabilistic predictor to differentiate between sealing and non-sealing faults (Fristad et al., 1996), it is suggested that it is a good estimate of the upscaled shale content of the fault zone (Yielding et al., 1997, Yielding et al., 1999). Others go further (Manzocchi et al., 1999, Harris et al., 2002, Sperrevik et al., 2002) and suggest it directly predicts the volumetric shale fraction of a central gouge , which forms the dominant element of the fault core. The ratio is calculated as the average volumetric shale content of the entire displaced stratigraphy. This suggests an equal contribution of material from all host rock, which a point in the fault has slipped past. As a consequence the SGR value is the same for a fault which has displaced 9m of pure quartz sandstone and a 1m thick bed of shale, as for a fault displacing pure sandstone with 10 shale beds of 10 cm thick and the same for a fault which has displaced a 10m section of shaly sandstone with 10% clay in the sandstone pores. Many hydrocarbon industry applications will focus on faults in high porosity reservoir sandstones with very low clay contents, so the last scenario is less likely to be encountered..

The assumption that SGR predicts the composition of fault gouge implies that the fault gouge corresponds to the average composition of the displaced stratigraphy, this would require homogenous mixing of all displaced stratigraphy. In addition these authors assume that the gouge is the dominant part of the fault core, occupying its entire width.

8.1.2 Shale smearing architectures

Another group of algorithms focuses on shale smearing, which implies a very different architecture. Here sandstone and shale do not undergo grain scale mixing, but instead shale beds are dragged into the fault zone, forming discrete volumes in the fault core. The algorithms attempt to differentiate between faults with a shale smear continuous along the fault plane and those with discontinuous smears. The main algorithms for evaluating shale smear are the Shale Smear Factor (SSF, Lindsay et al., 1993) and the Clay Smear Potential (CSP, Bouvier et al., 1989). The SSF can be used to estimate the likeliness of continuous smearing for a single shale bed. This probability decreases as displacement increases relative to the thickness of the shale bed. The CSP is underlain by the same assumptions as the SSF, but integrates the effect of several shale beds being smeared along the same fault zone.

8.1.3 Field observations

The architectures encountered at the studied outcrops clearly do not match the SGR style architecture where the fault is dominated by a homogenously mixed central gouge. All observed architectures are more complex than that and do not show dominant grain scale mixing of the different fault rocks. Several outcrops (M191SE, Ketobe knob) have developed gouges, but these are relatively thin (3-30% and 5-10% of the fault core width respectively). All other outcrops are composed of fault rocks in which the original host rock type can still be recognized. The quantitative map analysis shows that the outcrop fault core shale volume does not correlate with the calculated SGR for these outcrops (section 4.3). This suggests that the host rock is not incorporated uniformly into the fault zone.

The shale smear architecture applies well to some outcrops studied here. Outcrops Corral Canyon, Goblin Valley and the minor strand of the Moab fault at 191SE match this type well. In other outcrops discrete lenses of shale and silt can be found, which is at least compatible with the shale incorporation mechanisms associated with shale smearing.

8.1.4 Bulk permeabilities and SGR based estimates

The comparison in section 6.5, showed a very poor correlation between the modelled bulk permeability values and the Shale Gouge Ratio or workflows relying on the SGR. This demonstrated that the Shale Gouge Ratio and displacement alone do not provide enough information to successfully estimate the permeability and hydraulic resistance of the faults studied here. Purely looking at the modelled values it becomes apparent that the bulk fault permeabilities tend to gravitate towards the end member host rock permeabilities used. The modelled bulk permeability values tend to be close to either the host sandstone permeability or the shale/siltstone host permeability. None of the studied fault architectures shows homogeneous mixing of sand, silt and shale and this is reflected in the modelled permeability. Basically, the models can be subdivided into two sets; those which have a continuous shaley/silty core continuous along the entire studied section and those faults where the low permeability core is discontinuous or breached by sandstone lenses. Including open slip surfaces in the model can have strong effect on a subset of the first group, if the slip surfaces allow full breaching of the low permeability core it takes the model from the first group to the breached group. The bulk permeability of the continuous core group could be approximated analytically by a thickness

weighted harmonic average of the rock units the fluids have to traverse. Harmonic averages emphasize the lowest values, which in this case is shown in many of the faults having a bulk permeability near the shale permeability. Similarly, breached fault cores can be approxitated analytically as a thickness weighted geometric average of the pathway, which emphasizes the higher values.

Figure 8.1 further demonstrates the effect of baffle continuity. It shows 6 simple models consisting of a 10 cm thick shale fault core in permeable sandstone host rock. Three models have a shale core which is continuous along the length of the model. In the other three models, the shale core contains gaps filled with sandstone, connecting the hanging wall with the footwall. Fluid flow modelling through these models shows again a striking difference in the resulting bulk permeability, with the continuous shale core models having bulk permeability vales around 1e-5 mD(close to the shale permeability 1e-6 mD) and the discontinuous shale core models having bulk permeabilities around 2-20 mD (close to the sandstone permeability (200 mD). This emphasises the control that the continuity of low permeability fault core has on bulk permeability. The three continuous shale core models show different degrees of heterogeneity; the first is completely homogenous, the second has large thick and thin patches and the third has smaller thick and thin patches. The amount of shale is the same in all three models. Here the heterogeneous models have 30-50% higher bulk permeabilities than the homogenous models.

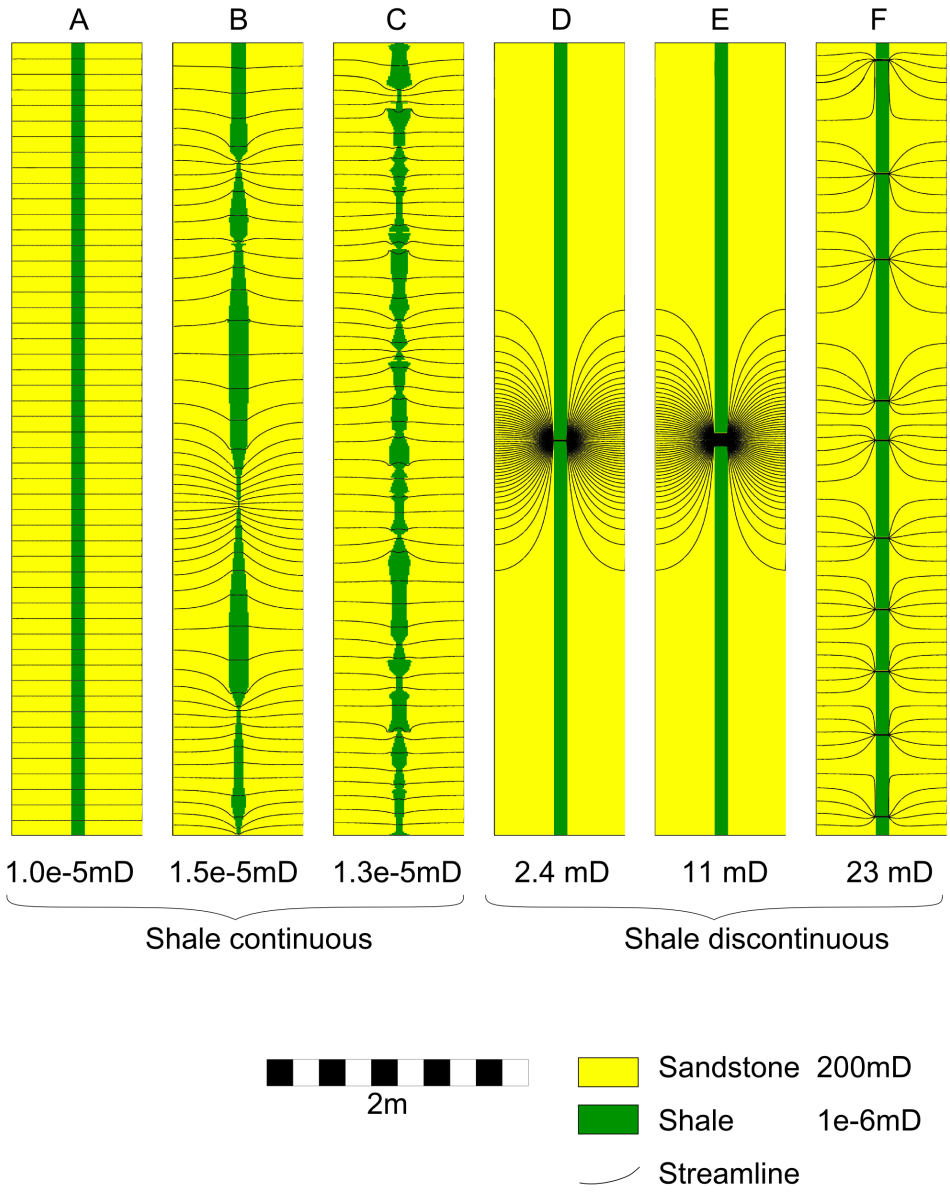

Figure 8.1: Six flow models for simplified hypothetical fault zones, illustrating the effect of discontinuities. Flow modelling is done using the same approach as in Chapter 6. All models contain approximately the same amount of shale (6000 cm^2). The modelled bulk permeability values are shown below each model. A: Homogenous thickness shale fault core. B: Heterogenous thickness shale, large patches. C: Heterogenous thickness shale, small patches.D: Homogenous thickness shale fault core with a 1cm wide gap. E: Homogenous thickness shale fault core with a 10cm wide gap. F: Homogenous thickness shale fault core with 10 gaps, each 1cm wide.

This approximately binary behaviour means that fault heterogeneity and architecture have a crucial effect on the final bulk permeability. Rather than heterogeneity causing a slight deviation from a sand and shale mixing curve, it can cause a much bigger change from close to shale permeability, to close to sand permeability and vice versa. Figure 8.2 illustrates these concepts, the shale gouge ratio suggests homogeneous mixing of sand and shale and a permeability which decreases smoothly with increasing shale content. Some uncertainty can be expected around this mixing curve. The data from this study suggest a different model where fault permeab-

ility gravitates towards either the permeability of shale or the permeability of sand. It seems reasonable to assume that for low SGR values, it is likely that the sand-like permeabilities are most common and for higher SGR values the shale-like permeabilities become more likely.

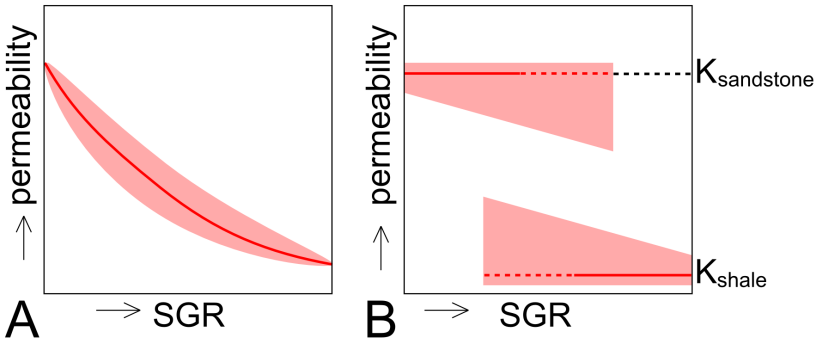

Figure 8.2: Conceptual sketch illustrating across-fault permeability prediction and uncertainty. Pink areas represent uncertainty, values are expected to lie within these areas. A: Homogeneous mixing of sand and shale as suggested by SGR based workflows. This assumes that the shale content of the gouge increases with the shale content of the host rock (SGR), and that with increasing shale content, the permeability will decrease. Most SGR to permeability algorithms are independent of the local host rock permeability and are instead derrived from global published or industry datasets.
B: Simple conceptual model for the fault architectures observed during this study and the resulting fault bulk permeabilities. The modelled bulk permeabilities in this study show a breakdown into two groups, depending on the presence of a continuous central barrier of shale, silt or gouge. The high permeability group of faults where there is no continuous barrier, or where this barrier has been breached by sandstone lenses or open slip surfaces. And low permeabilities for faults where a continuous central barrier exists. The permeability of the high permeability group tends to be similar to the permeability of the host rock sandstone, whereas for the low permeability it tends to be similar to the permeability of the shale or silt. As a consequence SGR has a limited predictive ability for these permeabilities; reliable predictions can only be made for the extremes, faults in sandstone or shale dominated sequences. For faults in intermediate host rock compositions, uncertainty increases.

One important process contributing to the poor relationship between SGR and actual fault permeability lies in the smearing of shale and other ductile lithologies. The resulting shale smears consist purely of shale and as such their effect is poorly estimated using the SGR based approaches that assume homogeneous mixing of sand and shale from the wall rock forms a shaley gouge. Since SGR is purely an average, it does not describe the distribution of the shale, and a fault in a shaley sandstone can have the same SGR value as a fault in clean sandstone with a single shale bed. Shale smears are most likely to form if the shale is concentrated in thick, pure shale beds.

Shale smears have been observed in this data set at three outcrops (Corral Canyon, Goblin Valley 1, Cedar Mountain trust). Corral Canyon and Goblin Valley have a continuous shale smear and a bulk permeability much lower than predicted using the Manzocchi and Sperrevik approaches, instead the bulk permeability approaches that of the shale. The Cedar Mountain Thrust has a core characterized by many short discontinuous smears in a sandstone-dominated fault core, which results in a bulk permeability much higher than estimated, here the bulk permeability approaches the permeability of the sand. The importance of shale smears has long

been recognized and several approaches exist to estimate the likeliness of shale smears for a given fault. The most common are the Shale Smear Factor (SSF) and Clay Smear Potential (CSP). Which are based on the thickness of shale beds in the host rock and fault displacement. Several authors recommend the use of these algorithms in favour of, or in combination with SGR, wherever shale smearing is deemed likely (Faerseth et al., 2007).

The Shale Gouge Ratio ignores all lithologies but shale and sandstone. Besides sand and shale, several other lithologies can affect the bulk permeability. In the outcrops studied here silt often (but not always) behaved in a similar manner as shale (smearing and incorporation into fault gouges). Measurements of the permeability of silt show values similar to shale, suggesting silt can be just as important for the fault architecture and bulk permeability as shale. The V-shale logs used to calculate SGR are often derived from gamma ray logs, on which the typically non-radiogenic silt can not be distinguished from sandstone. Modern petrophysical workflows encompassing a full suite of well logs, can identify siltstone (Crain, 2013).

In addition to the fault architectures which are incompatible with the Shale Gouge ratio's mixing model, cementation forms another complication. In several models the bulk permeability is strongly reduced by the presence of cementation. Thick cemented zones, which are continuous over the scale of the outcrop), occur at five outcrops (Arches National Park Entrance, Corral Canyon, Goblin Valley 1, Goblin Valley 2, Wadi Khaboba). The occurrence of cementation is not related to the amount of shale in the host rock but to other factors such as temperature, burial depth and fluid flow history. As such it is not predicted by the Shale Gouge Ratio and consequently the bulk permeability for the outcrops affected by cementation tends to be far lower than predicted by the SGR based algorithms from Manzocchi et al., 1999 and Sperrevik et al., 2002. In the literature, cementation is often dismissed as an important fault sealing mechanism due to concerns about its continuity (Cerveny et al., 2004, Eichhubl et al., 2009). These concerns are certainly valid for fault sealing over the longer times scales involved with hydrocarbon exploration, but they do not invalidate cementation as an important factor controlling the permeability of fault zones in production scenarios.

8.2 Evaluating fault processes and fault architectures

The combined fieldwork and modelling shows that for the faults studied here, the Shale Gouge Ratio is not useful for predicting the bulk permeability or hydraulic resistance of fault zones. The modelled bulk permeabilities differ strongly from the SGR-based estimates and the observed fault architectures are incompatible with a fault bulk permeability that is inversely proportional to SGR. The mapped fault architectures and the principles of Darcy flow suggest that fault permeabilities will cluster around the permeability of the dominant sandstone permeability and the dominant shale permeability. Second order architectural changes can increase or reduce these permeabilities but these effects are unlikely to correlate directly with SGR. As such many more parameters will need to be evaluated to obtain a robust estimate of fault permeability. Succesful evalutaion of fault permeability depends on succesful evaluation of fault architecture. To be able to do this all the processes affecting fault architecture need to be taken into account. Here an attempt is made to integrate the observation from this study with the available scientific literature, to highlight the important processes and find strategies for their evaluation.

8.2.1 Segment linkage

An important mechanism for fault growth is the linkage of smaller faults. This process has been observed on many scales, ranging from centimetre scale (Tchalenko, 1970, Kristensen et al., 2008) to kilometre scale fault patterns (Larsen 1988, Dawers and Anders 1995, Ferril et al., 1999, Walsh et al., 1999). Peacock and Sanderson, 1994 describe the process in four stages: 1. The fault segments exist as isolated non-interacting faults. 2. As the faults propagate further, they do not yet intersect but start to interact mechanically. Displacement is transferred between segments by rotation of bedding in between them, forming relay ramps. 3. Further deformation leads to the formation of faults connecting overstepping fault segments and breaking of the relay ramp. Stewart 2001 suggests linkage is aided by faults formed due to fault stretch; extension caused by the displacement gradient along the fault. 4 As displacement along the fault continues, the relay ramp is destroyed, forming a composite fault with bend. Childs et al., 2009 add to this that the relay ramp first becomes incorporated into the fault zone as a lens. Further deformation breaks this down to finer gouges, breccias and cataclasites.

The main control on segment linkage is formed by the mechanical heterogeneity of the host rock (Wilkins and Gross 2001, Ferril and Morris, 2008, Childs et al., 2009). The thickness of the mechanical units will determine the approximate size of fault segments developing. As such the thickness of mechanical units is very important for assessing fault segmentation and the resulting processes such as smearing, development of lenses and multiple strands.

8.2.1.1 Lens formation

Lenses are tabular bodies of intact rock inside the fault zone. Lenses typically consist of brittle rock types such as sandstone and carbonates, whereas ductile lithologies tend to form smears. They are commonly observed in fault zones at a variety of scales. Gabrielsen and Clausen, 2001 observed five processes for forming lenses in their analogue modelling using plaster of Paris. Most of these processes are related to the segmented nature of fault growth.

- Segment linkage. As discussed above, segment linkage will commonly form relay ramps and subsequently incorporate these into the fault zone as lenses.
- Asperity bifurcation. Bends in the fault plane are regions of concentrated stress, which can generate splay faults flattening the fault surface and forming a lens. Asperities themselves are commonly caused by segment linkage. - Tip-line bifurcation. Here the outer edge of the fault plane splits up due to irregularities in the host rock, non-uniformity of the stress field or stress field reorientation (Walsh et al., 2002). Subsequent linkage of the bifurcated tip line creates lenses.
- Segment Splaying. Here splay faults develop from the main fault plane, but are not related to asperities in the fault surface. The splay can generate a lens either by curving back to the main fault plane or by linking up with another secondary fault plane.
- Segment amalgamation. This is the process where secondary faults form in the damage zone and link up with the main fault surface. To generate a lens in this geometry a second fault is required, breaking off the rock mass in between the main fault and the amalgamated secondary fault.

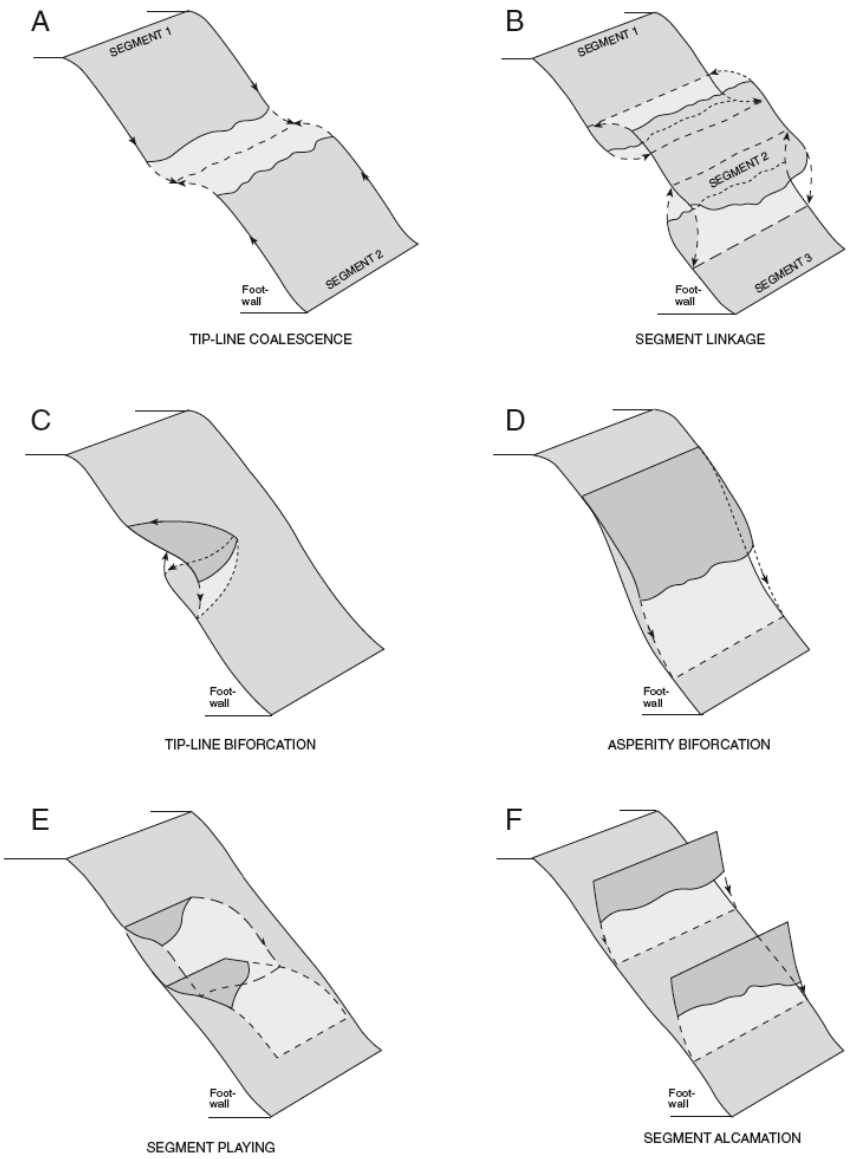

Figure 8.3: Sketches illustrating different mechanisms of lens formation (from Lindanger et al., 2007 and Gabrielsen and Clausen 2001). A: Tip-line coalescence. B: Segment linkage. C: Tip-line bifurcation. D: Asperity bifurcation. E: Segment splaying. F: Segment amalgamation.

In addition to segment linkage, other processes that can cause asperities on the fault plane are likely contributors to lens formation. As such, bedding parallel slip, fault drag and sedimentary heterogeneity can potentially increase the abundance of lenses in the fault zone. The importance of these additional processes is unknown, as the origins of a lens can not usually be determined.

8.2.1.2 Development of slip surface bounded fault zone

A common observation on the studied fault outcrops, and especially on seismic scale faults is a central fault zone bounded by slip surfaces on both sides. In this study, architectures consisting of a single slip plane are observed only for small faults (mm to m scale displacement). This has clear implications for how fault rocks develop. In the single strand model, strain is

expected to be greatest at centre of the fault. This concentration of strain also concentrates many of the processes which reduce fault rock permeability, such as mixing and cataclasis. Fault architectures consisting of a fault zone bounded by two slips surfaces can have more complicated strain distributions. Deformation can be accommodated by both the two slip surfaces as well as the fault zone itself. Where strain localizes depends on the rheology of the material in the fault zone. Phyllosilicate materials seem to strongly localize strain, as in the narrow shaley gouge at Moab fault exposure 191SE. Sandstone lenses in the fault zone show much less signs of strong deformation, suggesting that they are largely bypassed during deformation. As the one strand architecture is only encountered for the small faults in this study, it is likely that the development of a core in between two slip surfaces is a consequence of fault growth. Faults typically grow by segment linkage, which is also the dominant process for the formation of lenses and smears. As such segment linkage can produce the two slip surfaces and the fault rock between them. The main control on segment linkage is formed by the mechanical heterogeneity of the host rock (Wilkins and Gross 2001, Ferril and Morris, 2008, Childs et al., 2009). Therefore knowledge of the sedimentary succession could provide a threshold value for the displacement after which a two-strand fault zone develops.

8.2.2 Smearing

Many authors have observed faults in sand-shale sequences to have developed a tabular body of shale along the fault plane (Weber et al., 1978, Weber, 1987, Burhannudinnur and Morley, 1997, Lehner and Pilaar, 1997, Aydin and Eyal, 2002, Doughty, 2003, van der Zee et al., 2003, van der Zee and Urai, 2005, Faerseth, 2006, Egholm, 2008). However there is some disagreement in the literature as to what constitutes a shale smear and the mechanisms responsible for its formation. Here smearing refers to the set of processes that redistribute shale from a shale bed into a discrete shale structure along the fault zone. This in contrast with abrasion type smearing which incorporates both shale and other host rocks and mixes these into a fine gouge. Although smearing is commonly associated with shale, it can also affect beds of coal, salt and siltstone (Faerseth, 2006). Several mechanisms have been proposed to explain smearing:

8.2.2.1 Shear between two overlapping fault segments

This model suggests that fault growth initiates in a brittle sandstone bed. Faerseth, 2006 integrates the models of several authors (Weber et al., 1978; Lehner and Pilaar, 1997; Foxford et al., 1998; Aydin and Eyal, 2002; Doughty, 2003; Koldoye et al., 2003; Eichhubl et al., 2005) for shear between two overlapping fault segments (figure 8.4). As the fault grows the adjacent shale bed first deforms ductilely, developing a restraining bend. Further displacement initiates the development of a second segment at the other side of the deforming shale bed. As a consequence the thickness of the shale bed controls the spacing between the two fault segments. Subsequent deformation leads to shearing of the shale between the two segments. Continued displacement can lead to the rupture of the shale smear, breaking it off from the sedimentary shale bed and transporting it along the fault.

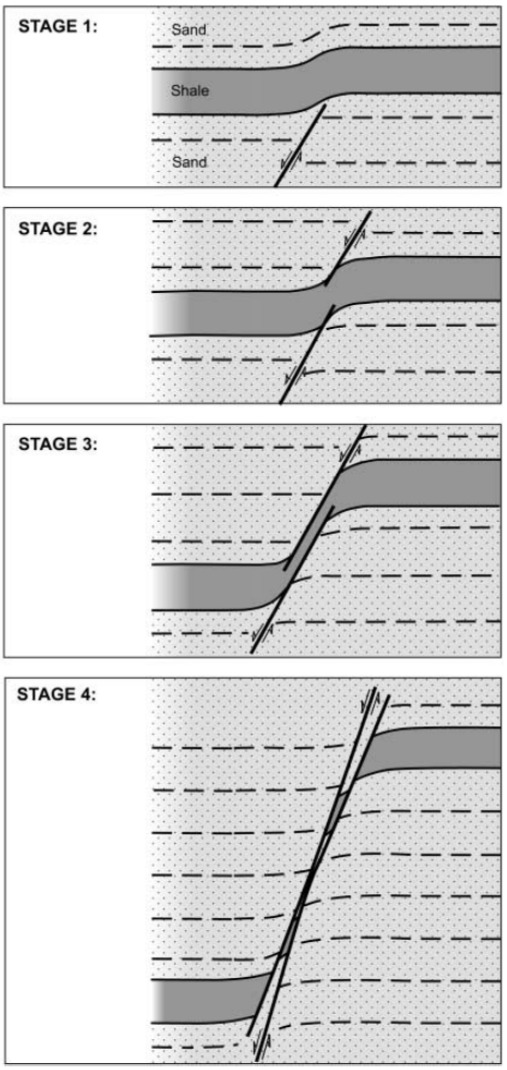

Figure 8.4: Sketches illustrating the formation of shale smears between two overlapping fault segments (from Faerseth 2006)

Eichhubl et al., 2005 add that the deformation in the sandstone beds is accompanied by the formation of deformation bands and fractures. These discontinuities can control the initial geometry of the shale smear. Subsequent deformation leads to two approximately planar fault planes on both sides of the smear.

8.2.2.2 Fault refraction

Egholm et al., 2008 suggest a different mechanism to explain shale smearing in soft sediments. Since shale and sand have different angles of internal friction, they use Mohr-Coulomb theory to argue that this will lead fault a fault segment growing from a sand bed into a shale bed to refract. As a consequence fault segments in shale will develop at a shallower angle (relative to $\sigma 3$) than in the sand. Subsequent movement of the fault will even out the asperity in the fault plane, redistributing shale and sand along the fault plane. Granular flow is responsible for flow of material into the fault zone. As the amount of shale being redistributed is limited to the width of the shallow angle shale segment, this can be related to the thickness of the shale

bed and the angle of internal friction of both the sandstone and shale. Using this the authors present an equation to predict the shale content of fault zones in soft sediments. This equation is very similar to the CSP algorithm, but its coefficients are controlled by material properties rather than empirical calibration.

8.2.2.3 Lateral shale injection

Lehner and Pilaar, 1997 and van der Zee et al., 2003 suggest lateral shale injection as a process which incorporates additional shale into the smear. Here shale is squeezed from shale beds in the host rock into the fault zone. Van der Zee et al,. 2003 show that where this mechanism is volumetrically important, an indentor block is present; the thinning of the shale source bed due to extrusion of the shale is accomodated by a subsidiary fault in the sandstone bed. This mechanism is most likely to be important for sequences with strong competency contrasts. Where active, it can incorporate significantly more shale into the fault zone, increasing the likeliness of a continuous shale smear.

8.2.2.4 Importance of shale bed thickness

Both the 'Fault refraction' model and the 'Shear between overlapping segments' model imply that the thickness of the shale bed being smeared is a strong control on the total amount of shale incorporated into the fault zone. According to these models a fault displacing a 10m thick shale bed will incorporate more shale than a fault displacing 10 shale bed of 1m thick. This prediction should be tested against faults in outcrops and analogue models, as it clearly has strong implications for fault seal evaluation and fault permeability workflows.

8.2.2.5 Formation of thin membrane smears

Several authors describe the occurrence of faults with very thin yet continuous shale smears (van der Zee et al., 2005, Clausen et al., 2003, Kristensen et al., 2013). All these observations are made on subseismic scale faults. Continuous smears have been observed on faults with large SSF factors (displacement / bed thickness > 7). According to Faerseth, 2006 the SSF values for faults with continuous smears cover a wide range (1-50), unlike seismic scale faults where a SSF $<= 4$. This suggests that these thin membranes are limited to small subseismic faults and not likely to form the main structure of seismic scale faults. No explanation has been offered for the difference between these structures and the larger smears along seismic scale faults. These membrane structures occur along faults consisting of a single slip surface, suggesting that segment linkage is not the main mode of formation. For seismic scale faults such thin membranes could potentially occur on secondary structures in the damage zone. As their thinness makes them relatively fragile, these thin smears are unlikely to contribute to sealing over longer time scales, but can make flow pathways more tortuous and act as a baffle on production timescales.

8.2.2.6 Modelling of smearing

In addition to field studies, several researchers have modelled clay smearing to understand this process better. Weber et al., 1978, Clausen and Gabrielsen 2001, and Clausen et al., 2003 use ring shear experiments to model the shearing of shale sand mixtures. Giger et al.,

2011, Schmatz et al., 2010, Giger et al., 2013, Ciftci et al., 2013 use setups modelling the shearing of sand-shale sequences using linear shearing, rather than rotational. The experiments produce different geometries depending on the shale properties, pressure conditions and water saturation. In experiments by Giger et al., 2013 and Ciftci et al., 2013 clay smear continuity increases with increasing effective stress. Meanwhile it decreases with the consolidation state of the shale; shales made 'stiffer' through the addition of Portland cement produced broken smears. Experiments by Clausen and Gabrielsen 2002 show the effect of water content, both increasing the water content of the sand and the shale increase the continuity of the shale smear, with the strongest effect when both sand and shale water content is high. In the same set of experiments they show mixed results for the influence of strain rate. In experiments by Schmatz et al., 2010 a strong competence contrast between the sand and shale leads to the development of more heterogeneous fault zones and the development of multiple strands. There are several problems in comparing these modelled structures to natural examples. The Schmatz et al. study is performed without confining pressure and the Clausen and Gabrielsen study at low confining pressure, making these studies mostly relevant for faulting at shallow depths. The apparatus used by Giger et al and Ciftci et al does allow experiments to be performed under large confining stresses. The ring shear apparatus used by Clausen and Gabrielsen assumes the faulting is localized onto a single plane, thereby modelling a very different architecture than encountered for seismic scale faults. Similarly the shear apparatus used by Giger et al and Ciftci et al., only shears a narrow zone, restricting the development of a wider fault zone. The resulting narrow fault zone limits the development of secondary strands and therefore lateral shale injection, which is strongly dependent on subsidiary faults to accommodate the thinning of the shale beds. Schöpfer et al., 2006 use discrete element modelling to study the development of faults in multilayer sequences. Their experiments show a pattern similar to the Egholm et al., 2008 model; strong layers deform by steep extensional faults, while the weak layers in between deform by shear, forming lower angle faults.

8.2.3 Abrasion processes

8.2.3.1 Grain scale mechanical wear

The movement along slip surfaces is associated with mechanical processes that create fault rock. Abrasion leads to the crushing of grains and the mixing of different lithologies. Both processes can produce a fault gouge with a porosity and permeability lower than the surrounding host rock. In this study grainscale crushing and mixing have been observed on all studied fault outcrops, however it is only volumetrically important at one exposure; Moab fault exposure 191SE. At all other faults the fault zone is composed of more complex assemblages of deformed rocks. In almost all these fault rocks the original sedimentary rock type can still be recognized. This suggests that abrasion and gouge development have a limited influence on the architecture of large faults in sand-shale sequences.

One explanation for this would be that larger offset faults seem to distribute deformation over several slip surfaces. This would lead to the development of a fault zone consisting of several strands/slip surfaces with gouge along them and relatively undeformed lenses of rock in between them. This seems a good model for the Ketobe knob outcrop. However for the other faults studied here it is not appropriate.

Another possibility is that with increasing entrainment of lower friction material (phyllo-

silicates and fine grained gouge) the effectiveness of the abrasion itself decreases. This would mean a rapid development of fault rock during the first stages of faulting, but subsequent deformation is accommodated progressively by deformation of the gouge and smears rather than by the formation of additional gouge. This is supported by experimental studies by Power et al., 1988, which show a decrease in wear efficiency with increasing displacement along a fault. Pure abrasion falls short as a model for the architecture of seismic scale faults. As faults grow by segment linkage, larger faults will be more complex than a single flat fault plane. Only the initial deformation on segments is accommodated on isolated fault planes. Abrasion and smearing produce thin fault rocks along these segments. As strain increases, the different segments link up. Segment linkage leads to fault architectures containing an assemblage less deformed lenses and smears. Both Power et al., 1988 and Childs et al., 2009 suggest such a combined abrasion and segment linkage model to explain the often observed approximately linear relationship between fault rock thickness and displacement.

8.2.3.2 Clast/lens break down

Once incorporated into the fault zone clasts and lenses of intact rock are likely to be broken up into smaller parts during progressive fault movement. If strain is distributed constantly over the wider fault core, clasts and lenses would experience strong stresses due to the strain gradient. Indeed many clasts and lenses show signs of fracturing and shearing. However many lenses are remarkably intact, suggesting that the lenses undergo less strain than the surrounding shale and gouges. Irregularities in the walls of the fault zone are likely to contribute to a strongly heterogeneous stress field inside the fault zone. Interaction between different clasts and lenses could also concentrate stress.

8.2.3.3 Fracturing

Fracturing is commonly associated with faulting, for this thesis it is a very important process as it can strongly affect both the mechanics of the fault and its fluid flow properties. By generating a set of planar discontinuities it is likely to form a local control on how host rocks are incorporated into the fault zone and how lenses break down inside the fault zone. Soden and Shipton 2013 show that the thickness of faults in welded ignimbrites is controlled by joint spacing. In addition fractures are likely to be the main source of permeability in the damage zone, controlling where fluids flow. As such they can affect the actual permeability of the fault zone and steer processes caused by fluids, such as cementation and geochemical weakening.

8.2.4 Geochemical processes in the fault zone

8.2.4.1 Cementation

Cementation in and near fault zones is commonly observed (e.g. Chester and Logan 1986, Sibson 1990, Yielding et al., 1997, Mozley and Goodwin 1995, Leveille et al., 1997, Fisher and Knipe 1998, Sperrevik et al., 2002, Dewhorst and Jones 2003, Eichhubl et al., 2009, Heynekamp et al., 1999). Cementation on its own is commonly rejected as an important mechanism to seal faults over geological time scales due to its suggested discontinuity (Cerveny et al., 2004, Eichhubl et al., 2009). Cementation can be related to fluid flow through fault zones (Eichhubl and Boles, 2000) or to local processes such as pressure solution (Shipton et al., 2002). Calcite

is the most common mineral for cementation due to fluid flow. The solubility of quartz is too small at low temperatures to make its transportation feasible. Bjørlykke 1994 shows that quartz cementation of a single pore requires 3*10^9 times pore volume fluid due to limited silica solubility. Therefore quartz cements are likely formed mostly due to local processes such as pressure solution. Silica solubility increases strongly at temperatures above 90 ^{o}C, as a consequence the abundance of quartz cementation strongly increases with burial depth (Fisher and Knipe 1998).

In addition to lowering the permeability, cementation can affect the mechanical properties of fault rocks. Fisher et al., 2003 describe how the mode of failure of porous sandstones changes with increasing burial depth. As cementation increases, the sandstones start to accommodate deformation in localized slip surfaces rather than by more distributed deformation. The localized slip surfaces are more permeable than the host rock, allowing the faults to act as conduits. This model is derrived for small structures encountered in drill cores, but is also relevant for small brittle structures inside seismic scale faults. It is not necessarily a good model for the bulk behaviour of seismic scale faults, as many more processes affect their mode of deformation and permeability.

8.2.4.2 Authigenic clay growth

Extensive evidence has been presented to show that in many faults part of the clay present has been formed in situ (Vrolijk and van der Pluijm 1999, Solum et al., 2005, Solum et al., 2010 and Haines and van der Pluijm 2012). The authigenic clay minerals can be formed by transformation of existing clay minerals to new clay minerals and by the breakdown of K-feldspar and detrital mica to clay. The volumetrical importance of this process is unclear. Solum et al., 2005 state that at the 191SE exposure of the Moab fault, both the fault gouge and the damage zone contain 40% newly formed clay minerals. As this is partly formed by dissolution of existing clay minerals, the net increase in clay caused by authigenic growth is likely to be less. Interestingly Solum et al., 2010 show that the authigenic growth of clays increases the continuity of slip surfaces. They compare natural slip surfaces with synthetic slip surfaces in the same lithology. They find that in the natural slip surfaces of the Moab fault, pore throats have been filled up by authigenic clays.

Due to the difficulty of quantifying the volumetric importance of this effect, it is unclear what the magnitude of the permeability reduction of this process will be. However taking in mind the Revil and Cathles, 1999 model for the permeability of sand and clay mixtures, the effect might be strong. A clay volume equal to the sandstone porosity can completely clog all the pores, reducing the permeability by several orders of magnitude.

8.2.4.3 Geochemical weakening of fault rocks

Fluid flow through fault zones also has the potential to weaken fault rocks. This is analogous to the long recognized development of secondary porosity in reservoir sandstones. Reactive fluids can dissolve detrital framework grains (feldspars, carbonate rock fragments and unstable heavy minerals), carbonate fossil fragments and cement minerals (calcite and evaporates) (Loucks et al., 1979, McBride 1979, Schmidt and McDonald, 1979). The common occurrence of dissolution is well established, however the mechanism is still actively debated (Taylor et al., 2010). It is likely that faults which experience large quantities of fluid flow are host to similar processes.

Dissolution of cements and transformation of feldspars and micas to clay can affect both the fluid flow and the mechanical properties of rocks. This potentially creates complex feedbacks between fluid flow and fault architecture. The process is likely to be most effective in the high permeability elements of fault zones; connected (permeable) lenses and the damage zone.

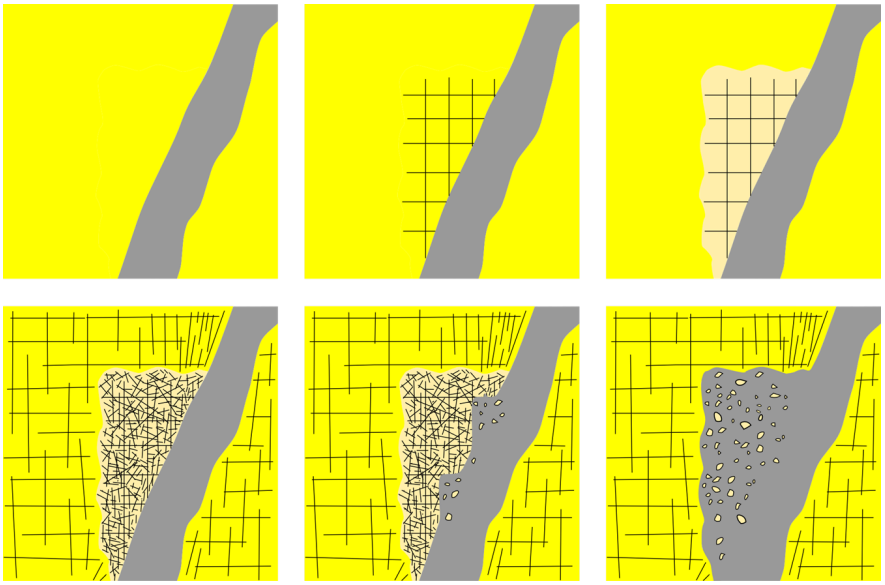

Figure 8.5: Sketch illustrating the combined mechanical and chemical break down of host rock sandstone at Moab fault exposure 191SE.

At the 191SE exposure of the Moab fault several examples of this phenomenon can be seen. Figure 8.5 provides a sketch illustrating combined fluid-mechanical host rock weakening. Intersection of bedding planes and near vertical fractures increase fluid flow in triangular wedges of host rock. The fluids weaken the rocks and induce a colour transformation. The weakened rocks are preferentially abraded into the fault gouge. Figure 8.6 shows another example, here a sandstone lens inside the gouge has been strongly deformed. Rather than breaking up in a pure brittle mode of failure, the lens remains largely continuous in a somewhat brittle fashion. This increased continuity has potential implications for fluid flow through fault zones. Solum et al., 2005 and Solum et al., 2010 provide evidence of fluid related dissolution and clay growth in both gouge and damage zone of this exposure.

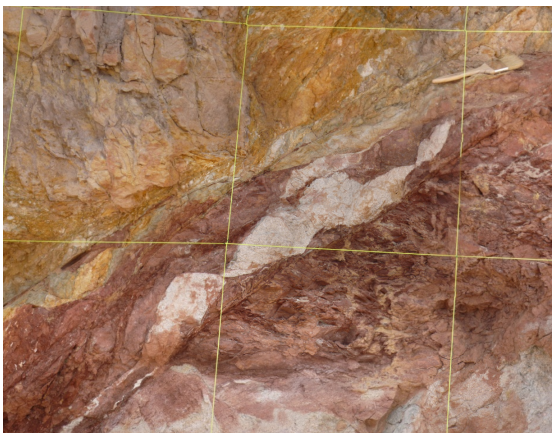

Figure 8.6: Moab fault exposure 191 SE. Photo of weakened sandstone lens in gouge.

8.2.5 Phyllosilicates and strain localization

The incorporation of phyllosilicates is often inferred to reduce friction along the fault (Wu et al., 1975, Chester and Logan 1987, Vrolijk and van der Pluijm, 1999). Reducing the friction would also allow the concentration of strain in a narrower part of the fault zone. Knott et al., 1996 and Sperrevik et al., 2002 have indeed observed faults in sand-shale sequences to have lower thickness to throw ratios than those in pure sandstone sequences. The outcrops studied here do show that most of the strain is accommodated in the shale rich parts. This does not necessarily mean that these faults are less thick. For example at Corral Canyon, the fault core is dominated by a thick shale smear and strain has been accommodated over the entire shale thickness. Moab fault 191SE oucrop has a very narrow (0.1-0.7m) clay rich gouge, which seems to have accommodated the bulk of the strain. The nearby Moab fault 191NW outcrop is dominated by siltstone and strain is distributed over a much wider area.

8.2.6 Faults in porous sandtstone

8.2.6.1 Deformation bands

Deformation bands are common features in porous rocks such as reservoir sandstones. They both occur in close association with faulting and due to more dispersed deformation. As such, deformation bands are relevant for the development of faults in sand-shale sequences. Deformation bands form planar discontinuities which can affect the geometry of fault walls and sandstone lenses. This is observed at Goblin Valley fault 1, where the lens geometry is clearly affected by deformation bands. In addition the deformation bands have permeabilities several orders of magnitude lower that the original sandstone. However due to their limited thickness, individual deformation bands only slightly reduce the permeability of affected wall rock and lenses.

8.2.6.2 Deformation band cluster faults

Provided that the sandstone beds are of sufficient thickness and porosity, segments in sandstone will develop as typical high porosity sandstone faults. Shipton et al., 2005 provides a model for the development of such faults. Initial deformation is accommodated by strain hardening de-

formation bands. Inside a dense cluster of deformation bands, slip surfaces can then develop. As the fault grows, slip surfaces link up resulting in a fault core consisting of several anastomozing slip surfaces, zones of densely clustered deformation bands and relatively undeformed sandstone. This development of deformation band cluster faults in the sandstone segments of the fault is likely to affect the final geometry of the sand-shale fault. This has been observed at a fault in the Black Diamond mines by Eichhubl et al 2005, where the shale smear is bounded by sandstone with clustered deformation bands. Above and below the smear, the fault is similar to faults in high porosity sandstones.

It would also be expected that remnants of the sandstone segment fault core consisting of condensed deformation bands and cataclasites would be encountered inside the the core of large sand-shale faults. The clustered deformation bands are stronger than the host rock sandstones and would therefore be more likely to survive as lenses inside the fault zone. However during this study this has never been observed. This could be attributed to limited observations, or perhaps the condensed deformation band core does not preserve during progressive deformation in a shale rich environment. Unlike individual deformation bands, deformation band fault core does significantly affect fault zone permeability (Shipton et al., 2005, A. Bright, unpublished thesis). These zones are much thicker and often strongly affected by cementation. In contrast the abundant slip surfaces inside the fault core are potential pathways for along fault flow.

8.2.7 Faults in unconsolidated sediments

Because the lithification state of an exposure during faulting is not always known exactly, it is very possible that this parameter has not been accounted for sufficiently. Analogue modelling such as performed by Schmatz et al., 2010 and Ciftci 2013, shows a dependency of the architecture over a range of material properties. As such the binary subdivision between unconsolidated and consolidated is likely an oversimplification. However except for very recent faulting it is often difficult to establish the consolidation state during faulting.

8.2.7.1 Mixed zone

Several authors have studied faults in unconsolidated sand-shale sequences (Heynekamp et al., 1999, Doughty 2003, Loveless et al., 2011, Bense 2004). From these studies it becomes apparent that there are some differences in fault architecture depending on consolidation state. The most striking difference is the occurrence of a mixed zone in faults which developed in unconsolidated sediments. Inside mixed zones sediments have undergone significant tectonic mixing. Sedimentary structures such as bedding have been partially or completely destroyed and overprinted by a deformational fabric. The transition between the damage zone and the mixed zone tends to be gradual. The mixed zone is typically part of a more complex zone with features such as shale smears and sand lenses.

8.2.8 Bedding parallel slip

Watterson et al., 1998 and Childs et al., 2009 suggest another mechanism for the incorporation of host rock into fault zones. Bedding can form planes of weakness allowing slip along them. Especially beds of ductile lithologies such as shale, coal or silt can act as local detachments. Movement of parts of the sedimentary succession along bedding could make the fault less planar,

introducing asperities which can be incorporated into the fault zone by subsequent deformation. Although bedding parallel slip has not been observed during this study, several examples are presented in the literature (e.g. Nino et al., 1997, Sharp et al., 2000, Jackson et al., 2006, Maher and Braathen, 2010). However these publications focus on the structure of the fault and do not discuss the effect on fault rock formation.

8.2.9 Fault-propagation-fold breaching

Folding is commonly associated with thrust faulting. Fault propagation folds typically develop above the tip of blind thrust faults. Continued fault growth leads to interaction between the fault and fold, breaching the fold. As the folding has rotated beds to a rather steep orientation relative to the fault, this can lead to a thrust fault architecture with mostly intact sedimentary bedding perpendicular to the fault zone.

8.2.10 Near surface faulting

Faults formed near the surface can exist as open fissures. These open fissures can subsequently be filled by sedimentary processes. One example of this has been documented in Canyonlands National Park Utah, where both open fissures and faults filled with rubble and Aeolian deposits are visible (Cartwright et al., 1995).

8.2.11 Towards a predictive framework

It is important to note that the above processes are not isolated, but instead are likely to affect each other, leading to a potentially complex set of feedbacks determining the evolution of the fault zone architecture. Fault zone architecture and its permeability are therefore inherently four dimensional. Both can change strongly over time, along strike and along dip. Any studied outcrop, analogue or numerical model or empirical prediction is only a valid description at the studied moment in time. For example fracturing can strongly increase permeability, which in turn affects fluid related processes such as cementation and/or fluid weakening. This can be seen at Moab fault exposure 191SE, where highly fractured parts of the damage zone are geochemically altered and are weaker (figure 8.5). Conversely cementation can change the deformation mode of a porous sandstone from deformation bands to fracturing (e.g. Fisher et al., 2003 and Johansen et al., 2005). Both examples affect both fault architecture and permeability.

Considering all the different processes acting inside the fault zone it is probably impossible to achieve a perfect prediction for the architecture of an unexposed fault. However with knowledge of the fault's host rock, displacement and history there is potential for estimating the range of architectures possible and select the most plausible hydrological properties. Table 8.1 lists the processes discussed in this chapter and factors contributing to their likeliness. From this process analysis it becomes clear that the average shale content as used by SGR is only a small part of the problem at hand. Much more important is the distribution of the shale and other smearable lithologies over the sedimentary sequences. If the shale is concentrated into thick beds, it is likely to form continuous smears. In addition the thickness of the shale beds can be used to estimate the thickness of the smears. Of the faults studied here, smearing is the most likely mechanism for forming a continuous barrier along the fault zone.

Another important factor for the stratigraphy is its impact on segment linkage. The most important constraint on segment linkage has been established to be the thickness of the mechanical units. As such this provides a direct constraint on the maximum size of lenses. Using the knowledge of the stratigraphy provides an estimate of the size of lenses and the thickness of the shale smears. It is reasonable to argue that the ratio between these two sizes provides a measure for the heterogeneity of the fault zone. Large sandstone lenses in thin shale smears will likely mean a plethora of pathways for fluids to traverse the fault zone. Whereas small sandstone lenses in thick shale smears are much less likely to affect the permeability of the fault zone.

Fluids travelling through the fault zones can have several different effects on the architecture and permeability of the fault zone, including authigenic clay growth, cementation and weakening of fault rocks. A very detailed knowledge of the fault rocks and fluids is required to make a realistic prediction of the effects of fluids on the fault zone. But overall it is likely that fluids have a homogenizing effect. Authigenic clays and cementation are likely to decrease the permeability of rocks which were previously high permeability.

The processes active in fault zones result in strongly heterogeneous structures.. Different outcrops can show strongly differing architectures. Within the same outcrop strong lateral variation in the properties of the architecture can be visible. An excellent example is the Moab fault, along which very different architectures can be observed. At Corral Canyon the fault has an architecture dominated by a single shale smear. At 191SE, 191 NW and Arches entrance the outcrops consist of more complex assemblages of silt and shale smears and sandstone lenses. At the Northernmost segment Davatzes et al., 2002 identify architectures dominated by deformation bands, jointing and cementation. Measurements of the thickness of the shale smear demonstrate strong variation along strike. Robust prediction methods will need to be able to predict the most likely architecture. For proper evaluation of the hydrological properties of these architectures, it is necessary to have data on the lateral variation. The key flow control concept assists in the collection of this data. By determining what statistic is best able to predict bulk flow properties, the data collection can be performed more efficiently. Chapter 7 demonstrates how key flow control data can be used to calculate probabilistic estimates of permeability. This allows better representation of fault permeability uncertainty.

In summary the way forward lies in fault permeability prediction using a detailed geological model rather than a single statistic. Detailed knowledge of the fault structure, lithological and mechanical stratigraphy and the deformation, temperature and fluid flow history of the basin will need to be integrated to allow for a reallistic prediction. If so many variables need to be evaluated, a large data set of studied fault exposures is needed. The faults studied in this thesis are enough to highlight the variety and complexity of fault zones and even show small trends, but for developing a reliable workflow, many more examples are needed. As this can never be achieved by an individual scientist, pooling of data from both academia and industry seems key to achieving a robust fault architecture and permeability evaluation tool.

Process	Contributing factors	Effect on across-fault permeability	Effect on along-fault permeability	Effect on fault architecture	Importance
Smearing	• Abundance of smearable lithologies (shale, coal, silt, salt) • Thickness of smearing beds relative to displacement • Analogue modelling show a variety of other parameters to affect shale continuity, including shale consolidation, effective stress and water content. However these parameters have not yet been verified by field observations.	If continuous it can have a very strong effect on permeability forming an excellent seal.	Likely limited, but a strong barrier for across fault flow can limit a fault's role for bypassing stratigraphic seals.	Abundance of phyllosilicates and other ductile lithologies in the fault core can reduce friction and localize strain, leading to a more narrow fault zone.	Very high
Lens formation	• The current literature does not extensively debate the parameters contributing to lens formation. • The thickness of sandstone mechanical units is a likely control on the maximum size and abundance of the lenses.	Lenses of high permeability lithologies can form pathways for fluids to traverse low permeability fault cores.	Lenses of high permeability lithologies can form pathways for fluids to traverse low permeability fault cores.	Lenses introduce large volumes of rock into the fault zone and can significantly widen the fault zone.	high
Fracturing	• Occurrence of brittle rocks. Porous sandstones can become more likely to fracture by cementation. Siltstones and shales can become more likely to fracture by overconsolidation and cementation. • High pore pressures	Connected fractures can strongly increase permeability. The aperture of the fractures is likely to depend on the stress conditions	Connected fractures can strongly increase permeability. The aperture of the fractures is likely to depend on the stress conditions	Fracturing can contribute to the break down of lenses and wall rock.	high

Table 8.1: Summary of processes affecting the architecture of fault zones in sand shale sequences.

Process	Contributing factors	Effect on across-fault permeability	Effect on along-fault permeability	Effect on fault architecture	Importance
Authigenic clay growth	• Abundant along fault fluid flow	Can decrease the permeability of fault gouges, lenses and damage zone. Can increase the continuity of slip surfaces.	Can decrease the permeability of fault gouges, lenses and damage zone. Can increase the continuity of slip surfaces.	Increase of fault phyllosilicates content can localize strain. Conversion of feldspars and micas to clays can weaken sandstones.	medium
Cementation	Cements can precipitate from mineral rich fluids, requiring large volumes of fluids flowing through the fault. Or it can be caused by local dissolution and redeposition, which is largely temperature dependent.	Can strongly decrease the permeability of rocks in both fault core and damage zone. Strongly lowering across fault permeability. Unclear if it can form a continuous seal over large distances.	As it is the main mechanism known to decrease the permeability of the damage zone, it can have a strong effect on along fault flow.	Cementation can change the deformation characteristics of affected rocks. It can increase the strength and reduce porosity and ductility.	medium
Geochemical weakening of fault rocks	Abundance of reactive fluids and the presence of soluble/changeable phases in the fault rocks.	Likely small	Likely small	Weakening of rocks can have a variety of effects; easier incorporation of host rock into the fault zone, shearing of sandstone lenses.	low
Bedding parallel slip	Sedimentary sequence with mechanically poorly coupled beds.	Sandstone beds pushed into the fault core could potentially form pathways for across fault flow.	Not likely to strongly affect flow.	Potential source of fault asperities and therefore fault zone thickness and lens formation.	low
Strain localization	Abundance of ductile (e.g. phyllosilicates) material in fault zone.	A narrower fault zone is more easily breached, decreasing the chance of a constant seal.	Strain localization could also affect the width of the damage zone, decreasing its along fault flow potential.	A narrower fault zone relative to displacement.	medium
Deformation bands	Porous sandstones	Very limited	Very limited	Deformation bands can form potential planes of weakness.	low

Table 8.1 Continued

Process	Contributing factors	Effect on across-fault permeability	Effect on along-fault permeability	Effect on fault architecture	Importance
Dense deformation bands clusters	Thick (several meters) beds of porous sandstone are required for fault segments to develop as typical faults in porous sandstones without the effect of shale.	Dense clusters of deformation bands can form significant barriers to flow.	Dense clusters of deformation bands can host open slip surfaces which can act as pathways for flow.	Dense deformation band type faults tend to be wider relative to displacement than faults in shalier lithologies. Existing slip planes are likely to continue to guide faulting after the segment grows into a shale bed.	medium
Clast/lens break down	Continued fault movement after lens/clast incorporation. A strongly	Break down of sandstone lenses is likely to reduce the effectiveness of lenses to be part of connected high permeability pathways. Progressive breakdown of sandstone clasts and lenses decreases the shale/sand ratio of the gouge.	Break down of sandstone lenses is likely to reduce the effectiveness of lenses to be part of connected high permeability pathways. Progressive breakdown of sandstone clasts and lenses decreases the shale/sand ratio of the gouge.	Homogenizes the fault core	medium
Cataclasis/ grain crushing	More likely if ductile material is absent, in which deformation would otherwise be localized.	Crushing of grains reduces grain size, forming a low permeability gouge potentially forming a barrier to across fault flow.	Likely to only affect a narrow part of the fault core, not necessarily influencing along fault flow.	Formation of a central gouge.	high
Near surface fault infill	Faulting near surface	Infill with aeolian sediments is likely to provide a high permeability	Infill with aeolian sediments is likely to provide a high permeability	This process is likely to only affect a very small section of the fault.	Low, likely to affect few faults
Shear fractures	Strain distributed over a wider fault zone	Potentially significant where displacement on the shear fractures exceed the typical thickness of permeable beds.	Small	Creates potential planes of weakness, which can increase host rock incorporation and lens break up.	Low.

Table 8.1 Continued

Chapter 9

Recommendations

The work presented in this thesis shows that the average phyllosilicate content of the host rock stratigraphy (SGR) is a very limited predictor of fault permeability. For the faults studied here, fault architecture had a much more pronounced effect on flow. Different fault architectures can occur along different parts of the same fault. In addition fault architecture and permeability can change over time. Reliable prediction of bulk fault permeability will require the development of workflows realistically incorporating the 4D evolution of fault zones. This requires evaluation using detailed stratigraphy, petrophysics, rock mechanics and the history of stress/strain, temperature and fluid flow geochemistry. To achieve this, a much larger dataset of fault zone architecture observations is needed. With such data, a qualitative and quantitative understanding of the processes contributing to fault zone architecture can be developed. Statistical tools, such as those discussed in this thesis can subsequently be used to provide realistic predictions of bulk permeability and the associated uncertainty.

This is a considerable amount of work, requiring a long-term collaborative effort of industry and academia. There are conclusions that can be drawn from this thesis, which can be implemented on shorter time-scales. These recommendations will be discussed first, followed by recommendations for the development of a more thorough workflow for the prediction of fault bulk permeability.

9.1 Recommended adjustments to existing workflows

Evaluate all smearing lithologies Commonly used workflows focus on the incorporation of shale into the fault zone. At many faults studied in this thesis, silt is frequently encountered as smears or in gouges in faults. Due to its low permeability, it has a similar effect on bulk permeability as shale. Siltstone is compositionally different from shale and is therefore not detected by gamma-ray logs. More advanced well log analysis can detect silt. Including siltstone in fault permeability evaluation seems a simple step to improve the effectiveness. Other lithologies which have been identified as prone to smearing include coal and salt.

Fault thickness Both the Manzocchi et al., 1999 and the Sperrevik et al., 2002 workflows for calculating fault transmissibility multipliers estimate the fault thickness from displacement. The uncertainty plaguing thickness displacement relationships has been discussed extensively in the literature (e.g. Evans, 1990, Shipton et al., 2006, Torabi and Berg, 2011). For this

study, the thickness values predicted by the algorithms show 1.5 orders of magnitude scatter around the thicknesses measured at outcrops. The Sperrevik algorithm consistently overestimates thicknesses for faults with a throw greater than 100m. The Manzocchi algorithm consistently underestimates the thickness of faults with less than 100m throw. Using the Manzocchi algorithm for faults with less than 100m throw and the Sperrevik algorithm for faults with throws over 100m should yield better results. With the caveat that the number of faults here is fairly small and this observation should be tested against a larger dataset.

A problem with existing fault thickness-displacement datasets is their poor definition. Many entries do not specify what has been measured (fault core, damage zone), or how it has been measured (minimum, average, maximum thickness and the size of the sampling window). Where it is specified, the authors of these papers have collected the average thickness. For across-fault fluid flow the minimum thickness is a much better predictor for the bulk effect on flow. Even more important are gaps in the low permeability fault core. This can for example be caused by a broken shale smear or a sandstone lens providing a pathway across the fault. As discussed in section 8.1.4, a single discontinuity can increase the bulk permeability by several orders of magnitude compared to a continuous low permeability barrier along the fault.

9.2 Semi-realistic fault modelling

None of the seismic-scale faults encountered during this study reflects a process of homogenous grain-scale mixing of sand and shale. Instead fault cores consist of slices, slivers and lozenges of rocks that still resemble the original (sedimentary) rock type. The permeability of the fault rocks is not homogenized, but instead strongly contrasting permeabilities can be found side by side. The volumetrically most important processes for incorporating host rock into the fault core are smearing of incompetent rock types (i.e. shale, silt, coal) and the formation of lenses of the more competent rock types (i.e. sandstone and limestone). SGR type mixing models are underlain by the assumption that material from the entire displaced stratigraphy contributes to the fault rock at a point along the fault. This is not supported by the observations in this thesis. Fault rock mostly resembles sedimentary units stratigraphically close to the exposure. As such a simple distance weighting scheme might improve the performance of algorithms trying to estimate the average fault rock shale content. Also for determining the upscaled permeability of fault zones, SGR-style mixing is unsuitable. Bulk permeabilities calculated in this study do not resemble the (arithmetic) average permeability of the fault rocks or host rocks. Instead the architecture of the fault zone exerts a much greater control. Fault architectures defined by a continuous low permeability fault core have a bulk permeability resembling the permeability of the fault core. Faults where such a barrier is not continuous show a much higher bulk permeability, close to the permeability of sandstone.

It will be more effective to prioritize the prediction of the occurrence of smears and lenses. These two features have been commonly observed in this study and can strongly affect fluid flow. First shale smearing needs to be evaluated. This is the most important mechanism for incorporating shale into the fault zone. The Shale Smear Factor (SSF, Lindsay et al., 1993, Faerseth, 2006) could serve as a starting point for estimating the probability of smear continuity. Thick shale beds displaced over relatively short distances (low SSF value) are likely to have a continuous shale smear along the fault plane. Fault architectures with a continuous shale smear along the fault plane are likely to have a bulk permeability close to that of shale. Faults with

large SSF values are likely to have detached shale smears. A detached smear does not form a continuous barrier across the entire displaced length, but can form a single barrier over a shorter interval. Progressive deformation can rework detached smears and sandstone wall rock and lenses into an assemblage of smaller smears and sandstone lenses. Such assemblages are likely to contain connected pathways, for example sandstone lenses and or slip surfaces, leading to a much higher bulk permeability.

The abundance of large sandstone lenses is a key flow control for flow along-faults. In addition lenses can form pathways for across-fault flow through low permeability fault cores. A standard tool for the prediction of sandstone lens abundance, size and orientation is currently not available. Gabrielsen and Clausen, 2002 and Lindanger et al., 2007 discuss lenses observed in outcrops and plaster of Paris analogue modelling. Their research provides information on the formation and shape, but not on the size of sandstone lenses. They show that lenses are commonly formed by segment linkage. Segment linkage is controlled by mechanical stratigraphy (Wilkins and Gross 2001, Ferril and Morris, 2008, Childs et al., 2009), suggesting a tool for the maximum length of sandstone lenses can be developed using the thickness of (sandstone) mechanical units. Lindanger et al., 2007 shows that lenses are broken down to smaller lenses with progressive deformation.

Evaluation of shale smearing and sandstone lens formation can be used to make fault seal and permeability prediction more reliable. Object-based modelling approaches can be used to include these processes into flow models (e.g. Jolley et al., 2007, Fredman et al., 2008), giving a more realistic model for the fault zone. However several uncertainties remain. Most importantly, the distribution of the shale incorporated as detached smears is unknown. In addition several other processes can affect fault architecture and permeability.

9.3 Full architecture evaluation

The approaches discussed so far are ways to quickly improve the prediction of fault bulk permeability. However as shown in this thesis, the bulk permeability of a fault zone is dependent on the architecture of the fault zone, which results from an extensive set of processes. To come up with the best possible prediction of fault permeability and a reliable estimate of uncertainty, all these processes need to be evaluated. The data presented in this thesis highlight the many processes active during faulting and how these processes are interdependent. The current data are not sufficient to properly quantify the relationship between different processes, host rock parameters, fault kinematics, pressure, temperature and fluid flow history. To make this possible more data are needed. Pooling data from many researchers from academia and industry seems the way forward to generate the critical mass of data required. With sufficient data the processes affecting fault architecture and permeability can be fully evaluated. This can be used to design advanced workflows for estimating fault sealing and permeability and the associated uncertainty.

Figure 9.1 presents a framework for such a workflow as a decision tree. It is important to note that this workflow is presented as a hypothesis rather than a finished product. A large dataset of fault observations is necessary to provide the quantitative underpinning required to make this applicable for usage in industry workflows. The framework presented here is based primarily on the faults studied for this thesis. These faults all formed in moderately consolidated sand-shale sequences. Further research is necessary to extend the framework to unconsolidated, overconsolidated and low grade metamorphic rock sequences.

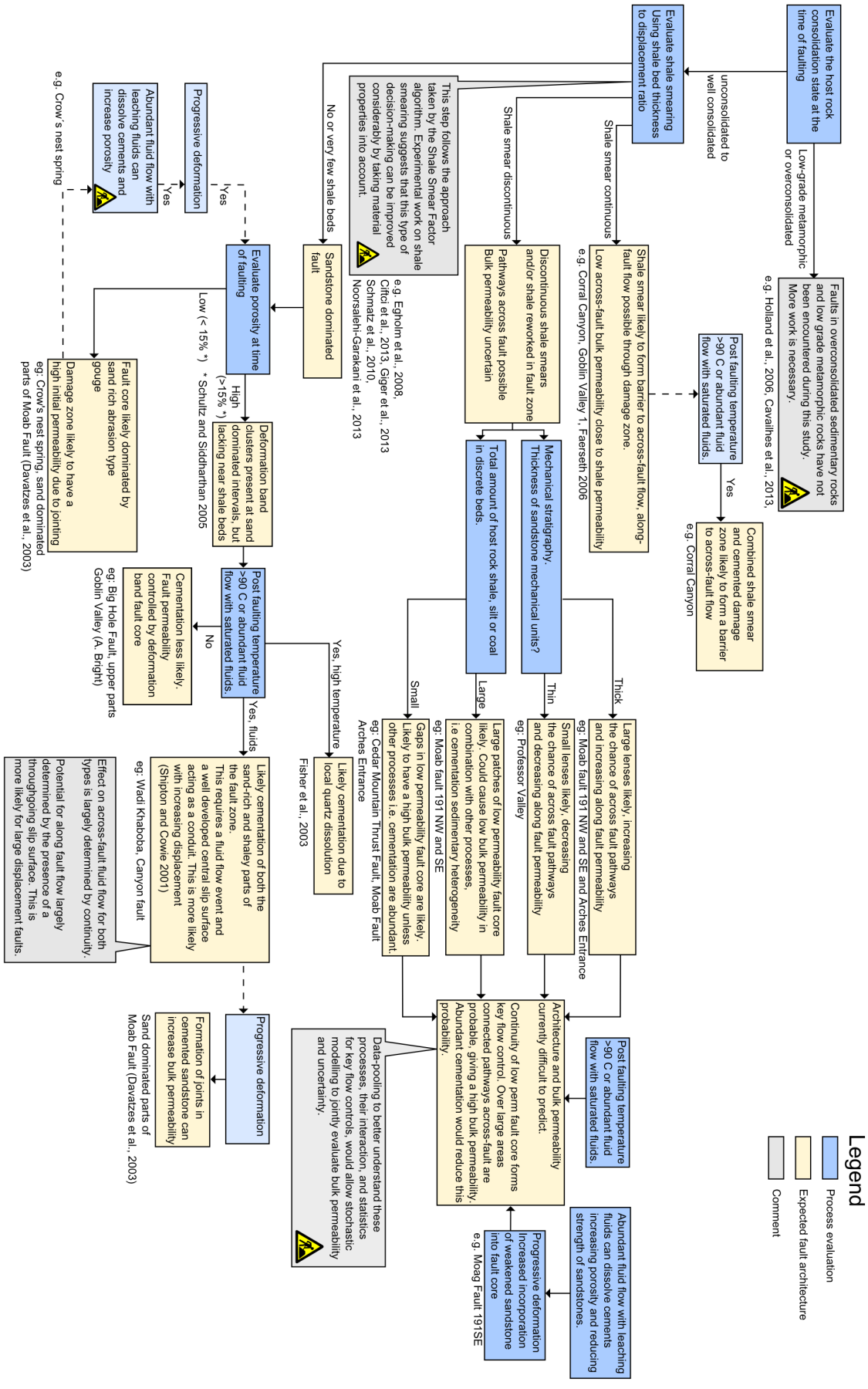

Figure 9.1: Decision tree for fully evaluating fault core architecture.

The first step is to analyze the detailed host rock stratigraphy. This allows a crude subdivision of basic fault architectural processes. Using the thickness of smearable beds (shale, silt, coal, salt), the role of smearing can be evaluated. The SSF algorithm provides a basic tool for distinguishing between faults with a high probability of continuous smears and those with a low probability of continuous smears. The Shale Smear Factor is simple to use, but several caveats exist. First of all the threshold value does not separate continuous shale smears from discontinuous shale smears. Figure 9.2 shows the original dataset from Lindsay et al., 1993, showing that faults with an SSF of 7 and lower all have a continuous smear, and faults with a higher SSF value can either have a continuous smear or a discontinuous smear. The actual level of the threshold is debated; Lindsay et al., 1993 suggest a value of 7 based on their observations on faults with relatively small throw (up to 15m). Faerseth 2006 suggests that for small (subseismic) faults the shale smear factor threshold is highly variable (1-50). For seismic scale faults he recommends an SSF threshold values of 4. Work by Clausen and Gabrielsen 2002, Egholm et al., 2008, Schmatz et al., 2010, Giger et al., 2013 and Ciftci et al., 2013 show that a variety of material properties (shale competence, shale water content, shale-sand competency contrast) and effective stress can affect the shale smearing process. Similarly the smearing properties of silt, coal and salt are likely to differ from those of shale. As such there is potential to develop a calibrated version of the SSF algorithm, incorporating the smearing properties of different materials and the stress state at the time of faulting.

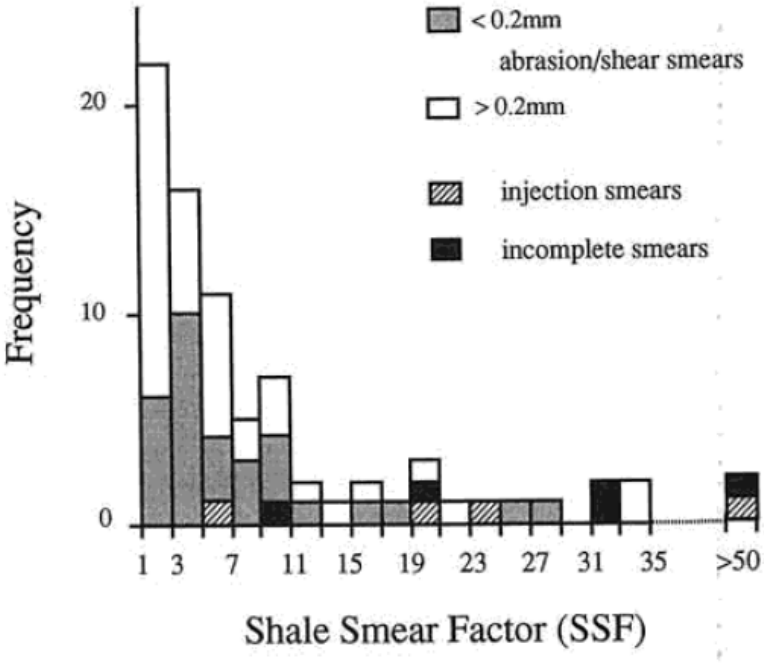

Figure 9.2: Shale Smear Factor observations from Lindsay et al., 1993.

For faults with a continuous smear, the across-fault bulk permeability can be predicted to be close to the permeability of the smeared lithology. The bulk permeability can simply be calculated as the thickness-weighted harmonic average of the footwall host rock, smear and hanging wall host rock. along-fault flow will depend on the properties of the damage zone. At both continuous smear outcrops evaluated in this study (Moab fault Corral Canyon and Goblin Valley I) evidence for along-fault paleo fluid flow has been observed. As can be seen at the

Corral Canyon exposure such fluid flow can further reduce the permeability of the fault zone by causing dense cementation of the damage zone.

For faults developed in host rocks where shale is abundant but not concentrated in sufficiently thick beds relative to displacement, smearing is not likely to form continuous smears. Here the prediction becomes more complicated. Shale will be incorporated into the fault zone as detached smears, locally affecting the permeability and mechanics of the fault zone. Progressive deformation can rework detached smears and redistribute the shale through the fault zone. As the thickness of the smear is related to the thickness of the donor bed (with possible further calibration from material properties), this gives an estimate of the amount of shale occurring inside the entire fault zone.

Several outcrops in this thesis show architectures consisting of a complex assemblage of small smears of shale and silt and lenses of sandstone and other competent lithologies, with slip surfaces in between the different elements (i.e. Moab fault 191SE, 191NE, Arches Entrance, Professor Valley and Cedar Mountain thrust). Faults consisting of such assemblages are highly heterogeneous and their bulk permeabilities are highly variable. The main control on the bulk permeability for across-fault flow is formed by the presence of connected pathways across the fault core. Such pathways can be formed by sandstone lenses and/or open slip surfaces. In addition, the permeability of these elements can change over time. The permeability of slip surfaces is likely to be dependent on the local stress state and fault reactivation. The permeability of sandstone lenses can be affected by both geochemical and mechanical processes. Exposure to high temperatures or abundant flow of saturated fluids is likely to cause cementation, reducing the permeability of the sandstone lenses (e.g. Ecihhubl et al., 2009). Conversely flow of leaching fluids can dissolve existing cements, increasing porosity and permeability while reducing sandstone competence. Mechanical deformation of sandstone lenses can be accommodated by fracturing, brecciation or formation of deformation bands, depending on the porosity of the sandstone. Cementation of the sandstone by fluids or high temperatures can reduce the porosity, causing a change of deformation mode from deformation bands to fracturing (Fisher et al., 2003, Johansen et al., 2005, Eichhubl et al., 2009). With the currently available data it is difficult to make a good prediction for the bulk permeability for these faults. Considering the likely presence of sandstone lenses and slip surfaces, it is likely that pathways across the fault exist, suggesting a relatively high bulk permeability for across-fault flow. These lenses and slip surfaces are also likely to increase the permeability for along-fault flow. These pathways could potentially be closed off by cementation. As such, abundant along-fault flow of saturated fluids or high temperatures ($>90^o$) could strongly reduce the bulk permeability for across-fault flow. Evaluating the fluid flow history of the basin could therefore improve the prediction of this type of fault.

To make more robust predictions for deformabtion band cluster faults, will require a dataset of many more field observations. With sufficient data, it is possible to develop a better understanding of the processes active. This will allow the development of predictive schemes based on rock mechanics and geochemistry quantified by statistical observations. Stochastic modelling tools can be developed using these schemes to calculate both permeability and uncertainty.

Faults displacing sequences without shale, silt or coal beds will develop different architectures than those which do. Faults displacing sequences with very few and thin shale beds will develop both architectures, with sandstone type faulting where the fault juxtaposes only sandstone and smearing near the shale or silt beds. The nature of sandstone faulting is controlled primarily

by the porosity of the sandstone. High porosity sandstones form fault cores dominated by deformation band cluster fault rock. In the damage zone, strain is accommodated by the formation of deformation bands rather than fracturing. The effect on fluid flow is controlled by the thickness and permeability of the fault core (Shipton et al., 2002). The work in chapter 7 shows that the along-fault variation in thickness can be modelled using spatial statistics. This study addresses variation over short distances (1-20 m). Variation over larger distances seems to be controlled by stratigraphic changes and fault segmentation, but this requires further research. Further research is needed to understand this larger scale variation and relate it to common hydrocarbon industry parameters. Variation in the permeability of the fault core is less well understood. Both Shipton et al., 2002 and Tueckmantel 2010 shows a fault core permeability variation of 1 to 3 orders of magnitude per fault. No data are currently available for the spatial nature of the permeability variation. The modelling in chapter 7 shows that statistical characterization of fault zones can be a powerful tool. With more research on the large scale fault core thickness variation and the spatial variation of permeability, this can be developed into a reliable tool for predicting the permeability and uncertainty of this type of fault on a reservoir scale. Faults formed in low porosity sandstone form a very different fault architecture. Low porosity sandstone accommodates strain by fracturing. Faults initiate by the localization of shear along pre-existing discontinuities, leading to the development of splay fractures linking the pre-existing joints. Continued deformation leads to the development of a through-going slip surface (Davatzes and Aydin 2003, Davatzes et al., 2003, Davatzes and Aydin, 2005). Intense fracturing can create breccias in the fault core. Abrasion can further break down the fault rocks to a sand dominated gouge. These faults can therefore be expected to have a relatively high across-fault permeability. The damage zone forms by fracturing and is therefore likely to contribute to a high along-fault permeability. Both fluid flow history and temperature should be considered because cementation could strongly reduce both the across-fault and along-fault permeability.

Bibliography

- Ahmadov, R., A. Aydin, M. Karimi-Fard, and L. J Durlofsky. 2007. 'Permeability Upscaling of Fault Zones in the Aztec Sandstone, Valley of Fire State Park, Nevada, with a Focus on Slip Surfaces and Slip Bands'. Hydrogeology Journal 15 (7): 1239–50.
- Allan, U. S. 1989. 'Model for Hydrocarbon Migration and Entrapment within Faulted Structures'. AAPG Bulletin 73 (7): 803–11.
- Aydin, A. 1978. 'Small Faults Formed as Deformation Bands in Sandstone'. Pure and Applied Geophysics 116 (4): 913–30.
- Aydin, A., and Y. Eyal. 2002. 'Anatomy of a Normal Fault with Shale Smear: Implications for Fault Seal'. AAPG Bulletin 86 (8): 1367.
- Barton, Colleen A., Mark D. Zoback, and Daniel Moos. 1995. 'Fluid Flow along Potentially Active Faults in Crystalline Rock'. Geology 23 (8): 683. doi:10.1130/0091-7613(1995)023<0683:FFAPAF>2.3.CO;2.
- Bense, Victor Franciscus. 2004. 'The Hydraulic Properties of Faults in Unconsolidated Sediments and Their Impact on Groundwater Flow: A Study in the Roer Valley Rift System and Adjacent Areas in the Lower Rhine Embayment'. S.l.: s.n.].
- Boles, James R., Peter Eichhubl, Grant Garven, and Jim Chen. 2004. 'Evolution of a Hydrocarbon Migration Pathway along Basin-Bounding Faults: Evidence from Fault Cement'. AAPG Bulletin 88 (7): 947–70.
- Bouvier, J. D., C. H. Kaars-Sijpesteijn, D. F. Kluesner, C. C. Onyejekwe, and R. C. van der Pal. 1989. 'Three-Dimensional Seismic Interpretation and Fault Sealing Investigations, Nun River Field, Nigeria'. AAPG Bulletin 73 (11): 1397–1414.
- Braathen, A., J. Tveranger, H. Fossen, T. Skar, N. Cardozo, S. E. Semshaug, E. Bastesen, and E. Sverdrup. 2009. 'Fault Facies and Its Application to Sandstone Reservoirs'. AAPG Bulletin 93 (7): 891.
- Bretan, P., G. Yielding, and H. Jones. 2003. 'Using Calibrated Shale Gouge Ratio to Estimate Hydrocarbon Column Heights'. AAPG Bulletin 87 (3): 397.
- Bright, A.M. 2006. 'Characterising the Structure and Petrophysical Properties of Deformation Band Fault Cores in Reservoir Sandstone'. PhD, Trinity College, Dublin.
- Caine, J. S, J. P Evans, and C. B Forster. 1996. 'Fault Zone Architecture and Permeability Structure'. Geology 24 (11): 1025.

- Cartwright, Joe, Mads Huuse, and Andrew Aplin. 2007. 'Seal Bypass Systems'. AAPG Bulletin 91 (8): 1141–66. doi:10.1306/04090705181.
- Cerveny, K, R Davies, G Dudley, R Fox, P Kaufman, R Knipe, and B Krantz. 2004. 'Reducing Uncertainty with Fault-Seal Analysis'. Oilfield Review 16 (4).
- Chan, M. A, W. T. Parry, and J. R. Bowman. 2000. 'Diagenetic Hematite and Manganese Oxides and Fault-Related Fluid Flow in Jurassic Sandstones, Southeastern Utah'. AAPG Bulletin 84 (9): 1281.
- Chan, Marjorie A., William T. Parry, Erich U. Petersen, and Chris M. Hall. 2001. '40Ar/39Ar Age and Chemistry of Manganese Mineralization in the Moab and Lisbon Fault Systems, Southeastern Utah'. Geology 29 (4): 331–34. doi:10.1130/0091-7613(2001)029<0331:AAAA
- Childs, C. J., T. Manzocchi, J. J. Walsh, and M. P. J. Schopfer. 2012. 'Fault Core/damage Zone; an Unhelpful Description of Fault Zone Structure?' In . http://earthdoc.eage.org/publication/publicationdetails/?publication=62786.
- Childs, C., Ø. Sylta, S. Moriya, J. J. Walsh, and T. Manzocchi. 2002. 'A Method for Including the Capillary Properties of Faults in Hydrocarbon Migration Models'. In Norwegian Petroleum Society Special Publications, edited by Andreas G. Koestler and Robert Hunsdale, Volume 11:127–39. Hydrocarbon Seal Quantification Norwegian Petroleum Society Conference. Elsevier.

  http://www.sciencedirect.com/science/article/pii/S092889370280011X.
- Childs, Conrad, Tom Manzocchi, John J. Walsh, Christopher G. Bonson, Andrew Nicol, and Martin P.J. Schöpfer. 2009. 'A Geometric Model of Fault Zone and Fault Rock Thickness Variations'. Journal of Structural Geology 31 (2): 117–27. doi:10.1016/j.jsg.2008.08.009.
- Çiftçi, N. Bozkurt, Silvio B. Giger, and Michael B. Clennell. 2013. 'Three-Dimensional Structure of Experimentally Produced Clay Smears: Implications for Fault Seal Analysis'. AAPG Bulletin 97 (5): 733–57. doi:10.1306/10161211192.
- Clarke, Stuart M., Stuart D. Burley, and Graham D. Williams. 2005. 'A Three-Dimensional Approach to Fault Seal Analysis: Fault-Block Juxtaposition & Argillaceous Smear Modelling'. Basin Research 17 (2): 269–88. doi:10.1111/j.1365-2117.2005.00263.x.
- Clausen, J. A, and R. H Gabrielsen. 2002. 'Parameters That Control the Development of Clay Smear at Low Stress States: An Experimental Study Using Ring-Shear Apparatus'. Journal of Structural Geology 24 (10): 1569–86.
- Corona, F. V., J. S. Davis, S. J. Hippler, and P. J. Vrolijk. 2010. 'Multi-Fault Analysis Scorecard: Testing the Stochastic Approach in Fault Seal Prediction'. Geological Society, London, Special Publications 347 (1): 317–32. doi:10.1144/SP347.18.
- Crain, E. R.. 2013. 'Crain's Petrophysical Handbook, Online Shareware Petrophysics Training and Reference Manual', url:http://www.spec2000.net, Accessed: December 2013.

- Damsleth, Elvind, Charlotte Tjolsen, Henning Omre, and Helge Haldorsen. 1992. 'A Two-Stage Stochastic Model Applied to a North Sea Reservoir'. Journal of Petroleum Technology 44. doi:10.2118/20605-PA. http://www.onepetro.org/mslib/servlet/onepetropreview?id=00020605&soc=SPE.

- Davatzes, N. C., and A. Aydin. 2003. 'Overprinting Faulting Mechanisms in High Porosity Sandstones of SE Utah'. Journal of Structural Geology 25 (11): 1795–1813.

- Davatzes, N. C., and A. Aydin. 2005. 'Distribution and Nature of Fault Architecture in a Layered Sandstone and Shale Sequence: An Example from the Moab Fault, Utah'. MEMOIRS-AMERICAN ASSOCIATION OF PETROLEUM GEOLOGISTS 85: 153.

- Dee, S., B. Freeman, G. Yielding, A. Roberts, and P. Bretan. 2005. 'Best Practice in Structural Geological Analysis'. First Break 23 (4). http://www.earthdoc.org/publication/publicationdetails/?publication=26500.

- Dockrill, Ben, and Zoe K. Shipton. 2010. 'Structural Controls on Leakage from a Natural CO2 Geologic Storage Site: Central Utah, USA'. Journal of Structural Geology 32 (11): 1768–82.

- Doelling, Hellmut H., Charles Gifford Oviatt, and Peter W. Huntoon. 1988. Salt Deformation in the Paradox Region. Utah Geological Survey.

- Egholm, D. L., O. R. Clausen, M. Sandiford, M. B. Kristensen, and J. A. Korstg\aard. 2008. 'The Mechanics of Clay Smearing along Faults'. Geology 36 (10): 787–90.

- Eichhubl, P., N. C Davatz, and S. P Becker. 2009. 'Structural and Diagenetic Control of Fluid Migration and Cementation along the Moab Fault, Utah'. AAPG Bulletin 93 (5): 653.

- Eichhubl, Peter, and James R. Boles. 2000. 'Focused Fluid Flow along Faults in the Monterey Formation, Coastal California'. Geological Society of America Bulletin 112 (11): 1667–79.

- Eichhubl, Peter, Peter S. D'Onfro, Atilla Aydin, John Waters, and Douglas K. McCarty. 2005. 'Structure, Petrophysics, and Diagenesis of Shale Entrained along a Normal Fault at Black Diamond Mines, California–Implications for Fault Seal'. AAPG Bulletin 89 (9): 1113–37. doi:10.1306/04220504099.

- Evans, James P., Craig B. Forster, and James V. Goddard. 1997. 'Permeability of Fault-Related Rocks, and Implications for Hydraulic Structure of Fault Zones'. Journal of Structural Geology 19 (11): 1393–1404. doi:10.1016/S0191-8141(97)00057-6.

- Fachri, Muhammad, Jan Tveranger, Nestor Cardozo, and Øystein Pettersen. 2011. 'The Impact of Fault Envelope Structure on Fluid Flow: A Screening Study Using Fault Facies'. AAPG Bulletin 95 (4): 619–48. doi:10.1306/09131009132.

- Faerseth, R. B. 2006. 'Shale Smear along Large Faults: Continuity of Smear and the Fault Seal Capacity'. Journal of Geological Society 163 (5): 741.

- Faerseth, R.B., E. Johnsen, and S. Sperrevik. 2007. 'Methodology for Risking Fault Seal Capacity: Implications of Fault Zone Architecture'. AAPG Bulletin 91 (9): 1231.

- Fairley, Jerry. 2003. 'Geostatistical Evaluation of Permeability in an Active Fault Zone'. Geophysical Research Letters 30 (18). doi:10.1029/2003GL018064. http://doi.wiley.com/10.1029/2003GL018064.
- Faulkner, D.R, A.C Lewis, and E.H Rutter. 2003. 'On the Internal Structure and Mechanics of Large Strike-Slip Fault Zones: Field Observations of the Carboneras Fault in Southeastern Spain'. Tectonophysics 367 (3-4): 235–51. doi:10.1016/S0040-1951(03)00134-3.
- Faulkner, D.R., C.A.L. Jackson, R.J. Lunn, R.W. Schlische, Z.K. Shipton, C.A.J. Wibberley, and M.O. Withjack. 2010. 'A Review of Recent Developments Concerning the Structure, Mechanics and Fluid Flow Properties of Fault Zones'. Journal of Structural Geology 32 (11): 1557–75. doi:10.1016/j.jsg.2010.06.009.
- Ferrill, David A, John A Stamatakos, and Darrell Sims. 1999. 'Normal Fault Corrugation: Implications for Growth and Seismicity of Active Normal Faults'. Journal of Structural Geology 21 (8–9): 1027–38. doi:10.1016/S0191-8141(99)00017-6.
- Ferrill, David A., and Alan P. Morris. 2008. 'Fault Zone Deformation Controlled by Carbonate Mechanical Stratigraphy, Balcones Fault System, Texas'. AAPG Bulletin 92 (3): 359–80. doi:10.1306/10290707066.
- Ferrill, David A., Alan P. Morris, and Ronald N. McGinnis. 2009. 'Crossing Conjugate Normal Faults in Field Exposures and Seismic Data'. AAPG Bulletin 93 (11): 1471–88. doi:10.1306/06250909039.
- Fisher, Quentin J., Martin Casey, Simon D. Harris, and Robert J. Knipe. 2003. 'Fluid-Flow Properties of Faults in Sandstone: The Importance of Temperature History'. Geology 31 (11): 965–68.
- Flodin, E. A, L. J Durlofsky, and A. Aydin. 2004. 'Upscaled Models of Flow and Transport in Faulted Sandstone: Boundary Condition Effects and Explicit Fracture Modelling'. Petroleum Geoscience 10 (2): 173.
- Foxford, K. A., J. J. Walsh, J. Watterson, I. R. Garden, S. C. Guscott, and S. D. Burley. 1998. 'Structure and Content of the Moab Fault Zone, Utah, USA, and Its Implications for Fault Seal Prediction'. Geological Society London Special Publications 147 (1): 87.
- Fredman, N., J. Tveranger, N. Cardozo, A. Braathen, H. Soleng, P. Røe, A. Skorstad, and A. R. Syversveen. 2008. 'Fault Facies Modeling: Technique and Approach for 3-D Conditioning and Modeling of Faulted Grids'. AAPG Bulletin 92 (11): 1457–78. doi:10.1306/06090807073.
- Fristad, T., A. Groth, G. Yielding, and B. Freeman. 1997. 'Quantitative Fault Seal Prediction: A Case Study from Oseberg Syd'. Norwegian Petroleum Society Special Publications 7: 107–24.
- Gabrielsen, and J. A Clausen. 'Horses and Duplexes in Extensional Regimes: A Scale-Modeling Contribution'. In Tectonic Modeling: A Volume in Honor of Hans Ramberg (eds: Ramberg,H., Koyi,H.A., Mancktelow, N.S.). Geological Society of America 193.

- Garden, I. R., S. C. Guscott, S. D. Burley, K. A. Foxford, J. J. Walsh, and J. Marshall. 2001. 'An Exhumed Palaeo-Hydrocarbon Migration Fairway in a Faulted Carrier System, Entrada Sandstone of SE Utah, USA'. Geofluids 1 (3): 195–213.

- Giger, S. B., M. B. Clennell, C. Harbers, P. Clark, M. Ricchetti, J. H. Ter Heege, B. B. T. Wassing, and B. Orlic. 2011. 'Design, Operation and Validation of a New Fluid-Sealed Direct Shear Apparatus Capable of Monitoring Fault-Related Fluid Flow to Large Displacements'. International Journal of Rock Mechanics and Mining Sciences 48 (7): 1160–72. doi:10.1016/j.ijrmms.2011.09.005.

- Giger, Silvio B., Michael B. Clennell, N. Bozkurt Çiftçi, Craig Harbers, Peter Clark, and Mark Ricchetti. 2013. 'Fault Transmissibility in Clastic-Argillaceous Sequences Controlled by Clay Smear Evolution'. AAPG Bulletin 97 (5): 705–31. doi:10.1306/10161211190.

- Gloyn, R.W., C.D Morgan, D.E. Tabet, R.E. Blackett, B.T. Tripp, and M. Lowe. 1995. 'Mineral, Energy, and Ground-Water Resources of San Juan County, Utah'. Utah Geological Survey, Special Study 86, Salt Lake City, Utah, 1995.

- Haldorsen, H. H., and E. Damsleth. 1990. 'Stochastic Modeling' 42 (4): 404–17.

- Harbaugh, A. W., E.R. Banta, M.C. Hill, and M. G. McDonald. 2000. 'MODFLOW-2000, the U.S. Geological Survey Modular Ground-Water Model – User Guide to Modularization Concepts and the Ground-Water Flow Process'. 00-92. USGS Open-File Report. http://water.usgs.gov/nrp/gwsoftware/modflow2000/ofr00-92.pdf.

- Harris, D., G. Yielding, P. Levine, G. Maxwell, P. T. Rose, and P. Nell. 2002. 'Using Shale Gouge Ratio (SGR) to Model Faults as Transmissibility Barriers in Reservoirs: An Example from the Strathspey Field, North Sea'. Petroleum Geoscience 8 (2): 167.

- Heynekamp, Michiel R., Laurel B. Goodwin, Peter S. Mozley, and William C. Haneberg. 1999. 'Controls on Fault-Zone Architecture in Poorly Lithified Sediments, Rio Grande Rift, New Mexico: Implications for Fault-Zone Permeability and Fluid Flow'. Faults and Subsurface Fluid Flow in the Shallow Crust: 27–49.

- Hintze, Lehi F., Grant C. Willis, Denise YM Laes, Douglas A. Sprinkel, and Kent D. Brown. 2000. Digital Geologic Map of Utah. Utah Geological Survey, Utah Department of Natural Resources.

- Ilg, Bradley R., Samuel Hemmings-Sykes, Andrew Nicol, Jan Baur, Miko Fohrmann, Rob Funnell, and Mike Milner. 2012. 'Normal Faults and Gas Migration in an Active Plate Boundary, Southern Taranaki Basin, Offshore New Zealand'. AAPG Bulletin 96 (9): 1733–56. doi:10.1306/02011211088.

- Jackson, C. A. L., R. L. Gawthorpe, and I. R. Sharp. 2006. 'Style and Sequence of Deformation during Extensional Fault-Propagation Folding: Examples from the Hammam Faraun and El-Qaa Fault Blocks, Suez Rift, Egypt'. Journal of Structural Geology 28 (3): 519–35.

- Johansen, Tord Erlend Skeie, Haakon Fossen, and Richard Kluge. 2005. 'The Impact of Syn-Faulting Porosity Reduction on Damage Zone Architecture in Porous Sandstone:

An Outcrop Example from the Moab Fault, Utah'. Journal of Structural Geology 27 (8): 1469–85. doi:10.1016/j.jsg.2005.01.014.

- Jolley, S. J., D. Barr, J. J. Walsh, and R. J. Knipe. 2007. 'Structurally Complex Reservoirs: An Introduction'. Geological Society, London, Special Publications 292 (1): 1–24. doi:10.1144/SP292.1.

- Jourde, H., F. Cornaton, S. Pistre, and P. Bidaux. 2002. 'Flow Behavior in a Dual Fracture Network'. Journal of Hydrology 266 (1-2): 99–119.

- Kampman, Niko, Neil M. Burnside, Zoe K. Shipton, Hazel J. Chapman, Joe A. Nicholl, Rob M. Ellam, and Mike J. Bickle. 2012. 'Pulses of Carbon Dioxide Emissions from Intracrustal Faults Following Climatic Warming'. Nature Geoscience 5 (5): 352–58.

- Klinkenberg, L.J. 1941. 'The Permeability of Porous Media to Liquids and Gases, Drilling and Production Practice'. In American Petroleum Institute.

- Knipe, R. J. 1997. 'Juxtaposition and Seal Diagrams to Help Analyze Fault Seals in Hydrocarbon Reservoirs'. AAPG Bulletin 81 (2): 187–95.

- Knott, Steven D., Alastair Beach, Paul J. Brockbank, J. Lawson Brown, Jean E. McCallum, and Alastair I. Welbon. 1996. 'Spatial and Mechanical Controls on Normal Fault Populations'. Journal of Structural Geology 18 (2): 359–72.

- Koledoye, Bashir A., Atilla Aydin, and Eric May. 2003. 'A New Process-Based Methodology for Analysis of Shale Smear along Normal Faults in the Niger Delta'. AAPG Bulletin 87 (3): 445–63. doi:10.1306/08010200131.

- Kora, M., A. El Shahat, and M. Abu Shabana. 1994. 'Lithostratigraphy of the Manganese-Bearing Um Bogma Formation, West-Central Sinai, Egypt'. Journal of African Earth Sciences 18 (2): 151–62.

- Kristensen, M.B., C. Childs, N.ø. Olesen, and J.A. Korstgård. 2013. 'The Microstructure and Internal Architecture of Shear Bands in Sand–clay Sequences'. Journal of Structural Geology 46: 129–41. doi:10.1016/j.jsg.2012.09.015.

- Lehner, F. K., and W. F. Pilaar. 1997. 'The Emplacement of Clay Smears in Synsedimentary Normal Faults: Inferences from Field Observations near Frechen, Germany'. P. Moller-Pederson and AG Koestler, Hydrocarbon Seals: Importance for Exploration and Production: Norwegian Petroleum Society Special Publication 7: 15–38.

- Leveille, G. P, R. Knipe, C. More, D. Ellis, G. Dudley, G. Jones, Q. J Fisher, and G. Allinson. 1997. 'Compartmentalization of Rotliegendes Gas Reservoirs by Sealing Faults, Jupiter Field Area, Southern North Sea'. Petroleum Geology of the Southern North Sea: Future Potential: 87–104.

- Lindanger, Merethe, Roy H. Gabrielsen, and Alvar Braathen. 2007. 'Analysis of Rock Lenses in Extensional Faults'. NORSK GEOLOGISK TIDSSKRIFT 87 (4): 361.

- Lindsay, N. G., F. C. Murphy, J. J. Walsh, and J. WATTERSON. 1993. 'Outcrop Studies of Shale Smears on Fault Surfaces'. International Association of Sedimentologists Special Publication 15 (1): 113–23.

- Losh, S., L. B. Eglinton, M. Schoell, and J. R. Wood. 1999. 'Vertical and Lateral Fluid Flow Related to a Large Growth Fault, South Eugene Island Block 330 Field, Offshore Louisiana'. AAPG Bulletin 83 (2): 244–76.

- Loucks, R. G., M. M. Dodge, and W. E. Galloway. 1979. 'Importance of Secondary Leached Porosity in Lower Tertiary Sandstone Reservoirs Along the Texas Gulf Coast'. Trans., Gulf Coast Assoc. Geol. Soc.; (United States) 29. http://www.osti.gov/scitech/biblio/6412987.

- Loveless, Sian, Victor Bense, and Jenni Turner. 2011. 'Fault Architecture and Deformation Processes within Poorly Lithified Rift Sediments, Central Greece'. Journal of Structural Geology 33 (11): 1554–68. doi:10.1016/j.jsg.2011.09.008.

- Luffel, D. L., C. W. Hopkins, and Schettler PD. 1993. 'Matrix Permeability Measurement of Gas Productive Shales'. In SPE Annual Technical Conference and Exhibition.

- Lunn, R. J., Z. K. Shipton, and A. M. Bright. 2008. 'How Can We Improve Estimates of Bulk Fault Zone Hydraulic Properties?' Geological Society London Special Publications 299 (1): 231.

- Maerten, Laurent, Paul Gillespie, and Jean-Marc Daniel. 2006. 'Three-Dimensional Geomechanical Modeling for Constraint of Subseismic Fault Simulation'. AAPG Bulletin 90 (9): 1337–58. doi:10.1306/03130605148.

- Maher, H. D., and A. Braathen. 2010. 'Løvehovden Fault and Billefjorden Rift Basin Segmentation and Development, Spitsbergen, Norway'. Geological Magazine 148 (01): 154–70. doi:10.1017/S0016756810000567.

- Manzocchi, T., A. E. Heath, B. Palananthakumar, C. Childs, and J. J. Walsh. 2008. 'Faults in Conventional Flow Simulation Models: A Consideration of Representational Assumptions and Geological Uncertainties'. Petroleum Geoscience 14 (1): 91.

- Manzocchi, T., J. J. Walsh, P. Nell, and G. Yielding. 1999. 'Fault Transmissibility Multipliers for Flow Simulation Models'. Petroleum Geoscience 5: 55–63.

- Morley, C. K., and M. Burhannudinnur. 1997. 'Anatomy of Growth Fault Zones in Poorly Lithified Sandstones and Shales: Implications for Reservoir Studies and Seismic Interpretation: Part 2, Seismic Reflection Geometries'. Petroleum Geoscience 3 (3): 225–31.

- Morris, Alan P., Kevin J. Smart, David A. Ferrill, Nathaniel E. Reish, and Peter F. Cowell. 2012. 'Production-Induced Fault Compartmentalization at Elk Hills Field, California'. AAPG Bulletin 96 (6): 1001–15. doi:10.1306/10241111030.

- Morrison, S. J., and W. T. Parry. 1986. 'Formation of Carbonate-Sulfate Veins Associated with Copper Ore Deposits from Saline Basin Brines, Lisbon Valley, Utah; Fluid Inclusion and Isotopic Evidence'. Economic Geology 81 (8): 1853–66. doi:10.2113/gsecongeo.81.8.1853.

- Nelson, Stephen T., Matthew T. Heizler, and Jon P. Davidson. 1992. New 40Ar/39Ar Ages of Intrusive Rocks from the Henry and La Sal Mountains, Utah. Utah Geological Survey.
  http://utah.ptfs.com/Data/Library2/publications/dc024929.pdf.

- Neuhauser, K. R. 1988. 'Sevier-Age Ramp-Style Thrust Faults at Cedar Mountain, Northwestern San Rafael Swell (Colorado Plateau), Emery County, Utah'. Geology 16 (4): 299–302. doi:10.1130/0091-7613(1988)016<0299:SARSTF>2.3.CO;2.

- Niño, Fernando, Hervé Philip, and Jean Chéry. 1998. 'The Role of Bed-Parallel Slip in the Formation of Blind Thrust Faults'. Journal of Structural Geology 20 (5): 503–16.

- Nuccio, Vito F., Steven M. Condon, and A. C. Huffman. 1996. Burial and Thermal History of the Paradox Basin, Utah and Colorado, and Petroleum Potential of the Middle Pennsylvanian Paradox Formation. US Government Printing Office. http://pubs.usgs.gov/bul/b2000o/b2000o.pdf.

- Olsthoorn, T.N. 2012. 'User Guide for mfLab'. https://code.google.com/p/mflab/.

- Ottesen Ellevset, S., R. J. Knipe, T. Svava Olsen, Q. J. Fisher, and G. Jones. 1998. 'Fault Controlled Communication in the Sleipner Vest Field, Norwegian Continental Shelf; Detailed, Quantitative Input for Reservoir Simulation and Well Planning'. Geological Society, London, Special Publications 147 (1): 283–97. doi:10.1144/GSL.SP.1998.147.01.19.

- Peacock, D. C. P., and D. J. Sanderson. 1994. 'Geometry and Development of Relay Ramps in Normal Fault Systems'. AAPG Bulletin (American Association of Petroleum Geologists);(United States) 78 (2). http://www.osti.gov/energycitations/product.biblio.jsp?osti_id=6965697.

- Power, William L., Terry E. Tullis, and John D. Weeks. 1988. 'Roughness and Wear during Brittle Faulting'. Journal of Geophysical Research: Solid Earth (1978–2012) 93 (B12): 15268–78.

- Remy, Nicolas, Alexandre Boucher, and Jianbing Wu. 2009. Applied Geostatistics with SGeMS: A User's Guide. Cambridge University Press.

- Revil, A., and L. M. Cathles. 1999. 'Permeability of Shaly Sands'. Water Resources Research 35 (3): 651–62. doi:10.1029/98WR02700.

- Rotevatn, A., A. Torabi, H. Fossen, and A. Braathen. 2008. 'Slipped Deformation Bands: A New Type of Cataclastic Deformation Bands in Western Sinai, Suez Rift, Egypt'. Journal of Structural Geology 30 (11): 1317–31.

- Rudolph, Tobias, Christian Melchers, Andreas Minke, and Wilhelm G. Coldewey. 2010. 'Gas Seepages in Germany: Revisited Subsurface Permeabilities in the German Mining District'. AAPG Bulletin 94 (6): 847–67. doi:10.1306/10210909074.

- Schmatz, J., P.J. Vrolijk, and J.L. Urai. 2010. 'Clay Smear in Normal Fault Zones – The Effect of Multilayers and Clay Cementation in Water-Saturated Model Experiments'. Journal of Structural Geology 32 (11): 1834–49. doi:10.1016/j.jsg.2009.12.006.

- Schöpfer, Martin P.J., Conrad Childs, and John J. Walsh. 2006. 'Localisation of Normal Faults in Multilayer Sequences'. Journal of Structural Geology 28 (5): 816–33. doi:10.1016/j.jsg.2006.02.003.

- Sharp, Ian R., Rob L. Gawthorpe, John R. Underhill, and Sanjeev Gupta. 2000. 'Fault-Propagation Folding in Extensional Settings: Examples of Structural Style and Synrift Sedimentary Response from the Suez Rift, Sinai, Egypt'. Geological Society of America Bulletin 112 (12): 1877–99.

- Shipton, Z. K., J. P. Evans, and L. B. Thompson. 2005. 'The Geometry and Thickness of Deformation-Band Fault Core and Its Influence on Sealing Characteristics of Deformation-Band Fault Zones'.

- Shipton, Z. K., A. M. Soden, J. D. Kirkpatrick, A. M. Bright, and R. J. Lunn. 2006. 'How Thick Is a Fault? Fault Displacement-Thickness Scaling Revisited'. GEOPHYSICAL MONOGRAPH-AMERICAN GEOPHYSICAL UNION 170: 193.

- Shipton, Zoe K., James P. Evans, Kim R. Robeson, Craig B. Forster, and Stephen Snelgrove. 2002. 'Structural Heterogeneity and Permeability in Faulted Eolian Sandstone: Implications for Subsurface Modeling of Faults'. AAPG Bulletin 86 (5): 863–83.

- Solum, J. G, B. A van der Pluijm, and D. R Peacor. 2005. 'Neocrystallization, Fabrics and Age of Clay Minerals from an Exposure of the Moab Fault, Utah'. Journal of Structural Geology 27 (9): 1563–76.

- Solum, John G., Nicholas C. Davatzes, and David A. Lockner. 2010. 'Fault-Related Clay Authigenesis along the Moab Fault: Implications for Calculations of Fault Rock Composition and Mechanical and Hydrologic Fault Zone Properties'. Journal of Structural Geology 32 (12): 1899–1911. doi:10.1016/j.jsg.2010.07.009.

- Sperrevik, Susanne, Paul A. Gillespie, Quentin J. Fisher, Trond Halvorsen, and Rob J. Knipe. 2002. 'Empirical Estimation of Fault Rock Properties'. In Norwegian Petroleum Society Special Publications, edited by Andreas G. Koestler and Robert Hunsdale, Volume 11:109–25. Hydrocarbon Seal Quantification Norwegian Petroleum Society Conference. Elsevier.

- Srodon, Jan, Victor A. Drits, Douglas K. McCarty, Jean CC Hsieh, and Dennis D. Eberl. 2001. 'Quantitative X-Ray Diffraction Analysis of Clay-Bearing Rocks from Random Preparations'. Clays and Clay Minerals 49 (6): 514–28.

- Stephan K. Matthäi, Atilla Aydin, David D. Pollard, and Stephen G. Roberts. 1998. 'Simulation of Transient Well-Test Signatures for Geologically Realistic Faults in Sandstone Reservoirs'. SPE Journal 3 (1): 62–76.

- Sverdrup, E., J. Helgesen, and J. Vold. 2003. 'Sealing Properties of Faults and Their Influence on Water-Alternating-Gas Injection Efficiency in the Snorre Field, Northern North Sea'. AAPG Bulletin 87 (9): 1437–58.

- Taylor, Thomas R., Melvyn R. Giles, Lori A. Hathon, Timothy N. Diggs, Neil R. Braunsdorf, Gino V. Birbiglia, Mark G. Kittridge, Calum I. Macaulay, and Irene S. Espejo. 2010. 'Sandstone Diagenesis and Reservoir Quality Prediction: Models, Myths, and Reality'. AAPG Bulletin 94 (8): 1093–1132.

- Tchalenko, J. S. 1970. 'Similarities between Shear Zones of Different Magnitudes'. Geological Society of America Bulletin 81 (6): 1625. doi:10.1130/0016-7606(1970)81[1625:SBSZOD]2.0.CO;2.

- Terzaghi, Ruth D. 1965. 'Sources of Error in Joint Surveys'. Geotechnique 15 (3): 287–304.
- Torabi, Anita, and Silje Støren Berg. 2011. 'Scaling of Fault Attributes: A Review'. Marine and Petroleum Geology 28 (8): 1444–60. doi:10.1016/j.marpetgeo.2011.04.003.
- Tueckmantel, C., Q. J Fisher, R. J Knipe, H. Lickorish, and S. M Khalil. 2010. 'Fault Seal Prediction of Seismic-Scale Normal Faults in Porous Sandstone: A Case Study from the Eastern Gulf of Suez Rift, Egypt'. Marine and Petroleum Geology 27 (2): 334–50.
- Van der Zee, W., J. L Urai, and P. D Richard. 2003. 'Lateral Clay Injection into Normal Faults'. GEOARABIA-MANAMA- 8: 501–22.
- Van der Zee, W., and J. L. Urai. 2005. 'Processes of Normal Fault Evolution in a Siliciclastic Sequence: A Case Study from Miri, Sarawak, Malaysia'. Journal of Structural Geology 27 (12): 2281–2300.
- Vrolijka, P., and B. A van der Pluijmb. 1999. 'Clay Gouge'. Journal of Structural Geology 21: 1039–48.
- Walsh, J. J., W. R. Bailey, C. Childs, A. Nicol, and C. G. Bonson. 2003. 'Formation of Segmented Normal Faults: A 3-D Perspective'. Journal of Structural Geology 25 (8): 1251–62.
- Walsh, J. J., J. Watterson, W. R. Bailey, and C. Childs. 1999. 'Fault Relays, Bends and Branch-Lines'. Journal of Structural Geology 21 (8): 1019–26.
- Watterson, J., C. Childs, and J. J. Walsh. 1998. 'Widening of Fault Zones by Erosion of Asperities Formed by Bed-Parallel Slip'. Geology 26 (1): 71–74.
- Watts, N. L. 1987. 'Theoretical Aspects of Cap-Rock and Fault Seals for Single-and Two-Phase Hydrocarbon Columns'. Marine and Petroleum Geology 4 (4): 274–307.
- Weber, K. J., G. Mandl, W. F. Pilaar, F. Lehner, and R. G. Precious. 1978. 'The Role of Faults in Hydrocarbon Migration and Trapping in Nigerian Growth Fault Structures'. In Offshore Technology Conference, 10:2643–53.
- Welch, Michael J., Rob J. Knipe, Christine Souque, and Russell K. Davies. 2009. 'A Quadshear Kinematic Model for Folding and Clay Smear Development in Fault Zones'. Tectonophysics 471 (3-4): 186–202. doi:10.1016/j.tecto.2009.02.008.
- Wu, F. T., L. Blatter, and H. Roberson. 1975. 'Clay Gouges in the San Andreas Fault System and Their Possible Implications'. Pure and Applied Geophysics 113 (1): 87–95.
- Yielding, G., B. Freeman, and D. T. Needham. 1997. 'Quantitative Fault Seal Prediction'. AAPG Bulletin 81 (6): 897–917.
- Yielding, G., J. A. Øverland, and G. Byberg. 1999. 'Characterization of Fault Zones for Reservoir Modeling: An Example from the Gullfaks Field, Northern North Sea'. AAPG Bulletin 83 (6): 925–51.

Appendix A

Dataset of studied faults

This file is included on the DVD-rom as a Microsoft Excel file and to ensure compatibility also provided as an XML file and a CSV file.

Appendix B

Flow Modelling Results

The images are included on the DVD rom as two Microsoft PowerPoint files; one for the DAFM permeability set and one for the LAFM permeability set. To ensure future compatibility, also PDF files are provided of the images.

Appendix C

Matlab functions developed for this thesis

The Matlab functions developed for this study are included on the DVD rom. Here a description is provided of the most important scipts and functions. The functions not discussed here provide a supporting role and should be kept in the same folder with the main functions.

Well logs and SGR

Well log digitization using image processing

Well logs used for this study consist of scans of old well logs from the 1950-1990s, the quality of the scans is variable. If the quality is good enough these can be digitized automatically using image processing. The scripts assume the logs to be black and white, with a single black log line and a black grid on white paper. Anything other than the log line and the grid should be cropped off using an image editing program (e.g. Gimp, Photoshop). Logs with more than one log-line on the same grid, or very poor quality logs need to be digitized manually, using GIS software.

The well logs are printed on gridded paper, this grid needs to be removed first. The function gridremover.m does this. Gridremover processes the image row by row (i.e. scanline). Rows consisting entirely of black pixels are discarded as being a horizontal grid line. For the remaining rows, the thickest patch of black pixels is detected and assumed to be the log line. All other black patches are removed as they are assumed to be vertical grid lines.

After removal of the grid lines, the log itself can be digitized using the function image2log.m. This function processes the image row by row. For each row, all black pixels are detected. The median of the pixel locations is assumed to be the centre of the line determining the log value. As the image resolution is much higher than the log resolution, the median of 10 rows is taken to further remove noise from the dataset. Inspection by the user is recommended to verify the quality of the conversion. Testing of these two functions have yielded good results for all but the worst quality log scans.

Usage:

```
% read in the well log image:  [IM, cmap] = imread( 'Well_4301910232_GR2_Cropped.gif'
);
```

```
% Remove the grid lines:
IMf = gridremover( IM);
% Process the filtered log:
[ logout, zout ] = image2log( IMf);
% Plot the log on top of the image to verify the results.
image(IM),
colormap(cmap)
hold on
plot(logout, zout)
```

The well logs can be scaled properly using the welllogscaler function, discussed in the section on manual well log digitization.

Manual well log digitization.

For well log scans of very poor quality, the image processing routines might not work as expected. In these cases, the scans will have to be digitized manually using GIS software. For this study ARCGIS has been used.

Steps:

- Import the scanned image file into ARCGIS.
- Create a shapefile for the log in ARCGIS
- Create one or more shapes in the shapefile, tracing the log line from the image.
- Create a shapefile for the scaling in the x-direction and a shapefile for the scale in the y-direction. To both files add a field called 'scale'.
- Using the x-scale shapefile, trace the left most grid line with one shape and the rightmost grid line using a second shape. For both lines set the scale attribute value to the value indicated on the log image.
- Using the y-scale shapefile, trace the top most grid line with one shape, the rightmost grid line using another shape and several horizontal grid lines in between (about 5- 10 lines should do, depending on the distortion of the scanned image). For all the lines set the scale attribute value to the value indicated on the log image.
- The shapefiles can be converted to log values using the MATLAB script wellogscaler.m.

Usage:

```
% Read in the shapefiles using the ykshaperead.m function.  Ykshaperead is an
alternative to the shaperead function from the Mathworks Mapping Toolbox.  As both
produce slightly different data structures, they can not be uses interchangeably.

logshp = ykshaperead( 'well4301910232_log.shp');
yscaleshp = ykshaperead( 'well4301910232_yscale.shp');
xscaleshp = ykshaperead( 'well4301910232_xscale.shp');
% Convert the shape files to well log data in MATLAB. The function has been written
for logs with depth recorded in feet.  Xlscaled is returned in the units of the
log, ylscaled is returned in feet, ylmtr is returned in metres.
```

```
[xlscaled, ylscaled, ylmtr] = welllogscaler( logshp, xscaleshp, yscaleshp )
```

Well Log processing

Index Gamma Ray Calculation The Index Gamma Ray value calculation is simply normalizing the gamma ray log. This can be done with the function normalize.m, which was developed for this study.

```
igr = normalize( gammaray );
```

larionov1969tertiary.m This function uses the Larionov 1969 function for rocks of Tertiary age, to convert an Index Gamma Ray log to a V-shale log. The function expects a vector igr containing the Index Gamma Ray values. The function does not require the depth of the sample.

```
vsh = larionov1969tertiary( igr)
```

larionov1969older.m This function uses the Larionov 1969 function for rocks older then Tertiary, to convert an Index Gamma Ray log to a V-shale log. The function expects a vector igr containing the Index Gamma Ray values. The function does not require the depth of the sample.

```
vsh = larionov1969older( igr)
```

SGR triangle diagrams

These diagrams can be calculated from a V-shale log using the function sgrtriangle_ri.m. This function expects a well log sampled at regular intervals. The well logs should be provided as two vectors, one vector z with the depth values and one vector vshale with the V-shale values. The function calculates and plots the triangle diagram. For best results it is recommended to only provide well data for the relevant section of the fault.

```
triangle = sgrtriangle_ri( z, vshale);
```

If necessary, vectors can be resampled to regular intervals using the commands: zi = linspace(min(z), max(z), 5*length(z)); vshalei = interp1(z, vsshale, zi);

This resamples the log to a regular depth interval, using 5 times as many samples as the original log, this should be precise enough to appropriately represent the log if the original sampling is fairly regular. Logs with large irregularities might need a higher value to appropriately represent the shape of the log.

Log2SVG.m

This functions renders well log data to an SVG (Scalable Vector Graphics) file. This file can be opened and edited in a variety of vector graphics programs and also displayed in most internet browsers.

Usage:

```
log2svg( z, logvalues, fnames, ftops, filename, logname )
```

It expects the following variables

z : vector of depth of log values

logvalues : vector with log values

fnames : cell array with formation top names

ftops : depths of picked formation tops

filename : name of svg file to write

Cell arrays can be entered using curly brackets:

```
fnames = {'Navajo', 'Kayenta', 'Entrada'};
```

Fault thickness (geo-)statistics

Shapetothicknesses.m Fault thicknesses can be quickly extracted from photos or maps using this script. First the image needs to be opened in a GIS program. Using the GIS software, lines are drawn reflecting the thickness along the fault, as if placing rulers across the fault. The lines need to be stored in a shapefile. This function calculates the lengths of the lines in the shapefile, only the euclidean distance between the first and last point of each line segment is calculated. x is the average x coordinate

Usage :

```
shape = shaperead( 'myshapefile.shp');
[x, l] = shapetothicknesses( shape );
```

The units of the resulting x and l variable depends on the units and scale set in the GIS before tracing the image. If no scale has been set, the thicknesses will be returned in pixels. Scaling can achieved by measuring a known length in the GIS, and using this to scale the variables in MATLAB.

1D Variogram analysis A variety of functions has been developed to calculate and plot experimental variograms for 1D (along-strike) data. It is also perfectly possible to calculate such variograms with conventional tools for 2D/3D data, just by entering all the y (or y and z) coordinates as 0 (or another constant value). These scripts have been developed for the purpose of convenience and greater control.

variogram1D.m This is the main function for plotting variograms for 1D data. It calculates and displays the experimental variogram of a 1D dataset.

```
[averages, bins] = variogram1d(xdata, values, numberofbins, showpaircount)
```

`xdata`: x-coordinates of the sampled points.

`values`: the values at those coordinates.

`numberofbins`: defines the number of bins for which the variogram (which is a histogram) is calculated.

`showpaircount` : A Boolean value, if set to TRUE, the variogram is labelled with the number of datapairs in each bin. The higher the number of datapairs per bin, the more reliable the shape of the variogram. For reliable results, each bin should at the very least contain 20 data pairs.

The result is displayed immediately, and if the output veriables are specified, given as:

`averages`: The average covariance for each domain.

`bins`: the boundary values of the bins used. If necessary for plotting, bincentres can be calculated using:

```
bincentres = ( bins(2:end)+bins(1:end-1) ) /2;
```

Variogram1dmanualbins.m This function is identical to variogram1d, except that the bins can be specified manually, using the extra parameter 'bins'. For example bins = [0, 1, 2, 8] will give three bins; 0-1, 1-2 and 2-8.

`[averages, bincentres] = variogram1dmanualbins(xdata, values, bins, showpaircount, style)`

variogram1dvaribins.m This function is identical to variogram1d, except that the bins are chosen to get a fixed number of pairs per bin.

`[averages, bincentres] = variogram1dvaribins(xdata, values, perbin)`

Variogrammodels.m This function is provided to calculate theoretical variograms.

`model = variogrammodels(x, p, type)`

`x` : the x-coordinates for the points to be calculated.

`type`: the type of model. The following variogram model types are supported: - 'linear' - 'linear_with_sill' - 'spherical' - 'exponential' - 'gausian'

`p`: The parameter p should be a 3x1 vector. With p(1) : nugget p(2) and p(3) : defining the shape of the theoretical variogram, the meaning of p(2) and p(3) depends on the chosen model.

Flow modelling through faults using MFLAB

MFLAB flow modelling

This thesis has made a lot of use of the MFLAB modelling system. This is a MATLAB toolkit developed by Theo Olsthoorn. It provides tools to define MODFLOW groundwater flow models in MATLAB. Several modifications have been made to the standard MFLAB files to optimize the workflow of modelling fluid flow through and along faults. To use the GMG solver in MOFLOW, support for this solver has been added to MFLAB. A modified version of MFLAB with this modification is included on the DVD-rom. The GMG solver can solve models with strong permeability contrasts much faster than the other solvers, and as such is very useful for modelling fluid flow through fault zones. In addition a slightly different workflow has been developed than the standard MFLAB workflow, using a separate set of scripts and functions. These are discussed here.

A standard MFLAB model consists of at least three files;

- mf_adapt.m : This file contains all the MATLAB code to define a model.
- mf_analyze.m: This file contains code to analyze the results produced by MODFLOW
- One excel (.xls, Excel 97) file with the same name as the basename defined in mf_adapt. This file contains all the MODFLOW settings, such as which solver to use.

Each MFLAB model is stored in it's own unique directory.

For this study a slightly different setup is used. For all models, the same mf_adapt and mf_analyze functions are used, which are stored in the 'yk_mf_code' directory. This directory needs to be added to the MATLAB search path, using the addpath function (e.g. `addpath( 'D:\MFLAB\yk_mf_code')`). Instead each model is defined using a file called 'mf_settings.m'.

In addition each model consists of a set of images. The names of these images are defined in mf_settings.m. The excel file with the appropriate name should be stored in the same directory.

The mf_analyze and mergemapandlegend functions rely on ImageMagick for their image processing and conversion. Imagemagick needs to be installed on the computer, it can be downloaded from www.imagemagick.org.

Settings in mf_settings.m: `basename='Moab191SE';`

The name of the model, used for all files produced for and by MODFLOW.

```
% Map for analysis:
[MAP, cmap] = imread('map_calibrated.gif');
```

Here the filename of the map is defined.

```
% Map for show:
baseimagefile = 'map.gif';
```

This is the filename of the map image used as the backdrop for the figures produced. This image can contain cosmetic differences compared to the map for analysis. Both maps should have exactly the same size.

```
% Specify if an alteration map is available for plotting,
% uncomment the altimagefile and change the name if it is.
altavailable = true;
altimagefile = 'map_alt.gif';
```

Set altavailable to true if alteration data has been mapped for the exposure. If true, a specific image in which the alteration is indicated should be provided, so it can be used as a backdrop for the results.

```
% Size of pixels in the image and subsequently grid cells in the model.
cellsize = 0.005; % 5 mm grid cells
```

This parameter is used to specify the size of the pixels in the image.

```
% Flow direction:
FlowDirection = 'vertical'
```

This parameter specifies 'vertical' flow (left to right side of the map) or horizontal flow (flow from the base to the top of the map).

```
% Vertical inflow range
inflowrange = 25:951;
```

In case of vertical flow, This specifies the cells in the bottom row which are open for fluid flow. This is used to simulate fluids flowing up through the fault core rather than bypassing it through the damage zone.

```
% Permeability assignment
imagevaluesused = [0, 1, 2 ];
namesandperms = { 'Shale', 1e-6, 'Fine sst', 58, 'Very fine sst', 5};
```

This specifies the conversion from pixel colour of the image to permeability of the grid cells. Imagevaluesused specifies the index values used in the map. Names and perms contains a set of value pairs, corresponding to the name and permeability (mD) of the image index values in the same order as imagevaluesused. Showcolormap can be used to find the index values of the colours in the image. Alternatively the image can be displayed using MATLAB's image command, and the datacursor can be used to find the index values.

Example:

```
% Read image into MATLAB: [IM, cmap] = imread( 'mymap.gif' );
% show image image(IM) colormap( cmap )
% show the colormap and indices:  showcolormap( cmap )
makenewlegend = true;
legendtouse = 'legendwithslipsurfaces.svg';
```

makenewlegend is a Boolean which determines if a new legend image is created from the permeability data and names supplied above (TRUE), or that an existing legend is loaded (FALSE). TRUE should usually work well, FALSE is useful for using a legend made/edited by the user. In this case a name for the legend to use should be specified in the legendtouse parameter. This should be an SVG file.

```
% colour of the streamlines; k for black, w for white, see matlab help plot
% for more examples streamlinestyle = '-k';
```

Specify the colour of the streamlines using standard MATLAB line style and colour specification. Please refer to the MATLAB documentation for more information (doc plot).

```
% Size of the scale bar to plot on top of the model
scale_bar_length = 1; %10 cm scale bar barlabel = '1 m';
```

Specify the length and label for the scale bar which gets added to the model.

Additional functions

Mf_setup.m This function which is the standard function form MFLAB, runs the model found in the current directory. If MODFLOW completes successfully, the line 'Normal termination of MODFLOW-2000' will show up in the MATLAB window. Normal termination of MODFLOW does not necessarily mean that the model is correct. This can be tested by calculating a mass balance error, which is performed automatically by mf_analyze and mf_bulkperm.

Mf_analyze.m This function reads the results produced by MODFLOW, calculates bulk permeability, and produces a set of figures visualizing the results. Figures are automatically saved in the model directory. The actual MATLAB figures are not automatically shown to the user, but kept hidden, as the constant popping up of figures can be annoying when analyzing multiple models at once. These hidden figures can be shown using 'unhidefigures.m', or cleared from memory by typing 'close all'. If the mass balance error is larger than the 1% threshold used in this study, the figures will be annotated with a red cross.

Mf_bulkperm.m This function calculated the bulk permeability in an identical way as mf_analyze, but does not generate all the figures, thereby saving time when the figures are not desired.

Makelegend2.m This function reads the mf_settings file and generates a legend using the permeability and name pairs. It looks up the colours in the image files.

Mergemapandlegend.m This processes the images created by mf_analyze and concatenates the result images with the legend images.

Mergemapandlegendalt.m Same as mergemapandlegend, except for the images with alteration.

fixslipsurfaces.m This function is used to validate and constrain the thickness of slip surfaces in the rasterized image used for generating the flow model. Conversion of vector maps to raster images sometimes leads to raster images with thicker slip surfaces. For correct representation of the slip surfaces, they should have a thickness of 1 pixel in the image. This script scans the slip surfaces and thins slip surfaces if necessary. Slip surface pixels which are removed, are replaced by the rocktype of the nearest pixels in the image. Careful inspection of the new image by the user using image editing software is still recommended. The fill bucket and/or Magic Wand selection tool, available in many image editors (e.g. Adobe PhotoShop, GIMP, Paint DotNet) are very useful tools for testing the flow compatibility of slip surfaces.

```
MAPOUT = fixslipsurfaces( MAP, slipsurfacevalue )
```

ShowColorMap.m This is a small helper function for visualizing the colormap of a GIF map read into MATLAB. It displays all the colours in the colormap, together with the corresponding index value. This can be used to quickly find the index values for permeability assignment in the mf_settings.m scripts.

[IM, cmap] = imread('myimagefile.gif'); function showcolormap(cmap);

Batch processing multiple models To run several models as a batch job, these need to be setup as follows:

- Each model is stored in its own directory
- All the model directories are stored in one directory with no directories without models.
- Move the MATLAB commandline to this main folder and type runallmodels. This will run all models.
- After completion type analyzeallmodels, this will run mf_analyze for all models in the directory. It will also merge the results with legend images. In addition an excel file will be created in the directory containing all the modelled bulk permeabilities and mass balance errors.
- The function allmodels_to_powerpoint, will take the resulting figures for each model and put them in a powerpoint file for easy analysis of all models.